

Synaptic modifications in hippocampal CA3 pyramidal cells in an Alzheimer's mouse model

Dissertation for the award of the degree

Doctor of Philosophy

by Département Sciences du vivant et de la santé, Université de Bordeaux
and Division of Mathematics and Natural Sciences, Georg-August-Universität Göttingen

submitted by **Pei Zhang**
June 2017, Bordeaux

Members of the Jury Committee:

Yoon Cho	Maître de Conférences at CNRS INCIA, France	President/Examiner
Hélène MARIE	Principal Investigator at CNRS IPMC, France	Reporter
Lionel Dahan	Maître de Conférences at CNRS CRCA, France	Reporter
André Fischer	Principal Investigator at DZNE, Germany	Co-supervisor
Christophe Mulle	Principal Investigator at CNRS IINS, France	Supervisor

Acknowledgements

First of all, I would like to express my heartfelt thanks to Dr. Christophe Mulle, for granting me this opportunity to explore in science, also for his patient instruction and help along my way in the last four years.

I would also like to say thanks to all the members of Mulle team, especially to Silvia Viana da Silva, Bernat Gonzalez, Adam Gorlewicz, Vincent Maingret, Jimmy George, Sabine Fièvre, Stefano Zucca for being there to help when I started patch-clamp, to Mario Carta, Marilena Griguoli, Gael Barthet, Thierry Amédée, Christophe Blanchet, Sandrine Pouvreau for generous help and instruction as experienced researchers, to Noelle Grosjean for all the work we've done together in behavioral experiments, to Severine Deforges, Audrey Lacquemant, Julie Rumi-masante, Fanny bernadou for technical support on many issues, to Meryl Malezieux for mental support during ups and downs, Ashley Kees, Mariela Escande, Nan Jiang, Dario Cupolillo, Ania Ramalho-Goncalves, Tomas Jorda-Siquier, Ruth Betterton, Eva Rodrigues for daily discussions about science and about life.

Equally important, I want to thank my co-supervisor Dr. Andre Fischer for welcoming me into his group to learn. I really appreciated the everyday supervision of Dr. Cemil Kerimoglu, who helped me to start in molecular biology and answered all of my naïve questions, and to all the team members: Susanne Burkhardt, Daniel Riestler, Farahnaz Sananbenesi, Sadman Sakib, Rezaul Islam, Eva Benito, Rashi Halder, Tea Berulava, Hendrik Urbanke, Magdalena Navarro, Christian Schiffmann, Lalit Kaurani, Gaurav Jain, Ashish Rajput, who have helped me a great deal on a daily basis.

I would like to thank Dr. Andreas Frick, Elisabetta Aloisi, Dr. Yoon Cho, Dr. Wenhui Peng, whom I have done collaboration work with.

I'd also like to thank the animal facility staff, without them taking care of the mice, this work would have been impossible, and the BIC team for their very professional support and suggestions.

I am very grateful to my funding, Erasmus Mundus joint doctorate program and the ENC network. Especially Ms. Maaïke Leusden, Ms. Laurie, Francois, Ms. Florina Camarasu, and Dr. Michael Hoerner made this happen by dealing with a great amount of paper work.

Finally, I wish to express my gratitude to my family and to all my friends, who

supported me patiently and encouraged me endlessly throughout the whole journey.

Life is not all about science, but I am very grateful to have this wonderful experience of my doctoral study. It made me more mature, open-minded, and more resilient in the face of frustrations and challenges. To continue in academic or not, I will always cherish this experience at the bottom of my heart. With the advancement of new research tools and numerous devoted scientists, we might be standing in the timepoint where the scope of knowledge of mankind is being broadened at speed never seen, and I feel very lucky to be able to participate in or at least spectate this great cause.



GEORG-AUGUST-UNIVERSITÄT
GÖTTINGEN



Abstract

Memory encoding is thought to proceed from durable changes in the activity of synaptic circuits, leading to the storage of patterns of electrical events in a sparsely distributed ensemble of neurons. Located at the entry level of hippocampal circuitry, the CA3 region is thought to be important for episodic memory encoding, especially at the initial stage of acquisition, by presumably developing an instant representation of a context. CA3 pyramidal cells receive a variety of inputs, among which the mossy fiber (Mf) inputs draw special attention for their peculiar structure and unique synaptic properties. However, the links between the plasticity of CA3 circuits and memory encoding are not well understood.

This thesis project aimed to address the synaptic mechanisms of episodic memory encoding in physiological conditions as well as in a mouse model of Alzheimer's disease (AD).

AD is characterized at an early stage by impaired episodic memory, which may involve dysregulation of the plasticity of CA3 circuits.

First of all, we searched for synaptic deficits in CA3 local circuit in the early stage of AD pathology in acute slices, taking advantage of a familial AD mouse model: 6-month male APP/PS1 mice. We report that there is a reduction in spontaneous IPSC frequency in CA3 pyramidal cells (PCs) together with decreased inhibitory charges of evoked events at Mf-CA3 synapses, whereas the short-term plasticity of these synapses and intrinsic properties of CA3 PCs remain unaffected. Furthermore, there is a robust reduction in Kainate receptor (KAR) mediated currents at Mf-CA3 synapses. The same results were obtained from PSKO mice, suggesting that disturbed function of γ -secretase and N-Cadherin processing pathways may underlie the dysfunction of KARs at Mf-CA3 synapses.

In the next step, we explored the changes in CA3 circuits shortly after one-trial contextual fear conditioning in adult C57Bl6j mice. We show that despite hardly any changes in filopodia number of Mf terminals, an increase in spontaneous IPSC

frequency can be registered, while the EPSCs and short-term plasticities of these synapses are unaltered. However, this increase cannot be seen anymore 24 hours after the contextual learning. We also tried to do simplified computational modeling of the DG-CA3 neuronal networks, to investigate if and to what extent the local interneurons in CA3 region contribute to memory encoding precision.

Finally, to screen for changes at a transcriptome level, we performed RNA-seq with dissected CA3 tissue from APP/PS1 mice and identified up- and down-regulated genes at this early stage of AD. Moreover, we carried out ChIP-seq for a histone modification marker: H3K4me3, which has been shown to be directly related to one-trial contextual memory, and we report that there is a significant decrease in H3K4me3 levels at the promoter areas of various genes in CA3 PCs. However, these genes are hardly overlapping with the down-regulated genes from RNA-seq result, suggesting that other epigenetic mechanisms may play more important roles in expressing early deficits in this AD mouse model.

Taken together, we show that inhibitory connections of hippocampal CA3 circuits may be important for episodic memory encoding, and in early AD mouse model with memory deficits, there is reduced GABAergic transmission and reduced KAR-mediated currents in CA3 PCs, together with many active transcriptional regulations across the genome. Our study may contribute to the understanding of early AD pathologies at a synaptic level as well as a transcriptional level, and provide novel insights into the mechanisms underlying rapid encoding of contextual memory.

Keywords: Alzheimer's, hippocampus, synaptic modifications

Résumé

L'encodage de la mémoire dépend de changements durables dans l'activité des circuits synaptiques dans un ensemble de neurones interconnectés. La région CA3 de l'hippocampe reçoit des informations directement ou indirectement (à travers le gyrus denté - GD) en provenance des structures corticales. Des données théoriques et comportementales ont montré que la région CA3 est importante pour l'encodage de la mémoire épisodique, en particulier au stade initial de l'acquisition, en développant vraisemblablement une représentation instantanée d'un contexte. Les neurones pyramidaux CA3 reçoivent une variété de connections afférentes, parmi lesquelles les fibres moussues (FM), les axones des cellules du gyrus denté. Ces connections synaptiques ont attiré une attention par leurs propriétés morphologiques et fonctionnelles uniques. Malgré les nombreuses études, les liens entre plasticité des circuits CA3 et encodage de la mémoire ne sont pas bien compris.

Le cadre général de ce projet de thèse se situe dans l'étude des mécanismes synaptiques de l'encodage de la mémoire épisodique dans des conditions physiologiques ainsi que dans un modèle de souris de la maladie d'Alzheimer (MA). En effet, la MA se caractérise à un stade précoce par une mémoire épisodique altérée, qui peut être associée à une dysrégulation de la plasticité des circuits CA3.

À l'aide de techniques d'enregistrement électrophysiologique, nous avons d'abord exploré les modifications dans les circuits CA3 peu de temps (quelques heures) après conditionnement de la peur contextuelle chez les souris adultes C57Bl6j. Nous avons observé une augmentation de la fréquence des IPSC spontanés accompagnée de changements mineurs dans le nombre de filopodia issus des boutons synaptiques des FM, tandis que les EPSCs et les plasticités à court terme de ces synapses ne sont pas modifiés.

Nous avons ensuite comparé les propriétés synaptiques des circuits CA3 au stade précoce de la pathologie de la MA, en profitant d'un modèle de souris de MA familiale : les souris APP/PS1 males à 6 mois. Nous avons observé une réduction de la fréquence des IPSC spontanés dans les neurones CA3 avec une diminution de la charge des

courants synaptiques évoqués des synapses FM-CA3, alors que la plasticité à court terme de ces synapses et les propriétés intrinsèques des neurones CA3 restent inchangées. En outre, il existe une réduction marquée des courants médiés par les récepteurs kainate (KAR) aux synapses FM-CA3 dans ce modèle de MA. Cette réduction est aussi observée en invalidant la préséniline sélectivement dans les cellules pyramidales de CA3. Ceci suggère que perturber des voies de signalisation de la γ -secretase, en particulier son action protéolytique sur la N-Cadhérine pourrait sous-tendre la perte de KAR aux synapses FM-CA3.

Enfin, j'ai comparé le transcriptome des souris contrôle et APP/PS1, et j'ai pu établir une liste de gènes dont l'expression est modifiée à ce stade précoce de la MA. De plus, nous avons effectué une analyse en ChIP-seq et rapportons ici qu'il existe une diminution des niveaux de H3K4me3, qui s'est révélé être directement lié à la mémoire contextuelle à un coup.

Dans l'ensemble ce travail a révélé que la transmission inhibitrice des circuits locaux CA3 de l'hippocampe pourrait être importante dans l'encodage de la mémoire épisodique. Dans le modèle murin de la MA avec déficit de mémoire, il y a une réduction de la transmission GABAergique et des courants médiés par les KAR réduits cellules pyramidales de CA3. Finalement, avons observé une modification transcriptionnelle d'un certain nombre de gènes dans CA3, à des stades précoces de développement de la pathologie dans notre modèle de MA. Notre étude pourrait contribuer à la compréhension des mécanismes pathologiques précoces de la MA, au niveau synaptique ainsi qu'au niveau transcriptionnel, et fournir des idées nouvelles sur les mécanismes sous-jacents au codage rapide de la mémoire contextuelle.

Mots clés: la maladie d'Alzheimer, l'hippocampe, Modifications synaptiques

Abbreviations

A/C	Associative/commissural
AC	Adenylate cyclase
aCSF	Artificial cerebrospinal fluid
ADAM	A disintegrin and metalloproteinase
AMPA	α -amino-3-hydroxy-5-methyl-4-isoxazolepropionic acid
AMPA	α -amino-3-hydroxy-5-methyl-4-isoxazolepropionic acid receptor
AP	Action potential
APP	Amyloid precursor protein
ATP	Adenosine 5'-triphosphate
A β	Amyloid β
bp	Base pair
CA	Cornu Ammonis
CaMK II	Ca ²⁺ /calmodulin-dependent protein kinase II
CB1R	Cannabinoid 1 receptors
CCK	Cholecystokinin
CFC	Contextual fear conditioning
CNS	Central nervous system
D-APV	D-(-)-2-Amino-5-phosphonopentanoic acid
DG	Dentate gyrus
DIC	Differential interference contrast
EC	Entorhinal cortex
eCB	Endocannabinoids
GFP	Green fluorescent protein
EGTA	Ethylene glycol-bis(β -aminoethyl ether)-N,N,N',N'-tetraacetic acid
EPSC	Excitatory postsynaptic current
FAD	Familial Alzheimer's disease
FF	Frequency facilitation
GABA	γ -Aminobutyric acid
GTP	Guanosine 5'-triphosphate
H3K4Me3	Trimethylated lysine 4 on histone 3
HEPES	4-(2-hydroxyethyl)-1-piperazineethanesulfonic acid
iGluRs	Ionotropic glutamate receptors
KARs	Kainate receptors

L-CCG-I	(2S,1'S,2'S)-2-(Carboxycyclopropyl)glycine
LMT	Large mossy fiber terminals
LTD	Long-term depression
LTP	Long-term potentiation
mEPSC	Miniature excitatory postsynaptic current
Mf	Mossy fiber
MfBs	Mossy fiber boutons
mGluR	Metabotropic glutamate receptor
min	Minute
mIPSC	Miniature inhibitory postsynaptic current
MWM	Morris water maze
NBQX	2,3-dihydroxy-6-nitro-7-sulfamoyl-benzo[f]quinoxaline-2,3-dione
NCad	N-Cadherin
NFT	Neurofibrillary tangles
NMDA	N-methyl-D-aspartate
NMDAR	N-methyl-D-aspartate receptor
PBS	Phosphate buffered saline
PCs	Pyramidal cells
PEN-2	Presenilin enhancer 2
PS1	Presenilin 1
PS2	Presenilin 2
PSD	Postsynaptic density
PFA	Paraformaldehyde
PKA	protein kinase A
PP	Perforant path
PPF	Paired-pulse facilitation
Pr	Probability of release
PS1	Presenilin 1
PS2	Presenilin 2
PSD	Post synaptic density
PTP	Post-tetanic potentiation
PV	Parvalbumin
RAWM	Radial arm water maze
S/C	Schaffer collateral
SEM	Standard error of mean

sIPSC	Spontaneous postsynaptic currents
SOM	Somatostatin
ThEs	Thorny excrescences
TSS	transcription start sites
TTX	Tetrodotoxin
VIP	Vasoactive intestinal polypeptide
WT	Wild type

Table of contents

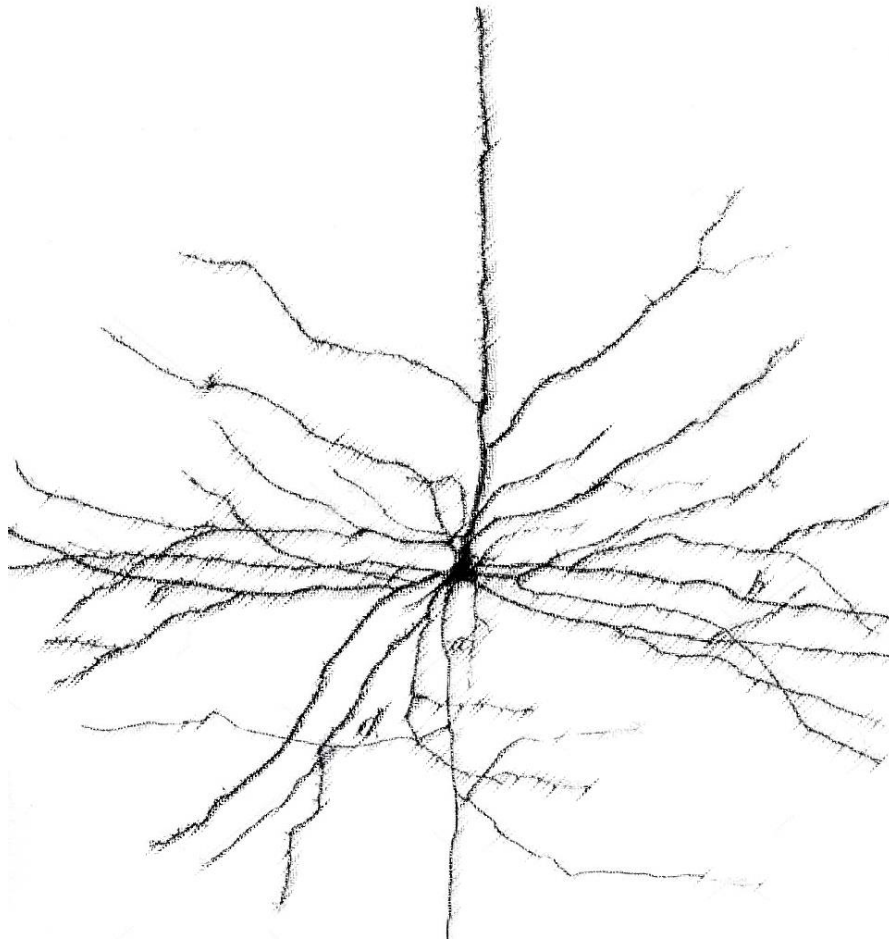
Acknowledgements	1
Abstract	3
Résumé	5
Abbreviations	7
Table of contents	10
1 Introduction	15
1.1 Synapses.....	15
1.1.1 Morphology of synapses.....	15
1.1.2 Neuronal transmitters.....	17
1.1.3 Glutamate receptors.....	17
1.1.4 Synaptic plasticity.....	20
1.2 Hippocampus and its circuitry.....	24
1.2.1 Learning and memory.....	24
1.2.2 Hippocampus in learning and memory.....	27
1.2.3 Hippocampal anatomy and circuitry.....	30
1.2.4 Hippocampal CA3 circuits.....	31
1.2.5 Computational modeling of CA3 circuits.....	36
1.3 Brain plasticity on a molecular level.....	37
1.3.1 Epigenetics and chromatin plasticity.....	37
1.3.2 Histone Methylation as a transcription regulator.....	38
1.3.3 H3K4me3 in learning and memory.....	40
1.4 Alzheimer's disease (AD).....	41
1.4.1 Historical background and clinical aspects of AD.....	41
1.4.2 Familial AD (FAD) on genetic and molecular level.....	44
1.4.3 Mouse models of FAD.....	46
1.4.4 APP ^{swe} /PSEN1 ^{dE9} (APP/PS1) mice as an FAD model.....	48
1.5 Objectives of the work.....	50

2 Materials and Methods	53
2.1 Animal Use.....	53
2.1.1 Ethical Considerations	53
2.1.2 Mice	53
2.1.3 APP/PS1 Mice Genotyping	53
2.2 Electrophysiology	55
2.3 Genomic profiling and ChIP-seq.....	57
2.3.1 Tissue Preparation and Neuron Sorting	57
2.3.2 RNA Isolation and qPCR.....	59
2.3.3 Chromatin immunoprecipitation (ChIP).....	61
2.4 Immunohistochemistry and Imaging	63
2.4.1 Immunofluorescent Staining for c-Fos	63
2.4.2 Confocal Imaging of Mf Terminals	63
2.5 Behavioral tests	63
2.6 Computational modeling.....	64
2.7 Statistical Analysis	64
3 Results.....	67
3.1 Input-specific synaptic alterations in CA3 pyramidal cells at an early stage in a mouse model of Alzheimer's disease.	67
3.2 Electrophysiological studies of KAR-mediated currents in CA3 PCs of 6-month male APP/PS1 mice	95
3.2.1 KAR-EPSCs of Mf-CA3 synapses are reduced in APP/PS1 mice	95
3.2.2 KAR-EPSCs of Mf-CA3 synapses is also reduced in PS KO mice	97
3.3 CA3 circuits modifications after contextual fear conditioning (CFC).....	100
3.3.1 One-trial CFC can induce changes in CA3 circuits	100
3.3.2 Electrophysiological studies of Mf-CA3 circuit 3h after CFC	102
3.3.3 Electrophysiological studies of Mf-CA3 circuit 24h after CFC.....	106
3.4 Genomic and epigenetic studies of APP/PS1 mice	109
3.4.1 RNA-sequencing of hippocampal CA3 region in APP/PS1 mice	109
3.4.2 H3K4Me3 level is decreased at gene promoters in APP/PS1 mice.....	111
4 Discussion.....	117
4.1 CA3 circuits deficits in early AD mouse models	117

4.1.1 Unaltered presynaptic features and loss of LTP of NMDARs at Mf-CA3 synapses	117
4.1.2 Decreased GABAergic transmissions onto CA3 PCs	119
4.1.3 Reduced KAR-mediated EPSCs in CA3 PCs	120
4.2 CA3 circuits modifications after contextual learning	122
4.3 Transcriptome changes in CA3 region in early AD	124
4.4 Perspectives	125
5 Bibliography	129
5.1 Books	129
5.2 References	130
6 Annexes	163
6.1 Computational modeling of hippocampal DG-CA3 networks	163
6.1.1 Single pyramidal neuron model	163
6.1.2 Network design of DG-CA3 circuits	164
6.1.3 Test of the model with input/output correlation	166
6.1.4 NEST code of DG-CA3 model	169
6.2 Publication 1 (as co-second author)	174
6.3 Publication 2 (as co-second author)	185
6.4 Publication 3	211
6.5 List of genes differentially expressed in 6-month APP/PS1 mice by RNA-seq	226
6.6 List of genes with low H3K4me3 levels in 6-month APP/PS1 mice by ChIP-seq	235
6.7 Curriculum Vitae	241

CHAPTER 1

INTRODUCTION



1 Introduction

1.1 Synapses

1.1.1 Morphology of synapses

The connection and communication between neurons (or neurons with other faculties) are realized through synapses. A typical synapse consists of two components: a presynaptic compartment, and a postsynaptic compartment, with a synaptic cleft in between. Depending on the nature of pre- and postsynaptic compartments, the synapses can be called axodendritic, axosomatic, axoaxonic, axosecretory, dendrodendritic synapses, etc., with the vast majority in the mammalian nervous system being axodendritic. In addition, astrocytes also exchange information with neurons, responding to synaptic activity, and regulating neurotransmission in a “tripartite synapse” configuration (Perea, Navarrete, & Araque, 2009). Further down this path, a concept of “quadripartite synapse” has also been proposed, arguing that the role extracellular matrix (ECM) in regulating synaptic functions and plasticity (Sykova & Nicholson, 2008)

Synapses can be categorized as chemical synapses and electrical synapses, and in some cases, both at the same synapse (Pereda, 2014) (Figure 1.1).

Electrical synapses are also known as gap junctions, propagating action potentials (APs) very rapidly. Gap junctions can conduct electrical signal in both directions, and are usually found at systems requiring fast synchronization of neurons. Due to the nature of transmission here is the passive flow of ionic currents, these synapses lack gain, and the possibility to modify the synaptic strength is very limited.

The much more common form of synapses is chemical synapse. Although more complex, the chemical synapses are more primitive in an evolutionary point of view (Bennett, 2000), because the sequences of gap-junction-forming proteins are markedly different between vertebrates and invertebrates, while the genes underlying chemical transmission are almost homologs among species (Bennett, 2000; Bruzzone, Hormuzdi, Barbe, Herb, & Monyer, 2003).

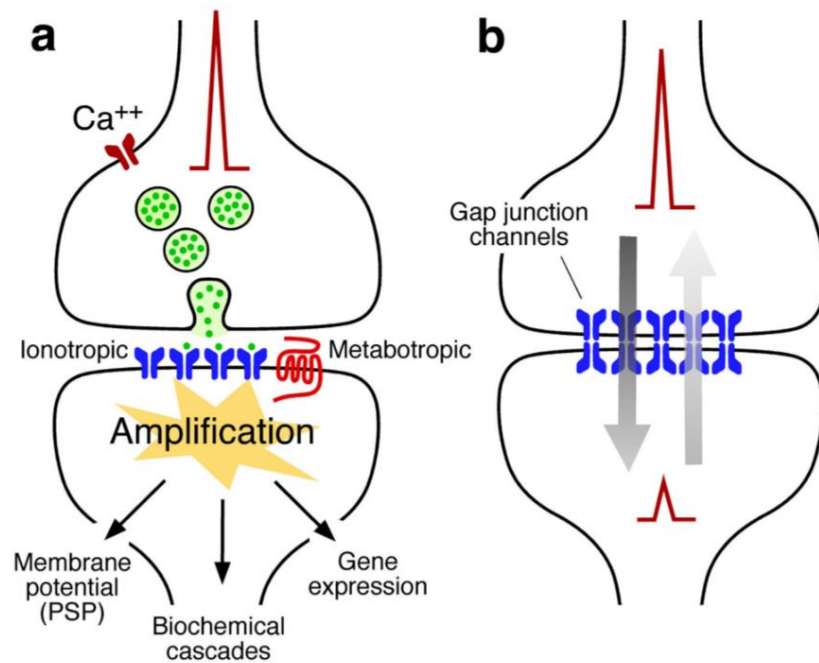


Figure 1.1. The two main modalities of synaptic transmission.

A. Schematic representation of a chemical synapse. Chemical transmission requires sophisticated presynaptic machinery that releases neurotransmitters upon depolarization of the presynaptic terminal (e.g. the arrival of an AP). An equally complex postsynaptic machinery includes ionotropic and metabotropic receptors is capable of detecting and translating the presynaptic message (neurotransmitter) into various postsynaptic events (e.g. resting potential changes or signaling cascades). **B.** Schematic representation of an electrical synapse. Electrical transmission is mediated by clusters of gap junctions that linking two adjacent cells, directly allowing the bi-directional traffic of electrical currents as well other small molecules. Adapted from (Pereda, 2014).

The synaptic cleft of a chemical synapse (20~40nm) is much wider than that of an electrical synapse (2~4nm) (Goyal & Chaudhury, 2013). When an AP arrives at presynaptic terminals, vesicles containing neurotransmitters are released into the synaptic cleft. The neurotransmitters can activate receptors on the postsynaptic side, resulting in the opening of the channels and ion flows across the postsynaptic membrane. These alterations in membrane potential on the postsynaptic side can summate in the soma and generate the next AP once over the threshold. Therefore, the signal is conveyed in an electrical-chemical-electrical manner (Pereda, 2014). Chemical synapses are considered to be unidirectional. However, they are subject to certain retrograde modulations, via conventional neurotransmitters, gasses, peptides, growth factors, or membrane-derived lipids (Carta, Lanore, et al., 2014; Regehr, Carey, & Best,

2009).

1.1.2 Neuronal transmitters

A chemical synapse is usually described according to the type of neurotransmitters it releases (Table 1.1). These neurotransmitters cause different responses on the postsynaptic side depending on the context, which can be developmental, homeostatic, pathological states, etc. Glutamatergic synapses are excitatory in the vertebrate central nervous system (CNS), while GABAergic synapses are mainly inhibitory, albeit a major excitatory role during development (Ben-Ari, 2002). Most of the other neurotransmitters in the CNS are considered to be modulatory, the effect of which can vary depending mainly on the type of receptors they interact with. Furthermore, the co-release of different neurotransmitters at the same synapse is not rare (Hnasko & Edwards, 2012; Trudeau & Gutierrez, 2007).

Table 1.1 An incomplete list of neurotransmitters

Amino acids	Glutamate
	Aspartate
	Glycine (in spinal cord)
Amino acid derivatives (mono amines)	GABA
	Histamine
	Norepinephrine
	Epinephrine
	Dopamine
	Serotonin (5-HT)
Purine derivatives	ATP
	Adenosine
Gas	Nitric oxide
	Carbon monoxide
Miscellaneous	Acetylcholine
Neuropeptides	Opioid peptides
	Somatostatin
	Substance P
	Neuropeptide Y
lipid	Endocannabinoids

1.1.3 Glutamate receptors

Glutamatergic synapses are the most abundant type of synapses in vertebrate CNS (>50%), comparing to GABAergic synapses (30~40%) and other modulatory synapses

(~10%) (Hendry, Schwark, Jones, & Yan, 1987; Nadim & Bucher, 2014; Roberts, 1986). The actions of glutamate are mediated via a broad range of ionotropic glutamate receptors (iGluRs, including AMPA, NMDA, Kainate and Delta receptors), and metabotropic glutamate receptors (mGluRs, including group I, II, III). These receptors can locate both pre- and post-synaptically. iGluRs are ligand-gated ion channels. Ligand binding leads to rapid changes in membrane potential and cell excitability (Bleakman & Lodge, 1998; Yamakura & Shimoji, 1999). mGluRs are G-protein coupled modulatory receptors, and their activation will trigger a series of reactions in certain signaling pathways and may indirectly open or close other channels (Conn & Pin, 1997; Schoepp, Jane, & Monn, 1999) (Figure 1.2, 1.3).

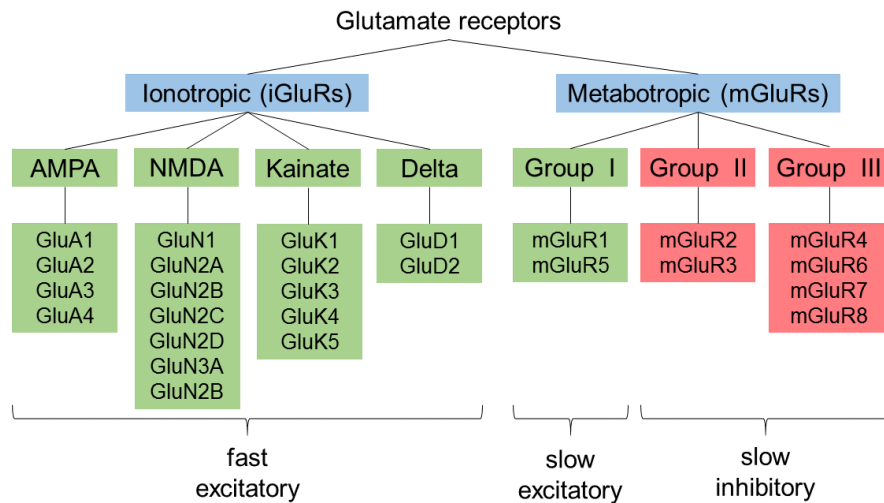


Figure 1.2. Classification of glutamate receptors.

Ionotropic glutamate receptors are tetramers, including AMPARs (α -amino-3-hydroxy-5methyl-4-isoxazolepropionic acid receptors), NMDARs (N-methyl-D-aspartic acid receptors), KARs (Kainic acid receptors) and Delta receptors. Their properties are defined by the subunit composition and their modifications (Dingledine, Borges, Bowie, & Traynelis, 1999; Dingledine & Conn, 2000).

AMPARs are hetero-oligomers of four subunits: GluA1 to GluA4 (Hollmann & Heinemann, 1994), and are mediating the fast component of excitatory postsynaptic currents (EPSCs), permeable to cations: Na^+ and K^+ . The majority of AMPARs in adult CNS are GluA1/2 or GluA2/3 heterodimers (Lu et al., 2009; Mansour, Nagarajan, Nehring, Clements, & Rosenmund, 2001; Wenthold, Petralia, Blahos, & Niedzielski, 1996), whereas GluA4-containing AMPARs can be found in hippocampus during development (Zhu, Esteban, Hayashi, & Malinow, 2000). However, there's a small

portion of AMPARs lacking the GluA2 subunit (e.g. GluA1/3 heterodimers or homomeric GluA1), and thus permeable to Ca^{2+} (Seeburg, Higuchi, & Sprengel, 1998; Wisden & Seeburg, 1993).

NMDARs are heterotetramers composed of subunits GluN1, GluN2A, GluN2B, GluN2C, and GluN2D (in some rare cases also GluN3A and GluN3B), and mediate the slow component of EPSCs (Lieberman & Mody, 1999; Stern, Behe, Schoepfer, & Colquhoun, 1992). As cation channels, NMDARs are highly Ca^{2+} permeable (Mayer & Westbrook, 1987). Ca^{2+} entry triggers several downstream events which are important for synaptic plasticity (Berridge, 1998). Apart from glutamate binding, the activation of NMDARs also requires the co-agonist glycine and the removal of the blockage by extracellular Mg^{2+} . The blockage is voltage-sensitive and can be unblocked upon depolarization (Kleckner & Dingledine, 1988; Schoepfer et al., 1994).

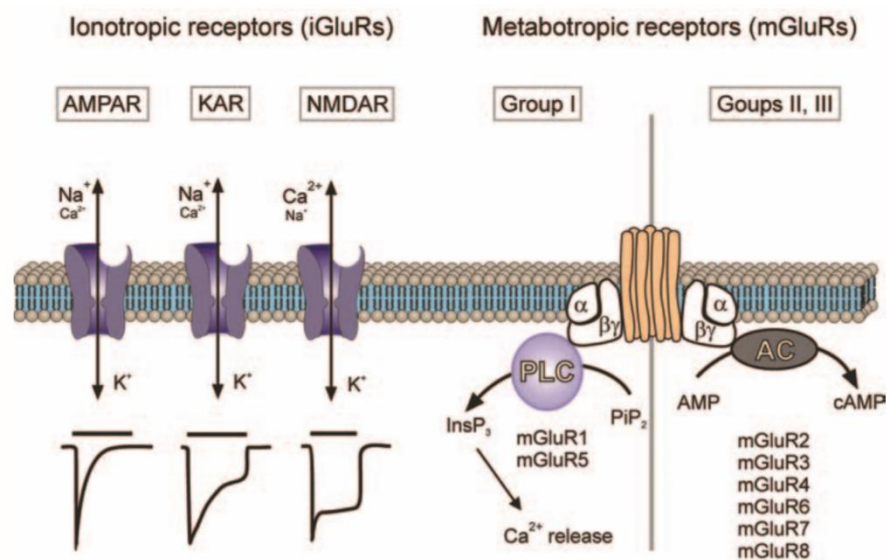


Figure 1.3. Ionotropic and metabotropic glutamate receptors.

Schematic representations of the two classes of glutamate receptors. The ionotropic receptors were further subdivided into three distinct subtypes AMPA, NMDA, and Kainate receptors. The iGluRs are assembled from four subunits, which will determine their functional properties. The AMPARs and KARs are predominantly permeable for Na^+ and K^+ , although there are certain Ca^{2+} -permeable subtypes, whereas NMDA receptors are highly Ca^{2+} -permeable. When activated by glutamate, AMPA receptors undergo rapid desensitization (time constant ~ 100 ms); KA receptors desensitize slower, and NMDA receptors show almost no desensitization. Metabotropic glutamate receptors (mGluRs) control intracellular second messenger signaling cascades as represented. Adapted from (Verkhratsky & Kirchhoff, 2007).

KARs are homo- and heteromeric tetramers composed of 5 subunits: GluK1 – 5. The KAR-mediated synaptic current is much smaller and slower compared to AMPAR current (Lerma, 2003; Traynelis et al., 2010). Unlike AMPARs and NMDARs which are normally enriched at excitatory postsynaptic densities (PSDs), KARs can be located at both pre- and postsynaptic sites. In hippocampus, the postsynaptic KARs are predominantly present at Mf-CA3 synapses, where it has been extensively studied (Castillo, Malenka, & Nicoll, 1997; Darstein, Petralia, Swanson, Wenthold, & Heinemann, 2003).

The delta receptors (subunit: GluD1 and GluD2) are regarded as ionotropic glutamate receptors solely because of sequence homology. To date, the wild type delta receptors stay closed in the presence of molecules that have been proved to bind its ligand-binding domain, although the ion channel function has been observed in some mutant or chimera delta receptors (Orth, Tapken, & Hollmann, 2013). Knock-out studies suggested they play important roles in cerebellar function and high-frequency hearing (Schmid & Hollmann, 2008).

1.1.4 Synaptic plasticity

Synaptic plasticity is thought to be one of the mechanisms underlying learning and memory. It exists in many forms, ranging from changes of property in a single synapse to large-scale modifications of synaptic strengths, also including formation or pruning of synaptic connections (Figure 1.4). Synaptic plasticities are normally categorized as short-term and long-term. While short-term synaptic plasticity leads to transient changes in synaptic functions (lasting from milliseconds to minutes) that regulate the moment-to-moment information flow through the circuits, long-term synaptic plasticity leads to persistent changes in synaptic strengths (lasting from hours to the lifetime of the synapse) that adaptively alter synaptic function in response to activities and computational demands (Collingridge, Peineau, Howland, & Wang, 2010; Granger & Nicoll, 2014; Zucker & Regehr, 2002).

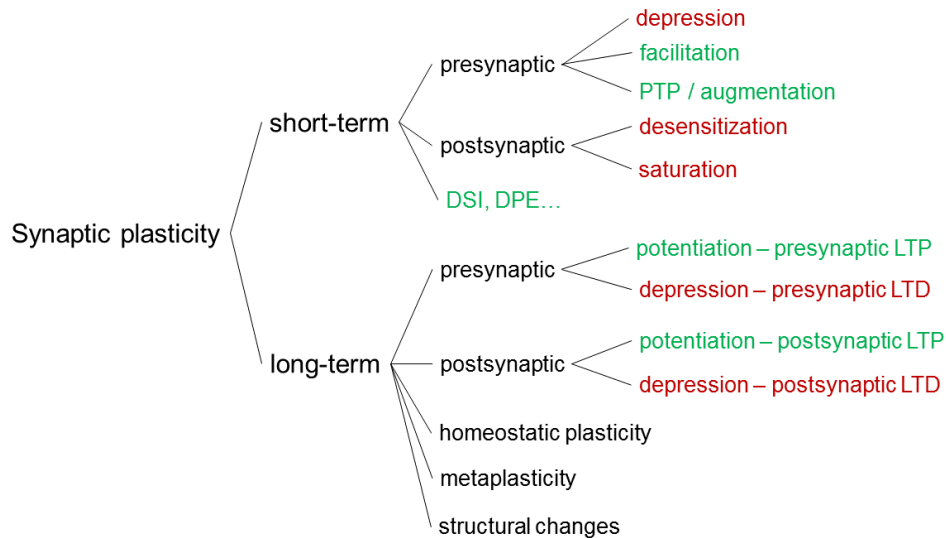


Figure 1.4. Different forms of synaptic plasticity.

Short-term plasticity can be further divided into presynaptic and postsynaptic plasticities. In the presynaptic forms of short-term plasticity, there can be depression (hundreds of milliseconds to seconds), facilitation (hundreds of milliseconds to seconds), as well as augmentation and post-tetanic potentiation (PTP) (tens of seconds to minutes) (Fioravante & Regehr, 2011) (Figure 1.5).

Presynaptic depression can be observed at many synapses when stimulated repetitively at short time intervals. Several factors can account for the reduced synaptic strength, including depletion of the readily releasable pool, inactivation of release sites, and decreased presynaptic calcium influx.

Presynaptic facilitation is often found at synapses with a low initial release probability (e.g. mossy fiber synapses), and repeated stimulation at short time intervals can lead to a transient increase in release probability of these synapses. Increased presynaptic residual calcium level, saturation of endogenous calcium buffers, and facilitation of calcium currents are considered to be contributing to this phenomenon (Fioravante & Regehr, 2011). At Mf-CA3 synapses, this type of plasticity are often registered with two protocols: paired-pulse (PP) or even longer train protocol with repetitive stimulation at short intervals, and frequency facilitation (FF) protocol with increasing stimulation frequency from basal (0.1Hz) to moderate (1-3 Hz) (Gundlfinger, Breustedt, Sullivan, & Schmitz, 2010; Nicoll & Schmitz, 2005; Salin, Scanziani, Malenka, & Nicoll, 1996). Post-tetanic potentiation (PTP) and augmentation is another form of short-term plasticity noticed at Mf synapses, which means enhancement in

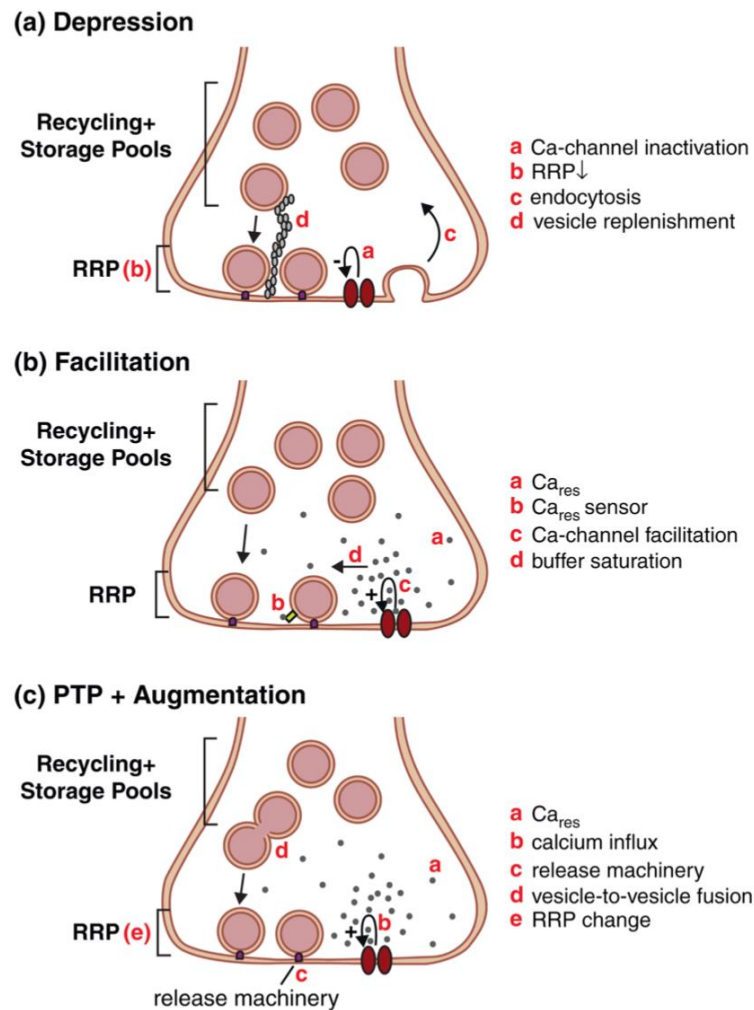


Figure 1.5. Presynaptic mechanisms of use-dependent short-term plasticity.

Schematic illustrations of different mechanisms for use-dependent short-term plasticity:

A. depression, **B.** facilitation, **C.** post-tetanic potentiation (PTP) and augmentation.

RRP: readily releasable pool of vesicles; Ca_{res} : residual calcium. Adapted from (Fioravante & Regehr, 2011)

synaptic strength following sustained, high-frequency synaptic activation (Vyleta, Borges-Merjane, & Jonas, 2016).

Other forms of short-term plasticity involving both pre- and postsynaptic elements and retrograde messengers have been reported, such as endocannabinoids mediated depolarization-induced suppression of inhibition (DSI) (Regehr et al., 2009; Wilson & Nicoll, 2002), and depolarization-induced potentiation of excitation (DPE) at the Mf synapses (Carta, Lanore, et al., 2014).

On the other hand, long-term plasticity also exists in various forms, including but

not limited to: NMDA-dependent LTP, presynaptic LTP, NMDA-dependent LTD, mGluR-dependent LTD, eCB-LTD, which were nicely reviewed by Kauer & Malenka (Kauer & Malenka, 2007) (Figure 1.6). Interestingly, albeit the presence of functional NMDA receptors (Weisskopf & Nicoll, 1995), a form of presynaptic NMDA-independent LTP is characterized at Mf-CA3 synapses, which is quite different from the canonical NMDA-dependent LTP found in other regions of the brain (Harris & Cotman, 1986).

In addition, other forms of plasticity such as homeostatic plasticity (up- or down-scaling of excitability), metaplasticity (plasticity of synaptic plasticity), structural plasticity like formation or deletion of synapses are also actively regulating neuronal network activities (Fernandes & Carvalho, 2016; Holtmaat, Randall, & Cane, 2013; Hulme, Jones, & Abraham, 2013).

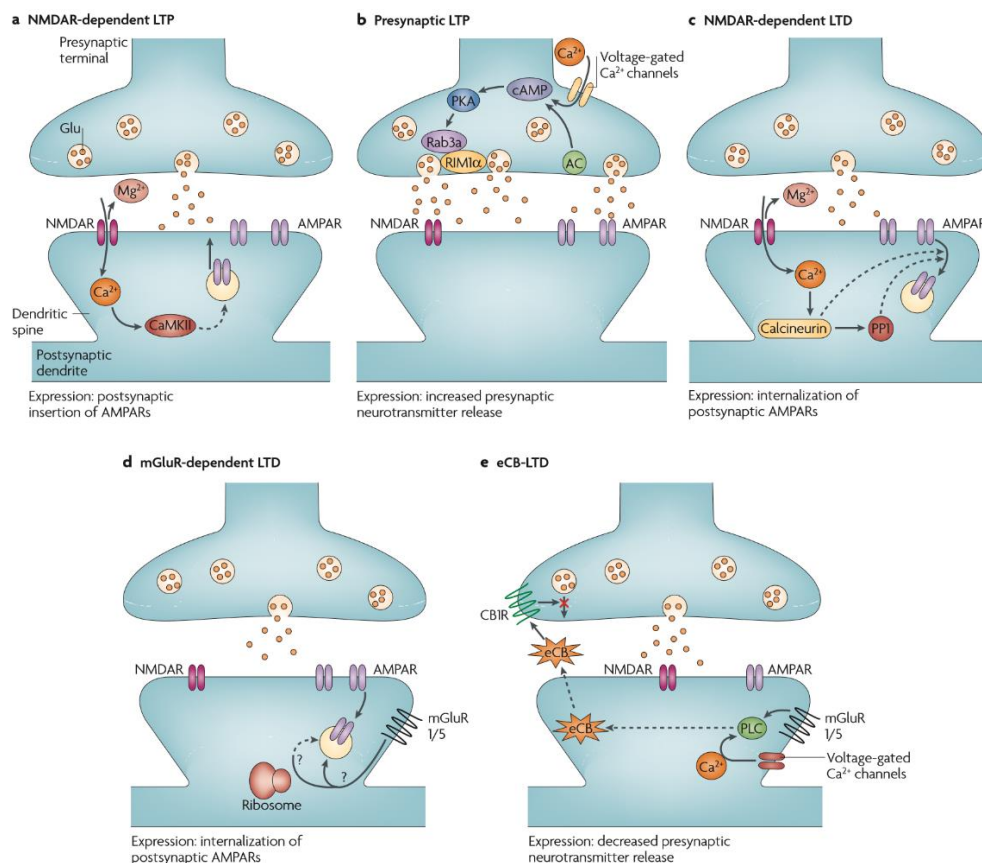


Figure 1.6. Well-described forms of LTP and LTD.

Highly simplified diagrams of the induction and expression of synaptic plasticity observed in the rodent brain. **A.** NMDAR-dependent LTP is dependent on postsynaptic NMDAR activation and calcium/CaMKII signaling pathway for its initiation. The voltage-dependent relief of the magnesium block of the NMDAR allows the synapse

to detect coincident presynaptic release of glutamate and postsynaptic depolarization, leading to AMPAR insertion into the postsynaptic membrane. **B.** Presynaptic LTP has been best characterized at hippocampal Mf–CA3 synapses. Repetitive synaptic activity leads to the entry of presynaptic Ca^{2+} , which activates a Ca^{2+} -sensitive adenylate cyclase (AC) leading to a rise in cAMP and the activation of cyclic AMP-dependent protein kinase A (PKA). This in turn modifies the functions of Rab3a and RIM1 α leading to a long-lasting increase in glutamate release. **C.** NMDAR-dependent LTD is triggered by Ca^{2+} entry through postsynaptic NMDAR channels, leading to increases in the activity of the protein phosphatases calcineurin and protein phosphatase 1 (PP1). The primary expression mechanism involves internalization of postsynaptic AMPARs and a downregulation of NMDARs by an unknown mechanism. **D.** mGluR-dependent LTD has been best characterized at cerebellar parallel fibre–purkinje cell synapses and hippocampal synapses. Activation of postsynaptic mGluR1/5 triggers the internalization of postsynaptic AMPARs, a process that under some conditions appears to require protein synthesis. **E.** Endocannabinoid-LTD is the most recently discovered form of LTD. Either mGluR1/5 activation, leading to activation of phospholipase C (PLC) or an increase of intracellular Ca^{2+} (or both), in the postsynaptic neuron initiates the synthesis of an endocannabinoid (eCB). The eCB is subsequently released from the postsynaptic neuron, travels retrogradely to bind to presynaptic cannabinoid 1 receptors (CB1R), and this prolonged activation of CB1Rs depresses neurotransmitter release via unknown mechanisms. Adapted from (Kauer & Malenka, 2007).

1.2 Hippocampus and its circuitry

1.2.1 Learning and memory

Learning and memory are closely related concepts. Learning is the acquisition of skill and knowledge, while memory is the faculty by which the mind stores and remembers information, and is the retention of information over time for the purpose of influencing future action (Kazdin, 2000). Learning and memory are so immediately relevant to everyone’s daily life, yet remain poorly understood in terms of mechanisms. Questions such as what is the nature of memory, where the memories are stored, how they are engraved and retrieved have intrigued generations of people till today.

In 400 B.C., Hippocrates was the first one to declare brain as the major controlling center for the body despite Egyptian, biblical, and earlier Greek views, which were heart-centered theory (Finger, 2005). And the first sign that certain parts of the brain might be involved in memory storage came from the very famous case of patient Henry

Molaison. He was an American epileptic patient who had a bilateral medial temporal lobectomy to surgically resect the anterior two thirds of his hippocampi, parahippocampal cortices, entorhinal cortices, piriform cortices, and amygdalae in an attempt to cure his epilepsy. After the surgery, he exhibited severe anterograde amnesia characterized by the inability to form new memories, while his remote memories together with his ability of reasoning and acquiring new motor skills seemed intact (Scoville & Milner, 1957). Numerous clinical case-studies have demonstrated in the last century that the anterior hippocampus and hippocampal gyrus, either separately or together, are critically concerned in the retention of current experience (Scoville & Milner, 2000). Altogether, it is now widely-accepted that the ability of learning and memory exist in many different forms involving various regions in the brain.

In an effort to categorize forms of memory, Richard Atkinson and Richard Shiffrin proposed in 1968 the Atkinson–Shiffrin model (also known as the multi-store model or modal model) dividing memory as sequential events of: sensory register, short-term memory (also known as working memory, <1min), and long-term memory (Spence & Spence, 1968).

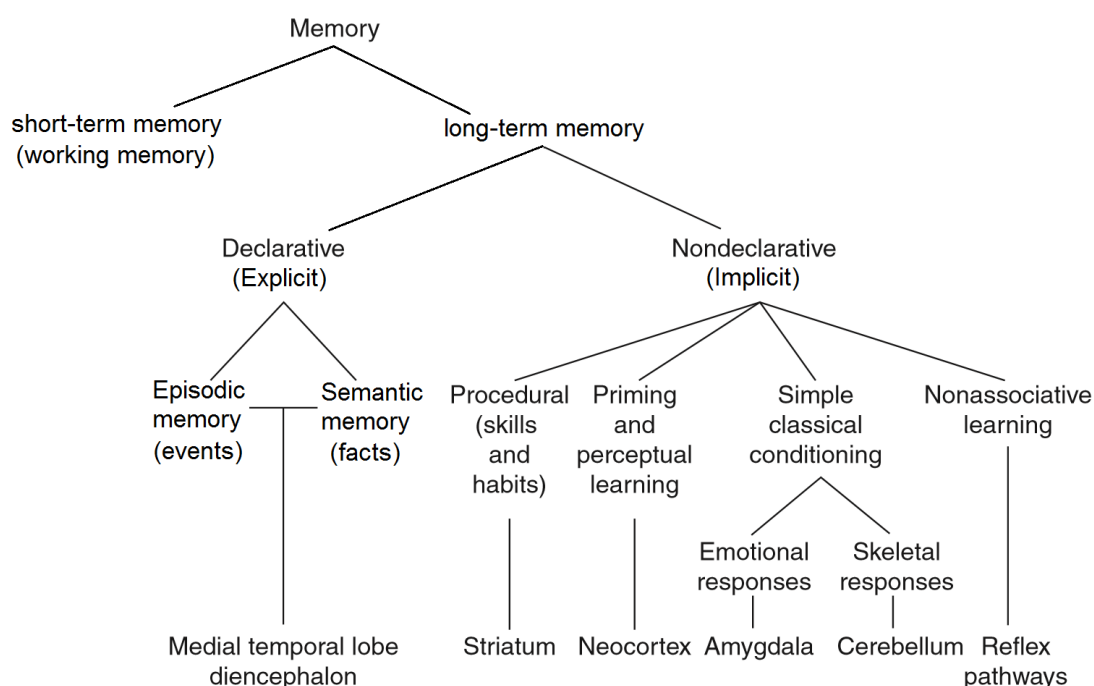


Figure 1.7. Different forms of memory and the brain regions involved.

Scheme of categorization of mammalian memory. Adapted from Squire et al. (Squire & Dede, 2015)

Long-term memory involves many processes such as encoding, consolidation, storage and retrieval of memories, and is normally divided into declarative and non-declarative memories, also known as explicit and implicit memories. Declarative memory is the conscious storage and recollection of data, and can be further divided into semantic and episodic memory (Clayton & Russell, 2009; Eichenbaum, 1997). Semantic memory refers to memory that encodes notion, concepts, or specific meaning (Grilli & Verfaellie, 2014), while episodic memory refers to the ability to re-experience a time-and-place-specific event in its original context (Schacter, Addis, & Buckner, 2007; Szpunar, 2010). Declarative memory is usually the primary process thought of when referencing memory (Eysenck, 2012). Declarative memory is a very complicated process involving many different brain regions, among which hippocampus mostly lies in the center of attention (Huijgen & Samson, 2015) (Figure 1.8).

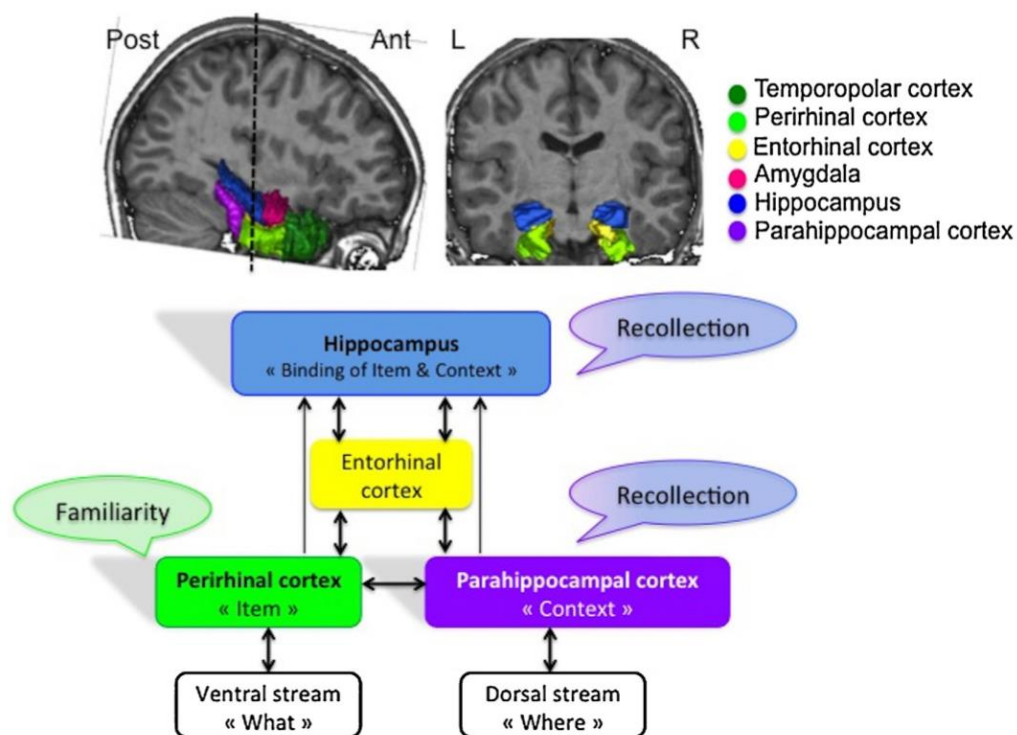


Figure 1.8. Proposed roles of different medial temporal lobe regions in declarative memory tasks by fMRI studies.

Scheme of the anatomical connections between the medial temporal lobe regions and the proposed roles of the hippocampus, entorhinal cortex, parahippocampal cortex, and perirhinal cortex in recognition memory according to the ‘binding of item and context’ (BIC) model (Diana, Yonelinas, & Ranganath, 2007).

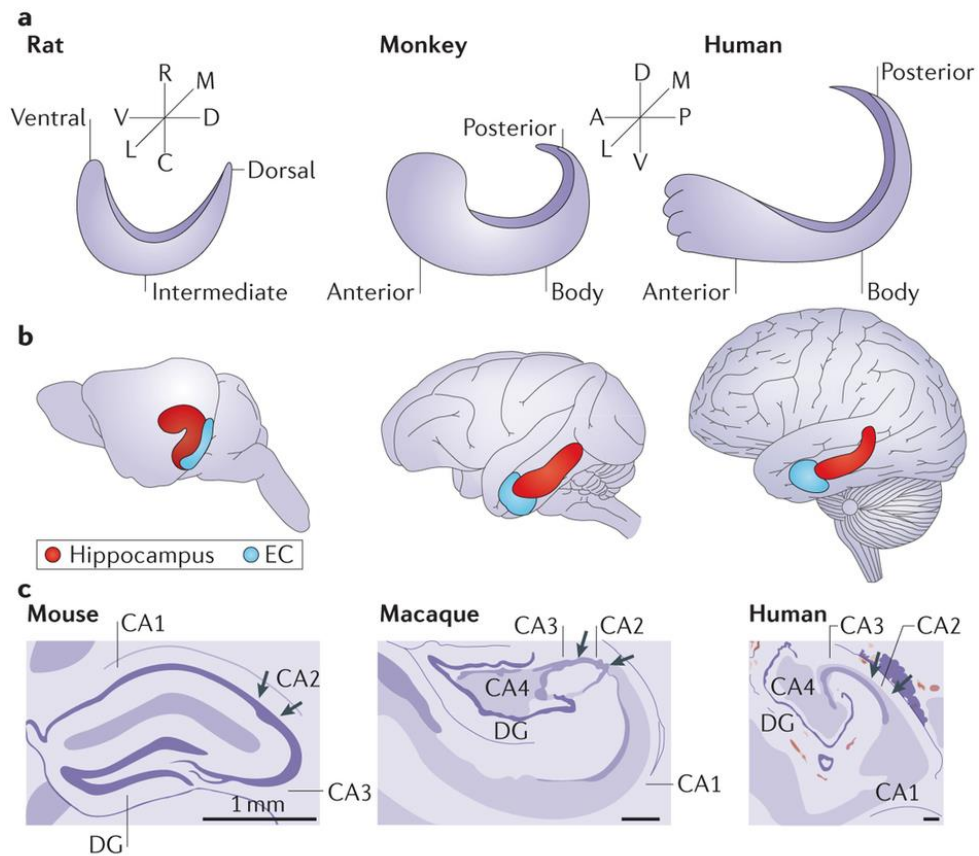
Normally when people refer to memory, declarative memory is usually the one they are thinking of. However, non-declarative memory also plays a significant role in daily life. Non-declarative memory is the storage and recollection of information without conscious attention to learning (Fitts, 1992; Ullman, 2001). An example of a non-declarative learning could be for example acquiring the skills of riding a bicycle or playing the violin. When needed, these memories are unconsciously activated (Tulving & Schacter, 1990).

Memory is not a perfect system, and it can be affected by many factors or even manipulated. However, learning and memory is an essential activity in daily life not only for higher organisms but also for invertebrates such as honeybees (Menzel, 2012) and *Drosophila* (Ostrowski, Kahsai, Kramer, Knutson, & Zars, 2015).

1.2.2 Hippocampus in learning and memory

The earliest description of hippocampal formation comes from the Venetian anatomist Julius Caesar Aranzi (1587), who likened it first to a silkworm and then to a seahorse, and that is why it got its name from the Greek word “seahorse”. Humans and other mammals have two hippocampi, one in each hemisphere, located in the limbic system of cerebral cortex. The anatomy and neural circuitry of the hippocampal formation are very similar across different species of mammals (Anderson, Morris, Amaral, Bliss, O’Keefe, 2007) (Strange, Witter, Lein, & Moser, 2014) (Figure 1.9).

Over the years, many theories have been proposed trying to explain the exact role of hippocampus in learning and memory, which are summarized by Bird et al. (Bird & Burgess, 2008) (Table 1.2).



Nature Reviews | Neuroscience

Figure 1.9. Scheme showing the comparative structures of hippocampal formation in humans, monkeys, and rodents respectively.

A. Schematic illustrations of hippocampus in the longitudinal axis in rats, macaque monkeys, and humans. The longitudinal axis is described as ventrodorsal in rodents and anteroposterior in primates. **B.** The relative locations of the hippocampus (red) in brains of rats, macaque monkeys, and humans, and the entorhinal cortex (EC) is shown in blue. **C.** Drawings of Nissl cross-sections of mouse, rhesus, and human hippocampi. A, anterior; C, caudal; D, dorsal; DG, dentate gyrus; L, lateral; M, medial; P, posterior; R, rostral; V, ventral. Adapted from (Strange et al., 2014).

Table 1.2 Theories on the role of the hippocampus in learning and memory.

Declarative Theory (Squire, 1986; Squire, Stark, & Clark, 2004)	The hippocampus, acting in concert with other medial temporal lobe regions, is crucial for all forms of consciously accessible memory processes (episodic and semantic, recollection and familiarity) for a time-limited period. Ultimately all memories are consolidated to neocortical sites and are thus unaffected by subsequent medial temporal lobe damage.
Multiple-Trace Theory (Nadel & Moscovitch, 1997)	The hippocampus, together with other medial temporal lobe regions, is crucial for the acquisition of episodic and semantic memories. The recollection of episodic memories remains dependent on the hippocampus for the duration of one's life and becomes more resistant to partial damage with repetition and/or rehearsal, whereas semantic memories become independent of the hippocampus and are stored in other brain regions over time.
Dual-Process Theory (Aggleton & Brown, 1999; Eichenbaum, Yonelinas, & Ranganath, 2007; Norman & O'Reilly, 2003; Rugg & Yonelinas, 2003)	The hippocampus is crucial for episodic recollection of the contextual details of an event. Familiarity-based recognition processes are subserved by other medial temporal lobe regions. Recollection is required for the associative recognition of non-unitized items (for example, voice–face pairs).
Relational Theory (Cohen, Poldrack, & Eichenbaum, 1997)	The hippocampus allows the flexible association of information in neocortical modules that could not otherwise communicate. This enables the relations between elements of a scene or event to be retrieved or used for inference in novel situations, in addition to retrieval of the elements themselves. The Cognitive-Map Theory can be subsumed as a special case of spatial relational processing.
Cognitive-Map Theory (O'Keefe & Nadel, 1978)	A primary role of the mammalian hippocampus is to construct and store allocentric (world-centered) representations of locations in the environment to aid flexible navigation, for example, from a new starting position. In humans, these predominantly spatial processes have evolved to support the spatial–temporal context of episodic memories.

All of these theories acknowledged the importance of hippocampus in learning and memory, especially in consolidation stage of declarative memory and spatial navigation, remaining differences and disputes in whether hippocampus has a time-limited role in episodic memory and hippocampus's function in the acquisition of non-contextual information.

1.2.3 Hippocampal anatomy and circuitry

The hippocampus is made up of four regions or subfields: CA1, CA2, CA3, and CA4. The CA4 region is also known as hilus, or hilar region if considered as a part of the dentate gyrus (Amaral, 1978; Blackstad, 1956). The abbreviation CA comes from “Cornu Ammonis”, which is an earlier name of the hippocampus.

The dentate gyrus is composed of three layers: molecular layer (relatives cell-free, with the exception of some interneurons), granular layer (densely packed with granule cells), and polymorphic layer (contains a number of cell types the most prominent being mossy cells) (Amaral, Scharfman, & Lavenex, 2007). The CA regions are also structured in layers: stratum oriens (SO, inhibitory basket cells and horizontal trilaminar cells, recurrent fibers contacting the basal dendrites of pyramidal neurons here), stratum pyramidale (SP, contains the cell bodies of the pyramidal neurons and some interneurons), stratum lucidum (SL, only found in the CA3 where mossy fibers course through), stratum radiatum (SR, contains some interneurons, and Schaffer collateral fibers, part of recurrent fibers contacting the apical dendrites of pyramidal neurons here), stratum lacunosum-moleculare (SLM, perforant path fibers form synapses onto the apical tufts of the apical dendrites of pyramidal cells) (van Strien, Cappaert, & Witter, 2009) (Anderson, Morris, Amaral, Bliss, & O’Keefe, 2007).

The input of hippocampus comes from neurons in Entorhinal cortex (EC) via the perforant path. Neurons in layers II of entorhinal cortex (EC) project to DG and CA3 (the indirect pathway), whereas layer III neurons project to CA1 and the subiculum (the direct pathway). Subsequently, cells in DG project to CA3 through mossy fibers (Mf), and CA3 PCs project to CA1 through the Schaffer collaterals (Witter, Canto, Couey, Koganezawa, & O’Reilly, 2014). The hippocampal output is made by CA1 and the subiculum, reciprocally projecting to the deeper layers of EC (layer V and VI). There are also substantial projections of CA3 PCs to other CA3 PCs, through associational/commissural or recurrent fibers (Le Duigou, Simonnet, Telenczuk, Fricker, & Miles, 2014; X. G. Li, Somogyi, Ylinen, & Buzsaki, 1994) (Figure 1.10).

Moreover, in rodents the two hippocampi are highly connected at the stems by the commissure of fornix (also called the hippocampal commissure), while in primates this commissural connection is much sparser (Gloor, Salanova, Olivier, & Quesney, 1993).

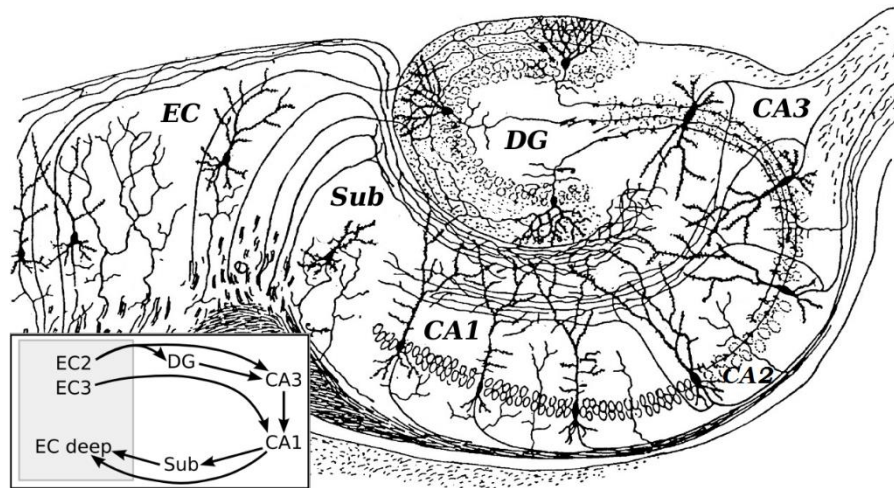


Figure 1.10. Basic circuitry of the hippocampus.

Schematic drawing of basic circuitry of the hippocampus. DG: dentate gyrus. Sub: subiculum. EC: entorhinal cortex. Adapted from hand drawings of Santiago Ramón y Cajal (1852 - 1934).

1.2.4 Hippocampal CA3 circuits

As is described in the last chapter, the DG has relatively simple connection, receiving inputs from EC and projecting to CA3. The DG is only sparsely activated for any input (Chawla et al., 2005), probably because DG has significantly more granule cells (~1,000,000) than cells of EC (~200,000) projecting to DG (Amaral, Ishizuka, & Claiborne, 1990; Rebola, Carta, & Mulle, 2017) (Figure 1.11). This type of connection makes it easier for DG to have distinct, non-overlapping activation patterns during each input from EC (O'Reilly & McClelland, 1994). Besides, DG granular cells are interconnected by excitatory mossy cells and inhibitory interneurons located in the hilus (Scharfman & Myers, 2012). However, the DG-CA3 connection is found not to be strictly unidirectional, with CA3 collateral fibers reciprocally influencing DG granule cells through mossy cells and hilar interneurons (Myers & Scharfman, 2011). In contrast to DG, CA3 receives more complicated excitatory inputs: from DG granule cell through mossy fibers (Blackstad, Brink, Hem, & Jeune, 1970; Swanson, Wyss, & Cowan, 1978), directly from layer II of the EC via the perforant path (Witter, 1993), and through recurrent collaterals from CA3 itself (Myers & Scharfman, 2011).

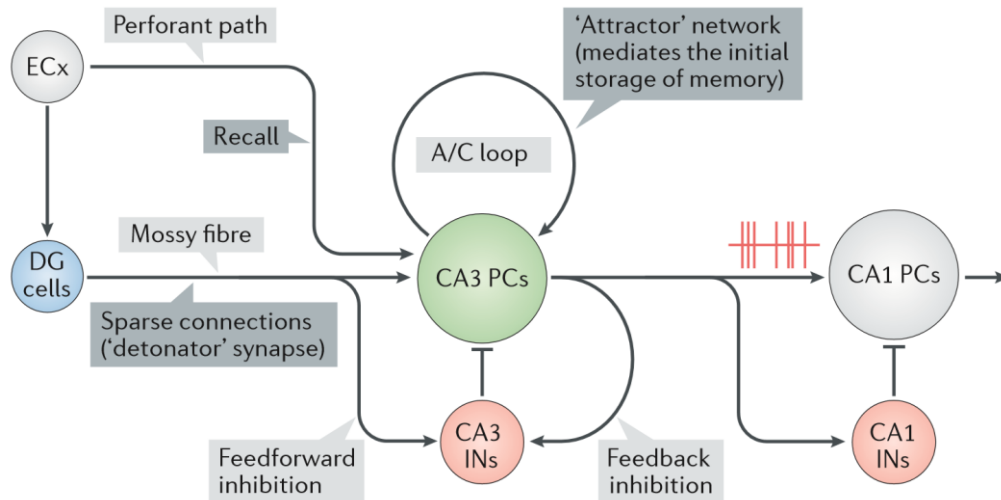


Figure 1.11. CA3 circuits and their proposed role in memory.

This schematic illustration shows the different elements of CA3 circuits and their hypothesized involvement in memory encoding and recall. The CA3 PCs receives three types of glutamatergic inputs, including the input from EC through perforant path, from DG through mossy fibers, and from CA3 layer itself through A/C fibers. The CA3 PCs also receive inhibitory signals from local interneurons, this can be either feedforward inhibition coming from DG, or feedback inhibition coming from CA3 cells. Adapted from Rebola, Carta & Mulle, 2017.

The Mf-CA3 connection is especially interesting for its peculiar structure. The mossy fibers (Mfs) were named by Ramon y Cajal for the varicosities all along their axons, giving them a "mossy" appearance. They form three morphologically different synaptic terminals, include the large mossy terminals (LMTs), filopodial extensions of the terminals, and smaller "en passant" synapses (Acsady, Kamondi, Sik, Freund, & Buzsaki, 1998). The mossy fiber boutons are large complex terminals with multiple releasing sites and packed with synaptic vesicles (Blackstad & Kjaerheim, 1961; Laatsch & Cowan, 1966). They form synapses with the proximal dendritic spines of CA3 PCs in stratum lucidum of CA3 region, consisting the feedforward excitation of Mf-CA3 pathways. These spines on CA3 pyramidal cell dendrites are called "thorny excrescences" (ThEs) (Gonzales, DeLeon Galvan, Rangel, & Claiborne, 2001). Meanwhile, the filopodia of LMT form synapses with local interneurons for feedforward inhibition onto CA3 PCs (Ruediger et al., 2011) (Figure 1.12).

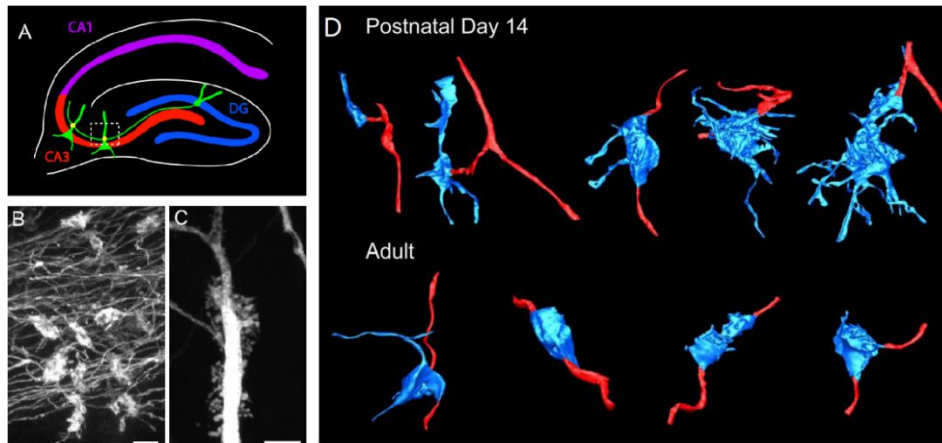


Figure 1.12. Mossy fiber terminals.

A. Schematic representation of the hippocampus with the region of mossy fiber terminals indicated (dashed box). **B.** Dil-labeled MfBs. Scale bar, 5 μ m. **C.** CA3 neuron with TE spines labeled by intracellular injection of LY dye in fixed tissue. Scale bar, 5 μ m. **D.** Reconstructed Mf axons (red) with boutons (regions of vesicle accumulation; blue) in P14 and adult mice. Adapted from (Wilke et al., 2013).

A single mossy fiber axon may make as many as 37 contacts with a single CA3 PC, but innervates only about 14 different CA3 PCs (Claiborne, Amaral, & Cowan, 1986). In contrast, each DG granule cell is innervating as many as 40 to 50 interneurons in CA3 area (Acsady et al., 1998). Intriguingly, these numbers can be dynamically changed by, for example, contextual or spatial learning (Crusio & Schwegler, 2005; Ruediger et al., 2011).

On the other hand, each CA3 pyramidal cell receives input from about 50 different DG granule cells (Crusio, Genthner-Grimm, & Schwegler, 2007), as well as ~3600 excitatory inputs from EC layer II via perforant path (PP), and ~12000 contacts from recurrent collaterals of other CA3 PCs (Rolls, 2013). However, the number of contacts doesn't necessarily mean stronger innervation, considering the synaptic-distance-dependent scaling in the brain (de Jong, Schmitz, Toonen, & Verhage, 2012; K. J. Lee et al., 2013). Although sparse, Mf-CA3 synapses at the proximal dendrites of CA3 pyramidal cells are a powerful connection on the main path of information flow, and are thought to enhance the signal-to-noise ratio and optimize the selection of populations of CA3 PCs firing in a correlated manner.

In CA3 area, inhibitory neurons play a pivotal role in information transfer as well. The CA3 interneurons receive inputs from various sources, including the associational/commissural fibers (A/C), the mossy fibers (MF), and the perforant path

(PP). These interneurons serve both the feed-forward and feed-back circuits and can contact hundreds of CA3 pyramidal cells (Lawrence and McBain, 2003). It has been shown in the last century that MF synapses on interneurons (may be via filopodial extensions or small en passant boutons and occasional large boutons) are significantly more than MF synapses on CA3 pyramidal cells, the ratio being approximately 10 to 1 (Acsady et al., 1998). This MF preferential innervation of interneurons may underlie the overall inhibitory effect of DG innervation of the CA3 network (Bragin et al., 1997, Penttonen et al., 1997).

The interneurons located in the CA3 area are not a homogenous group and can be classified into various subtypes by their morphology, physiology, molecular expression patterns (such as receptors, neuropeptides or calcium-binding proteins), or biophysical features. For the convenience of our MF synapse electrophysiological studies, one functional classification of CA3 interneurons receiving MF inputs by Szabadics and Soltesz is shown below (Figure 1.13) (Szabadics and Soltesz, 2009). To be more specific, there are fast spiking basket cells and spiny lucidum cells receiving more MF inputs, which exhibit low release probability and small EPSC amplitudes; there are also regular spiking basket cells and Ivy cells receiving fewer MF inputs, which have high release probability and large EPSCs amplitudes. Long-term plasticities of MF-interneuron synapses in CA3 area is review by Galván et al. (Galván et al., 2011).

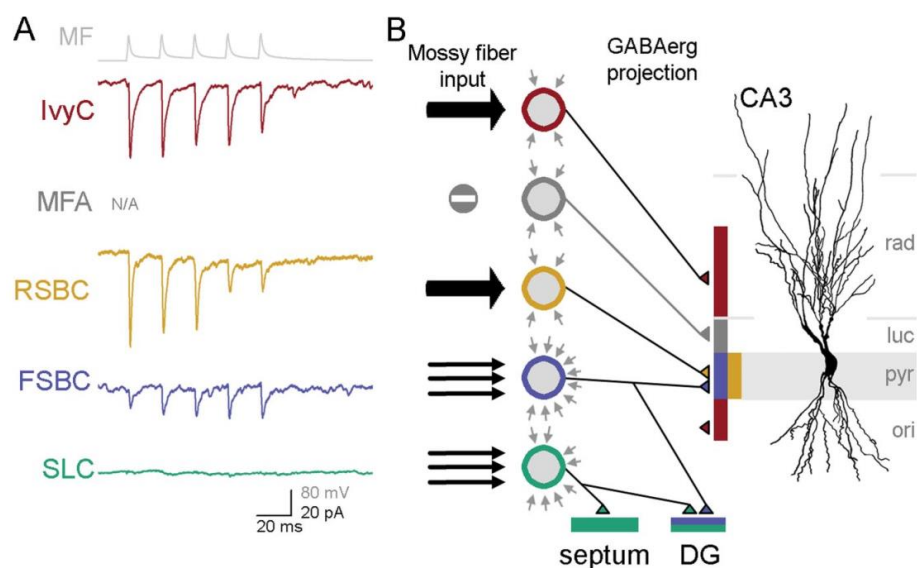


Figure 1.13. Functional classification of some CA3 interneurons.

A. Non-normalized averages from each cell type that received monosynaptic EPSCs from MFs after five presynaptic spikes at 50 Hz (top in gray: average of action

potentials from a representative MF). Note that no traces are shown for MFAs, since these cells were not found to be receiving monosynaptic inputs from MFs. **B.** Schematic presentation of the number and the strength of monosynaptic MF inputs (black arrows from the left) (the number of arrows represent the approximate relative abundance of MF inputs to the different cell types and the strength is illustrated by the width of the arrows) to CA3 GABAergic cells (color-coded circles), background synaptic events (gray arrows around the schematic GABAergic cells; number of arrows reflect spontaneous synaptic event frequency), and the GABAergic projections of the cells within and outside of the CA3 area. A representative CA3 pyramidal cell is shown for illustration. MF, mossy fiber; IvyC, Ivy cell; MFA, MF-associated cell; RSBC, regular-spiking basket cell; FSBC, fast-spiking basket cell; SLC, spiny lucidum cell. Adapted from (Szabadics and Soltesz, 2009).

Although there have been many attempts to explain populational activities through cell-type-specific interactions, we still lack the concrete evidence of how different subtypes of CA3 interneurons control information flow in the local circuits.

DG–CA3 connections have been implicated in pattern separation and assistance in memory encoding and the recall of contextual and spatial memory (Rebola et al., 2017). For example, it has been shown that transgenic inactivation of output of adult versus developmentally born DG neurons has differential impacts on pattern separation and completion (Nakashiba et al., 2012). Some other study has demonstrated that pharmacological impairment of DG–CA3 transmission alters novel contextual representation (Daumas, Ceccom, Halley, Frances, & Lassalle, 2009; Lassalle, Bataille, & Halley, 2000). Further evidence includes that mice with impaired Mf LTP are deficient for incremental learning (Otto et al., 2001), exposure to novel context regulates electrically induced plasticity (Hagena & Manahan-Vaughan, 2011), and that there is structural remodeling of Mf boutons upon learning (Holahan, Rekart, Sandoval, & Routtenberg, 2006; Routtenberg, 2010; Ruediger et al., 2011).

However, there are still open questions and missing evidence about the specific role of Mf-CA3 connections in memory encoding. For instance, whether there is a causal link between Mf LTP and memory encoding is still under debate (Kaifosh & Losonczy, 2016). Moreover, other questions remain, such as the impact of NMDAR plasticity and its role in metaplasticity and synaptic integration (Hunt, Puente, Grandes, & Castillo, 2013; Rebola, Carta, Lanore, Blanchet, & Mulle, 2011), and the role of Mf-dependent heterosynaptic plasticity (input-unspecific synaptic plasticity) in memory encoding.

1.2.5 Computational modeling of CA3 circuits

The relative simplicity of the hippocampal networks, when compared with e.g. neocortex, strongly appealed to computational neuroscientists to build models and test theories about memory mechanisms as early as since the 1970s. The original idea was built on Hebbian theory, stating “when an axon of cell A is near enough to excite cell B and repeatedly or persistently takes part in firing it, some growth process or metabolic change takes place in one or both cells such that A's efficiency, as one of the cells firing B, is increased” (Hebb, 1949). In the most influential early model of Marr, he constructed an “autoassociator” that learns to associate all components of an input pattern with all other components of the same pattern (Marr, 1971).

With the computational power and accessibility change in the 1990s, the amount of publication surged in this field. Computational models of the hippocampus, especially of DG-CA3 circuits have been numerous proposed, because this network shares many of the basic connectivity requirements for an autoassociator (Hasselmo, Wyble, & Wallenstein, 1996; Korol, Abel, Church, Barnes, & McNaughton, 1993). These models focused mainly on the ability of the hippocampal regions to perform sequential learning, spatial navigation, and the consolidation of episodic memories.

For example, Levy presented a model of hippocampal CA3 region as a sequence predictor, and the model was able to learn and use context by solving sequence and configural learning problems, providing a computational unification of a variety of putative hippocampal-dependent functions (Levy, 1996). Liaw & Berger described a simple hippocampal network consisting of a small number of neurons connected with dynamic synapses could perform speech recognition, suggesting that the dynamic interplay between synapses (facilitative and inhibitory) results in an emergent “temporal chunking” mechanism for sequential pattern recognition (Liaw & Berger, 1996).

In some more recent works, Myers & Scharfman presented a simple computational model of the dentate gyrus to demonstrate that hilar cells may mediate dynamic regulation of pattern separation, by mediating the backprojection from CA3 to DG (Myers & Scharfman, 2009). Hiratani et al. constructed an associative memory network model of spiking neurons that stores multiple memory patterns in a connection matrix with a lognormal weight distribution, demonstrating that heavy-tailed distributions of connection weights can generate noise which is useful for associative memory recall (Hiratani, Teramae, & Fukai, 2012).

Computational models provide us a chance to connect data at multiple levels including molecular, cellular, anatomical and behavioral levels, no matter they are developed in a top-down (computational models predicting biological details) or bottom-up (computational models simulating biological data) fashion (Gluck & Granger, 1993). The computational and biological fields of neuroscience can inform each other and jointly lead to better understanding of our brain.

1.3 Brain plasticity on a molecular level

1.3.1 Epigenetics and chromatin plasticity

Now diving to an even deeper and more basic level under learning and memory, right to the eukaryotic cell nuclei, scientists have been trying to explain plasticities happening in the brain on an epigenetic level.

The notion “epigenetics” was first proposed by C. H. Waddington in 1942 to describe that the genes might interact with each other and with their environment to produce a phenotype (Waddington, 1953).

A gene is a locus or region of DNA and the molecular unit of heredity (Alberts, Johnson, Lewis, Raff, Roberts, & Walter, 2002). Genes are compactly stored on chromosomes (the condensed form) or chromatins (the unraveled form) (Figure 1.14). The more condensed form of chromatin is called heterochromatin, and the genes located in heterochromatic region usually are less active or not active, while euchromatin is dispersed and loose, making the genes located at euchromatic regions relatively active (Grewal & Moazed, 2003).

Approximately 146 base pair (bp) of DNA strand is wrapped around a histone octamer core protein, forming a structure called nucleosome. The "linker DNA" between two nucleosomes can be up to 80 bp long. The histone octamer consists of 4 types of histones: H2A, H2B, H3, and H4, with two copies of each (Luger, Mader, Richmond, Sargent, & Richmond, 1997). The histone proteins are overall positively charged, making them attracted to negatively charged DNAs. Importantly, each histone protein has an N-terminal tail sticking out, which is subject to many forms of modifications, such as acetylation, methylation, phosphorylation, ubiquitylation and ADP-ribosylation (Strahl & Allis, 2000; Vaquero, Loyola, & Reinberg, 2003).

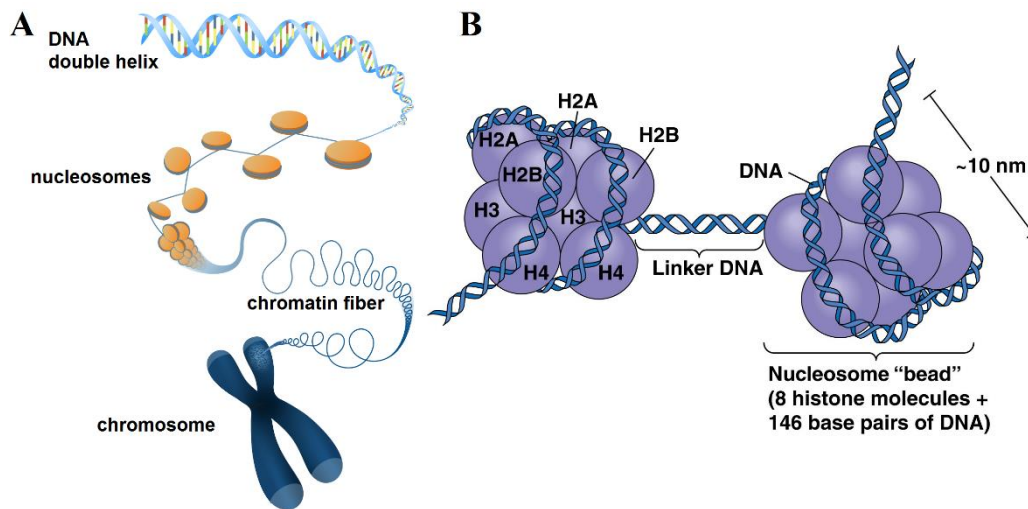


Figure 1.14. Schematic representation of chromosome, chromatin, nucleosome, and histone octamers.

A. Illustration showing how DNA is packaged into a chromosome. DNA wraps around the histone cores to form nucleosomes. These units then condense into a chromatin fiber, which condenses further to form a chromosome. Image copyright: Genome Research Ltd. **B.** Nucleosome as a “beads-on-a-string” structure. The nucleosome core is comprised of a histone octamer with histone 2A, 2B, 3 and 4, two copies each. The DNA double helix strand is wrapped around (~1.7 times) the histone octamer. Image copyright: Pearson Education Inc.

These post-translational modifications on histone tails actively regulate the interaction between DNA and histones. If the positive charge is reduced by the modification, the attractive force between histone and DNA decreases, thus making DNA more accessible for translational machinery; conversely, when the positive charge is increased, DNAs are less likely to be translated.

1.3.2 Histone Methylation as a transcription regulator

Unlike histone acetylation, which almost always facilitates local gene expression, histone methylation can either promotes or represses gene expression, depending on which residue is modified (Justin, De Marco, Aasland, & Gamblin, 2010; Scharf & Imhof, 2011; Shi & Whetstine, 2007; Shilatifard, 2008). It occurs on lysine (K) or arginine (R) residues of histone tails, and it can happen more than once on the same

residue, resulting in monomethylation, dimethylation or trimethylation (Mosammaparast & Shi, 2010; Santos-Rosa et al., 2002; Schneider et al., 2005). A summary of known histone methylation types is listed in Table 1.3 (Di Lorenzo & Bedford, 2011).

Table 1.3 Histone tail methylations.

Histone	Modification	Role	Reference
H3	H3K4me2	Permissive euchromatin	(Santos-Rosa et al., 2002)
	H3K4me3	Transcriptional elongation; active euchromatin	(Roguev et al., 2001; Strahl, Ohba, Cook, & Allis, 1999)
	H3K9me3	Transcriptional repression; imprinting; DNA methylation	(Rea et al., 2000; K. Zhang et al., 2002)
	H3R17me	Transcriptional activation	(Bauer, Daujat, Nielsen, Nightingale, & Kouzarides, 2002; Chen et al., 1999)
	H3K27me3	Transcriptional silencing; X-inactivation; bivalent genes/gene poising	(K. Zhang et al., 2002)
	H3K36me3	Transcriptional elongation	(K. Zhang et al., 2002)
H4	H4R3me	Transcriptional activation	(Wang et al., 2001)
	H4K20me	Transcriptional silencing	(Nishioka et al., 2002)
	H4K20me3	Heterochromatin	(Schotta et al., 2004)

H3K4 is the one of the most extensively targeted positions among all possible histone methylation sites (Vallianatos & Iwase, 2015), and is always facilitating translation. With the advances of technological nowadays, especially chromatin immunoprecipitation (ChIP) together with quantification of associated DNA by next-generation sequencing (ChIP-seq), it has been shown that H3K4 methylation has wide-ranging roles on a genome-wide scale, and is closely related to transcriptional regulation and epigenetic tagging of promoter and enhancer sequences in both neurodevelopment and neuropsychiatric diseases (Barski et al., 2007).

ChIP-seq studies have shown that the distribution of the trimethylated form of histone 3 (H3K4me3) in the human brain shows approximately 30 000 sharp “peaks” genome-wide (Cheung et al., 2010; Shulha, Crisci, et al., 2012). These “peaks” (1–2 kb in length) can differ among different cell types, and are mostly located around transcription start sites (TSSs) of proximal gene promoters and other regulatory

sequences (e.g. CpG islands) (Barrera et al., 2008; Guenther, Levine, Boyer, Jaenisch, & Young, 2007). In contrast, the di- and mono-methylated forms of histone 3 (H3K4me2 and H3K4me1) are organized as much broader peaks and appear in a much larger proportion of open chromatin, including promoters and enhancers (Barski et al., 2007; Maston, Landt, Snyder, & Green, 2012).

1.3.3 H3K4me3 in learning and memory

As is mentioned in the last chapter, H3K4me3 markers appear in promoter areas across the genome in a more concentrated and cell-type specific manner compared to H3K4me1 and H3K4me2 (Guenther et al., 2007), and is thought to be an important additional layer of transcriptional regulation (Shilatifard, 2008, 2012).

One study showed that H3K4me3 level is upregulated in hippocampus 1 h following contextual fear conditioning and returned to baseline levels at 24 h (Gupta et al., 2010). In a more recent study, people have found that retrieval of a recent contextual fear conditioned memory increased global levels H3K4me3 in hippocampal CA1 area, and in vivo knockdown of the H3K4me3 methyltransferase Mll1 in CA1 impaired fear memory (Webb et al., 2017). Another report stated that baseline resting levels of H3K4me3 were altered in the aged rat hippocampus as compared to young adults, and object learning can increase hippocampal H3K4me3 levels in young adult rats but not aged ones with memory deficits, which can be rescued by increasing H3K4me3 levels in aged rats with a histone demethylase inhibitor treatment (Morse, Butler, Davis, Soller, & Lubin, 2015). In line with these results, increased levels of H3K4me3 were found in the hippocampus of mice with enhanced hippocampal-dependent learning and memory (offspring of high licking/grooming mothers), and this results in higher expression of mGluR1 in hippocampus together with increased mGluR1-induced LTD and paired-pulse depression (PPD) (Bagot et al., 2012)

Moreover, altered levels of H3K4me3 were also found in a few mouse models with intellectual disabilities. For example, a ketogenic diet modulated H3K4me3 levels in the granule cell layer, rescuing both the neurogenesis defect and hippocampal memory abnormalities in a mouse model of Kabuki syndrome (Benjamin et al., 2017). Disruption of KDM5C in mice, which predominantly represses genes with high levels of H3K4me3 at the promoters, recapitulates adaptive and cognitive abnormalities seen in human patients with X-linked intellectual disability (XLID) (Iwase et al., 2016).

Interestingly, abnormal levels of H3K4me3 were also observed in brains of

patients with other neuropsychiatric disorders, such as Huntington disease (Vashishtha et al., 2013), autism (Shulha, Cheung, et al., 2012), schizophrenia (Kano et al., 2013), and addiction to cocaine or alcohol (Zhou, Yuan, Mash, & Goldman, 2011).

Collectively, these findings suggest that the levels of H3K4me3, especially in the hippocampus, are actively regulated and closely correlated with learning and memory functions.

1.4 Alzheimer's disease (AD)

1.4.1 Historical background and clinical aspects of AD

First reported in 1907 by the German psychiatrist and pathologist Alois Alzheimer (Berchtold & Cotman, 1998), Alzheimer's disease (AD) has been identified as the most common form of dementia, accounting for 60 - 70% of all dementia cases nowadays (Burns & Iliffe, 2009). Its global prevalence is considerably high, affecting about 6% of the population over 65 years old, and the incidence increases with age (Ferri et al., 2005). According to estimation, over 30 million people worldwide are suffering from AD (Querfurth & LaFerla, 2010), which makes AD a major public health concern and a research priority in the academic world.

To be more specific, Alzheimer's disease is a chronic and progressive neurodegenerative disorder characterized by various cognitive and non-cognitive symptoms. The cognitive symptoms comprise memory loss, which is normally the first and universal symptom in the vast majority of cases, together with language difficulties, and executive dysfunctions and intellectual impairments (Tarawneh & Holtzman, 2012). The non-cognitive or neuropsychiatric symptoms include depression, hallucinations, delusions, and agitation (Burns, 1992). In addition, difficulties with performing daily life activities and coexistence of vascular diseases are also quite common in AD cases (Snowdon et al., 1997). Although the progression of AD can be very slow, the average life expectancy after diagnosis is usually 3 - 9 years (Todd, Barr, Roberts, & Passmore, 2013). Suggested diagnostic criteria are shown in Figure 1.15 (Ballard et al., 2011).

Panel: Research diagnostic criteria for Alzheimer's disease	
Probable Alzheimer's disease: A plus one or more supportive features B, C, D, or E	
Core diagnostic criteria	
A	Presence of an early and significant episodic memory impairment that includes the following features: <ol style="list-style-type: none"> 1 Gradual and progressive change in memory function reported by patients or informants over more than 6 months 2 Objective evidence of significantly impaired episodic memory on testing: this generally consists of recall deficit that does not improve significantly or does not normalise with cueing or recognition testing and after effective encoding of information has been previously controlled 3 The episodic memory impairment can be isolated or associated with other cognitive changes at the onset of Alzheimer's disease or as Alzheimer's disease advances
Supportive features	
B	Presence of medial temporal lobe atrophy: volume loss in the hippocampus, entorhinal cortex, or amygdala on MRI with qualitative ratings by visual scoring (referenced to well characterised population with age norms) or quantitative volumetry of regions of interest (referenced to well characterised population with age norms)
C	Abnormal cerebrospinal fluid biomarker: low amyloid β_{1-42} concentrations, increased total tau concentrations, or increased phosphotau concentrations, or combinations of the three; or abnormalities in other well-validated markers that will be discovered in the future
D	Specific pattern of reduced glucose metabolism in bilateral temporal parietal regions on functional neuroimaging with PET or with other well validated ligands, such as Pittsburgh compound B or FDDNP (2-(1-(6-[(2-[18 F]fluoroethyl)(methyl)amino]-2-naphthyl)ethylidene)malononitrile)
E	Proven Alzheimer's disease autosomal dominant mutation within the immediate family

Figure 1.15. Diagnostic criteria of AD (revised from NINCDS-ADRDA criteria)

The cause of Alzheimer's disease is still mostly unknown, but many risk factors have been linked with the disease in case-control studies (Burns & Iliffe, 2009) (Table 1.4).

Most of the AD cases are sporadic, and only 1% to 5% of cases are familial, where genetic mutations can be identified as single risk factors (Reitz & Mayeux, 2014). The familial AD (FAD) typically has an early onset before the age of 65 (Blennow, de Leon, & Zetterberg, 2006). In most of the early onset familial AD cases, autosomal dominant inheritance mutations in one of three genes can be found: the amyloid precursor protein (APP), presenilin 1 (PS1), and presenilin 2 (PS2), on chromosomes 21, 14, and 1 respectively (Waring & Rosenberg, 2008). However, a summary of all possible genetic factors is shown in Table 1.5 (Ballard et al., 2011).

Table 1.4. Risk factors for Alzheimer's disease.

Sociodemographic	Age: increasing age
	Sex: no consistent evidence
	National and ethnic profile: some evidence of regional variations
Genetic factors	Family history: 3.5-fold increase in risk when a first degree relative is affected
	Diseases causing mutations: on chromosomes 1, 14, and 21
	ApoE genotype
	Down's syndrome: everyone eventually develops the neuropathological features of

	Alzheimer's disease
	Premorbid cognitive reserves: longer education and higher intelligence are protective
Medical history	Head injuries: anti-inflammatory drugs are associated with a reduction in risk
	Oestrogen replacement: no consistent evidence
	Vascular risk factors: hypertension, diabetes, homocysteine, and cholesterol are all implicated
	Depression: associated with Alzheimer's disease
	Herpes simplex: a risk factor, possibly mediated by the presence of ApoE e4
Habits	Alcohol: drinking wine is protective
	Smoking: no consistent evidence
	Diet: no consistent evidence (including for aluminium)
	Occupational and recreation factors: no consistent evidence

Table 1.5. Genetic factors of AD.

Role in Alzheimer's disease	Effect on risk of Alzheimer's disease	
Familial genes		
APP	APP is a membrane protein cleaved by secretases. Cleavage of APP by secretases leads to both non-amyloidogenic processing and production of A β . Familial APP mutations result in preferential processing of APP through the amyloidogenic pathway ³	NA
PSEN1	PSEN1 is a component of α secretase, which is involved in APP processing to A β . Familial PSEN1 mutations can alter the production of A β_{1-40} , which forms plaques more readily than A β_{1-42} ⁴	NA
PSEN2	Processes APP into A β as part of the α -secretase complex. Familial mutations can alter the production of A β_{1-42} , which forms plaques more readily than A β_{1-40} ⁵	NA
SorL1	SorL1 interacts with APOE, affects APP trafficking, and overexpression of the protein results in reduced A β production. Binding of SorL1 to APP results in reduced A β production. SORL1 is a γ -secretase substrate. SorL1 concentrations are reduced in patients with Alzheimer's disease ⁶	NA
Risk genes		
APOE	APOE is transported with cholesterol; APOE isoforms have differing transport efficiencies. APOE binds A β in an isoform-specific manner. APOE is involved in A β clearance through interaction with LRP. APOE4 alleles are associated with increased amyloid burden and cholinergic dysfunction	3-10 times increased ⁷
GSK3 β	GSK3 β phosphorylates tau, leading to tangle formation. APP cleavage products can activate GSK3 β , leading to increased tau phosphorylation. GSK3 β phosphorylates tau more effectively if tau has already been phosphorylated by other kinases, such as cdk5. GSK3 β activity can also be promoted by PSEN complexes	1.7 times increased. ^{18,19} No Alzgene meta-analysis
DYRK1A	DYRK1A is located on chromosome 21. DYRK1A is involved in tau phosphorylation; its activity is upregulated by A β , therefore DYRK1A is a link between amyloid and tau pathologies. DYRK1A phosphorylates tau to prime the molecule for further phosphorylation by GSK3 β . DYRK1A also phosphorylates septin 4, another tangle protein. DYRK1A is involved in APP phosphorylation, which leads to increased amyloidogenic processing through increased BACE interaction	T allele is less frequent in people with Alzheimer's disease. No Alzgene meta-analysis ²⁰
Tau	Tau is hyperphosphorylated in NFTs. Tau exists as six splice isoforms depending upon inclusion of N-terminal exons 2 and 3, and the exon 10 microtubule binding domain. Tau mutations can affect splicing and microtubule binding efficacy. The tau haplotype is associated with Alzheimer's disease, and affects expression levels of tau splice isoforms	H1C haplotype more frequent in Alzheimer's disease. No Alzgene meta-analysis of the haplotype ^{21,22}
TOMM40	TOMM40 is a translocase of outer mitochondrial membrane 40 homolog on the same chromosome as APOE. TOMM40 interacts with APP and is associated with the age of onset in late-onset Alzheimer's disease ²³	Alzgene odds ratio of 0.66 for rs8106922
CLU	Clusterin is a chaperone involved in A β formation and is associated with severity and progression of Alzheimer's disease ²⁴	Alzgene odds ratio of 0.87 for rs1113600
PICALM	Phosphatidylinositol binding clathrin assembly protein, present in endosomes which are enlarged in early Alzheimer's disease ²⁵	Alzgene odds ratio of 0.87 for rs541458

A full meta-analysis of risk genes can be found on the Alzgene website (<http://www.alzgene.org/>). NA=not applicable. A β =amyloid β . APP=amyloid precursor protein. APOE=apolipoprotein E. NFT=neurofibrillary tangle.

In clinical practice of treating AD, apart from psychosocial interventions, a few pharmacotherapies are available (Ballard et al., 2011; Burns & Iliffe, 2009) (Table 1.6) to ameliorate symptoms, but none of these seem disease-modifying.

Table 1.6. Drug treatments for Alzheimer's disease.

	Drugs	Status	Evidence
Symptomatic treatments			
Cholinesterase inhibitors	Donepezil, rivastigmine, galantamine	Licensed for mild-to-moderate Alzheimer's disease	More than 30 placebo-controlled randomised controlled trials, mainly of 6 months duration in patients with mild-to-moderate Alzheimer's disease (MMSE 10-26). Significant benefits in cognition, function, and global outcome, with MMSE gain of 1.5-2 points over 6-12 months. Several studies suggest similar benefit in severe Alzheimer's disease ^{7,75}
NMDA receptor antagonist	Memantine	Licensed for moderate-to-severe Alzheimer's disease	Significant benefit in cognition, function, global outcome, and neuropsychiatric symptoms over 6 months in three trials of moderate-to-severe Alzheimer's disease ⁶
Treatments for neuropsychiatric symptoms			
Atypical antipsychotics	Risperidone, quetiapine, olanzapine, aripiprazole	Risperidone licensed for short-term treatment of severe aggression in Alzheimer's disease; other treatments are used off licence	Significant but modest efficacy for the treatment of aggression (SES 0.2-0.25) and psychosis (SES 0.15-0.2) over 6-12 weeks. Limited evidence of longer term benefits. Atypical antipsychotics associated with significant increase in stroke (RR 2.5-4.0) and death (RR 1.5-1.8) ⁷
Antidepressants	Citalopram, sertraline	All antidepressants used off licence in Alzheimer's disease	Evidence not clear-cut. The largest trial with sertraline suggested no benefit for the treatment of depression in patients with Alzheimer's disease. ⁷⁶ Severe depression should be treated, probably with a selective serotonin reuptake inhibitor
Anticonvulsants	Carbamazepine	Used off licence	There is preliminary evidence from small randomised controlled trials that carbamazepine might be an effective treatment for agitation or aggression in Alzheimer's disease ⁹

Due to so many non-modifiable risk factors, interventions by drug treatments are unlikely to result in a large-scale reduction in AD incidence. However, the picture is being changed by lifestyle interventions and perhaps ultimately by progress in basic research.

1.4.2 Familial AD (FAD) on genetic and molecular level

There are many current hypotheses trying to explain the pathogenic mechanisms of FAD. One of the most popular hypothesis on FAD is "amyloid cascade hypothesis", which postulates that abnormal accumulation of amyloid- β ($A\beta$) plaques in different areas of the brain is the initiating event in AD pathogenesis, and could trigger various downstream neuropathologies leading to neurodegeneration and full onset of AD (Barage & Sonawane, 2015).

The $A\beta$ peptide is derived from amyloid precursor protein (APP), which belongs to an evolutionarily conserved family of type I transmembrane glycoproteins consisted of 695-770 amino acids. APP can be cleaved by α -, β -, or γ -secretase (Ling, Morgan, & Kalsheker, 2003): α -secretase function can be carried out by 3 enzymes in the ADAM family (a disintegrin and metalloproteinase family enzyme): ADAM9, ADAM10 and ADAM17 (Allinson, Parkin, Turner, & Hooper, 2003); β -secretase activity has been found in β -site APP-cleaving enzyme 1 (BACE1) (Sinha et al., 1999; Vassar et al., 1999). The γ -secretase has been identified as a complex of enzymes composed of presenilin 1 or 2, (PS1, PS2), nicastrin, anterior pharynx defective (APH-1) and presenilin enhancer 2 (PEN2) (Francis et al., 2002; Levitan et al., 2001; Steiner et al., 2002; Wolfe et al., 1999; Yu et al., 2000).

The cleavage and processing of APP can be categorized into a non-amyloidogenic pathway and an amyloidogenic pathway as is shown in Figure 1.16 (Nicolas & Hassan, 2014). In the prevalent non-amyloidogenic pathway, APP is cleaved by α -secretase within the A β domain, thereby preventing the production of the A β peptide. Two fragments are released consequently, the smaller membrane-tethered C-terminal fragment (C83) and the larger N-terminal ectodomain (sAPP α) (Kojro & Fahrenholz, 2005). Furthermore, C83 is subsequently cleaved by γ -secretase, producing an even shorter fragment called P3 (Haass, Hung, Schlossmacher, Teplow, & Selkoe, 1993).

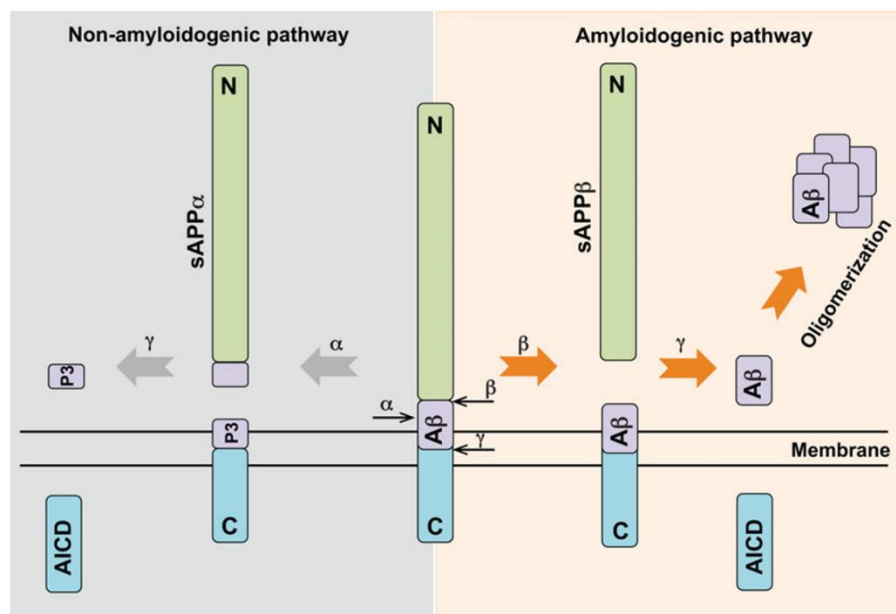


Figure 1.16. Scheme of the proteolytic processing of APP.

APP (shown in the middle in the illustration) can be cleaved by α -, β - and γ -secretases. The cleavage sites of these proteases are α -, β - and γ -sites respectively. When APP undergoes non-amyloidogenic pathway (to the left side): it is cleaved by α -secretase within the A β sequence to generate sAPP α and the membrane-tethered α APP-CT, which is then further cleaved by γ -secretase to release the P3 peptide and AICD; when APP undergoes amyloidogenic pathway (to the right side), it is cleaved by β -secretase resulting in the formation of soluble APP β (sAPP β) and β APP-CTF, which is then further cleaved by γ -secretase releasing A β and AICD (amyloid precursor protein intracellular domain). Adapted from Nicolas & Hassan, 2014.

Alternatively, there's also the amyloidogenic pathway for APP processing, leading to the generation of A β and later oligomers and plaques. In this pathway, APP is cleaved by β -secretase (β -site APP-cleaving enzyme 1; BACE1), resulting in an ectodomain

(sAPP β) in the extracellular medium, and a membrane-bound C-terminal fragment of 99 amino acids (known as C99). C99 is subsequently cleaved by the γ -secretase complex (consists of presenilin 1 or 2, nicastrin, anterior pharynx defective and presenilin enhancer 2) to release A β peptide. A β generated in this step are mainly A β ₄₀ (~90%), but the rarer product A β ₄₂ (~10%) is more hydrophobic and present as the predominant isoform in cerebral plaques in AD (Jarrett, Berger, & Lansbury, 1993; Younkin, 1998).

As we have mentioned, FAD-associated mutations are identified as APP, presenilin-1 (PS1) and presenilin-2 (PS2) (Waring & Rosenberg, 2008). Mutated APP might result in abnormal processing of the protein, for example, favoring the amyloidogenic pathway (the case of APP_{Swe}) (Haass et al., 1995), or increasing the aggregation of A β and fibrils (the case of APP_{ARC}) (Nilsberth et al., 2001). Moreover, increased copies of APP gene also result in AD (Cabrejo et al., 2006; Rovelet-Lecrux et al., 2006). Presenilin 1 (PS1) and PS2 are key components of the γ -secretase complex, so their mutations can alter γ -secretase cleavage and promote the production of A β ₄₂ (Guo et al., 1999; Jankowsky et al., 2004).

Therefore, mutations in these three genes will lead to disturbed metabolism of A β and eventually AD pathology (St George-Hyslop & Petit, 2005).

1.4.3 Mouse models of FAD

Mice are commonly used as models for neuroscience research, because they have comparable brain networks and similar neurobiological processes to humans. Besides, mice are also easy to be manipulated genetically, and can be easily bred in a rapid and inexpensive manner. Therefore, numerous transgenic mouse models of FAD have been created for research (Kitazawa, Medeiros, & Laferla, 2012).

Unlike humans, wild type mice do not develop A β plaques during normal aging, probably because of small differences in APP gene within the A β sequence compared to human (Dyrks, Dyrks, Masters, & Beyreuther, 1993). When wild type human APP is expressed or even overexpressed in mice, these mice still show no deposition of A β plaques and only very mild neuropathological changes (Buxbaum, Christensen, Ruefli, Greengard, & Loring, 1993; Lamb et al., 1993; Mucke et al., 2000). Therefore, transgenic mice with mutant APP genes were necessary for the creation of FAD models. The age of A β pathologies onset varied among these transgenic mice because of different mutations, different transgene promoters, and different expression levels in

each mouse line. In general, mice overexpressing mutant APP will exhibit age-dependent A β neuropathologies in the brain, including cognitive impairment, dystrophic neurites, reactive astrocytes and activated microglia, elevated innate immune and inflammatory responses, and synaptic loss (Games et al., 1995; Hsiao et al., 1996; Sturchler-Pierrat et al., 1997). However, these mice did not show robust neurodegeneration or tau pathology in the brain.

Again, unlike in humans, PS1 mutations alone do not cause A β plaques in mouse brain probably because of different sequence in mouse APP (in A β domain). As a result, mutant human APP is often introduced into PS1 transgenic mouse lines. Usually, the double transgenic mice exhibit accelerated production of A β ₄₂ and earlier formation of A β plaques than APP transgenic mice (Borchelt et al., 1997). In addition, knocking out PS1 is lethal for mice in the embryonic stage (Shen et al., 1997; Wong et al., 1997), but postnatal conditional knockout of PS1 is not lethal anymore, suggesting that it plays a vital role during embryonic development.

On the other hand, PS2 deletion in embryos only causes a very mild phenotype with mild pulmonary fibrosis and hemorrhage in senility (Herreman et al., 1999), and the effect of postnatal conditional PS2 KO was also minor. In these PS2 KO models APP cleavage and Notch signaling seem not affected, suggesting the role of PS2 is possibly redundant (Franberg, Svensson, Winblad, Karlstrom, & Frykman, 2011).

Apart from the histochemical pathologies, the AD mouse models need to be validated by behavioral tests for evidence of deficits in either short-term or long-term memory. It is needed to note that whether non-human species display episodic memory is still controversial. As a result, we tend to use terms such as reference memory, or associative learning, for episodic-like memory phenomena in rodents (Morris, 2001). Various behavioral tasks are available for evaluating the cognitive functions in rodent AD models, which have been nicely reviewed by Webster et al. (Webster, Bachstetter, Nelson, Schmitt, & Van Eldik, 2014) (Table 1.7).

Table 1.7. Commonly used mouse behavioral tasks for cognitive deficits.

Task	Description	Cognitive domains	References
Morris Water Maze (MWM)	Widely used behavioral task where mice are placed in a circular pool and must find a hidden escape platform	Reference memory and working memory	Morris et al., 1982
Radial Arm Maze (RAM)	The maze usually consists of 6–8 arms radiating from a round central space. Various arms are baited with a food reward.	Reference memory and working memory	Olton and Samuelson, 1976
Radial Arm Water Maze (RAWM)	A submerged version of the RAM where the food reward is replaced by an escape platform.	Reference memory and working memory	Diamond et al., 1999
Barnes maze	Consists of a circular platform with holes around the circumference and an escape box	Reference memory and working memory	Barnes, 1979
T-Maze/Y-Maze alternation	A three arm maze which forces the animal to choose between two arms	Reference memory and working memory	Blodgett and Mccutchan, 1947; Glickman and Jensen, 1961
Novel Object Recognition (NOR)	A two trial memory task which uses the animal's innate exploratory behavior to assess memory	Recognition memory	Ennaceur and Delacour, 1988
Contextual and cued fear conditioning	The animal learns to predict an aversive stimulus based on an associated context/cue	Reference memory (associative learning/memory)	Fanselow, 1980; Curzon et al., 2009
Passive avoidance	An avoidance task where the animal must refrain from entering a chamber where an aversive stimulus was previously administered	Reference memory (associative learning/memory)	Van Der Poel, 1967
Active avoidance	A fear-motivated associative avoidance test where an animal must actively avoid an aversive stimulus	Reference memory and working memory (associative learning/memory)	Vanderwolf, 1964
Delayed Matching (non-matching) to Position/Sample (DMTP/DMTS)	The animal receives a sample stimulus and then after a short delay is required to choose the correct corresponding response	Working memory	Dunnett, 1993; Robinson and Crawley, 1993
Multiple-Choice Serial Reaction Time Task (CSRTT)	The animal must attend to several spatial locations (usually 3–5), observe a corresponding stimulus, and then correctly respond	Attention, impulsivity, and executive function	Carli et al., 1983
Attentional set-shifting tasks	The animal must shift back and forth between changing rules to successfully obtain a reward	Executive function and cognitive flexibility	Birrell and Brown, 2000
Reversal learning	Adjustment to changes in reward contingency	Executive function and working memory	Butter, 1969; Bussey et al., 1997
What-Where-Which Task (WWWWhich)	The animal must associate an object (What) with its location (Where) in a specific visuospatial context (Which) to form an integrated memory	Recognition memory and episodic-like memory	Davis et al., 2013a,b

However, it is important to keep in mind that none of the current FAD mouse models fully recapitulate the whole spectrum of pathologies in FAD, including A β plaques accumulation, tangle formation, cognitive deficits, synaptic loss, and progressive neurodegeneration. However, transgenic mouse models of FAD remain invaluable tools in AD research to study specific aspects of the disease process, and meanwhile contributing to the evaluation of potential therapeutic strategies before clinical trials.

1.4.4 APP^{swe}/PSEN1^{dE9} (APP/PS1) mice as an FAD model

Various FAD mouse lines are currently being used for Alzheimer's research worldwide, among which some popular ones are single/multiple APP mutations, single presenilin (PS) mutations, APPxPS1 mutations, APPxPS1xtau mutations (3xTg) and anti-NGF expressing (AD11) mice. Their electrophysiological features have been

neatly reviewed by Marchetti and Marie (Marchetti and Marie, 2011).

The FAD model we used for this study, i.e. APP^{Swe}/PSEN1^{dE9} (APP/PS1) mice, were created by crossing mice that express mutant APP (APP^{Swe}) with mice that express mutant PS1 (PSEN1^{dE9}). APP^{Swe} is a chimeric mouse/human APP (isoform 695) with a Swedish mutation under the mouse prion promoter, resulting in increased total A β production by modulating β -secretase cleavage (Borchelt et al., 1996; Mullan et al., 1992; Savonenko, Xu, Price, Borchelt, & Markowska, 2003). PSEN1^{dE9} is the human PS1 lacking exon 9 (M. K. Lee et al., 1997), which can disturb γ -secretase cleavage and change it towards the more amyloidogenic direction.

The APP/PS1 mice start to have visible A β plaques in cerebral cortex and hippocampus at 6.5-month-old, aggravating with age (Jankowsky et al., 2001; Kim et al., 2012; Seo et al., 2011). Specifically, in the hippocampus, plaques start to be noticeable at 6-month in the molecular layer (ML) of the DG, later (at 10-month) in both ML of DG and stratum radiatum (SR) of CA3. However, A β plaques were not observed in the stratum lucidum (SL) of CA3 (Viana da Silva et al., 2016). In addition, APP/PS1 mice also exhibit tau hyperphosphorylation, but still lack neuronal loss and neurofibrillary tangles (NFTs) (Morrissette, Parachikova, Green, & LaFerla, 2009).

Many cognitive impairments in this model have been documented. By the age of 6 months, APP^{Swe}/PSEN1^{dE9} mice are reported to show working memory deficits in tests of Radial Arm Water Maze (RAWM) (Volianskis, Kostner, Molgaard, Hass, & Jensen, 2010), and Morris Water Maze (MWM) (Cao, Lu, Lewis, & Li, 2007; Ding et al., 2008). Deficits in associative learning have also been described in fear conditioning tasks starting at 6-8 months of age (Cramer et al., 2012; Knafo et al., 2009). Impairments in reference memory can be detected by 6 months (Bernardo et al., 2009; O'Leary & Brown, 2009; Reiserer, Harrison, Syverud, & McDonald, 2007). Passive avoidance deficits are developed at 12 months of age (W. Zhang et al., 2011). There are also deficits in alternation tasks such as Y-maze of working memory at 6-month (Viana da Silva et al., 2016).

As a link between the histochemical and behavioral findings, electrophysiological experiments have also been done to investigate the pathologies of APP/PS1 mice. Especially at the beginning stage of the disease, electrophysiological impairments can prelude visible A β plaques and behavioral deficits (Hsia et al., 1999). There have been reports about decreased DG LTP in 9-15 months APP/PS1 mice, and this might be due to upregulated GABA_A receptor-mediated inhibition (Yoshiike et al., 2008). Besides, some evidence showed impaired SC-CA1 LTP in 3-12 months APP/PS1 mice

(Volianskis et al., 2010). Furthermore, recently by our team, it has been shown that LTP within the associative network is abolished in CA3 PCs at 6 months of age in the APP/PS1 mice, and this loss of LTP was caused by activation of up-regulated neuronal adenosine A_{2A} receptors (Viana da Silva et al., 2016).

To sum up, although tau protein tangles cannot be observed in this APP/PS1 mouse model, it still captures a lot of other AD pathologies, including synaptic and neuronal loss, A β plaques, cognitive impairments, and gliosis, therefore it serves as a good model of AD research, at least for our purpose of amyloid pathology investigation. Our goal was to investigate the AD pathologies at early stage of onset, so we chose to use 6-month old mice, where visible plaques and cognitive declines are just about to appear and there's no neuronal loss yet. Therefore, 6-month was considered to be early stage in our case. Moreover, we used male mice only to reduce variability.

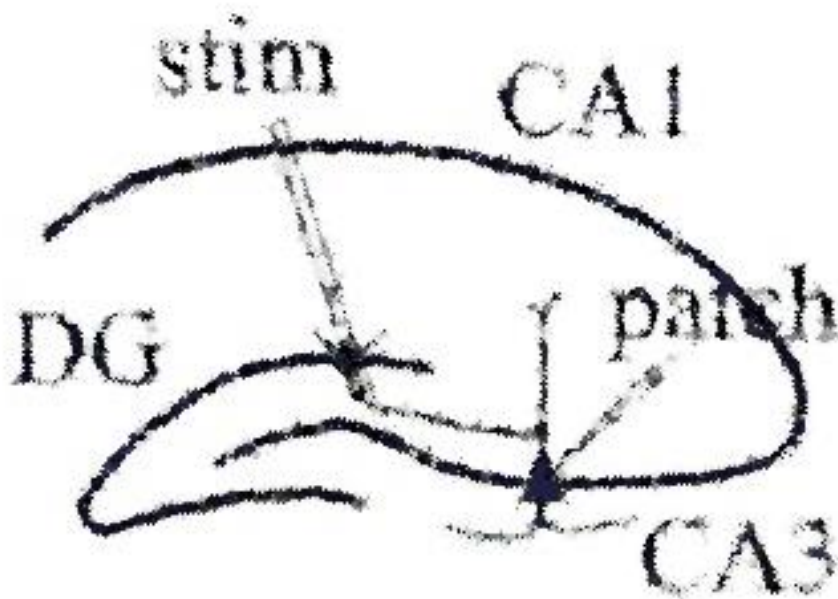
1.5 Objectives of the work

At the entry level of hippocampus, Mf-CA3 circuitry is thought have a key role in episodic memory encoding, especially at the early stage of acquisition. Many changes are actively taking place both in healthy learning models and in Alzheimer's disease models. To combine the strengths of my home team of Dr. Mulle in Bordeaux and my hosting team of Dr. Fischer in Goettingen, and also taking advantage of the opportunity of a one-month workshop in OIST Okinawa, we aimed at investigating the following issues:

- 1) Possible electrophysiological deficits in Mf-CA3 circuit of early FAD mouse model (APP^{swe}/PS1^{dE9}) at the age of 6-month, with a focus on short-term plasticity of glutamatergic synapses, GABAergic innervations onto CA3 PCs, and NMDAR and KAR-mediated events in CA3 PCs.
- 2) Electrophysiological changes in 2-month adult C57/B16j male mice shortly after contextual fear conditioning (CFC), at 3-hour and 24-hour time point respectively.
- 3) Screening of gene expression changes in 6-month APP/PS1 mice, and check for contextual memory-related epigenetic marker (histone modification: H3K4me3) changes in the hippocampal CA3 region.
- 4) Computational modeling of DG-CA3 neuronal networks in healthy condition, and test the fidelity of the output of the system with different spike patterns as inputs (shown in Annexes).

CHAPTER 2

MATERIALS AND METHODS



2 Materials and Methods

2.1 Animal Use

2.1.1 Ethical Considerations

All procedures (including anesthesia and euthanasia) were carried out in accordance with the European guidelines for the care and use of laboratory animals. The experiments performed in Bordeaux were approved by the animal care and use committee of Bordeaux Universities (CE50), and the experiments performed in Goettingen were approved by the animal ethics committee of the European Neuroscience Institute, Göttingen, Germany.

2.1.2 Mice

Adult C57/Bl6j male mice (8 weeks) were purchased from Janvier Labs (Daumas et al.). The cages were maintained on a 12-h dark/light cycle and kept in a temperature-regulated room, with free access to food and water. All the experiments were done in the light phase of their circadian cycles.

APP/PS1 mice and their WT littermates were obtained from Jackson Laboratory (Bar Harbor, ME, USA). Throughout their life, all the mice were group-housed, ranging from 4 to 10 animals per cage. Food and water were provided *ad libitum*. The transparent plexiglass cages (38.1 x 19.1 x 12.7 cm) were maintained on a 12-h dark/light cycle, kept in a temperature-regulated room, and protected from exterior pathogens by a filter. All experiments were performed in the light phase of the circadian cycle in 6 months (26-32 weeks) male APP/PS1 and age-matched male WT littermates. All mice were genotyped by the local animal facility and re-genotyped after each experiment with tail tissue taken by the experimenter.

2.1.3 APP/PS1 Mice Genotyping

-- DNA Isolation from mouse tail tissue.

The tip of the tail was cut in a postmortem way after sacrificing each mouse, and

put into a 1.5 ml tube (Eppendorf, Germany). 200 µl of DirectPCR® Lysis Reagent (Peqlab, Germany) were added into each tube together with 0.3 mg/ml Proteinase K (Peqlab, Germany). The tubes were then incubated at 55°C on a thermomixer (Eppendorf, Germany) for 16 h at 550 rpm. Afterwards, the tubes were incubated at 85°C for 45 min without shaking. 1.5 µl of the supernatant containing DNA was taken from the tube and kept at 4°C for later Polymerase Chain Reaction (PCR).

-- Polymerase Chain Reaction (PCR):

PCRs were performed targeting APP and PSEN genes to confirm the genotypes of mice used in our experiment. The primers are listed as follows:

Table 2.1. Primers of PCR

Primer	Targeted Gene	Sequence (5'-3')
P255	PSEN	AATAGAGAACGGCAGGAGCA
P256	PSEN	GCCATGAGGGCACTAATCAT
P257	APP	AAGCGGCCAAAGCCTGGAGGGTG
P258	APP	GTGGATAACCCCTCCCCCAGCCTAGACCA
P259	APP	GTTGAGCCTGTTGATGCCCG

The PCR mix contained the following to make a total volume of 25 µl each sample:

Dream Tag Green Buffer ---- 2.5 µl
dNTP mix (2.5 mM) ----- 2 µl
Primer P255 ----- 0.25 µl
Primer P256 ----- 0.25 µl
Primer P257 ----- 0.25 µl
Primer P258 ----- 0.375 µl
Primer P259 ----- 0.25 µl
DNA ----- 1.5 µl
Dream Tag ----- 0.2 µl
milliQ H2O ----- 17.425 µl

Dream Tag Green Buffer, Dream Tag Polymerase, and dNTP mix were purchased from Fermentas, Germany. The reaction mix was pipetted into 0.2 ml PCR tubes (Nerbe Plus, Germany) and spun down, and the reaction was performed using a Mastercycler ep gradient S (Eppendorf, Germany). The reaction conditions are described as follows:

95 °C --- 5 min
 95 °C --- 30 s
 60 °C --- 30 s
 72 °C --- 60 s
 72 °C --- 5 min
 15 °C --- HOLD

} X 37

2.2 Electrophysiology

Anesthesia drug (ketamine 75 mg/kg and xylazine 10 mg/kg) was diluted in saline and injected intraperitoneally to the mouse 5 min before decapitation or transcardial perfusion (for mice older than 2 months) followed by decapitation. The head was immediately placed into a petri dish filled with ice-cold cutting solution (Table 2.2) oxygenated with carbogen (95% O₂, 5% CO₂). The brain was rapidly removed from the skull, and parasagittal slices (350 μm) were cut with a Leica vibratome (Leica VT 1200S) in the cutting solution. The slices were then kept at 33°C in oxygenated resting solution (Table 2.2) for 20 min, before transferred to aCSF (Table 2.2). The slices were then left at room temperature for a maximum of 6h after cutting.

Table 2.2. Composition of extracellular solutions.

Ingredients	Cutting solution (mM)	Resting solution (mM)	aCSF (mM)
Sucrose	200	--	--
Glucose	20	20	20
CaCl ₂	0.5	0.8	2.3
MgCl ₂	7	7	1.3
NaCl	--	110	125
KCl	2.5	2.5	2.5
NaH ₂ PO ₄	1.25	1.25	1.25
NaHCO ₃	25	25	25
Na-Ascorbate	5	1.3	--
Pyruvate Acid	3	3	--
Kynurenic Acid	3	--	--

All electrophysiology recordings were conducted using the following setup:

- Nikon FN-S2N microscope (equipped with 10×/0.30 and 60×/1.0W objectives)
- Micromanipulator SM7 (Luigs & Neumann, Germany)
- EPC 10 amplifier (HEKA Elektronik) (filtered at 2.9 kHz with a Bessel filter, digitized at 10 kHz)
- DS3 constant current isolated stimulator (Digitimer Ltd., England)
- LED excitation system at 490nm (CooLED, UK)
- Greyscale CCD camera CoolSNAP HQ (Photometrics, USA)
- PatchMaster data acquisition software (HEKA, Germany).
- Igor Pro 6.37 with custom-made macros (WaveMetrics, USA) for off-line analysis

The recording chamber of the electrophysiology set-up was perfused with oxygenated aCSF (Table 2.2). CA3 pyramidal cells were identified by differential interference contrast microscopy at room temperature, and whole-cell patch-clamp configuration was achieved with borosilicate glass capillaries (Harvard Instruments, GC150F-10) pulled by a P-97 puller (Sutter Instrument). The pipettes were filled with variant intracellular solutions (Table 2.3) depending on experiments, and had resistance value ranging from 3 to 5 M Ω .

To monitor the access resistance during the whole recording time, a hyperpolarizing voltage step (-5mV, 10ms) was applied at the beginning of each trace. Series access resistance was <20M Ω , and when it changed by >20%, the recording was discarded. When held at -70mV, neurons with a holding current >300pA were also rejected. Liquid junction potential correction was not used for measurements of membrane potentials.

Mf-CA3 excitatory postsynaptic currents (EPSCs) were evoked using a patch pipette (~5M Ω) filled with aCSF positioned in the hilus of the dentate gyrus. Minimal intensity stimulation was reached as previously described in literature (Marchal and Mulle, 2004; Sachidhanandam et al., 2009).

Mf synaptic currents were identified according to the following criteria:

- robust frequency facilitation when comparing responses at 0.1Hz and 1Hz,
- obvious paired-pulse facilitation
- EPSCs had a steep rising phase (~1ms)

-- EPSCs decays free of secondary peaks that might indicate the presence of polysynaptic contamination.

The group II metabotropic glutamate receptor (mGluR) agonist L-CCG-I (10 μ M) was applied at the end of each recording. If the EPSCs were reduced by > 80%, we could confirm that the Mf synaptic currents were recorded.

Table 2.3. Composition of intracellular solutions.

Ingredients	For voltage-clamp experiments (mM)	For current-clamp experiments (mM)	For sIPSCs and mIPSCs (mM)
CsMSO ₃	100	--	--
KMSO ₃	--	120	--
CsCl	--	--	120
MgCl ₂	--	2	2
MgSO ₄	3	--	--
CaCl ₂	3.5	1	2
KCl	--	20	--
EGTA	20	10	5
phosphocreatine	5	--	5
ATPNa ₂	3	2	2
GTP	0.33	--	0.33
HEPES	10	10	10
QX314	--	--	10

All drugs for electrophysiological experiments were obtained from Tocris Biosciences or Sigma-Aldrich, unless otherwise stated.

2.3 Genomic profiling and ChIP-seq

2.3.1 Tissue Preparation and Neuron Sorting

The removal of hippocampal CA3 regions was performed under a stereomicroscope (Motic) as described previously (Sultan FA, 2013). The dissected CA3 tissues were snap frozen in liquid nitrogen immediately for later RNA isolation or

further FACS preparation.

FACS were done on the dissected CA3 tissues to separate neurons and non-neuronal cells and debris.

-- Nuclei Isolation:

The isolated tissues were homogenized with a mechanical homogenizer in 500 μ l of low sucrose buffer (Table 2.4). For crosslinking, 13.5 μ l of 37% formaldehyde were added, and samples were rotated 12rpm for 5 min at RT. Crosslinking was quenched by adding 51.4 μ l 1.25M glycine, and then the samples were kept on a rotator for 5 min before centrifuged at 2000 rcf for 3 min. The supernatant was discarded, and the cell pellet was resuspended in 1 ml low sucrose buffer and homogenize again. Then the samples were carefully pipetted onto 6 ml high sucrose buffer (Table 2.4), followed by centrifugation at 3200 rcf for 10 min at 4°C. In each tube, the supernatant was removed, and the nuclei pellet was resuspended in 600 μ l PBS.

-- Nuclei Staining:

0.6 μ l of NeuN-AF488 primary antibody (Millipore MAB 377X) was added to the resuspended solution containing nuclei. After 20 min incubation at 4°C on a rotator, the samples were centrifuged at 2000 rcf for 3 min. Then the pellets were washed twice with 1 ml PBST (Table 2.4).

-- Collection of sorted nuclei:

Nuclei were sorted with a BD FACSAria™ III cell sorter (BD Biosciences, USA) into falcon tubes pre-coated with PBTB (Table 2.4), then centrifuged at 3200 rcf for 15 min at 4°C. The supernatant was discarded, and the pellet was resuspended in leftover buffer and transferred to a new 1.5 ml low-binding Eppendorf to be centrifuged again at 10000 rcf for 2 min. The nuclei pellets were snap frozen in liquid nitrogen and ready for genomic DNA isolation.

Table 2.4. Buffers for FACS

Low sucrose buffer	0.32M sucrose, 5mM CaCl ₂ , 5mM Mg(Ac) ₂ , 0.1mM EDTA, 10mM HEPES (pH 8.0), 1mM DTT, 0.1% Triton X-100
High sucrose buffer	1M sucrose, 3mM Mg(Ac) ₂ , 10mM HEPES (pH 8.0), 1mM DTT
PBTB (pH 7.5)	5% BSA, 0.2% Tween-20 in 1×PBS, prepared freshly and filtered
PBST (pH 7.5)	0.2% Tween-20 in 1×PBS

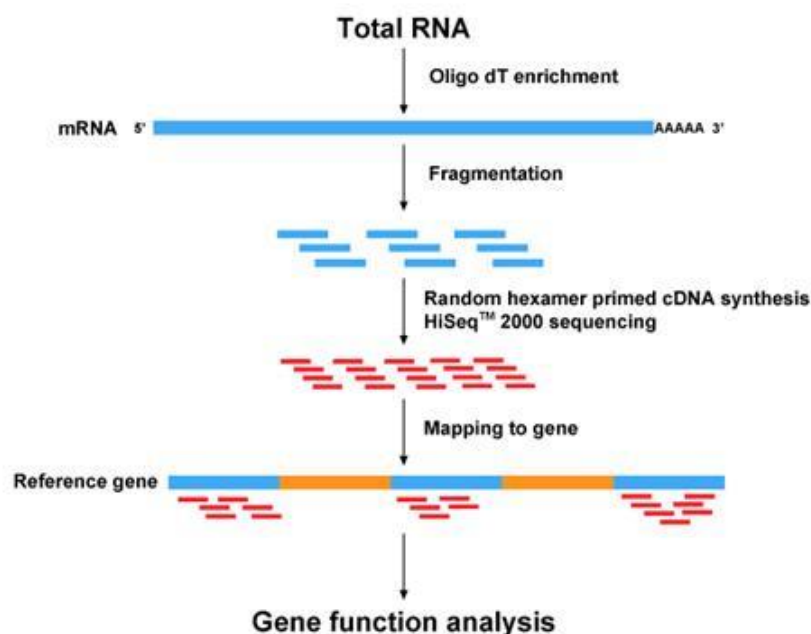
2.3.2 RNA Isolation and qPCR

- RNA isolation:

The dissected hippocampal CA3 tissue was homogenized in 400 μ l TRI Reagent (Invitrogen, Cat No: 15596-026), and incubated at RT for 5min. Then 80 μ l chloroform was added. After thorough shake by hand, the samples were incubated at RT for 5min, and centrifuged at 12000 ref for 15min at 4°C. The upper aqueous phase was carefully collected to mix with 200 μ l Isopropanol and 1.5 μ l Glycoblue (Ambion, 15 mg/mL, AM9515, L/N 1405030) and incubated at -20 °C for 30min, before centrifugation at 12000 ref for 15min at 4°C.

The supernatant was discarded, and 5 μ l 10X Incubation Buffer (Ambion), 1 μ l DNase I (Ambion, AM2222, 2000U, 2U/ μ l), 0.5 μ l RNase OUT (Invitrogen, P/N 100000840, 5000U, 40U/ μ l) and 43.5 μ l RNase-free water were added to the pellet, and the samples were incubated on thermomixer at 550 rpm for 20min at 37 °C. After adding 150 μ l RNase-free water and 200 μ l Phenol/Chloroform/Isoamylalcohol, the samples were vortexed and centrifuged at 13000 rpm at RT for 2 min.

The upper phase containing the RNA was carefully collected to mix with 20 μ l 3M Na-acetate pH 4.8, 200 μ l isopropanol, and 1 μ l Glycoblue, before incubation for 30 min at -20 °C. Afterwards, the samples were centrifuged at 13000 ref at 4 °C for 30min, and the pellets were washed and twice with 75% ethanol. The pellets were dried at RT and dissolved in 50 μ l of RNase-free water, snap-frozen at -80 °C, and ready for RNA-sequencing.



-- cDNA Synthesis:

cDNA synthesis was carried out using the Transcriptor First Strand cDNA Synthesis Kit (Roche Applied Science, Germany). A mixture of 13µl in volume was made with 1 µg of RNA from the sample, 2 µl random hexamer primers (600 pM/µl), and PCR-grade H₂O, and incubated at 65 °C for 10min to denature the RNA. Then the following were added to each sample: 4 µl Transcriptor Reverse Transcriptase Reaction Buffer, 0.5µl Protector RNase Inhibitor (40U/µl), 2µl Deoxynucleotide Mix (10mM), and 0.5µl Transcriptor Reverse Transcriptase (20U/µl). The samples were subsequently incubated at 25 °C for 10min, at 55 °C for 30min, at 85 °C for 5min. The synthesized cDNA was kept on ice or stored at 4 °C.

-- qRT-PCR (qPCR)

qPCR was performed to check the accuracy of CA3 dissection and the efficiency of ChIP in Light Cycler 480 (Roche Applied Science, Manheim, Germany) and its reaction kit (Roche, Germany). qPCRs were done in duplicate for each sample, and a mixture was pooled from each cDNA sample and diluted serially to the following standard dilutions: 1:1, 1:2, 1:4, 1:8, 1:16, to generate a standard curve for determining cDNA concentration of the samples. PCR-grade H₂O was used as a negative control, and the 1:16 cDNA mixture dilution was used as a positive control. In the dissection accuracy check, Tdo2 was used as a marker for DG, Lphn2 for CA3, and Lyd for CA1 region. In the ChIP efficiency check, Glyceraldehyde-3-phosphate dehydrogenase (GAPDH) promoter was used as the reference gene, and InterG was used as a negative control for the intergenic area. Primers used are listed in Table 2.5.

Table 2.5.

Primer	Forward sequence	Reverse sequence
GAPDH promoter	TTCACACCGACCTTCAC	GGCCACGCTAATCTCAT
InterG	AAAACTTCAACTACAGCAAC	GAGACGATCGTACTAAGTG
Tdo2	TCCAGGGAGCACTGATGATA	CTGGAAAGGGACCTGGAATC
Lphn2	GCCGAGTGAGAAGGATTCG	CCCTGCATGTCTTCTCTCGT
Lyd	AGTGTGTCCATCGCCTGTG	CGTCACTAGCCCTGCATTCT

The qRT-PCR mix contained the following to make a total volume of 15 µl in each sample:

- PCR-grade H₂O: 3 μ l
- Forward Primer (20 μ M): 0.75 μ l
- Reverse Primer (20 μ M): 0.75 μ l
- LC480 SYBR Green Master Mix (2X): 7.5 μ l
- Template cDNA: 3 μ l

The reaction conditions are described as follows:

95 °C -- 5min
95 °C -- 10s
60 °C -- 30s
72 °C -- 10s
40 °C-- 30s

} ×45

2.3.3 Chromatin immunoprecipitation (ChIP)

- Chromatin shearing:

Chromatin immunoprecipitation (ChIP) was performed to determine the H3K4Me3 level at promoter areas of variant genes. The frozen nuclei pellets of CA3 PCs were resuspended in 200 μ l of RIPA buffer (Table 2.6), and incubated on a rotator for 10min at 4°C. The samples were sonicated for 35 cycles in Bioruptor Plus (30s ON/30s OFF, high power), and centrifuged at 18000 rcf for 5min. The supernatant containing sheared chromatin was transferred to a new DNA low-binding tube for further immunoprecipitation.

- Shearing check:

Before proceeding, 5 μ l from each sample were taken to check the DNA concentration and shearing efficiency. 20 μ l of EB and 0.1 μ g/ μ l RNase A were added to the 5 μ l chromatin sample and incubated on a thermocycler at 450 rpm at 37 °C for 30min. Then 1 μ l of Proteinase K (20mg/ml) and 20 μ l of Wiemann Buffer 2X (Table 2.6) were added, and incubated on thermocycler at 13000 rpm at 65 °C for 2 hours. Afterwards, 3 μ l of LPA and 46 μ l of SureClean (Bioline, UK) were added, and incubated for 10min at RT, before centrifugation at 20000 rcf for 20min at RT. The supernatant was discarded, and the pellet was washed with 80% ethanol once, before being dried and resuspended in 20 μ l of EB. Now the DNA was ready for bioanalysis

for concentration check and NanoDrop (Thermo Scientific, USA) for fragment size distribution check.

Table 2.6. Buffers for ChIP

RIPA buffer	140mM NaCl, 1mM EDTA, 0.1% Na-Deoxycholate, 1% Triton X-100, 10mM Tris (pH 8.0), 1% SDS
Wiemann Buffer 2X	20mM EDTA, 100mM Tris (pH 8.0), 2% SDS
IP Buffer	140mM NaCl, 1% NP-40, 0.5% Na-Deoxycholate, 50mM Tris (pH 8.0), 20mM EDTA, 0.1% SDS
Wash Buffer	100mM Tris (pH 8.0), 1% NP-40, 1% Na-Deoxycholate, 20mM EDTA, 500 mM LiCl

- Immunoprecipitation:

1.8ml of IP Buffer without SDS were added to the samples in order to dilute the SDS to 0.1%. H3K4Me3 antibody (1 μ g/500ng of chromatin, Abcam, #ab8580) were added and incubated on a rotator at 4°C overnight. 15 μ l of blocked protein A coated magnetic beads were added and incubated on a rotator at 4°C for 1.5 h. The samples were then put on a magnetic rack, and the supernatant was discarded. The beads were washed twice with 1ml of IP Buffer, then three times with 1ml wash buffer, and 1ml of IP Buffer once again.

- DNA Isolation:

20 μ l of EB and 0.1 μ g/ μ l RNase A were added to the beads and the inputs, and incubated on a thermocycler at 450 rpm at 37 °C for 30min. Then 1 μ l of Proteinase K (20mg/ml) and 20 μ l of Wiemann Buffer 2X (Table 2.6) were added, and incubated on thermocycler overnight at 800 rpm at 65 °C. The supernatant was collected on a magnetic rack, and 3 μ l of LPA and 60 μ l of SureClean (Bioline, UK) were added, and incubated for 10min at RT, before centrifugation at 20000 rcf for 20min at RT. The supernatant was discarded and the pellet was washed twice with 80% ethanol, before being dried and resuspended in 30 μ l of EB. ChIP efficiency was confirmed with qRT-PCR as described in chapter 2.3.2. After concentration check and library preparation, ChIP-seq was performed.

2.4 Immunohistochemistry and Imaging

2.4.1 Immunofluorescent Staining for c-Fos

The post-fixation brain was kept in 4% PFA for 24h, before being transferred to PBS 1x (Euromedex, Ref ET330-A), and cut into 50 μ m slices on a vibratome. The slices were saturated in PBS 1x with 0.3% Triton (Sigma, T9284-100ml) and 2% Gelatin (Merck Chemicals, 1040721000) for 1h at RT. The primary antibody (rabbit anti-c-Fos, Merck, PC38-100 μ l) was added at a concentration of 1/10000 and incubated overnight at 4 °C. The slices were rinsed for 10min with PBS 1x -Triton 0.3%-Gelatin 2% for 3 times and kept in it. Then the biotinylated secondary antibody (donkey anti-rabbit, Fischer, AP182BMI) was added at a concentration of 1/200 and incubated for 3h at RT. The slices were rinsed for 10 min in PBS 1x for 3 times and transferred into PBS 1x -Triton 0.3%-Gelatin 2% with 5 μ g/ml Streptavidin-Alexa 568 (Fischer, W3319L) for incubation overnight at 4 °C. The slices were dried for 5min and mounted on glass slides with coverslips for epifluorescence microscopy.

2.4.2 Confocal Imaging of Mf Terminals

Taking advantage of the genetically encoded fluorescence in Thy1-mGFP-DG mice, we were able to visualize Mf terminals and their filopodia (Ruediger et al., 2011). Thy1-mGFP-DG mice bred in the local animal facility were anesthetized with intraperitoneal injection of pentobarbital (30 mg/kg), then transcardially perfused with physiological saline (9% NaCl) followed by 4% paraformaldehyde (4% PFA). Brains were removed and post-fixed overnight in 4% PFA. After fixation, coronal sections (70 μ m) were made on a vibratome (Leica, Germany), then mounted on a glass slide and covered with a thin glass coverslip. The brain sections were imaged on Leica DM6000 TCS SP5 confocal microscope (Leica Microsystems, Germany) for visualization of large mossy fiber terminals and filopodia.

2.5 Behavioral tests

Contextual fear conditioning, as one of the most relevant behavioral tests for hippocampal circuitry, was chosen in our experiment to activate Mf-CA3 networks.

Adult male mice were single-caged for at least one week before the start of fear conditioning. Contextual fear conditioning was performed using ANY-maze fear conditioning system and analyzed with its automatic freezing detection software (ANY-maze, Ireland). The mice received foot shocks in context A: the walls of the box were decorated with black-and-white striped papers. Mice were allowed to explore the box for 3min before receiving the first electrical shock. In total 5 mild electrical foot shocks (0.6 mA, 1s duration) were delivered through the metal grid at the bottom of the box, with 30s intervals in between. After the shocks, the mice were allowed to stay in the box for 2 more minutes before being taken out and transferred back to home cage. The box was cleaned with 30% ethanol and air-dried between each session to remove the residual smell. During the fear test, context B was used as the control: the walls were white decorated with orange triangles, and the floor was paved with normal padding. After the conditioning, the mice were tested at the following time points: 1 hour, 1 day, 2 days, 5 days, 7 days, 14 days. During each test, the mice were first tested in Context B and then Context A, with half an hour in between. Each mouse was tested on maximum three testing days to minimize extinction.

2.6 Computational modeling

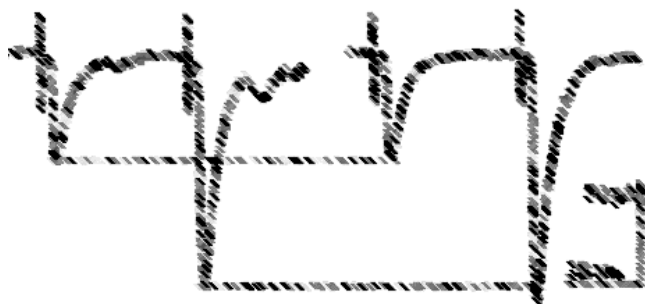
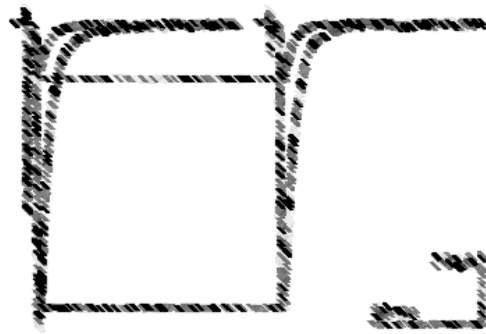
An open-source Python-based software NEST simulator (NEST initiative, Switzerland) was used to generate artificial neural networks of Mf-CA3 based on simplified anatomical data. Details of the construction of the artificial networks will be described in the first chapter of Annexes.

2.7 Statistical Analysis

Statistical analyses were performed with Prism6 (GraphPad Software, USA). First, the normality of data set was tested using the D'Agostino-Pearson omnibus normality test. If data was normally distributed, a Student's t-test or two-way ANOVA (Analysis of Variance) was performed; otherwise, nonparametric tests such as Mann–Whitney test (for unpaired data) and Wilcoxon test (for paired data) was used. The pathway analysis (the GO enrichment analysis) for genomic data was done using the topGO package (Bioconductor, USA) under the "weighted" option. Results were presented as mean \pm SEM. Statistical differences were considered significant at $P < 0.05$.

CHAPTER 3

RESULTS



3 Results

3.1 Input-specific synaptic alterations in CA3 pyramidal cells at an early stage in a mouse model of Alzheimer's disease.

Located at the entry level of hippocampus, the CA3 region is thought to be important for the storage of episodic memory. Meanwhile, loss of hippocampal-dependent episodic memory is one of the earliest clinical signs of AD (Sperling, 2007). Thus, it is intriguing to study the physiological status of CA3 circuits in models of early AD.

CA3 pyramidal cells (CA3 PCs) receive a variety of synaptic inputs which display diverse anatomical and functional properties. Three types of glutamatergic inputs are innervating CA3 pyramidal cells: recurrent collaterals (associational/commissural, A/C fibers), perforant path from the entorhinal cortex, and inputs from the dentate gyrus (DG) through mossy fibers (Mf). These inputs are precisely positioned along apical and basal dendrites, and greatly vary in their structural and functional properties (Rebola et al., 2017). Mfs also make synaptic contacts with GABAergic CA3 interneurons, creating the anatomical basis for robust feedforward inhibition of CA3 PCs (Torborg et al., 2010), which is amenable to structural plasticity upon memory encoding (Ruediger, Spirig, Donato, & Caroni, 2012; Ruediger et al., 2011). In AD mouse models, the inhibitory innervation in hippocampal circuits could be impaired (Hazra et al., 2013; Ramos et al., 2006).

We have previously shown that long-term synaptic potentiation (LTP) is abolished at A/C fiber synapses in CA3 pyramidal cells at an early stage (6-month of age) in a mouse model of AD, and this loss of LTP was caused by activation of up-regulated neuronal adenosine A_{2A} receptors and correlated with one-trial memory deficits (Viana da Silva et al., 2016). In this work, we focused on the Mf synapses in the same region of the same mouse model, to investigate early changes in the hippocampal Mf-CA3 circuits during AD pathology. We hypothesized that, in line with early signs of learning and memory impairments and formation of plaques, male APP/PS1 mice might have deficits in glutamatergic synaptic plasticities as well as GABAergic transmissions at Mf-CA3 synapses at the age of 6 months.

We first characterized the intrinsic properties of CA3 pyramidal cells and looked at the pre- and postsynaptic morphologies of Mf-CA3 synapses in 6-month APP/PS1 mice. Both being unaltered in this early stage of AD, we then explored the presynaptic short- and long-term plasticity of Mf-CA3 synapses in APP/PS1 mice, which are not significantly different from WT littermates either. However, we observed an impaired LTP of NMDA-EPSCs, and some subtle changes in GABAergic transmission and in feedforward inhibition in 6-month APP/PS1 mice.

Taken together, we report here in the form of a manuscript that early synaptic dysfunction in a mouse model of AD is differentially expressed at specific inputs onto a single CA3 neuron.

Input-specific synaptic alterations in CA3 pyramidal cells at an early stage in a mouse model of Alzheimer's disease.

In preparation

Pei Zhang^{1*}, Silvia Viana da Silva^{1,2*}, Matthias Georg Haberl, Noëlle Grosjean¹,
Virginie Labrousse, Gaël Barthet and Christophe Mulle¹.

¹ University of Bordeaux, Interdisciplinary Institute for Neuroscience, CNRS UMR 5297, F-33000 Bordeaux, France.

² BEB PhD program CNC Coimbra, Portugal.

**equal contribution*

Corresponding author: Christophe Mulle, email: christophe.mulle@u-bordeaux.fr

Abstract

Impaired episodic memory is an early manifestation of cognitive deficits in Alzheimer's disease (AD). The CA3 region of the hippocampus is thought to be important for the storage of episodic memory. Like many neuronal populations, CA3 pyramidal cells receive a variety of synaptic inputs which display diverse anatomical and functional properties. Here we explored whether the morphology, function and plasticity of specific synaptic inputs are differentially impaired in CA3 pyramidal cells in a mouse model of AD. We have previously shown that associative long-term synaptic potentiation (LTP) is abolished in CA3 pyramidal cells at an early stage in a mouse model of AD. We now show that the basal synaptic properties of a different glutamatergic input to CA3 pyramidal cells, the mossy fiber input, are not impaired at an early stage in a mouse model of AD. Whereas presynaptic short- and long-term plasticity was normal, we observed an impairment in long-term potentiation of NMDA-EPSCs. In addition, we report subtle changes in GABAergic transmission and in feedforward inhibition. Altogether this work demonstrates that early synaptic dysfunction in a mouse model of AD is differentially expressed at specific inputs onto a single neuron.

Introduction

AD is characterized by two neuropathological hallmarks, senile plaques and intracellular neurofibrillary tangles, which result from the accumulation and deposition of the β -amyloid peptide ($A\beta$) and the aggregation of hyperphosphorylated tau protein, respectively. It is now well accepted that soluble oligomeric forms of $A\beta$, may play a prominent role in triggering the cognitive deficits by specifically targeting synapses. Synaptic loss and dysfunction better correlates with cognitive impairment in early AD, than amyloid-beta ($A\beta$) plaques, tangle formation or neuronal loss (Selkoe et al., 2002). Loss of episodic hippocampal-dependent memory is the earliest clinical sign of AD and hippocampal regions show reduced activation during memory encoding tasks in patients with mild cognitive impairment (Sperling et al., 2007). The encoding of episodic memories is thought to initially require rapid synaptic plasticity within the hippocampus. The CA3 circuits of the hippocampus appear particularly well suited to encode memories, particularly at the earliest stage of acquisition, presumably by developing instant representations of a context (Kesner and Rolls, 2015). It is thus important to study the physiological status of CA3 circuits in models of AD. CA3 pyramidal cells (PCs) form an autoassociative network of recurrent connections which is thought to enable the storage of information through synaptic plasticity (Rebola et al., 2017). Synaptic dysfunction in hippocampal circuits has been observed in a variety of mouse models of AD, particularly in the CA1 region or dentate gyrus (DG), and

proposed to correlate with impairment in memory tasks (Marchetti and Marie, 2011; Pozueta et al., 2013). We recently showed that long-term synaptic potentiation (LTP) within the associative network is abolished in CA3 PCs at an early stage in the APP/PS1 mouse model of AD (Viana da Silva et al., 2016). This loss of LTP was caused by activation of up-regulated neuronal adenosine A_{2A} receptors and correlated with one-trial memory deficits (Viana da Silva et al., 2016).

Different synaptic connections onto a single neuron display a variety of anatomical and functional properties, which may be differentially affected in models of AD (Marchetti and Marie, 2011). This segregation of synaptic properties can be particularly well studied in laminated structures such as the hippocampus. CA3 PCs receive three types of glutamatergic inputs, from recurrent CA3 collaterals (associational/commissural, A/C fibers), from the entorhinal cortex (perforant path) and from the dentate gyrus (DG) through mossy fibers (Mf). These inputs are precisely positioned along apical and basal dendrites, and greatly vary in their structural and functional properties (Rebola et al., 2017). In contrast to A/C and perforant path synapses which are single site/single spine type, Mf inputs make synaptic contacts on proximal dendrites of CA3 PCs (in the stratum lucidum) via “giant” Mf boutons with multiple glutamate release sites facing large postsynaptic structures called thorny excrescences (Henze et al., 2000). At variance with A/C synapses, Mf-CA3 synapses display a wide dynamic range of short-term plasticity, and express presynaptic forms of LTD and LTP which are independent of NMDA receptor (NMDAR) activation (Nicoll and Schmitz, 2005; Rebola et al., 2017). In addition, at Mf-CA3 synapses, NMDARs are themselves subject to LTP (Kwon and Castillo, 2008; Rebola et al., 2008). Mfs also make synaptic contacts with GABAergic CA3 interneurons creating the anatomical basis for robust feedforward inhibition of CA3 PCs (Torborg et al., 2010), which is amenable to structural plasticity upon memory encoding (Ruediger et al., 2011).

Here we have directly explored whether different synaptic inputs to CA3 PCs were differentially impaired at an early stage in the APP/PS1 mouse model of AD. We have mainly focused on Mf-CA3 synaptic inputs and compared our results with previous observations made at A/C synaptic inputs on the same mouse model (Viana da Silva et al., 2016).

Results

Analysis of intrinsic properties of CA3 PCs in APP/PS1 mice

In order to extend our previous work on A/C synapses, we chose to compare morphological and synaptic properties in CA3 PCs of APP/PS1 and WT mice at 6 months of age, prior to obvious plaque deposits (Viana da Silva et al., 2016). We first performed current-clamp recordings from CA3b PCs in hippocampal slices to analyze

their intrinsic properties (Figure 1). The input resistance of CA3 PCs were not altered in APP/PS1 mice (Wt $356.7 \pm 41.74 \text{ M}\Omega$, $n=13$, and APP/PS1 $406.8 \pm 43.21 \text{ M}\Omega$, $n=12$, t-test p value=0.4132). We then examined the firing threshold and firing frequency of CA3 PCs by injecting a ramp of current from 0 to 200 pA current. The firing threshold of CA3b PCs was not altered in APP/PS1 mice as compared to Wt littermates (Wt $-43.04 \pm 1.13 \text{ mV}$, $n=13$ and APP/PS1 $-40.02 \pm 1.37 \text{ mV}$, $n=12$, t-test p value=0.1005). Although the firing frequencies during the ramp seemed lower in APP/PS1 mice, two-way ANOVA test of the two I/O curves did not reveal any significant difference (Wt $4.56 \pm 0.83 \text{ Hz}$, APP/PS1 $3.44 \pm 0.65 \text{ Hz}$; Two-way ANOVA test $p=0.5894$, Wt $n=13$ and APP/PS1 $n=12$). No major differences were found between the two genotypes when the aforementioned recordings were made in the presence of NBQX (20 μM), Bicuculline (10 μM), CGP (3 μM), D-AP5 (50 μM) (Figure 1 E-H). Therefore, we conclude that the intrinsic properties of CA3b PCs in 6-month APP/PS1 mice are not altered at this early stage of AD pathology, excluding the possibility that this could account for potential differences observed.

Morphometric analysis of Mf boutons and thorny excrescences in 6-month male APP/PS1 mice.

We started our phenotypic comparison of diverse synaptic inputs by comparing the morphological properties of Mf-CA3 synapses in control and 6-months old APP/PS1 mice. For this study two types of recombinant rabies viruses (RV) were stereotaxically injected into the mouse brain to label DG granule cells and CA3 PCs. Local infection was achieved by injecting an anterograde RV expressing a membrane-targeting td-Tomato fluorescent protein in the DG, allowing us to trace DG cell projections as well as presynaptic nerve terminals, i.e. Mf boutons (MfBs). MfBs from Wt and APP/PS1 mice were reconstructed from confocal z-stacks obtained from the CA3b region (the same area in which the electrophysiological experiments were performed). The mean surface area of MfBs did not differ between Wt and APP/PS1 mice (Wt $67.1 \mu\text{m}^2 \pm 1.8 \mu\text{m}^2$, $n=898$, 5 mice; APP/PS1 $67.9 \mu\text{m}^2 \pm 1.6 \mu\text{m}^2$, $n=609$, 5 mice; Mann-Whitney test $p=0.6624$), as also indicated by the cumulative distribution of areas (Figure 2 B; KS test $p=0.144$). In line with this result, the mean volume of MfBs was not different in APP/PS1 and Wt mice (Wt $15.2 \mu\text{m}^3 \pm 0.4 \mu\text{m}^3$, $n=609$, 5 mice; APP/PS1 $14.6 \mu\text{m}^3 \pm 0.4 \mu\text{m}^3$, $n=898$, 5 mice; Mann-Whitney test $p=0.1630$, Figure 2 C). Importantly, Mf also contact inhibitory interneurons in the hilus and stratum lucidum, through filopodial protrusions emerging from the MfBs. To get an estimate of the number of filopodia, we compared the complexity index of the reconstructed MfBs, since these structures represent a very small volume, but a considerable area of membrane. Our initial analyses show no significant difference in the average complexity index between two genotypes (Wt 3.0 ± 1.2 , $n=609$, 5 mice; APP/PS1 3.5 ± 1.4 , $n=898$, 5 mice; Mann-

Whitney test $p=0.3116$). However, a difference was observed when analyzing the cumulative distribution of MfBs complexity indexes between Wt and APP/PS1 mice (KS test $p<0.0001$; Figure 2 D). To further analyze the difference in complexity we divided MfBs in three categories based on their volume: small ($< 10\mu\text{m}^3$), medium ($10 - 20\mu\text{m}^3$) and large ($> 20\mu\text{m}^3$). We observed a tendency for an increased complexity for the large MfBs in the APP/PS1 mice (Wt, 4.3 ± 0.2 , $n=5$ mice; APP/PS1 mice 4.8 ± 0.2 for APP/PS1 mice, $n=5$ mice) (Figure 2 E). An increase in the complexity index may indicate an increase in the number and/or length of MfB filopodia.

To study the post-synaptic thorny excrescences (ThEs), a RV with the native envelope was used to infect CA3 PCs from their axon terminals. The injection performed in the hippocampal CA1 region resulted in a sparse labeling of CA3 PCs ideal for 3D reconstructions (Figure 2 F). Reconstructions were performed for ThEs located in the stratum lucidum, ThEs located on basal dendrites of CA3 PCs were not included in the study. Only cells with a complete ThE arborization within the $70\mu\text{m}$ slices were reconstructed and analyzed. The number of ThEs per cell was not different between the two genotypes (Wt 58.2 ± 4.0 , $n=9$ complete cells; APP/PS1 51.6 ± 5.8 , $n=8$ complete cells; t -test $p=0.3539$, Figure 2 G). We found no change of the mean surface values or distribution of reconstructed CA3 ThEs in APP/PS1 mice (Wt $16.6\mu\text{m}^2 \pm 0.6\mu\text{m}^2$, $n=1259$, 6 mice; APP/PS1 $14.2\mu\text{m}^2 \pm 0.5\mu\text{m}^2$, $n=945$, 6 mice; Mann-Whitney test $p=0.1074$; distribution, KS test $p=0.99$; Figure 2 H). Similarly, we found no alteration of mean volume of ThEs in APP/PS1 mice (Wt $2.4\mu\text{m}^3 \pm 0.1\mu\text{m}^3$, $n=1259$, 6 mice; APP/PS1 $2.0\mu\text{m}^3 \pm 0.08\mu\text{m}^3$, $n=945$, 6 mice; Mann-Whitney test $p=0.1221$) but a significant alteration in the distribution of volumes of ThEs (KS test $p<0.0001$; Figure 2 I). Summary plot of the area and volume of each ThE reconstructed (Figure 2 J) shows that the relationship between these two parameters is not altered by chronic overexpression of A during 6 months (Wt linear regression 5.7 ± 0.04 ; APP/PS1 linear regression 5.6 ± 0.06). Overall, careful morphometric examination of several parameters of Mf synapses showed not major alteration of pre- and post-synaptic compartments in APP/PS1 mice.

Analysis of basal properties and presynaptic plasticity at Mf-CA3 synapses in APP/PS1 mice.

To explore the electrophysiological features of APP/PS1 mice at the early stage of pathology, spontaneous miniature excitatory postsynaptic potentials (mEPSCs) were recorded from the soma of visually identified CA3b PCs in sagittal acute slices in the presence of $1\mu\text{M}$ TTX to block action potentials. Cells were held at -70 mV and left to stabilize for 8 minutes after whole-cell configuration was established. Synaptic activity was registered for 15 minutes in the presence of the GABA_A receptors blocker (bicuculline, $10\mu\text{M}$) in order to isolate the glutamatergic inputs.

The mean amplitude of all events occurring during 15 minutes was significantly smaller in APP/PS1 mice compared to Wt (Wt: $24.9\text{pA} \pm 1.1\text{pA}$, $n=15$, 8 mice; APP/PS1: $20.2\text{pA} \pm 0.6\text{pA}$, $n=15$, 9 mice, $t\text{-test } p=0.0009$) (Figure 3). Observing the cumulative probability distributions, we can conclude that the relative difference between the amplitudes is greater for smaller amplitudes, suggesting that APP/PS1 mice have an increased number of smaller events compared to Wt littermates at 6 months. The mean values of mEPSCs inter event intervals (IEI), indicative of the frequency of mEPSCs, was not statistically different between Wt and APP/PS1 mice (Wt: $0.8\text{ms} \pm 0.1\text{ms}$, $n=15$; APP/PS1: $0.7\text{ms} \pm 0.09\text{ms}$, $n=15$; $p=0.5863$; Figure 3 C), although the large variability in mEPSCs frequency between recordings may preclude drawing a conclusion.

Elimination of DG cells by γ -irradiation showed that 95% of the mEPSCs recorded from CA3 neurons, with an amplitude above 45pA derive from Mf synapses (Henze et al., 1997), whereas events smaller than 45pA have an equal probability of being from any of the three inputs contacting CA3 PCs. The percentage of mEPSCs larger than 45pA was not significantly different in the APP/PS1 CA3 PCs as compared to Wt (Wt $11.9\text{pA} \pm 1.5\text{pA}$, $n=15$; APP/PS1 $8.5\text{pA} \pm 0.8\text{pA}$, $n=15$; Mann-Whitney test $p=0.0718$) although a tendency for a decrease can be observed (Figure 3 D-F).

Since the extent to which different inputs to CA3 PCs are altered cannot be directly assessed with mEPSC recordings, we performed further experiments by recordings evoked Mf-CA3 EPSCs using minimal stimulation conditions (Marchal and Mulle, 2004). Firstly, we looked at the basal properties of Mf-CA3 synapses. Throughout the following experiments the group II mGluR agonist LCCG-I applied at the end of the recording session resulted in a decrease by more than 80% of the amplitude of EPSCs, confirming that they were Mf-EPSCs.

The failure rates registered in the APP/PS1 mice was not significantly different as compared to Wt littermates (data not shown), suggesting comparable stimulation strength was used. Paired pulse facilitation (PPF) is the ability of synapses to increase neurotransmitter release in response to the second of two temporally close afferent stimulations. We first observed that in 6 months-old Wt mice, PPF ratio was smaller when compared with PPF ratio values obtained from 3-4 weeks-old Wt mice (Wt 6 months: 2.11 ± 0.15 , $n=16$) (Pinheiro et al., 2007) (Lanore et al., 2010). No alteration of this presynaptic feature was seen when comparing Wt with APP/PS1 mice of the same age (Figure 4 C, D) (WT 2.11 ± 0.15 , $n=16$, and APP/PS1 mice 2.15 ± 0.16 , $n=16$; $t\text{-test } p=0.8556$). Altogether we observed no indication for a change in basal presynaptic release properties.

We also looked at low frequency facilitation, a characteristic presynaptic feature of Mf-CA3 PC synapses (Rebola et al., 2017) which can be observed by switching stimulation frequency from 0.1Hz to 1Hz. The mean value of facilitation was comparable between

genotypes as illustrated in the representative traces in Figure 4 (WT 4.67 ± 0.36 , $n=16$; APP/PS1 4.26 ± 0.37 , $n=16$; t-test $p=0.4298$, Figure 4 A, B).

We also found no difference between the genotypes in the facilitation of Mf-EPSCs in response to a train of 10 stimuli of 20Hz (average of 5 traces at the interval of 2min, the final facilitation rate for Wt 7.19 ± 0.81 , $n=14$ and for APP/PS1 6.98 ± 1.34 , $n=12$, Two-way ANOVA test $p=0.7745$, Figure XX).

We further analyzed presynaptic mechanisms of plasticity at Mf-CA3 synapses in response to high frequency trains which trigger a short lasting post-tetanic potentiation followed by an NMDA-independent form of LTP (Nicoll and Schmitz, 2005). We used a classical high frequency induction protocol consisting of 100 pulses at a frequency of 100Hz repeated 3 times with a 10 s inter train interval, in the presence of bicuculline (10 μ M), CGP-55845 (3 μ M) and D-AP5 (50 μ M) to block GABA_A, GABA_B and NMDARs, respectively. We compared both the PTP (5 minutes after the train) and LTP levels (30 minutes after the train) in Wt and APP/PS1 mice (Figure 4 G, H). Both genotypes displayed similar levels of PTP, measured as the percentage of increase in Mf-EPSC amplitudes (Wt $702.5\% \pm 75.1\%$, $n=12$; APP/PS1 $747.7\% \pm 112.5\%$, $n=11$; t-test $p=0.737$; Figure 4 I), as well as similar levels of LTP (Wt $182.9\% \pm 23.7\%$, $n=12$; APP/PS1 $199.8\% \pm 48.7\%$, $n=11$; Mann-Whitney $p=0.723$; Figure 4 J). Overall, we can conclude that basal properties and presynaptic plasticity, a characteristic feature of Mf-CA3 PC synapses, are mostly unaltered in the APP/PS1 model of AD at the age of 6 months.

Impaired LTP of NMDAR-EPSCs at Mf-CA3 synapses.

Dysregulation of NMDARs has been proposed as a link between A β accumulation and disruption of synaptic function and plasticity (Malinow, 2012). NMDARs are present at Mf-CA3 PC synapses where they have recently been shown to contribute to synaptic integration and plasticity (Kwon and Castillo, 2008; Rebola et al., 2008; 2011; Hunt et al., 2013; Rebola et al., 2011). At normal resting membrane potentials NMDARs are mostly blocked by extracellular Mg²⁺, but the large amplitude of unitary EPSPs at Mf-CA3 PC synapses may lead to the release of the Mg²⁺ block, either directly or indirectly by triggering action potentials in CA3 PCs (Henze et al., 2002).

After applying a frequency facilitation protocol at -70mV to record AMPAR-EPSCs, we imposed a holding potential of +40mV, and we isolated pharmacologically NMDAR-EPSCs with 20 μ M NBQX. With this experimental procedure, we measured the ratio between Mf-EPSC peak amplitude at +40mV and -70mV (NMDAR/AMPA ratio) in Wt and APP/PS1 mice, at both 0.1Hz and 1Hz (Figure 5). We observed that the NMDAR/AMPA ratio was similar in both genotypes (Wt $28.3\% \pm 3.3\%$, $n=9$; APP/PS1 $29.9\% \pm 3.4\%$, $n=9$; t-test $p=0.7449$; Figure 5 A-C). Although frequency facilitation of Mf-NMDA-EPSCs (~5 fold) appeared smaller compared to frequency

facilitation of AMPAR-EPSCs (~7 fold) in adult Wt mice, the frequency facilitation of Mf-NMDAR-EPSCs was not different between genotypes (Wt 4.78 ± 0.4 , n=29; APP/PS1 4.0 ± 0.2 , n=31; Mann-Whitney test $p=0.1932$; Figure 5 D, E).

The subunit composition of NMDARs determines its receptor properties (Paoletti et al., 2013). Particularly, the identity of the GluN2 subunit impacts on the affinity for glutamate, modulation by glycine, sensitivity to voltage-dependent block by Mg^{2+} , fractional Ca^{2+} current and, consequently, channel kinetics (Paoletti et al., 2013; Cull-Candy and Leszkiewicz, 2004). Several studies have ascribed a role for the GluN2B subunit in mediating most of the toxic effects of A β oligomers applied in culture neurons and acute slices (Rönicke et al., 2011; Hu et al., 2009). We tested if the chronic accumulation of A β peptides in APP/PS1 mice would change the composition of NMDARs at Mf-CA3 PC synapses.

The NMDAR-EPSC decay time is governed by the channel deactivation kinetics and it can be used as an indicator of the identity of the subunits assembling synaptic NMDARs. Similar decay times of Mf NMDAR-EPSCs were measured in Wt and APP/PS1 mice at 6 months (WT: $103.2ms \pm 12.4ms$, n=27; APP/PS1: $115.6ms \pm 12.0ms$, n=30, $p=0.4782$, t-test, Figure 5 F). The decay of NMDAR-EPSCs at 1Hz stimulation were slightly faster (WT: $97.5ms \pm 3.8ms$, n=27; APP/PS1: $99.0ms \pm 3.6ms$, n=30, $p=0.7707$, t-test; Figure 5 G). To further examine putative changes in subunit composition, we used a highly selective, activity dependent blocker of GluN2B-containing NMDARs (Ro 25-6981) (Fischer et al., 1997). NMDAR-EPSCs evoked by Mf stimulation at 0.1Hz were recorded at +40mV for eight minutes before applying Ro 25-6981 ($1\mu M$) and during 40 minutes following the application. We observed a progressive reduction of both the amplitude and decay time constants of NMDAR-EPSCs after pharmacological application of the GluN2B antagonist in both genotypes (Figure 5 H-K). However, there was no difference in the level of inhibition between the two genotypes, indicating a similar content in GluN2B (Wt $71.8\% \pm 9.6\%$, n=11; APP/PS1 $66.9\% \pm 9.2\%$, n=11; unpaired t-test $p=0.8315$). In line with this, we found no difference between Wt and APP/PS1 mice in the decay time of NMDARs EPSCs before (Wt control $87.0ms \pm 3.2ms$, n=11; APP/PS1 control $90.8ms \pm 5.0ms$, n=11; unpaired t-test $p=0.5200$) and after the application of Ro 25-6981 (Wt Ro25-6981 $71.2ms \pm 1.9ms$, n=11; APP/PS1 Ro25-6981 $77.3ms \pm 4.2ms$, n=11; unpaired t-test $p=0.1964$; Figure 5 K).

At Mf-CA3 PC synapses, repeated short bursts of Mf stimulation induce robust LTP of NMDAR-EPSCs which spares AMPAR-EPSCs (Rebola et al., 2008; Kwon and Castillo, 2008). Considering the importance of NMDARs for synaptic plasticity and memory formation (Nakazawa et al., 2002; Kishimoto et al., 2006; Rajji et al., 2006), it is relevant to study this form of plasticity in our model of AD. NMDAR-EPSCs evoked

by Mf stimulation in CA3 PC were recorded at +30mV in the presence of 10 μ M bicuculline, 3 μ M CGP-55845, 20 μ M NBQX to block GABA, AMPA and kainate receptors. After establishment of a stable baseline (10min) LTP was induced by 6 bursts of 6 stimuli at a frequency of 50 Hz with a 150s inter burst interval and recorded over a period of 40 min (Figure 5 L, M). We found that Mf LTP of NMDAR-EPSCs was absent in APP/PS1 mice (Wt 135.3% \pm 9.2%, n=10; 98.3% \pm 9.3%, n=10; t-test p=0.0109; Figure 5 N, O).

Hence, we report that the subunit composition of NMDARs at Mf-CA3 PC synapses is not impacted by chronic accumulation of A β in the APP/PS1 mouse model. However, we observe a striking impairment in LTP of NMDARs EPSCs at Mf-CA3 PC synapses.

GABAergic transmission and feedforward inhibition in CA3 PCs of APP/PS1 mice.

Monosynaptic innervation from Mf onto GABAergic interneurons in CA3 leads to robust feedforward inhibition of CA3 PCs (McBain, 2008), which is subject to structural plasticity upon memory encoding (Caroni et al., 2012). In line with early signs of memory impairments in APP/PS1 mice (Kilgore et al., 2009; Viana da Silva et al., 2016), we hypothesized that GABAergic transmission in CA3 PCs, and more particularly feedforward at Mf-CA3 synapses could be impaired.

We first recorded both spontaneous and miniature IPSCs from CA3 PCs, to compare the general properties of GABAergic innervation onto CA3 PCs between the two genotypes. Spontaneous IPSCs were recorded for 10min at -60mV in the presence of 20 μ M NBQX and 10mM QX-314 added intracellularly to prevent action potentials of the recorded cell. We observed that the frequency of spontaneous IPSCs was significantly reduced in APP/PS1 mice as compared to control mice (Wt, 7.87 \pm 1.06 Hz, n=16, 6 mice; APP/PS1 5.01 \pm 0.67 Hz n=18, 6 mice; t-test, p=0.0254), whereas the mean amplitudes were unchanged (Wt n=16, 6 mice; APP/PS1 mice n=18, 6 mice; t-test p=0.1147; Figure 6 A-C). This decrease of IPSCs may be caused either by a reduction of the activity of presynaptic interneurons to the recorded CA3 PCs in the slice, or to a change in the number or properties of GABAergic synapses onto CA3 PCs. To address this question, we recorded miniature IPSCs in the presence of 0.5 μ M TTX added to the extracellular medium. We observed no difference in the mean frequency (Wt n=15, 6 mice; APP/PS1 n=15, 6 mice; t-test, p=0.9756) and in the mean amplitude (Wt n=15, 6 mice; APP/PS1 n=15, 6 mice; t-test p=0.4292; Figure 6 D-F) of miniature IPSCs in CA3 PCs between APP/PS1 and WT mice. These results suggest that the decrease in the frequency of spontaneous IPSCs observed in APP/PS1 mice can be attributed to decreased spiking activity of presynaptic interneurons rather than to changes in the number of GABAergic synapses. However, this does not preclude changes in the properties of GABAergic synaptic transmission.

We thus explored whether these changes may translate into changes in feedforward

inhibition at Mf-CA3 PC synapses. For this we measured the excitatory/inhibitory ratio of evoked events at Mf-CA3 synapses using different regimes of presynaptic Mf stimulation (Torborg et al., 2010). We first recorded evoked Mf-EPSCs at -70mV in the presence of D-AP5 (20 μ M) to block NMDARs. We then switched to +10mV, the reversal potential for cationic ligand-gated channels, to record IPSCs. No significant differences in the ratio were found between APP/PS1 and Wt control mice at 0.1 Hz (Wt n=16, 10 mice; APP/PS1 n=16, 10 mice; t-test p=0.8703; Figure 6 G, H) or at 1 Hz (Wt n=16, 10 mice; APP/PS1 n=16, 10 mice; t-test with Welch's correction for unequal variances p=0.4882; Figure 6 I, J). We further recorded IPSCs evoked by trains of 5 stimuli at 20Hz. Similarly, the ratio between evoked EPSCs and IPSCs was not different during the train (Two-way ANOVA test p=0.9127, p=0.2672 for the normalized plot, Wt n=15 and APP/PS1 n=16, Figure 6 L). But when we normalized the amplitude of IPSCs in the train to the amplitude of the first IPSC to compare short-term plasticity of inhibition in the two genotypes, and found a significant decrease of plasticity in APP/PS1 mice as compared to Wt controls (Two-way ANOVA test p=0.0478, Wt 2.61 ± 0.51 , n=14 and APP/PS1 1.62 ± 0.19 , n=14; Figure 6 M). Taken together, we observed reduced GABAergic inputs onto CA3 PCs, and reduced inhibitory charges during 20Hz train stimulation at Mf-CA3 PC synapses.

Discussion

In the last decades, growing evidence indicates that synaptic loss and dysfunction, accompanied by neural network alterations, may be the major cause of cognitive impairments in AD, in particular at an early stage of the disease (Canter, Penney, & Tsai, 2016; Selkoe, 2002). It is yet important to precisely understand, for each circuit involved in memory encoding and retrieval, which aspects of synaptic physiology and plasticity is particularly impaired due to the AD pathology. Our work focuses on CA3 circuits which thought to be key for the initial stages of episodic memory encoding and recall (Kesner, Kirk, Yu, Polansky, & Musso, 2016; Rebola et al., 2017). A major question addressed through this work is whether A β -induced impairment of synaptic transmission and plasticity is specific for a type of input at the level of a single neuron, here CA3 PCs.

This work extends on our previous identification of marked changes in synaptic plasticity at CA3-CA3 synapses before the appearance of amyloid plaques in the APP/PS1 model (Viana da Silva et al., 2016). Our work explored whether pre- and postsynaptic properties of the other major glutamatergic input to CA3 PCs, the Mf-CA3 synapses were equally impaired in 6-month APP/PS1 mice. We also investigated potential alterations GABAergic synaptic transmissions onto CA3 PCs in these mice. After 6 months of overproduction of A β peptide and formation of A β oligomers, we

found no differences in the morphological features of Mf terminals. These results are in agreement with our electrophysiological data, which did not disclose any difference in presynaptic functional parameters, such as in different forms of presynaptic release properties or short-term facilitation. Furthermore, the characteristic presynaptic form of LTP expressed by MfB is normal in 6-month APP/PS1 mice. These results suggest that early behavioral impairment in this AD mouse model at 6 months (Kilgore et al., 2010; Viana da Silva et al., 2016) are not due to presynaptic failure at Mf-CA3 synapses. On the postsynaptic side, we found that the morphological features of thorny excrescences on CA3 PCs dendrites in APP/PS1 mice were comparable to those of Wt mice. Accordingly, glutamatergic transmission at Mf-CA3 synapses, in terms of mEPSCs and evoked EPSC amplitudes seemed unaltered.

We observed however that postsynaptic LTP of NMDARs, described at Mf synapses (Kwon & Castillo, 2008; Rebola, Lujan, Cunha, & Mulle, 2008), is markedly impaired in the APP/PS1 transgenic mice. This encouraged us to further investigate possible alterations in the number/composition/conductance of NMDARs. In contrast with some publications that describe an alteration of the ratio between NMDAR/AMPA in models of AD (Cisse et al., 2011; Roberson et al., 2011), we found no change in this ratio in the APP/PS1 mice with 6 months at Mf-CA3 synapses. More importantly, we found also no alterations in the subunit composition of NMDARs present at these synapses after application of Ro 25-6981. This suggests that the levels of synaptic GluN2B containing NMDARs are not affected in this AD mouse model, which is in contradiction with some other in-vitro studies that implicate GluN2B-containing NMDARs as particular mediators of neuronal damage in AD (Cui et al., 2013; Ferreira et al., 2012; Hu, Klyubin, Anwyl, & Rowan, 2009; Ronicke et al., 2011). Although the composition and conductance of NMDARs is not altered in 6-month APP/PS1 mice, we cannot rule out that the internal cascades activated by NMDAR activation might be altered, or in other words, that the lack of LTP of NMDARs might depend on the postsynaptic function as a whole. Furthermore, LTP of NMDARs is induced and expressed postsynaptically and depends on the co-activation of A_{2A}Rs and mGluR5 (Rebola et al., 2008). Previous work of our group has demonstrated that abolition of A/C fiber LTP in CA3 PCs in 6-month APP/PS1 mice was caused by activation of upregulated neuronal adenosine A_{2A} receptors (A_{2A}R) rather than by dysregulation of NMDAR signaling or altered dendritic spine morphology (Viana da Silva et al., 2016). Our current results thus may seem at odd with the notion that A_{2A}Rs are upregulated in CA3 PCs of 6-months old APP/PS1 mice. We may speculate that overexpression of A_{2A}Rs in APP/PS1 mice is accompanied with a change in the signaling mechanism downstream of A_{2A}R activation leading to the loss of LTP of NMDARs at Mf-CA3 synapses.

Last but not least, we found that spontaneous IPSC frequency was decreased, and inhibitory charges were subtly reduced during a 20Hz train stimulation protocol. This result can be indicative of alterations in the synaptic contacts between MfBs and local interneurons, or between local interneurons and CA3 PCs. In line with our results, some studies have reported remodeling of GABAergic neurotransmission in the human AD brain (Fuhrer et al., 2017; Limon, Reyes-Ruiz, & Miledi, 2012) and AD transgenic mouse models (Jo et al., 2014; Wu, Guo, Gearing, & Chen, 2014). Especially, APP/PS1 mice were shown to display spontaneous seizures, which are believed to be associated with an imbalance in the excitatory/inhibitory function in the pathology of AD (Hazra et al., 2013; Ramos et al., 2006). Moreover, in APP/PS1-L166P mice (a transgenic line which includes a different mutant of PS1), it was shown that there are age-dependent concomitant changes in the GABAergic pathway in the APP/PS1 mice (Oyelami et al., 2016). Thus, it would be very interesting to further study the features and activities of GABAergic neurons in hippocampal CA3 region.

Overall, our work explored the pre- and postsynaptic features of hippocampal CA3 synapses in an AD mouse model, providing new insights into synaptic dysfunction at an early stage of AD. As a general principle, this work highlights that early synaptic dysfunction in a mouse model of AD is differentially expressed at specific inputs onto a single neuron. This needs to be taken into account when establishing links between synaptic dysfunction and behavioral impairment.

Methods

Mice. APP/PS1 mice were obtained from Jackson Laboratory and used according to regulations of the University of Bordeaux/CNRS Animal Care and Use Committee. Throughout their life, all mice were group-housed, ranging from 4 to 10 animals per cage. Food and water were provided *ad libitum*. The transparent plexiglass cages (38.1 x 19.1 x 12.7 cm) were maintained on a 12-h dark/light cycle, kept in a temperature-regulated room, and protected from exterior pathogens by a filter. All experiments were performed in the light phase of the circadian cycle in 6 months (26-32 weeks) male APP/PS1 and age-matched male WT littermates.

Electrophysiology.

Anesthesia drug (ketamine 75 mg/kg and xylazine 10 mg/kg) was diluted in saline and injected intraperitoneally to the mouse 5 min before decapitation or transcardial perfusion (for mice older than 2 months) followed by decapitation. The head was immediately placed into a petri dish filled with ice-cold cutting solution (200mM of sucrose, 20mM glucose, 0.4mM CaCl₂, 8mM MgCl₂, 2mM KCl, 1.3mM NaH₂PO₄, 26mM NaHCO₃, 1.3mM ascorbate, 0.4mM pyruvate and 3mM kynurenic acid, pH 7.3) oxygenated with carbogen (95% O₂, 5% CO₂). The brain was rapidly removed from the skull and parasagittal slices (350 μm) were cut with a Leica vibratome (Leica VT 1200S) in the cutting solution. The slices were then kept at 33°C in oxygenated resting solution (110mM NaCl, 2.5mM KCl, 0.8mM CaCl₂, 8mM MgCl₂, 1.25mM NaH₂PO₄, 26mM NaHCO₃, 0.4mM ascorbate, 3mM pyruvate and 14mM glucose, pH 7.3) for 20min, before transferred to aCSF. The slices were then left at room temperature for a maximum of 6h after cutting.

The recording chamber of the electrophysiology set-up was perfused with oxygenated aCSF (125mM NaCl, 2.5mM KCl, 2.3mM CaCl₂, 1.3mM MgCl₂, 1.25mM NaH₂PO₄, 26mM NaHCO₃ and 14mM glucose, pH 7.4). CA3 pyramidal neurons were identified by differential interference contrast microscopy using an Olympus fixed stage upright microscope (BX51WI) equipped with a ×60 magnification immersion objective at room temperature, and whole-cell patch-clamp configuration was achieved with borosilicate glass capillaries with resistance value ranging from 3 to 5 MΩ. The pipettes were filled with variant intracellular solutions depending on experiments: KMSO₃-based solution (120mM KMSO₃, 2mM MgCl₂, 1mM CaCl₂, 20mM KCl, 10mM EGTA, 2mM ATPNa₂, 10mM HEPES, pH 7.2) was used for current-clamp recordings, CsCl-based solution (120mM CsCl, 2mM MgCl₂, 2mM CaCl₂, 5mM EGTA, 5mM phosphocreatine, 2mM ATPNa₂, 0.33mM GTP, 10mM HEPES, 10mM QX314, pH 7.2) was used for IPSC recordings, and CsMSO₃-based solution (100mM CsMSO₃, 3mM MgSO₄, 3.5mM CaCl₂, 20mM EGTA, 5mM phosphocreatine, 3mM ATPNa₂, 0.33mM GTP, 10mM HEPES, pH 7.2) was used for all other experiments.

To monitor the access resistance during the whole recording time, a hyperpolarizing voltage step (-5mV, 10ms) was applied at the beginning of each trace. Series access resistance was <20MΩ, and when it changed by >20%, the recording was discarded. When held at -70mV, neurons with a holding current >300pA were also rejected. Mf synaptic currents were identified according to the following criteria: 1) obvious paired-pulse facilitation; 2) EPSCs had a steep rising phase (~1ms); 3) EPSCs decays free of secondary peaks that might indicate the presence of polysynaptic contamination. Liquid junction potential correction was not used for measurements of membrane potentials.

Recordings were made using an EPC10.0 amplifier (HEKA Elektronik), filtered at 0.5–1kHz and analyzed using IGOR Pro and Neuromatic V2.6 software. All drugs for electrophysiological experiments were obtained from Tocris Biosciences or Sigma-Aldrich, unless otherwise stated.

Stereotaxic injections and confocal microscopy. Viral stocks were stored at -80°C until use and were thawed on ice before their in vivo administration. Prior to surgery the mice were anaesthetized by inhalation of isoflurane in an induction chamber connected to tubing that delivered a mix of air and 4% isoflurane. Once the animals were immobile they were placed on a heating pad (36 °C) while they continued to receive anesthesia via a mask (1.5-2% isoflurane) during the surgery. For labeling CA3 pyramidal neurons we injected the glycoprotein deleted rabies virus variant coated with the native glycoprotein (300nL, velocity 40nL/min) (Wickersham et al., 2007) into the CA1 stratum radiatum (coordinates: anteroposterior: -1.92mm; medio-lateral: ±1.50mm; and ventral: -1.35mm) to achieve a retrograde infection. For labeling mossy fiber terminals we injected an anterograde variant of the glycoprotein deleted rabies virus (500nL, velocity 50nL/min) (Haberl et al., 2014) into the hilus of DG (coordinates: anteroposterior: -1.92mm; medio-lateral: ±1.15mm; and ventral: -2.00mm). The mice were sacrificed 6 days after the injection. Injected mice were anesthetized with intraperitoneal injection of pentobarbital (30 mg/kg), then transcardially perfused with physiological saline (9% NaCl) followed by 4% paraformaldehyde (4% PFA). Brains were removed and post-fixed overnight in 4% PFA. After fixation, coronal sections (70mm) were cut on a vibratome (Leica, Germany), then mounted on a glass slide and covered with a thin glass coverslip. The sections were imaged on Leica DM6000 TCS SP5 confocal microscope (Leica Microsystems, Germany) for visualization of mossy fiber terminals and CA3 thorny excrescences.

Statistical analysis. Statistical analyses were performed with Prism6 (GraphPad Software, USA).

Results

First the normality of data set was tested using the D'Agostino-Pearson omnibus normality test. If data was normally distributed, a Student's t-test or two-way ANOVA (Analysis of Variance) was performed; otherwise, nonparametric tests such as Mann-Whitney test (for unpaired data) and Wilcoxon test (for paired data) was used. Data distributions were analyzed using the Kolmogorov-Smirnov test. Results were presented as mean \pm SEM (standard error of mean). Statistical differences were considered significant at $P < 0.05$.

References

Canter, R. G., Penney, J., & Tsai, L. H. (2016). The road to restoring neural circuits for the treatment of Alzheimer's disease. *Nature*, 539(7628), 187-196. doi:10.1038/nature20412

Caroni P, Donato F, Muller D (2012) Structural plasticity upon learning: regulation and functions. *Nat Rev Neurosci* 13:478–490.

Cisse, M., Halabisky, B., Harris, J., Devidze, N., Dubal, D. B., Sun, B., . . . Mucke, L. (2011). Reversing EphB2 depletion rescues cognitive functions in Alzheimer model. *Nature*, 469(7328), 47-52. doi:10.1038/nature09635

Cui, Z., Feng, R., Jacobs, S., Duan, Y., Wang, H., Cao, X., & Tsien, J. Z. (2013). Increased NR2A:NR2B ratio compresses long-term depression range and constrains long-term memory. *Sci Rep*, 3, 1036. doi:10.1038/srep01036

Cull-Candy SG, Leszkiewicz DN (2004) Role of distinct NMDA receptor subtypes at central synapses. *Sci STKE* 2004:re16.

Ferreira, I. L., Bajouco, L. M., Mota, S. I., Auberson, Y. P., Oliveira, C. R., & Rego, A. C. (2012). Amyloid beta peptide 1-42 disturbs intracellular calcium homeostasis through activation of GluN2B-containing N-methyl-d-aspartate receptors in cortical cultures. *Cell Calcium*, 51(2), 95-106. doi:10.1016/j.ceca.2011.11.008

Fischer G, Mutel V, Trube G, Malherbe P, Kew JN, Mohacsi E, Heitz MP, Kemp JA (1997) Ro 25-6981, a highly potent and selective blocker of N-methyl-D-aspartate receptors containing the NR2B subunit. Characterization in vitro. *J Pharmacol Exp Ther* 283:1285–1292.

Fuhrer, T. E., Palpagama, T. H., Waldvogel, H. J., Synek, B. J. L., Turner, C., Faull, R. L., & Kwakowsky, A. (2017). Impaired expression of GABA transporters in the human Alzheimer's disease hippocampus, subiculum, entorhinal cortex and superior temporal gyrus. *Neuroscience*, 351, 108-118. doi:10.1016/j.neuroscience.2017.03.041

Hazra, A., Gu, F., Aulakh, A., Berridge, C., Eriksen, J. L., & Ziburkus, J. (2013). Inhibitory neuron

-
- and hippocampal circuit dysfunction in an aged mouse model of Alzheimer's disease. *PLoS One*, 8(5), e64318. doi:10.1371/journal.pone.0064318
- Henze DA, Card JP, Barrionuevo G, Ben-Ari Y (1997) Large amplitude miniature excitatory postsynaptic currents in hippocampal CA3 pyramidal neurons are of mossy fiber origin. *J Neurophysiol* 77:1075–1086.
- Henze DA, Urban NN, Barrionuevo G (2000) The multifarious hippocampal mossy fiber pathway: a review. *NSC* 98:407–427.
- Henze DA, Wittner L, Buzsáki G (2002) Single granule cells reliably discharge targets in the hippocampal CA3 network in vivo. *Nat Neurosci* 5:790–795.
- Hu N-W, Klyubin I, Anwyl R, Anwyl R, Rowan MJ (2009) GluN2B subunit-containing NMDA receptor antagonists prevent Abeta-mediated synaptic plasticity disruption in vivo. *Proc Natl Acad Sci USA* 106:20504–20509.
- Hunt DL, Puente N, Grandes P, Castillo PE (2013) Bidirectional NMDA receptor plasticity controls CA3 output and heterosynaptic metaplasticity. *Nat Neurosci* 16:1049–1059.
- Jo, S., Yarishkin, O., Hwang, Y. J., Chun, Y. E., Park, M., Woo, D. H., . . . Lee, C. J. (2014). GABA from reactive astrocytes impairs memory in mouse models of Alzheimer's disease. *Nat Med*, 20(8), 886-896. doi:10.1038/nm.3639
- Kesner, R. P., Kirk, R. A., Yu, Z., Polansky, C., & Musso, N. D. (2016). Dentate gyrus supports slope recognition memory, shades of grey-context pattern separation and recognition memory, and CA3 supports pattern completion for object memory. *Neurobiol Learn Mem*, 129, 29-37. doi:10.1016/j.nlm.2015.08.010
- Kesner RP, Rolls ET (2015) A computational theory of hippocampal function, and tests of the theory: new developments. *Neuroscience & Biobehavioral Reviews* 48:92–147.
- Kilgore M, Miller CA, Fass DM, Hennig KM, Haggarty SJ, Sweatt JD, Rumbaugh G (2009) Inhibitors of Class 1 Histone Deacetylases Reverse Contextual Memory Deficits in a Mouse Model of Alzheimer's Disease. *Neuropsychopharmacology* 35:870–880.
- Kishimoto Y, Nakazawa K, Tonegawa S, Kirino Y, Kano M (2006) Hippocampal CA3 NMDA receptors are crucial for adaptive timing of trace eyeblink conditioned response. *Journal of Neuroscience* 26:1562–1570.
- Kwon H-B, Castillo PE (2008) Long-Term Potentiation Selectively Expressed by NMDA Receptors at Hippocampal Mossy Fiber Synapses. *Neuron* 57:108–120.
- Lanore F, Blanchet C, Fejtova A, Pinheiro P, Richter K, Balschun D, Gundelfinger E, Mülle C (2010) Impaired development of hippocampal mossy fibre synapses in mouse mutants for the presynaptic scaffold protein Bassoon. *J Physiol (Lond)* 588:2133–2145.

Results

- Limon, A., Reyes-Ruiz, J. M., & Milei, R. (2012). Loss of functional GABA(A) receptors in the Alzheimer diseased brain. *Proc Natl Acad Sci U S A*, *109*(25), 10071-10076. doi:10.1073/pnas.1204606109
- Malinow R (2012) New developments on the role of NMDA receptors in Alzheimer's disease. *Curr Opin Neurobiol* *22*:559–563.
- Marchal C, Mulle C (2004) Postnatal maturation of mossy fibre excitatory transmission in mouse CA3 pyramidal cells: a potential role for kainate receptors. *J Physiol (Lond)* *561*:27–37.
- Marchetti C, Marie H (2011) Hippocampal synaptic plasticity in Alzheimer's disease: what have we learned so far from transgenic models? *Rev Neurosci* *22*:373–402.
- McBain CJ (2008) Differential mechanisms of transmission and plasticity at mossy fiber synapses. Elsevier.
- Nakazawa K, Quirk MC, Chitwood RA, Watanabe M, Yeckel MF, Sun LD, Kato A, Carr CA, Johnston D, Wilson MA, Tonegawa S (2002) Requirement for hippocampal CA3 NMDA receptors in associative memory recall. *Science* *297*:211–218.
- Nicoll RA, Schmitz D (2005) Synaptic plasticity at hippocampal mossy fibre synapses. *Nat Rev Neurosci* *6*:863–876.
- Oyelami, T., Bondt, A., den Wyngaert, I. V., Hoorde, K. V., Hoskens, L., Shaban, H., . . . Drinkenburg, W. H. (2016). Age-dependent concomitant changes in synaptic dysfunction and GABAergic pathway in the APP/PS1 mouse model. *Acta Neurobiol Exp (Wars)*, *76*(4), 282-293.
- Paoletti P, Bellone C, Zhou Q (2013) NMDA receptor subunit diversity: impact on receptor properties, synaptic plasticity and disease. *Nat Rev Neurosci* *14*:383–400.
- Pinheiro PS, Perrais D, Coussen F, Barhanin J, Bettler B, Mann JR, Malva JO, Heinemann SF, Mulle C (2007) GluR7 is an essential subunit of presynaptic kainate autoreceptors at hippocampal mossy fiber synapses. *Proc Natl Acad Sci USA* *104*:12181–12186.
- Pozueta J, Lefort R, Shelanski ML (2013) Synaptic changes in Alzheimer's disease and its models. *Neuroscience* *251*:51–65.
- Rajji T, Chapman D, Eichenbaum H, Greene R (2006) The role of CA3 hippocampal NMDA receptors in paired associate learning. *Journal of Neuroscience* *26*:908–915.
- Ramos, B., Baglietto-Vargas, D., del Rio, J. C., Moreno-Gonzalez, I., Santa-Maria, C., Jimenez, S., . . . Vitorica, J. (2006). Early neuropathology of somatostatin/NPY GABAergic cells in the hippocampus of a PS1xAPP transgenic model of Alzheimer's disease. *Neurobiol Aging*, *27*(11), 1658-1672. doi:10.1016/j.neurobiolaging.2005.09.022

- Rebola N, Carta M, Lanore F, Blanchet C, Mulle C (2011) NMDA receptor-dependent metaplasticity at hippocampal mossy fiber synapses. *Nat Neurosci* 14:691–693.
- Rebola N, Carta M, Mulle C (2017) Operation and plasticity of hippocampal CA3 circuits: implications for memory encoding. *Nat Rev Neurosci* 18:209–221.
- Rebola N, Lujan R, Cunha RA, Mulle C (2008) Adenosine A2A receptors are essential for long-term potentiation of NMDA-EPSCs at hippocampal mossy fiber synapses. *Neuron* 57:121–134.
- Roberson, E. D., Halabisky, B., Yoo, J. W., Yao, J., Chin, J., Yan, F., . . . Mucke, L. (2011). Amyloid-beta/Fyn-induced synaptic, network, and cognitive impairments depend on tau levels in multiple mouse models of Alzheimer's disease. *J Neurosci*, 31(2), 700-711. doi:10.1523/jneurosci.4152-10.2011
- Rönicke R, Mikhaylova M, Rönicke S, Meinhardt J, Schröder UH, Fändrich M, Reiser G, Kreutz MR, Reymann KG (2011) Early neuronal dysfunction by amyloid β oligomers depends on activation of NR2B-containing NMDA receptors. *Neurobiol Aging* 32:2219–2228.
- Ruediger S, Vittori C, Bednarek E, Genoud C, Strata P, Sacchetti B, Caroni P (2011) Learning-related feedforward inhibitory connectivity growth required for memory precision. *Nature* 473:514–518.
- Selkoe DJ (2002) Alzheimer's disease is a synaptic failure. *Science* 298:789–791.
- Sperling R (2007) Functional MRI studies of associative encoding in normal aging, mild cognitive impairment, and Alzheimer's disease. *Ann N Y Acad Sci* 1097:146–155.
- Torborg CL, Nakashiba T, Tonegawa S, McBain CJ (2010) Control of CA3 Output by Feedforward Inhibition Despite Developmental Changes in the Excitation-Inhibition Balance. *Journal of Neuroscience* 30:15628–15637.
- Viana da Silva S, Haberl MG, Zhang P, Bethge P, Lemos C, Gonçalves N, Gorlewicz A, Malezieux M, Gonçalves FQ, Grosjean N, Blanchet C, Frick A, Nägerl UV, Cunha RA, Mulle C (2016) Early synaptic deficits in the APP/PS1 mouse model of Alzheimer's disease involve neuronal adenosine A2A receptors. *Nature Communications* 7:11915.
- Wickersham, I. R., Finke, S., Conzelmann, K. K., & Callaway, E. M. (2007). Retrograde neuronal tracing with a deletion-mutant rabies virus. *Nat Methods*, 4(1), 47-49. doi:10.1038/nmeth99
- Wu, Z., Guo, Z., Gearing, M., & Chen, G. (2014). Tonic inhibition in dentate gyrus impairs long-term potentiation and memory in an Alzheimer's [corrected] disease model. *Nat Commun*, 5, 4159. doi:10.1038/ncomms5159

Figures and legends

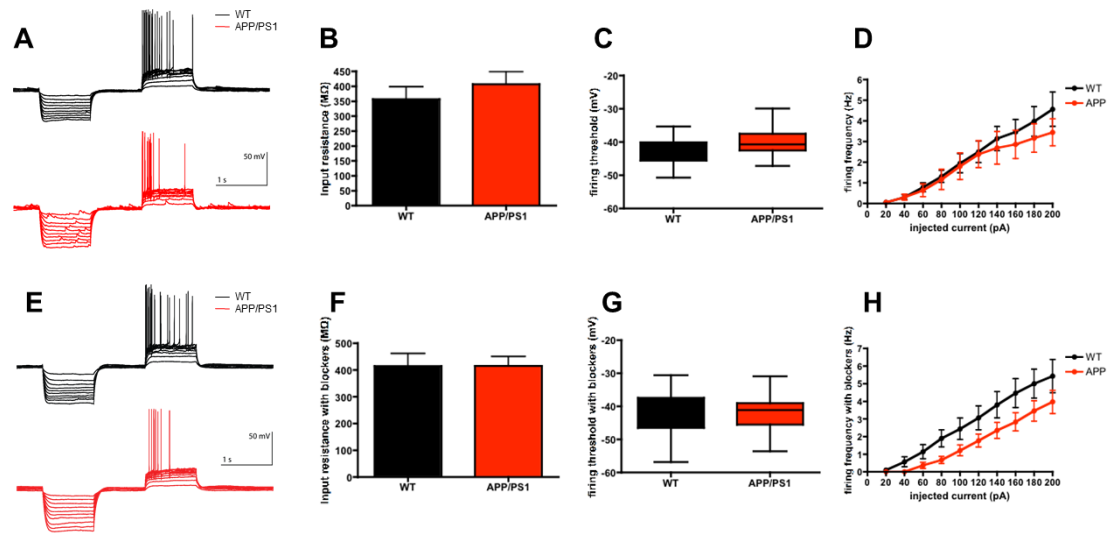


Figure 1. The intrinsic properties of CA3 pyramidal neurons are not altered in APP/PS1 mice
A. Representative traces of current-clamp recording during steps of increasing current injections for Wt (black traces) and APP/PS1 (red traces). **B.** Bar graph representing no difference in mean input resistance of CA3 pyramidal neurons between Wt (n=13) and APP/PS1 (n=12), t-test p value=0.4132, Data represented as mean \pm SEM. **C.** Box plot representing no difference in mean firing threshold of CA3 pyramidal neurons between Wt (n=13) and APP/PS1 (n=12), t-test p value=0.1005, Data represented as mean \pm SEM. **D.** Line chart representing the firing frequency during increasing current injections. Wt represented in black and APP/PS1 in red. Two-way ANOVA test p=0.6342 between Wt (n=13) and APP/PS1 (n=12). Data represented as mean \pm SEM. **E. F. G. H.** the same experiments as in A-D but with the presence of NBQX (20 μ M), Bicuculline (10 μ M), CGP (3 μ M), D-AP5 (50 μ M), n=10 for Wt and n=11 for APP/PS1. **F.** t-test p=0.9949, **G.** t-test p=0.7722. **H.** Two-way ANOVA test p=0.1643 (dots at 40pA and 80pA showed significant difference in t-test).

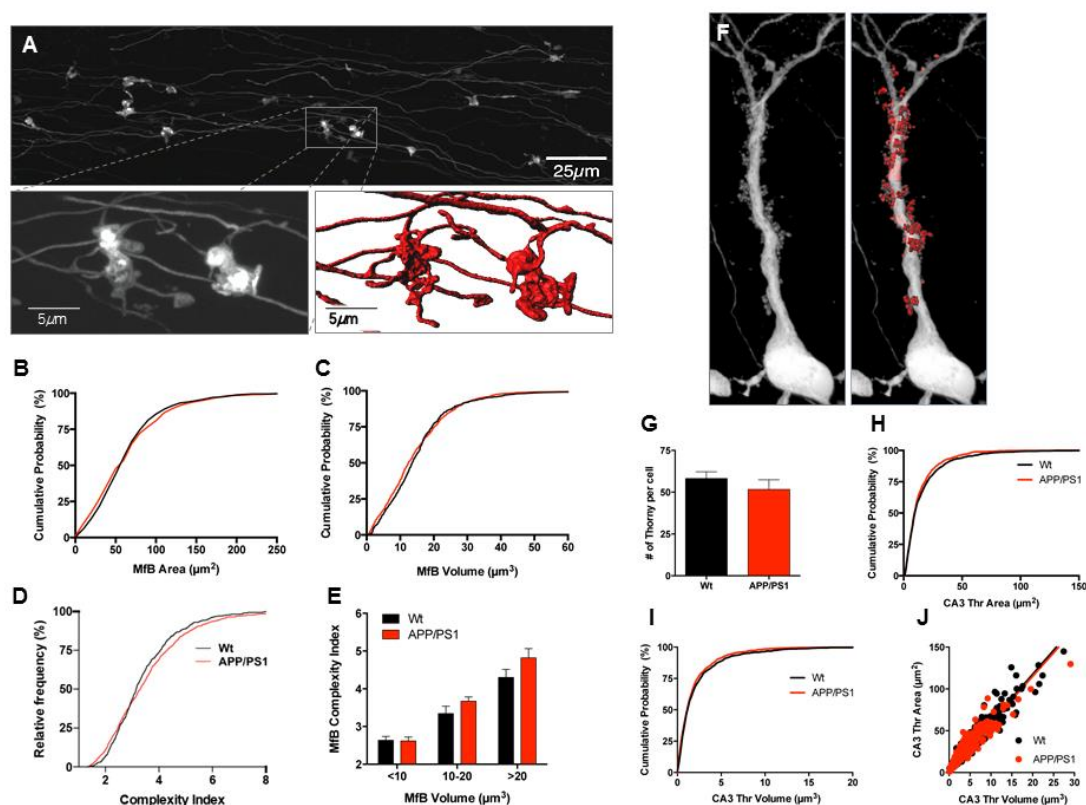


Figure 2. Morphology of the MfBs and postsynaptic thorny excrescences of CA3 cells is unaltered in APP/PS1 mice at 6 months of age.

A. Example image of Mf axons along stratum lucidum acquired with confocal microscopy (upper panel). Zoom in on two examples of MfBs (lower left panel) and a representative reconstruction obtained with IMARIS software (lower right panel). This type of 3D reconstruction allows accurate measurements of surface area and volume. **B.** Cumulative distribution of MfB area from reconstructed MfBs for Wt (black trace) and APP/PS1 mice (red trace), Ks test $p=0.144$. **C.** Cumulative distribution of volume from reconstructed MfBs from Wt (black trace) and APP/PS1 mice (red trace), Ks test $p>0.999$. **D.** Cumulative distribution of the complexity index calculated for reconstructed MfBs showing a significant difference between Wt (black trace) and APP/PS1 mice (red trace), Ks test $p<0.0001$. This index uses both area and volume of each MfB analyzed. **E.** Summary plot representing the complexity index of three classes of MfBs. Smaller MfB have a volume smaller than $10 \mu\text{m}^3$, medium MfBs have a volume ranging from 10 to $20 \mu\text{m}^3$, and large MfBs have volumes values above $20 \mu\text{m}^3$. For Small MfBs the complexity index is 2.6 ± 0.1 for Wt mice and 2.6 ± 0.1 for APP/PS1 mice, displaying no difference between genotypes. Medium sized MfBs are more complex in both genotypes (Wt 3.3 ± 0.2 ; APP/PS1 3.7 ± 0.17). Finally, for large MfBs with a volume larger than $20 \mu\text{m}^3$, the complexity index was, despite the visible tendency, not significantly altered in the APP/PS1 mice (Wt 4.3 ± 0.2 ; APP/PS1 4.8 ± 0.2 , $n=5$ mice for each genotype). Data represented as mean \pm SEM. **F.** Example image of the proximal dendrite of a CA3 pyramidal cell infected by RABV Δ G-eGFP (RG) acquired with confocal microscopy (left panel) and subsequent reconstruction of ThE in stratum lucidum obtained by IMARIS software. **G.** Bar graph representing the total number of ThE per pyramidal cell. The number is not different in APP/PS1 and Wt mice. Just ThE on apical dendrites were analyzed and only cells with complete

Results

apical dendritic arborization were used (Wt n=9, APP/PS1 n=8, t-test p=0.3539). **H.** Cumulative distribution of the area from reconstructed ThE shows no difference between Wt (black trace) and APP/PS1 mice (red trace), Ks test p=0.99. There is no difference regarding the mean surface area of reconstructed MfBs in the two genotypes (Wt $16.6\mu\text{m}^2 \pm 0.6\mu\text{m}^2$, n=1259, 6 mice; APP/PS1 $14.2\mu\text{m}^2 \pm 0.5\mu\text{m}^2$, n=945, 6 mice; Mann-Whitney test p=0.1074). **I.** Cumulative distribution of the volume of reconstructed ThE shows that there is a small difference in the distribution of ThE between Wt (black trace) and APP/PS1 mice (red trace), Ks test p<0.0001. Nevertheless, the mean volume values in the APP/PS1 mice is not different from those in the Wt littermates (Wt $2.4\mu\text{m}^3 \pm 0.1\mu\text{m}^3$, n=1259, 6 mice; APP/PS1 $2.0\mu\text{m}^3 \pm 0.08\mu\text{m}^3$, n=945, 6 mice; Mann-Whitney test p=0.1221). **J.** Summary plot of the relation between surface area and volume of CA3 thorns in the Wt (black circles) and APP/PS1 mice (green circles). The relation between the two parameters is not altered in the APP/PS1 animal (Wt n=945 and APP/PS1 n=1259). Data represented as mean \pm SEM.

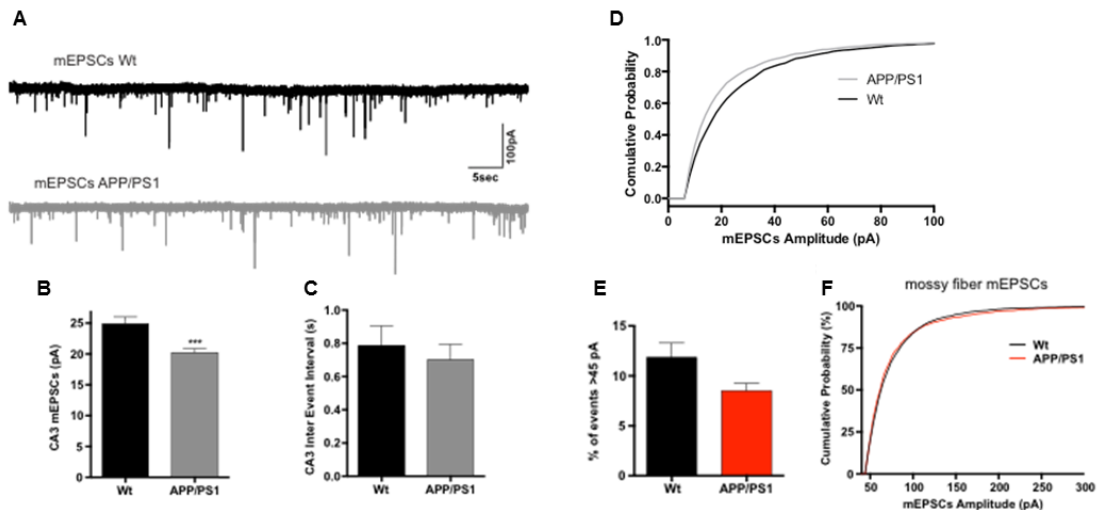


Figure 3. Mossy fiber input of CA3 neurons in terms of mEPSC is not selectively affected in 6-month APP/PS1 mice.

A. Representative recording of mEPSCs (1mM TTX) during one minute, illustrating the difference of amplitude registered between CA3 cells from Wt and APP/PS1 mice. **B.** Summary plot of the mean mEPSCs amplitude registered during 15 minutes showing a reduction in mEPSCs amplitude from the APP/PS1 cells. Black bar represents Wt cells (n=15, 8 mice), grey bar represents cells from APP/PS1 mice (n=15, 9 mice), t-test, p=0.0009. **C.** Summary graph showing no difference between genotypes of the mEPSCs mean inter event intervals registered during a 15-minute period. Black bar represents Wt cells (n=15, 8 mice) and grey bar represents cells from APP/PS1 mice (n=15, 9 mice), t-test p=0.5863. Data represented as mean \pm SEM, *** represents p<0.001. **D.** Cumulative probability distribution of the amplitudes from the first 100 mEPSCs registered from each cell. Black line represents the amplitude distribution of 1500 events from 15 CA3 cells successfully patched in Wt slices (n=8 mice); Mean values: Wt 26.7pA \pm 0.7pA; APP/PS1 22.5pA \pm 0.6pA; KS test p<0.0001, bin size of 2. **E.** Bar graphs representing the percentage of the putative Mf events (with an amplitude larger than 45pA) for each of the 15 cells recorded, during a 15-minute period. A tendency was found towards a reduced number of Mf-generated events, which is not statistically significant (Mann-Whitney test p=0.0718). Black bar, Wt cells (n=15, 8 mice). Grey bar, APP/PS1 mice (n=15, 9 mice). Data represented as mean \pm SEM. **F.** Cumulative distribution of the amplitudes of events with high probability of being from Mf synapses is not different between Wt and APP/PS1 mice. Plot used all the events larger than 45pA obtained over a period of 10 minutes per cell (150 minutes in total per genotype). Mean values are 76.8pA for Wt and 78.4pA for APP/PS1; KS test p>0.999, bin size 2.

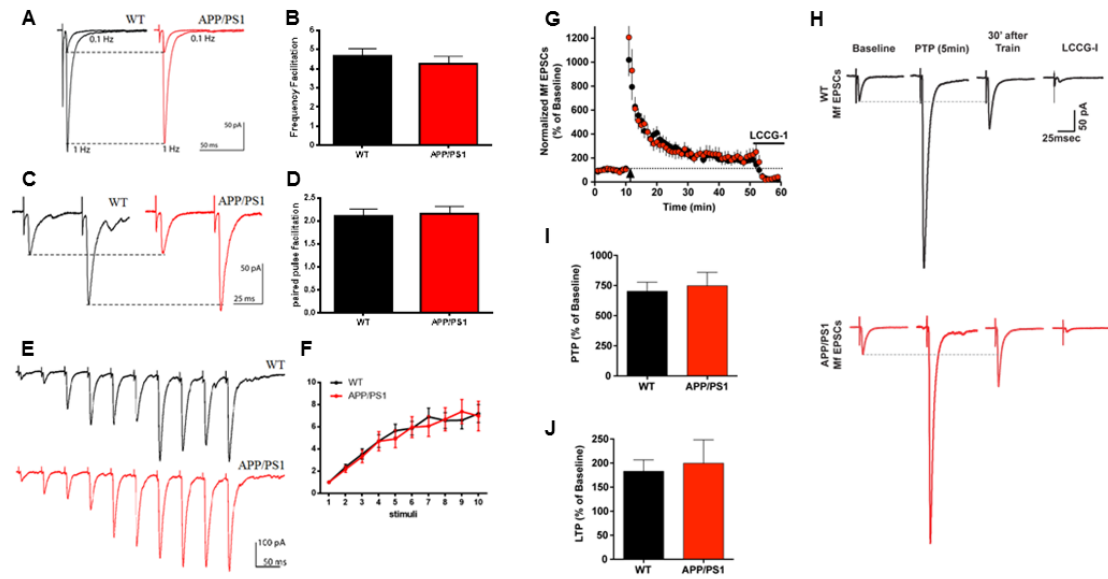


Figure 4. Normal presynaptic short-term plasticity and presynaptic LTP of Mf synapses in 6months APP/PS1 mice.

A. Representative average traces of the amplitude increase of Mf-EPSCs with FF. EPSCs obtained at 0.1Hz (30 sweeps) and 1Hz (30 sweeps) for Wt and APP/PS1 mice. **B.** Bar graph displaying comparable mean values of FF observed in Wt and APP/PS1. WT (4.67 ± 0.36) and APP/PS1 mice (4.26 ± 0.37). t-test $p=0.4298$, $n=16$ for WT and $n=16$ for APP/PS1. **C.** Average of 20 traces illustrating PPF at an inter-stimulus interval of 40ms for Wt (black traces) and APP/PS1 (red traces) Mf synapses. **D.** Bar graph representing the ratio between the amplitude of the second over the first EPSCs obtained during PP stimulating protocol. WT (2.11 ± 0.15) and APP/PS1 mice (2.15 ± 0.16). t-test $p=0.8556$, $n=16$ for WT and $n=16$ for APP/PS1. **E.** Average of 5 traces illustrating 10-stimuli 20Hz train at the interval of 2min apart, for Wt (black traces) and APP/PS1 (red traces) mice. **F.** Normalized amplitudes in the 10-stimuli 20Hz train. Two-way ANOVA test $p=0.7745$ between Wt ($n=14$) and APP/PS1 ($n=12$). Data represented as mean \pm SEM. **G.** Summary plot of the LTP time course for Wt (black circles, $n=12$) and APP/PS1 (red circles, $n=11$) cells. The LTP protocol (100 pulses at a frequency of 100Hz repeated 3 times with a 10s inter train interval) was applied at the time indicated by the arrow. Mf-EPSCs were averaged every minute and normalized to the mean amplitude of the 10min period preceding the LTP induction protocol. **H.** Traces represent Mf-EPSCs obtained at a stimulus frequency of 0.1Hz during Baseline (10min), PTP (5min), LTP (30-40min after the train) and LCCG (5min after drug application). Black and red traces from representative cells in Wt and APP/PS1 mice, respectively. **I.** Bar graph with average values of PTP recorded 5minutes after the high frequency train was applied shows no difference between the two animal genotypes. Values are expressed as percentage of the baseline amplitude of Mf EPSPs. **J.** Bar graph representing the mean amplitude of Mf-EPSCs recorded between 30 to 40 minutes after LTP induction. Values are expressed as percentage of the baseline Mf-EPSCs amplitude. Data represented as mean \pm SEM.

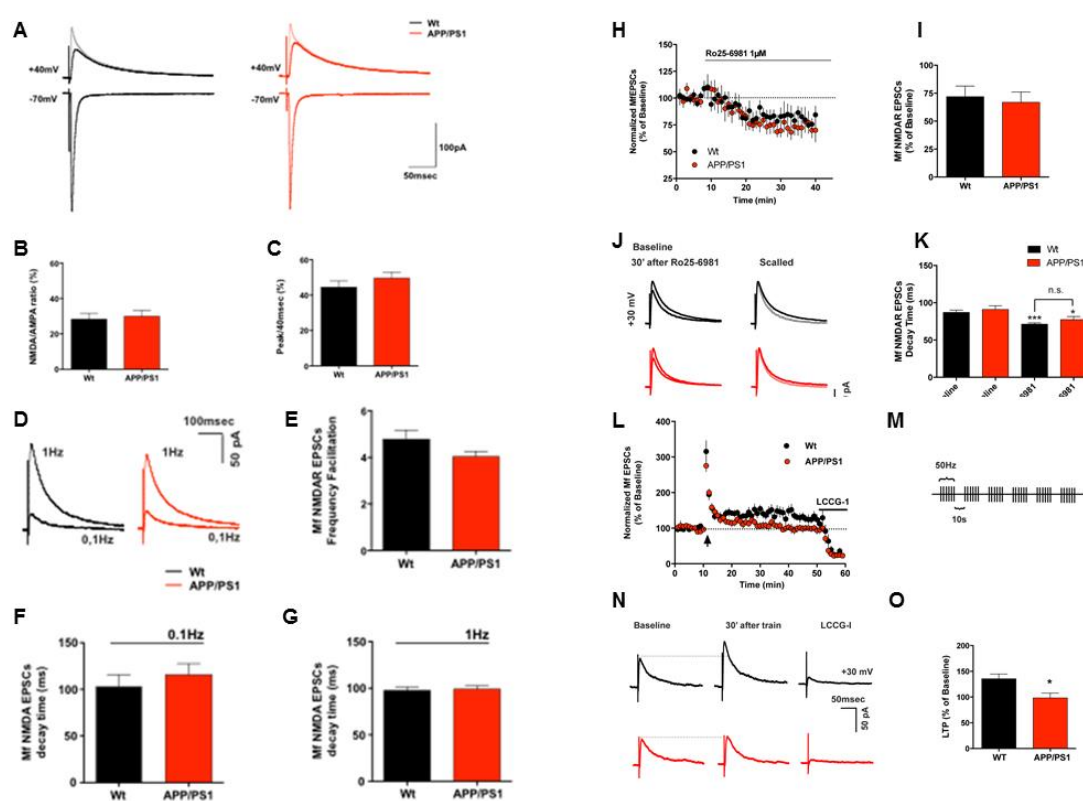


Figure 5. NMDAR-EPSCs and Short-term plasticity of NMDAR is maintained in APP/PS1 mice, whereas a loss of Mf-NMDAR dependent LTP is observed in APP/PS1 mice.

A. Representative traces of Mf-EPSCs recorded at negative (-70mV) and positive potentials (+40mV), with and without NBQX (20 μ M) illustrating no major differences between results obtained in the two genotypes. Bicuculline was present throughout all experiments. **B.** Bar graph resumming mean values of NMDAR/AMPA ratios obtained with isolated currents at -70mV (AMPA) and +40mV (NMDAR with NBQX). Black bar represents results from 9 cells from Wt mice and red bar represents results from 9 APP/PS1 cells. **C.** Bar graph representing mean values obtained for NMDAR/AMPA ratio performed at +40mV in the presence of bicuculline. The ratio, calculated as the amplitude 40ms after the peak divided by the peak amplitude, was not different between the Wt (n=9) and APP/PS1 (n=9) cells analyzed. Data represented as mean \pm SEM. **D.** Representative traces of NMDAR-mediated EPSCs recorded at +40mV, illustrating that both genotypes perform equivalent FF at positive potentials. Black traces illustrate average of 40 traces at 0.1Hz and 60 at 1Hz (from 0.1Hz to 1Hz) obtained from Wt cells (n=29). Red traces were obtained from APP/PS1 mice (n=31). **E.** Bar graph summarizing mean FF values obtained from NMDAR-EPSCs recorded at positive potentials from Wt and APP/PS1 cells, Mann-Whitney test $p=0.1932$. **F.** Summary plot of the mean decay time of Mf NMDAR-mediated EPSCs recorded at a frequency of 0.1Hz. Black and Red bars represent respectively Wt and APP/PS1 values of Mf NMDAR-EPSCs decay time (ms). Average decay times are not statistically different t-test, $p=0.4782$. **G.** Summary plot of the mean decay time of Mf NMDAR-mediated EPSCs recorded at a 1Hz frequency. Average decay times are not statistically different (t-test, $p=0.7707$) between Wt (black bars) and APP/PS1 mice (red bar). Data represented as mean \pm SEM. **H.** Summary plot describing the time course of

Results

Mf NMDARs-EPSCs inhibition after application of the GluN2B subunit antagonist Ro 25-6981 (1 μ M). Recordings from Wt cells are summarized by black circles (n=12) and APP/PS1 cells by red circles (n=11) cells. The antagonist was present from the ninth minute until the end of the recordings. Mf NMDAR-mediated EPSCs, obtained every 10sec (0.1Hz) were averaged every minute and normalized to the mean amplitude of the 8-minute period preceding the LTP induction protocol. **I.** Bar graph representing the mean amplitude of Mf NMDARs EPSCs recorded between 30 to 40 minutes after drug application. Values are expressed as percentage of baseline Mf NMDAR-EPSCs amplitude. **J.** Traces represent Mf NMDAR-EPSCs obtained at stimulus frequency of 0.1Hz during Baseline (8min), and after 30min of Ro 25-6981 action. Black and red traces from representative cells from Wt and APP/PS1 cells, respectively. **K.** Summary plot of mean decay time of Mf NMDAR-mediated EPSCs recorded at a frequency of 0.1Hz. Average decay times are not statistically different between Wt (black bars) and APP/PS1 mice (red bars). The mean decay time before and after Ro 25-6981 is different for both genotypes, Wt (paired t-test, $p < 0.0001$) and APP/PS1 (paired t-test $p = 0.0263$) mice. Data represented as mean \pm SEM, * represents $p < 0.05$, *** represent $p < 0.0001$. **L.** Summary plot of Mf NMDAR-LTP time course for Wt (black circles, n=12) and APP/PS1 (red circles, n=11) cells. The LTP protocol was applied at the time indicated by the arrow. Mf NMDAR-mediated EPSCs, evoked every 10sec (0.1Hz) were averaged every minute and normalized to the mean amplitude of the 10min period preceding the LTP induction protocol. **M.** Schematic representation of the train applied to trigger specific NMDAR-dependent LTP at Mf synapses: 6 bursts of 6 stimuli given at a frequency of 50 Hz. The 6 burst were separated by a 150ms interval. **N.** Traces represent Mf NMDAR-EPSCs obtained at stimulus frequency of 0.1Hz during Baseline (10min), LTP (between 30min to 40min after the train) and LCCG-I application (5 min after drug treatment). Black and red traces from representative cells from Wt and APP/PS1 cells, respectively. **O.** Bar graph representing the mean amplitude of Mf NMDARs EPSCs recorded between 30 to 40 minutes after LTP induction. Values are expressed as percentage of baseline Mf NMDAR-EPSCs amplitude. Data represented as mean \pm SEM, * represents $p < 0.05$.

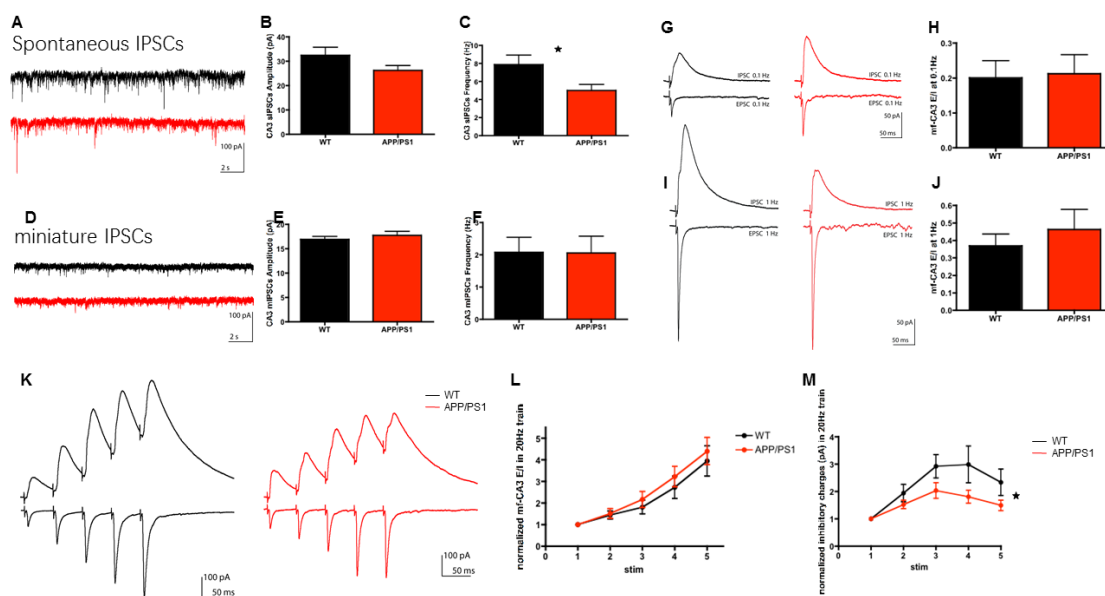


Figure 6. The frequency of spontaneous IPSCs and inhibitory charges in CA3 neurons are reduced, while the E/I ratio is maintained in APP/PS1 mice.

A. Representative traces of spontaneous IPSCs (20 μ M NBQX extracellularly, 10mM QX-314 intracellularly) during 20s, recorded at -60mV, from CA3 cells of Wt and APP/PS1 mice. **B.** Summary graph showing no difference between genotypes of the sIPSCs mean amplitude registered during a 10-minute period. Black bar represents Wt cells (n=16, 6 mice) and red bar represents cells from APP/PS1 mice (n=18, 6 mice), t-test p=0.1147. **C.** Summary plot of the mean sIPSCs frequency registered during 10 minutes showing a reduction in sIPSCs frequency from the APP/PS1 cells. Black bar represents Wt cells (n=16, 6 mice), red bar represents cells from APP/PS1 mice (n=18, 6 mice), t-test, p=0.0254. Data represented as mean \pm SEM, * represents p<0.05. **D.** Representative traces of spontaneous IPSCs (20 μ M NBQX and 0.5 μ M TTX extracellularly, 10mM QX-314 intracellularly) during 20s, recorded at -60mV, from CA3 cells of Wt and APP/PS1 mice. **E.** Summary graph showing no difference between genotypes of the mIPSCs mean amplitude registered during a 10-minute period. Black bar represents Wt cells (n=15, 6 mice) and red bar represents cells from APP/PS1 mice (n=15, 6 mice), t-test p=0.4292. **F.** Summary plot of the mean mIPSCs frequency registered during 10 minutes showing no difference in mIPSCs frequency from the APP/PS1 cells. Black bar represents Wt cells (n=15, 6 mice), red bar represents cells from APP/PS1 mice (n=15, 6 mice), t-test, p=0.9756. Data represented as mean \pm SEM. **G.** Representative traces of Mf-EPSCs recorded at negative (-70mV) and IPSCs recorded at positive potentials (+10mV) at 1Hz stimulation, for Wt (black traces) and APP/PS1 (red traces), D-AP5 (20 μ M) was present through the experiment. **H.** Bar graph representing slightly elevated E/I ratio in APP/PS1 mice, but no significant difference was found. Black bar represents Wt cells (n=16, 10 mice), red bar represents cells from APP/PS1 mice (n=16, 10 mice), t-test with Welch's correction for unequal variances p=0.4882. Data represented as mean \pm SEM. **I.** Representative traces of Mf-EPSCs recorded at negative (-70mV) and IPSCs recorded at positive potentials (+10mV) at 0.1Hz stimulation, for Wt (black traces) and APP/PS1 (red traces), D-AP5 (20 μ M) was present through the experiment. **J.** Bar graph illustrating no major differences between

Results

results obtained in the two genotypes in terms of E/I ratio. Black bar represents Wt cells (n=16, 10 mice), red bar represents cells from APP/PS1 mice (n=16, 10 mice), t-test $p=0.8703$. Data represented as mean \pm SEM. **K.** Average of 20 traces illustrating evoked EPSCs (recorded at -70mV) and IPSCs (recorded at +10mV) during 5-stimuli 20Hz train for Wt (black traces) and APP/PS1 (red traces) at Mf synapses. **L.** Line chart representing the E/I ratio of total charges during the train normalized against the first response, Wt represented in black and APP/PS1 in red. Two-way ANOVA test $p=0.2672$ between Wt (n=15) and APP/PS1 (n=16). Data represented as mean \pm SEM. **M.** Line chart representing the inhibitory charges during the train normalized against the first response, Wt represented in black and APP/PS1 in red. Two-way ANOVA test $p=0.0478$ between Wt (n=14) and APP/PS1 (n=14). Data represented as mean \pm SEM.

3.2 Electrophysiological studies of KAR-mediated currents in CA3 PCs of 6-month male APP/PS1 mice

3.2.1 KAR-EPSCs of Mf-CA3 synapses are reduced in APP/PS1 mice

While AMPARs and NMDARs mediate a large part of EPSCs in CA3 PCs, KARs also play distinct roles in regulating the activity of CA3 circuits. KARs are found to be abundantly expressed in the stratum lucidum of the CA3 region, both pre- and postsynaptically at Mf synapses (Darstein et al., 2003; Ruiz, Sachidhanandam, Utvik, Coussen, & Mulle, 2005). Knockout studies have demonstrated that KARs may also play important role in hippocampus-dependent memory (Ko, Zhao, Toyoda, Qiu, & Zhuo, 2005; Rebola et al., 2017). Moreover, there have been many pieces of evidence showing that KARs can modulate slow AHP and neuronal excitability in pyramidal neurons (Fisahn, Heinemann, & McBain, 2005; Melyan, Lancaster, & Wheal, 2004; Melyan, Wheal, & Lancaster, 2002; Ruiz et al., 2005). Therefore, we hypothesized that there may be dysfunction of KARs at Mf-CA3 synapses in APP/PS1 mice.

We first recorded evoked Mf-EPSCs from CA3 PCs in the presence of 20 μ M D-APV, 10 μ M Bicuculline, 3 μ M CGP 55845 at 0.1Hz, 1Hz and 3Hz respectively. These Mf-EPSCs corresponded to conductance of AMPA and Kainate receptors (noted as AMPAR+KAR EPSCs). We then added additional 25 μ M LY303070 to isolate the KAR component of Mf-EPSCs during 0.1Hz, 1Hz, and 3Hz of Mf stimulation. Minimal stimulation was achieved, and the failure rate and AMPAR-EPSC amplitude at 0.1Hz was compared between genotypes to ensure that comparable strength of stimulation was used (For failure rates of AMPAR-EPSCs at 0.1 Hz, WT $13.05 \pm 3.54\%$, n=13; APP/PS1 $19.06 \pm 6.41\%$, n=12; Unpaired t-test p=0.4110; For amplitudes of AMPAR-EPSCs at 0.1 Hz, WT 64.46 ± 8.86 pA, n=13; APP/PS1 55.91 ± 9.41 pA, n=12; Unpaired t-test p=0.5143; Figure 3.1). The AMPAR-EPSCs were comparable between the two groups (At 1Hz, WT 219.0 ± 20.25 pA, n=13; APP/PS1 mice 197.8 ± 33.93 pA, n=12; t-test p=0.5901; At 3Hz, WT 298.0 ± 21.23 pA, n=13; APP/PS1 mice 266.9 ± 41.72 pA, n=12; t-test p=0.5032; Figure 3.1).

We observed that the KAR-EPSCs were significantly reduced, and the KAR/AMPA ratio was significantly decreased in APP/PS1 mice (At 1Hz, WT 0.058 ± 0.005 , n=13; APP/PS1 0.032 ± 0.004 , n=12; t-test p=0.0003; At 3Hz, WT 0.054 ± 0.004 , n=13; APP/PS1 0.030 ± 0.004 , n=12; t-test p=0.0005; Figure 3.1). The KAR-EPSCs at 0.1Hz were not shown due to their very small amplitudes and corresponding large errors.

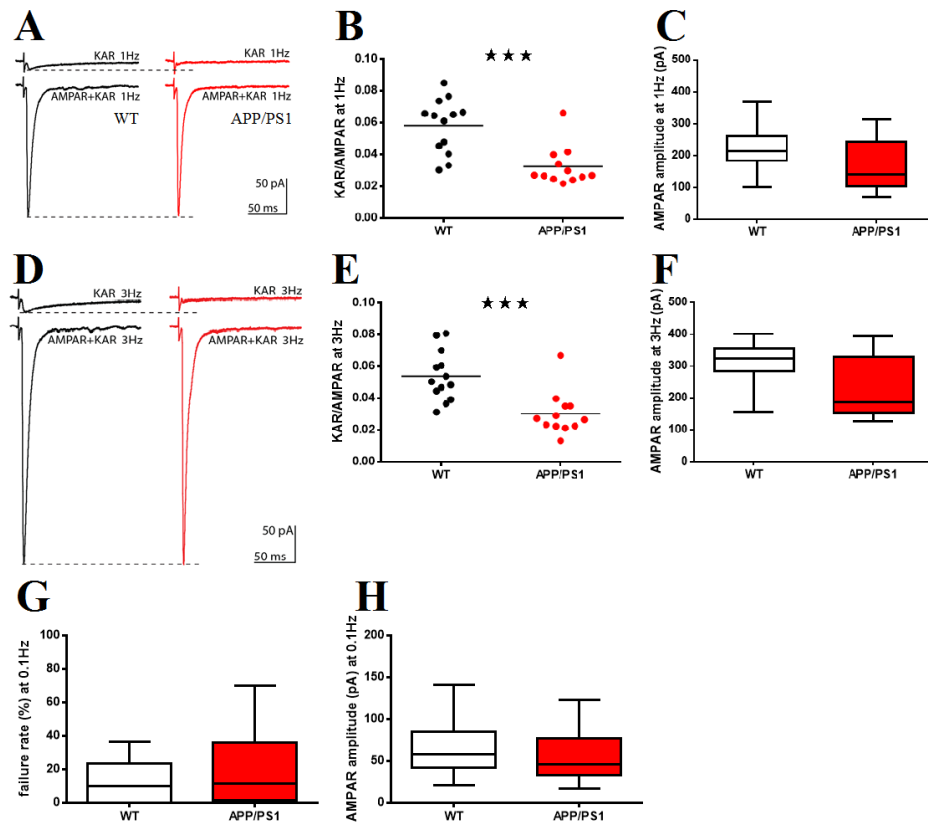


Figure 3.1. KAR-mediated EPSCs at Mf-CA3 synapses are significantly reduced in 6-month APP/PS1 mice.

A. Representative traces illustrating evoked Mf-EPSCs of AMPAR and KAR during 1Hz stimulation, and was an average of 30 sweeps. 20 μ M D-APV, 10 μ M Bicuculline, 3 μ M CGP 55845 was present through the experiment to isolate AMPAR+KAR currents, and for KAR response recording, additional 25 μ M LY303070 was present. In the graph, black color was used for WT and red for APP/PS1 mice. **B.** Dot plot displaying the ratio of KAR-EPSCs amplitudes over AMPAR-EPSCs amplitudes at 1Hz, and there was a significant reduction in mean KAR/AMPA ratio in the APP/PS1 mice comparing to WT littermates. Black dots represent WT (0.058 ± 0.005 , n=13, 9 mice) and red dots represent APP/PS1 (0.032 ± 0.004 , n=12, 6 mice), t-test p=0.0003. *** represents p<0.001. **C.** Box plot displaying the amplitude of AMPAR-EPSCs at 1Hz observed in Mf-CA3 synapses in WT (219.0 ± 20.25 pA, n=13, 9 mice) and APP/PS1 mice (197.8

$\pm 33.93\text{pA}$, $n=12$, 6 mice). t-test $p=0.5901$. **D.** Representative traces illustrating evoked Mf-EPSCs of AMPAR and KAR during 3Hz stimulation, and was an average of 30 sweeps. In the graph, black color was used for WT and red for APP/PS1 mice. **E.** Dot plot displaying the KAR/AMPA ratio at 3 Hz, and there was a significant reduction in mean KAR/AMPA ratio in the APP/PS1 mice comparing to WT littermates. Black dots represent WT (0.054 ± 0.004 , $n=13$, 9 mice) and red dots represent APP/PS1 (0.030 ± 0.004 , $n=12$, 6 mice), t-test $p=0.0005$. *** represents $p<0.001$. **F.** Box plot displaying the amplitude of AMPAR-EPSCs at 3 Hz observed in Mf-CA3 synapses in WT ($298.0 \pm 21.23\text{pA}$, $n=13$, 9 mice) and APP/PS1 mice ($266.9 \pm 41.72\text{pA}$, $n=12$, 6 mice). Unpaired t-test $p=0.5032$. **G.** Box plot illustrating comparable failure rates of AMPAR-EPSCs at 0.1 Hz between WT ($13.05 \pm 3.54\%$, $n=13$) and APP/PS1 mice ($19.06 \pm 6.41\%$, $n=12$). Unpaired t-test $p=0.4110$. **H.** Box plot illustrating comparable amplitudes of AMPAR-EPSCs at 0.1 Hz between WT ($64.46 \pm 8.86\text{pA}$, $n=13$) and APP/PS1 mice ($55.91 \pm 9.41\text{pA}$, $n=12$). Unpaired t-test $p=0.5143$.

These results suggest that there are less functional KARs at the postsynaptic sites of Mf-CA3 synapses. However, whether the number/functional state of extrasynaptic KARs is affected or not is unclear.

3.2.2 KAR-EPSCs of Mf-CA3 synapses is also reduced in PS KO mice

Previous work of our team has demonstrated that N-Cadherin (NCad) can recruit and stabilize KARs by interacting with the GluK2a C-terminal domain, and overexpression of a dominant-negative form of NCad or knockdown of NCad in CA3 PCs could lead to a strong reduction in the amplitude of KAR-EPSCs (Fievre et al., 2016). We suspect that similar mechanism is responsible for the reduction of KAR-EPSCs in APP/PS1 mice. APP/PS1 transgenic mice express a mutated form of Presenilin (i.e. PSEN1 delta E9), which is the catalytic component of the γ -secretase complex. Mutated PS1 could induce loss of function of γ -secretase, potentially leading to accumulation of NCad lacking the extracellular fragment at the cell membrane.

Therefore, we hypothesized that this mutated PS1 gene in APP/PS1 mice could cause accumulation of truncated NCad at the membrane and thus impair the presence or function of KARs at Mf-CA3 synapses. To investigate this question, we took advantage of existing mouse lines at the local institute and generated conditional PS KO mice by injecting 500nl of AAV2.9 Syn Cre-GFP in hippocampal CA3 region of one hemisphere of PS1-floxed/PS2 KO mice. We patched the GFP-positive CA3 PCs

as the PS KO cells, and non-fluorescent neurons from the other hemisphere were used as controls.

KAR and AMPAR-mediated EPSC recordings were performed as previously described in Chapter 3.3.5. Again, we observed a significant reduction of the KAR/AMPA ratio in APP/PS1 mice (At 1Hz, control 0.030 ± 0.005 , $n=9$; PSKO 0.014 ± 0.005 , $n=10$; t-test $p=0.0447$; At 3Hz, control 0.027 ± 0.005 , $n=9$; PSKO 0.009 ± 0.004 , $n=10$; t-test $p=0.0056$; Figure 3.2), while the AMPAR-EPSCs were comparable (At 1Hz, control 227.6 ± 24.85 pA, $n=9$; PSKO 178.8 ± 16.27 pA, $n=10$; t-test $p=0.1121$; At 3Hz, control 317.5 ± 26.06 pA, $n=9$; PSKO 243.8 ± 24.27 pA, $n=10$; t-test $p=0.0539$; Figure 3.2). The failure rates and AMPAR-EPSC amplitudes at 0.1Hz were also comparable between genotypes (For failure rates of AMPAR-EPSCs at 0.1 Hz, control $13.05 \pm 3.54\%$, $n=9$; PSKO $19.06 \pm 6.41\%$, $n=10$; t-test $p=0.6673$; For amplitudes of AMPAR-EPSCs at 0.1 Hz, control 65.67 ± 15.18 pA, $n=9$; PSKO 74.07 ± 12.07 pA, $n=10$; t-test $p=0.5143$; Figure 3.2).

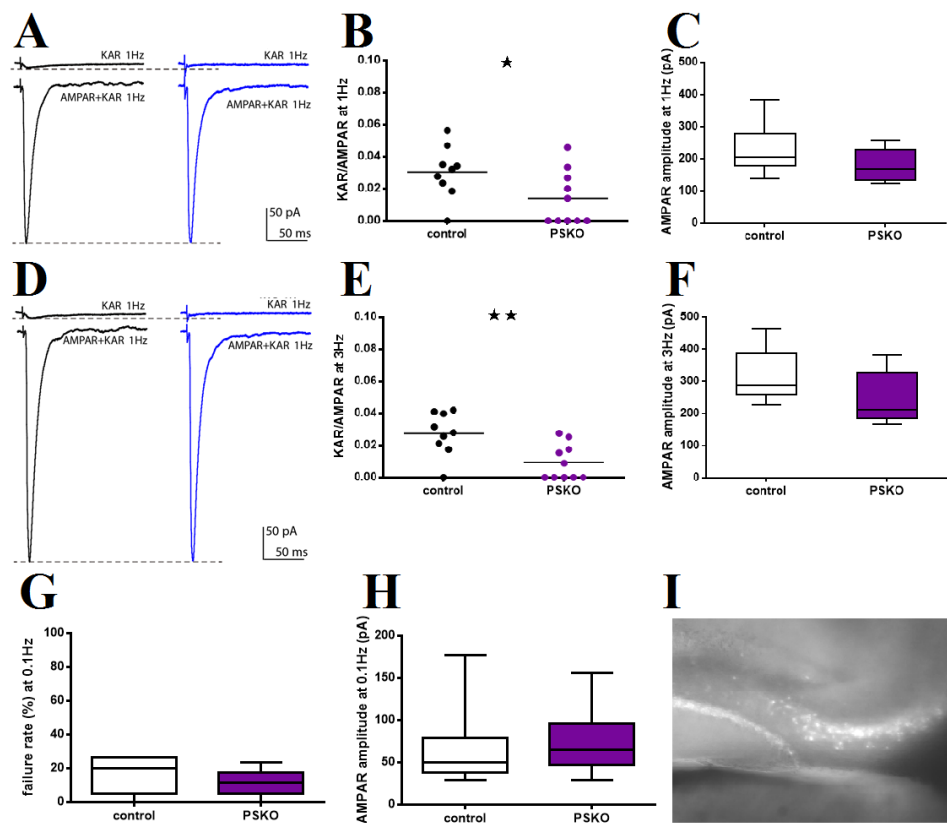


Figure 3.2. KAR-mediated EPSCs at Mf-CA3 synapses are significantly reduced in PSKO mice.

A. Representative traces illustrating evoked Mf-EPSCs mediated by AMPARs and KARs at 1Hz stimulation, average of 30 sweeps. $20\mu\text{M}$ D-APV, $10\mu\text{M}$ Bicuculline,

3 μ M CGP 55845 was present throughout the experiment to isolate AMPAR+KAR currents. For KAR-EPSCs recording, 25 μ M LY303070 was added to the aCSF. In the graph, black color was used for control and blue for PSKO mice. **B.** Dot plot displaying the ratio of KAR-EPSCs amplitudes over AMPAR-EPSCs amplitudes at 1Hz. There was a significant reduction in mean KAR/AMPA ratio in PSKO mice compared to controls. Black dots represent control (0.030 ± 0.005 , n=9, 9 mice) and blue dots represent PSKO (0.014 ± 0.005 , n=10, 9 mice), t-test p=0.0447. * represents p<0.05. **C.** Box plot displaying the amplitude of AMPAR-EPSCs at 1Hz observed in Mf-CA3 synapses in control (227.6 ± 24.85 pA, n=9, 9 mice) and PSKO mice (178.8 ± 16.27 pA, n=10, 9 mice). t-test p=0.1121. **D.** Representative traces illustrating evoked Mf-EPSCs mediated by AMPARs and KARs during 3Hz stimulation, average of 30 sweeps. In the graph, black color was used for control and blue for PSKO mice. **E.** Dot plot displaying the KAR/AMPA ratio at 3 Hz, indicating a significant reduction in mean KAR/AMPA ratio in PSKO mice as compared to controls. Black dots represent control (0.027 ± 0.005 , n=9, 9 mice) and blue dots represent PSKO (0.009 ± 0.004 , n=10, 9 mice), t-test p=0.0056. ** represents p<0.01. **F.** Box plot displaying the amplitude of AMPAR-EPSCs at 3 Hz observed in Mf-CA3 synapses in control (317.5 ± 26.06 pA, n=9, 9 mice) and PSKO mice (243.8 ± 24.27 pA, n=10, 9 mice). Unpaired t-test p=0.0539. **G.** Box plot illustrating comparable failure rates of Mf-EPSCs at 0.1 Hz between control ($13.05 \pm 3.54\%$, n=9) and PSKO mice ($19.06 \pm 6.41\%$, n=10). Unpaired t-test p=0.6673. **H.** Box plot illustrating comparable amplitudes of AMPAR-EPSCs at 0.1 Hz between control (65.67 ± 15.18 pA, n=9) and PSKO mice (74.07 ± 12.07 pA, n=10). Unpaired t-test p=0.5143. **I.** Epifluorescence microscopy (490nm channel) showing the sparse infection of AAV-Cre-GFP in the hippocampal CA3 region.

So far, we observed a significant reduction in KAR-EPSCs in CA3 PCs in both APP/PS1 mice and PS KO mice. This suggest that the mutated PS might be the common cause of this phenotype. To hypothesize one step further, the lack of normal NCad resulted from dysfunctional γ -secretase might underlie the dysfunction or inadequate presence of KARs at Mf-CA3 synapses.

3.3 CA3 circuits modifications after contextual fear conditioning (CFC)

3.3.1 One-trial CFC can induce changes in CA3 circuits

Located at the entry level of hippocampus, CA3 circuits play a key role in memory encoding. The main purpose of this project was to explore changes in CA3 circuits in regard to learning and memory. We started out by choosing contextual fear conditioning (CFC) as a behavioral paradigm to activate the CA3 circuits during memory encoding and recall. We first validated the one-trial CFC protocol in our lab.

Contextual fear conditioning was performed in adult C57bl6j male mice. Fear conditioning was induced in mice received one-trial foot shocks, and lasted for at least two weeks (Figure 3.3).

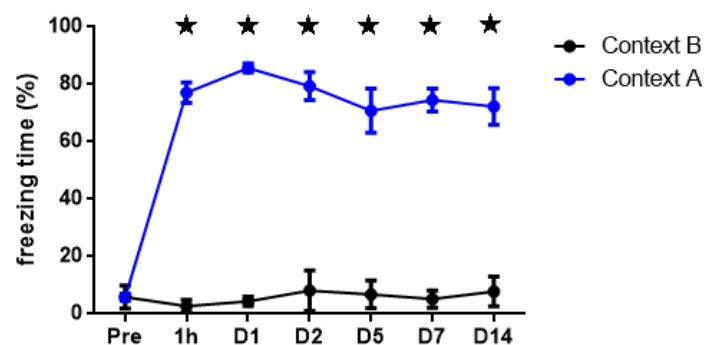


Figure 3.3. One-trial contextual fear conditioning induced long-lasting freezing behavior in adult WT mice.

Line chart displaying freezing time of mice after one-trial CFC. Mice received 5 foot shocks in Context A on the first day, and Context B was neutral and not fear-related. After CFC, mice were tested at 1 hour, 1 day, 2 days, 5 days, 7 days, and 14 days respectively, $n=6$ for each data point, and each mouse was tested in for a maximum of 3 timepoints to avoid possible extinction. Data represented as mean \pm SEM. *represents $p<0.05$.

Immunofluorescent staining of c-Fos was performed 1.5 hours after CFC, to confirm the successful activation of CA3 network. In DG, the number of c-Fos+ cells was not significantly elevated, but the signal strength and distribution pattern seemed different than controls. In CA3, there were significantly more c-Fos+ cells after CFC (Figure 3.4).

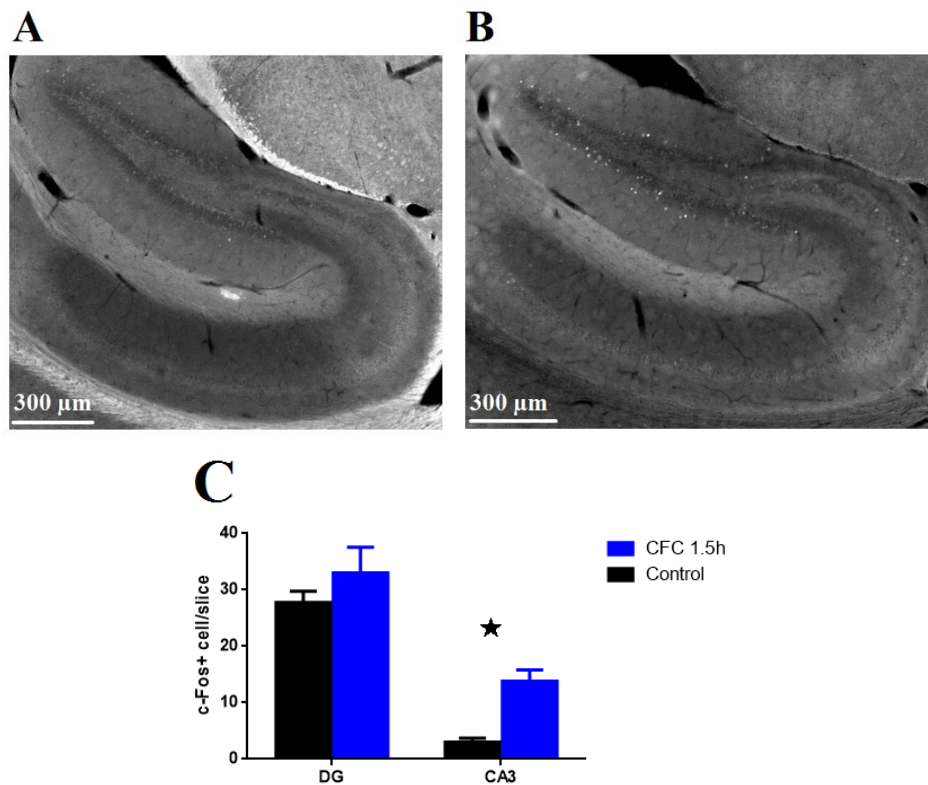


Figure 3.4. c-Fos staining and cell count in DG and CA3 region after CFC.

A. c-Fos signal in hippocampal sagittal slices of control mice. **B.** c-Fos signal in hippocampal sagittal slices of mice 1.5h post-CFC. **C.** Bar graph illustrating mean value of c-Fos+ cell count in each slice. n=12 slices in each group, 2 mice per group. Data represented as mean ± SEM. *represents $p < 0.05$.

It was shown previously that there is a robust filopodia growth at Mf terminals after CFC, where the number of filopodia was doubled within 5h and this lasted for at least 10 days (Ruediger et al., 2011). We attempted to reproduce this experiment. We used Thy1-mGFP-DG mice, and sacrificed the mice to count the filopodia numbers at large Mf terminals (LMTs) 5h after CFC. Unexpectedly, we did not see any difference between the two groups (Figure 3.5). Our count of filopodia in control condition is much higher than reported by Ruediger et al. in 2011, but consistent with some other studies in adult mice (Wilke et al., 2013). Further investigations are needed to interpret this result.

Whatsoever, in our hands one-trial CFC can be used as an efficient tool to induce fear memory and cell activity changes in terms of c-Fos expression in the CA3 region in adult mice.

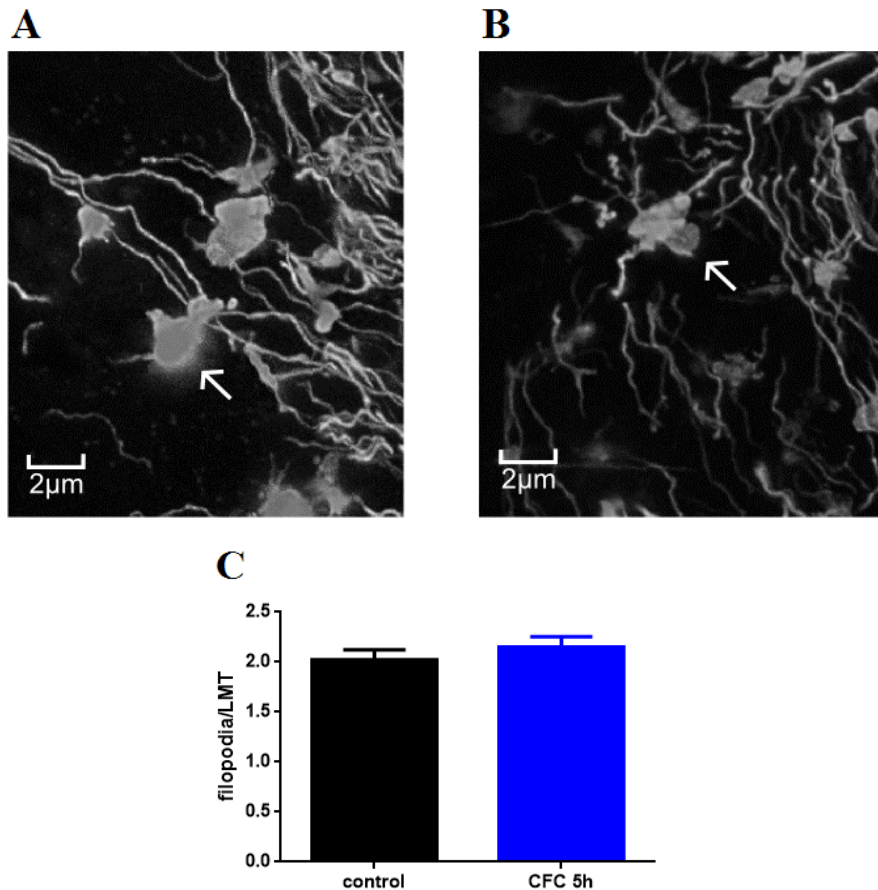


Figure 3.5. Filopodia number count after one-trial CFC at large Mf terminals.

A. Representative confocal image of LMTs and their filopodia in control mice. **B.** Representative confocal image of LMTs and their filopodia in mice sacrificed 5h after CFC. **C.** Bar graph displaying mean filopodia count per LMT in mice having received CFC vs. controls. 50 LMTs were examined for each mouse, and 5 mice were used in each group. Filopodia/LMT was 2.02 ± 0.10 for controls; 2.15 ± 0.10 for CFC 5h group. Unpaired t-test $p=0.3109$. Data represented as mean \pm SEM.

3.3.2 Electrophysiological studies of Mf-CA3 circuit 3h after CFC

As many changes can already happen within hours after CFC at the molecular and structural level in hippocampal neurons (Gupta et al., 2010; Ruediger et al., 2011), we explored the electrophysiological features of Mf-CA3 synapses rapidly after CFC. The mice were sacrificed 3h after CFC, and recordings were performed within the following 5 hours.

We started by investigating the prominent features of short-term plasticity at Mf-CA3 synapses shortly after CFC, by looking at frequency facilitation (FF) and paired-

pulse facilitation (PPF). After achieving minimal stimulation (failure rates at 0.1Hz ~20%), we performed FF protocol (0.1Hz to 1Hz) and PPF protocol at 20Hz. With comparable EPSC amplitudes between the two groups (data not shown), no significant differences were found in either type of facilitations (Figure 3.6). We could conclude at this point that the basal presynaptic properties measured from Mf-CA3 synapses were not significantly modified 3h after CFC in adult C57bl6j male mice.

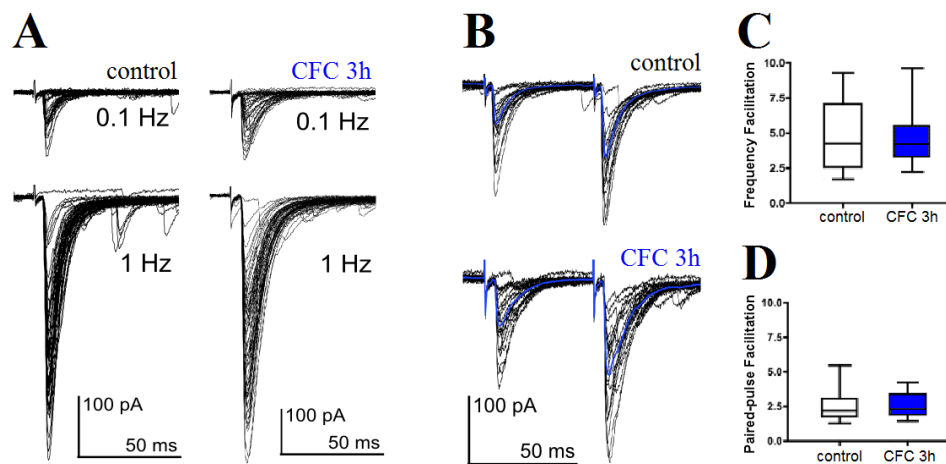


Figure 3.6. Normal short-term plasticity of Mf-CA3 glutamatergic synapses 3h after CFC in adult mice.

A. Representative of superimposed traces illustrating frequency facilitation (FF) at Mf-CA3 synapses. The evoked-EPSCs were obtained at 0.1Hz (60 sweeps) and 1Hz (60 sweeps) respectively. **B.** Representative of superimposed traces illustrating paired-pulse facilitation (PPF) at Mf-CA3 synapses. Paired-pulse recordings were performed every 30s for 20 sweeps, and the inter-stimuli interval is 50ms (20Hz). **C.** Box plot displaying the FF ratio observed in Mf-CA3 synapses in CFC 3h group (4.17 ± 0.51) and control (4.05 ± 0.46). t-test $p=0.8144$, $n=12$ for control and $n=10$ for CFC 3h group. **D.** Box plot displaying the FF ratio observed in Mf-CA3 synapses in CFC 3h group (2.38 ± 0.17) and controls (2.33 ± 0.14). t-test $p=0.7926$, $n=12$ for control and $n=10$ for CFC 3h group.

We further recorded the spontaneous EPSCs of CA3 pyramidal cells 3h after CFC, and saw no difference in either frequency or amplitude of glutamatergic activities comparing to controls (Figure 3.7).

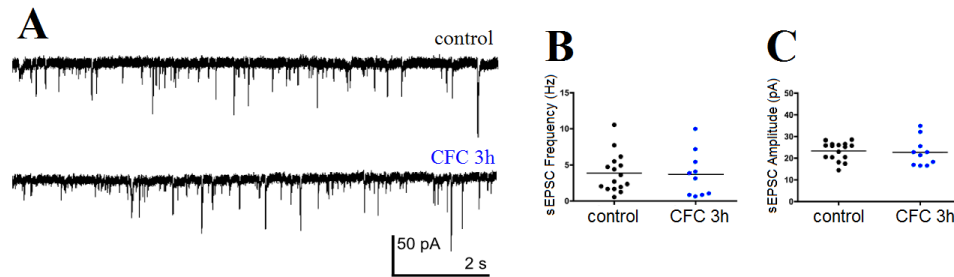


Figure 3.7. The spontaneous EPSCs in CA3 PCs are unaltered 3h after CFC in adult male mice.

A. Representative traces of spontaneous EPSCs (10 μ M Bicuculline in aCSF) during 10s, recorded at -70mV from hippocampal CA3 pyramidal cells of adult C57bl6j mice. **B.** Dot plot of the mean sEPSC frequency registered during 10 minutes showing no significant difference between groups. Black dots represent controls (n=16) and blue dots represent CFC 3h group (n=10), t-test p=0.9253. **C.** Dot plot showing no difference in mean amplitude of sEPSCs between groups. Black dots represent controls (n=16) and blue dots represent CFC 3h group (n=10), t-test p=0.8702.

Overall, we did not observe any major change in the plasticities of glutamatergic activities at Mf-CA3 synapses shortly after CFC.

We then explored GABAergic synaptic transmission onto CA3 PCs. We recorded spontaneous IPSCs and miniature IPSCs from CA3 pyramidal cells in mice sacrificed 3h after CFC. We found that the frequency of sIPSCs was significantly increased compared to naïve controls, while the mean amplitude of sIPSCs was not significantly modified. Also, neither the mean frequency nor the mean amplitude of mIPSCs of CFC 3h group was significantly different from controls (Figure 3.8).

These results suggest that the number of inhibitory synapses onto CA3 PCs are largely unchanged, while the spontaneous inhibitory activities are increased rapidly after CFC. This was somehow consistent with our morphological findings in Chapter 3.3.1 regarding filopodia numbers at LMTs, indicating no significant change in number of synapses in the Mf-CA3 interneuron feedforward inhibition after CFC. However, the increased frequency of sIPSCs could imply that the interneurons in CA3 region might be firing more actively rapidly after CFC, giving more GABAergic signals to CA3 PCs. This might be due to enhanced excitability of CA3 interneurons after CFC, or facilitated synaptic transmission at synapses of feedforward inhibition circuits, or some other unknown mechanisms. It will be interesting to further investigate the feedforward inhibition connections in CA3 region.

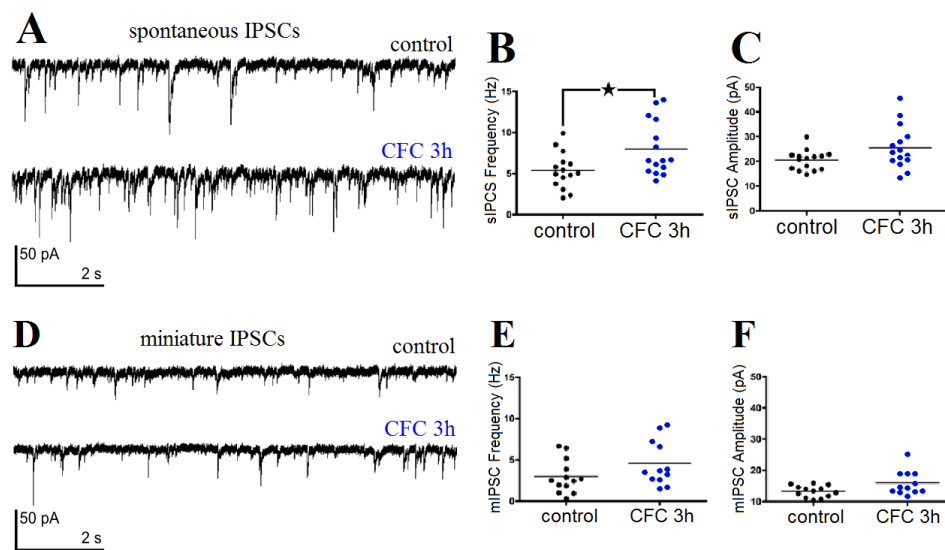


Figure 3.8. The frequency but not the amplitude of spontaneous IPSCs in CA3 PCs is increased 3h after CFC in adult mice

A. Representative traces of sIPSCs ($20\mu\text{M}$ NBQX in aCSF) during 10s, recorded at -60mV , from CA3 pyramidal cells. **B.** Dot plot of the mean sIPSC frequency registered during 10 minutes showing a significant increase in sIPSC frequency in CFC 3h group comparing to controls. Black dots represent controls ($n=15$) and blue dots represent CFC 3h group ($n=15$), t-test $p=0.0182$. * represents $p<0.05$. **C.** Dot plot showing no difference in mean amplitude of sIPSCs between groups. Black dots represent controls ($n=15$) and blue dots represent CFC 3h group ($n=15$), t-test with Welch's correction $p=0.0563$. **D.** Representative traces of miniature IPSCs ($20\mu\text{M}$ NBQX and $0.5\mu\text{M}$ TTX in aCSF) during 10s, recorded at -70mV , from CA3 pyramidal cells. **E.** Dot plot of the mean mIPSC frequency registered during 10 minutes showing no significant alteration between groups. Black dots represent controls ($n=13$) and blue dots represent CFC 3h group ($n=12$), Mann-Whitney test $p=0.0846$. **F.** Dot plot showing no difference in mean amplitude of mIPSCs between groups. Black dots represent controls ($n=13$) and blue dots represent CFC 3h group ($n=12$), t-test with Welch's correction $p=0.0578$.

3.3.3 Electrophysiological studies of Mf-CA3 circuit 24h after

CFC

We were curious to test whether further changes at Mf-CA3 synapses could be observed at a longer time range after CFC, for example, 24h. We performed again sIPSC recordings in mice sacrificed 24h after CFC, and observed no difference in either frequency or amplitude in CFC group compared to controls (Figure 3.9).

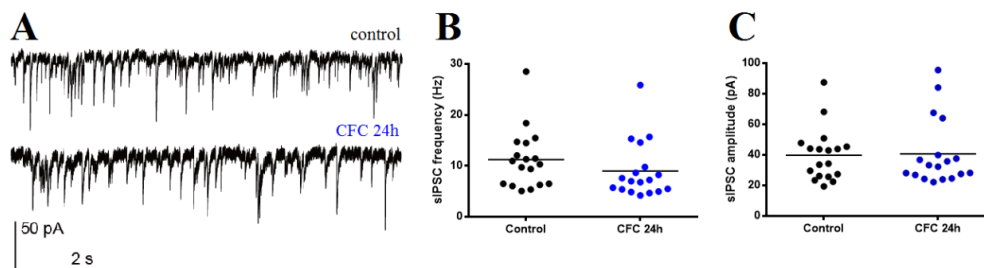


Figure 3.9. The sIPSCs were unaltered 24h after CFC in adult male mice.

A. Representative traces of spontaneous IPSCs (20 μ M NBQX in aCSF) during 10s, recorded at -60mV, from CA3 pyramidal cells. **B.** Dot plot of the mean sIPSC frequency registered during 10 minutes showing no significant difference in sIPSC frequency in CFC 24h group comparing to controls. Black dots represent controls (n=18, 6 mice) and blue dots represent CFC 3h group (n=18, 6 mice), t-test p=0.2429. **C.** Dot plot showing no difference in mean amplitude of sIPSCs between groups. Black dots represent controls (n=18, 6 mice) and blue dots represent CFC 24h group (n=18, 6 mice), t-test p=0.8922.

We also measured the FF and PPF of evoked synaptic transmission again, to look for changes in presynaptic short-term plasticities in larger time scale after CFC. Similarly, no significant differences were registered in the CFC group as compared to controls (Figure 3.10). However, it had to be noted that sIPSC frequency at 24h of both groups were at the same level as the CFC 3h group, so that previous conclusions for the 3h experiments had to be tempered.

In a last effort to search for modifications at Mf-CA3 synapses 24h after CFC, we calculated the accumulative charges of the evoked-EPSCs and evoked-IPSCs under the same stimulating intensity, and compared the excitation/inhibition ratio (E/I) between two groups.

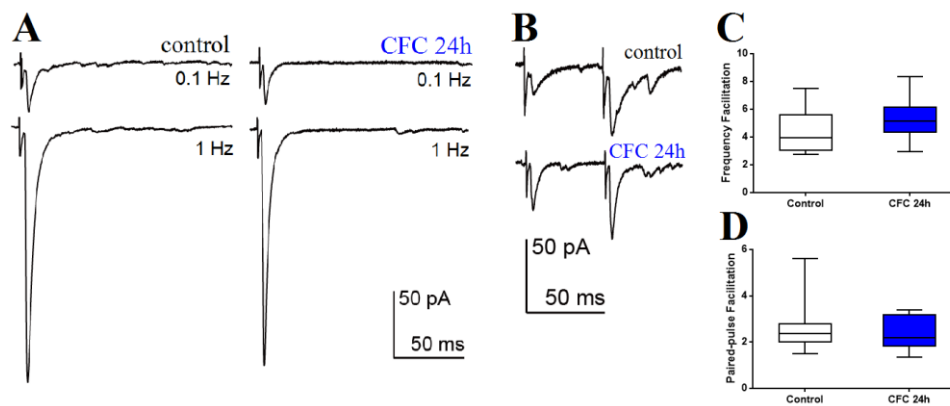


Figure 3.10. Normal short-term plasticity at Mf-CA3 glutamatergic synapses 24h after CFC in adult mice.

A. Representative of averaged traces illustrating the frequency facilitation (FF) at Mf-CA3 synapses. The evoked-EPSCs were obtained at 0.1Hz (30 sweeps) and 1Hz (30 sweeps) respectively. **B.** Representative of averaged traces illustrating the paired-pulse facilitation (PPF) at Mf-CA3 synapses. The paired-pulses were performed every 30s for 20 sweeps, and the inter-stimuli interval is 50ms (20Hz). **C.** Box plot displaying the FF ratio observed in Mf-CA3 synapses in CFC 24h group (5.32 ± 0.49) and control (4.48 ± 0.51). t-test $p=0.2468$, $n=10$ for control and $n=10$ for CFC 24h group. **D.** Box plot displaying the FF ratio observed in Mf-CA3 synapses in CFC 24h group (2.38 ± 0.23) and controls (2.67 ± 0.45). t-test $p=0.5428$, $n=8$ for control and $n=10$ for CFC 24h group.

After recording the evoked Mf-EPSCs in CA3 PCs at -70 mV, we switched the holding potential to +10 mV for evoked-IPSCs recording to explore the excitatory/inhibitory ratio of evoked events at these synapses. The NMDAR antagonist D-APV (20 μ M) was present throughout the experiments to block possible NMDA activities at positive holding potentials. The E/I ratio was calculated as the accumulative charges of the averaged EPSC event over that of the IPSC event. Still, no significant differences were found in these parameters (Figure 3.11).

Taken together, we observed no electrophysiological alterations at Mf-CA3 synapses 24h after CFC. However, we did register an increased frequency of sIPSCs 3h after CFC. Taken together, these results correspond to the role of hippocampal CA3 region in memory encoding when presented with a novel context, especially at the very initial stage of acquisition (Rebola et al., 2017). However, it will be interesting to further explore the GABAergic innervations onto CA3 PCs rapidly after CFC recall.

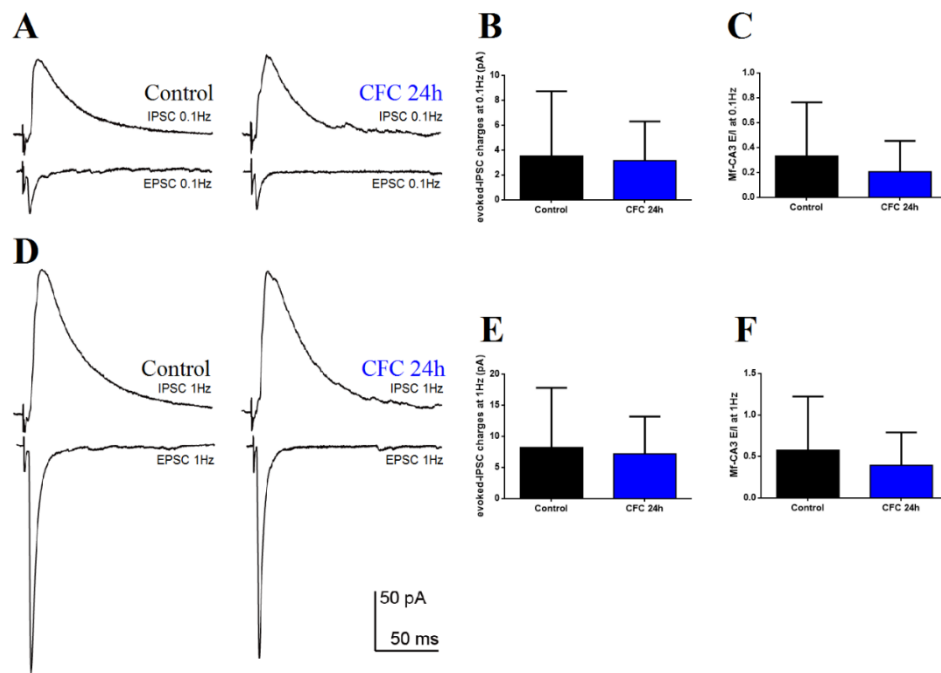


Figure 3.11. The ratio between evoked EPSCs and IPSCs at Mf-CA3 synapses is largely maintained in adult mice 24h after CFC.

A. Representative traces illustrating Mf-EPSCs (recorded at -70mV) and IPSCs (recorded at +10mV) at 0.1Hz stimulation, and was an average of 30 sweeps. 20 μ M D-APV was present through the experiment. **B.** Bar graph illustrating no significant differences in the IPSC charges at 0.1Hz between two groups. Black bar represents controls (3.52 ± 1.65 pA, n=10), blue bar represents CFC 24h group (3.15 ± 1.00 , n=10), t-test p=0.8504. Data represented as mean \pm SEM. **C.** Bar graph displaying no changes in the E/I ratio at 0.1Hz between two groups. Black bar represents controls (0.33 ± 0.14 , n=9), blue bar represents CFC 24h group (0.21 ± 0.08 , n=9), t-test p=0.4665. Data represented as mean \pm SEM. **D.** Representative averaged traces illustrating Mf-EPSCs and IPSCs at 1Hz stimulation. **E.** Bar graph illustrating no significant differences in the IPSC charges at 1Hz between groups. Black bar represents controls (8.20 ± 3.04 pA, n=10), blue bar represents CFC 24h group (7.20 ± 1.89 pA, n=10), t-test p=0.7818. Data represented as mean \pm SEM. **F.** Bar graph displaying no changes in the E/I ratio at 1Hz between groups. Black bar represents controls (0.58 ± 0.22 , n=9), blue bar represents CFC 24h group (0.39 ± 0.13 , n=9), t-test p=0.4810. Data represented as mean \pm SEM.

3.4 Genomic and epigenetic studies of APP/PS1 mice

3.4.1 RNA-sequencing of hippocampal CA3 region in APP/PS1 mice

mice

In pre-symptomatic AD models, many changes may already happen at a transcriptional level, involving signaling cascades, receptor composition and trafficking, and other vital functions in neurons. Identifying these genomic alterations can be very informative on mechanisms of AD onset, and provide us with potential therapeutic targets in treating AD. We were curious to test for genomic changes in our AD mouse model, especially in hippocampal CA3 region. We carried out RNA-seq study with micro-dissected CA3 tissues from 6-month-old male APP/PS1 mice and WT littermates.

We observed that there was a mild change in gene expression pattern in hippocampal CA3 tissue in 6-month-old APP/PS1 mice compared to WT. When the cut-off of $p < 0.01$ & $|\text{fold change}| > 1.2$ was chosen, there were 24 genes that were up-regulated and 16 genes that were down-regulated in APP/PS1 samples (Figure 3.12).

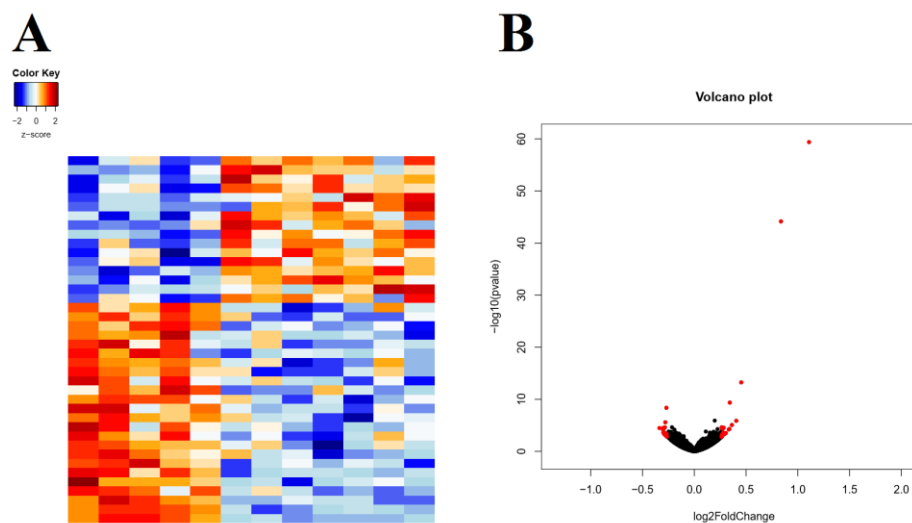


Figure 3.12. Down-regulated and up-regulated genes in 6-month APP/PS1 mice.

A. Heatmap of gene expression in hippocampal CA3 region of 6-month-old APP/PS1 mice (n=5) compared to WT littermates (n=7) (cut-offs: $p < 0.01$, fold change > 1.2). **B.** Volcano plot displaying the expression levels of various genes in APP/PS1 mice (n=5) compared to WT littermates (n=7). Red dots represent differentially regulated genes compared to WT ($p < 0.01$). To the left side are the down-regulated genes, and to the right side are up-regulated genes.

Among the up-regulated genes, apart from APP and PS1, there are PRNP (encoding for the major prion protein PrP), 2310067B10Rik (an ATPase), and CST7 (encoding a glycosylated cysteine protease inhibitor with a putative role in immune regulation). As for the down-regulated genes, there are Arpp21 (encoding a cAMP-regulated phosphoprotein), TRIB2 (an atypical protein kinase), and Dnajb5 (encoding a member of the DNAJ heat shock protein). For a more complete list please refer to Annexes 6.6.

Further pathway analysis revealed the functional group these genes belong in, as is shown in Figure 3.13. These changes indicate that there are impaired functions in many fundamental pathways, and also up-regulation of various genes as response or compensation for the loss of function.

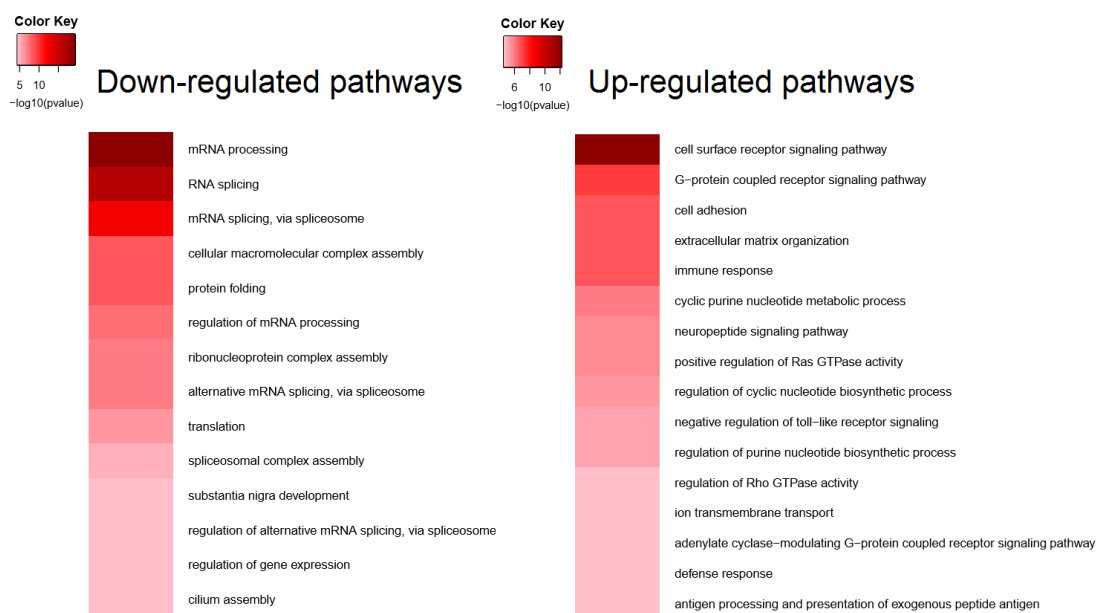


Figure 3.13. Pathway analysis of genes differentially down-regulated and up-regulated in 6-month APP/PS1 mice.

Left panel displaying the down-regulated pathways, and right panel the up-regulated pathways. More significant changes (Gupta et al., 2010) are shown in darker color.

3.4.2 H3K4Me3 level is decreased at gene promoters in APP/PS1

mice

As we have noticed the expression levels of many important genes have been up or down-regulated in early AD model of 6-month APP/PS1 mice, we further investigated the epigenetic changes which might contribute to this result. Histone modifications have been proposed as one of the key mechanisms regulating gene expression in eukaryotic organisms (Kouzarides, 2007; B. Li, Carey, & Workman, 2007). Especially trimethylated H3K4 (H3K4Me3) has been reported to be very relevant to contextual memory consolidation, where H3K4Me3 level was elevated after contextual learning, and decreased in mouse models with memory deficits (Gupta et al., 2010; Kerimoglu et al., 2013).

We hypothesized that there might be a reduction in H3K4Me3 levels at promoters in 6-month-old APP/PS1 mice, leading to the down-regulation of various genes.

Hippocampal CA3 regions were dissected from 6-month-old APP/PS1 mice and WT littermates, and nuclei of only neurons were sorted out using FACS (Figure 3.14).

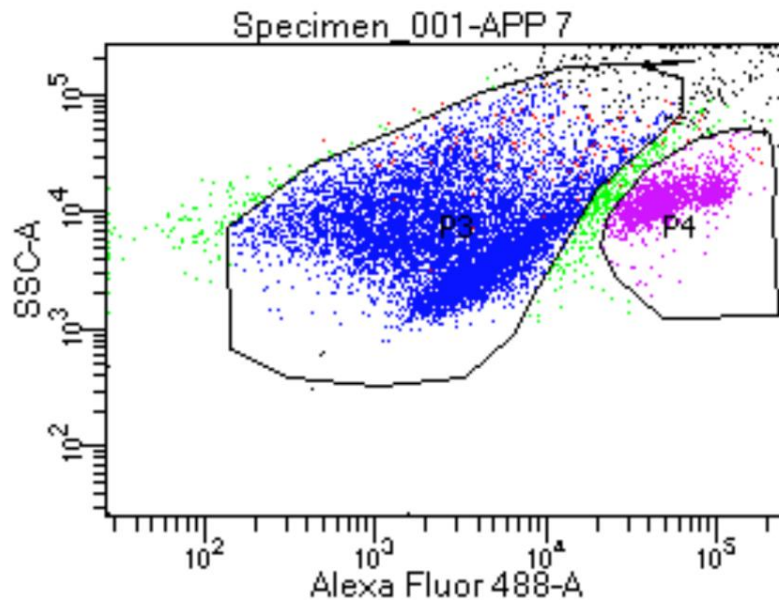


Figure 3.14. Example result of sorted neuronal nuclei by FACS.

Scatter plot of one sample displaying separated neuronal nuclei from non-neuronal cells and debris using FACS. Area P4 (shown in magenta) represents collected neurons, and area P3 (shown in blue) represents non-neuronal components. Note that the yield of neurons per tissue sample is just around 10%.

In line with the findings from the RNA-seq, ChIP analysis revealed a downregulation of H3K4me3 level at the gene promoters, while very few genes promoter areas showed increased H3K4Me3 level (Figure 3.15 A). To name just a few of the down-regulated genes detected: *Lats1* (large tumor suppressor kinase 1), *Dop1R1* (Dopamine 1-like receptor 1), *Mlf* (Myeloid leukemia factor), *Nxn* (nucleoredoxin). For a more complete list please refer to Annexes 6.7.

Again, the pathway analysis was performed, and the down-regulated genes with decreased H3K4Me3 at their promoters are listed in categories (Figure 3.15 B).

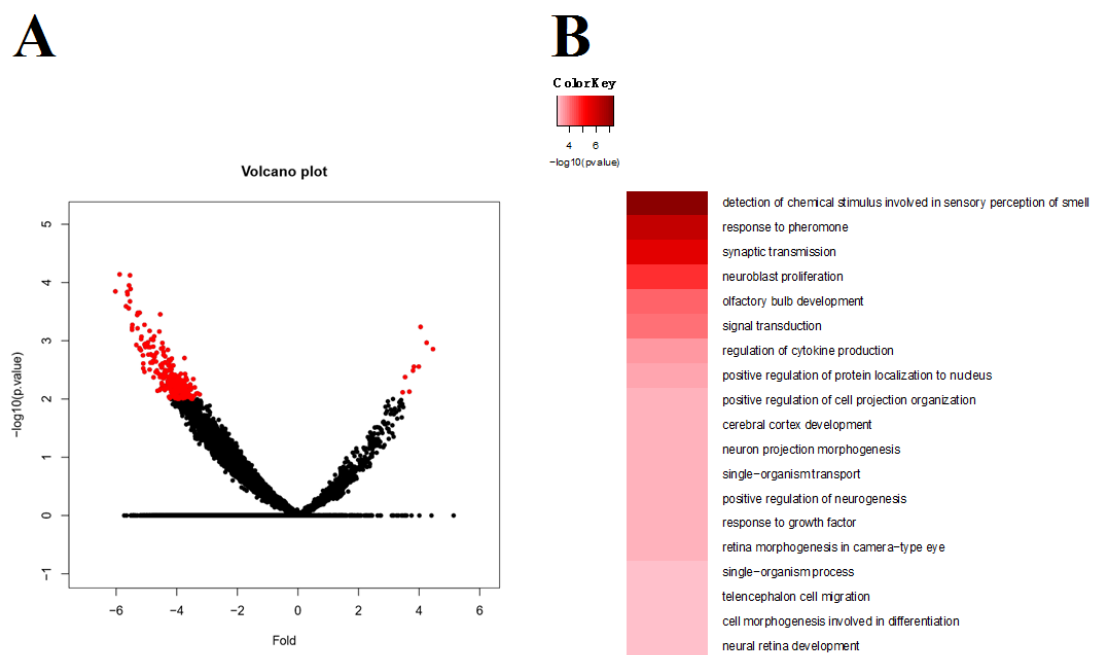


Figure 3.15. H3K4Me3 level is decreased at the promoter areas of many genes in hippocampal CA3 PCs of 6-month APP/PS1 mice.

A. Volcano plot of ChIP-Seq results displaying H3K4Me3 levels at promoters of various genes in APP/PS1 mice (n=4) compared to WT littermates (n=4). Red dots represent differential binding. To the left side are the numerous gene promoters with low H3K4Me3 levels, and to the right side are few gene promoters with high H3K4Me3 levels. **B.** Pathway analysis of genes with decreased H3K4Me3 at their promoters.

It is worth noticing that the most affected pathways are mainly involved in neuronal proliferation and function/development of olfactory bulb. This indirectly confirmed that adult neurogenesis could be impaired in 6-month APP/PS1 mice, which have been shown in many AD models. Especially, one study showed that hippocampal neurogenesis is dramatically impaired in 6-month APP^{swe}/PS1^{dE9} mice. To be more

specific, the late survival of newborn cells 4-6 weeks later is significantly diminished (Verret et al., 2007). Additional evidence is still needed to confirm whether newborn granule neurons are actively killed by A β , or are unable to survive because of changes in the brain associated with A β overexpression.

However, a closer look at the down-regulated genes with decreased H3K4Me3 levels showed that they were not overlapping much with the down-regulated genes from RNA-seq result. For this we even chose a more tolerant cut-off for the RNA-seq data to include more genes. Still, we detected only one gene which showed both low expression in RNA-seq and low H3K4Me3 levels at the promoter area, which is Synpr (synaptoporin) (Figure 3.16). Synaptoporin is a synaptic vesicle protein that at first was found to be exclusively enriched in the granule cell axons, the mossy fibers in rat hippocampus (Grabs et al., 1994). Later studies showed that synaptoporin also colocalized well with GAD 65 (a marker for GABAergic terminals) in the mouse hippocampus, and further in situ hybridization combined with immunocytochemistry revealed that various subtypes of interneurons expressed synaptoporin, e.g. in 44.2% of PV+ interneurons, 59.9% of VIP+ interneurons and 38.6% of CCK+ interneurons (Singec et al., 2002). Therefore, a reduction in synaptoporin expression might implicate that the activities of inhibitory synapses in the hippocampal CA3 area in APP/PS1 mice could be impaired, which coincides with our electrophysiological findings.

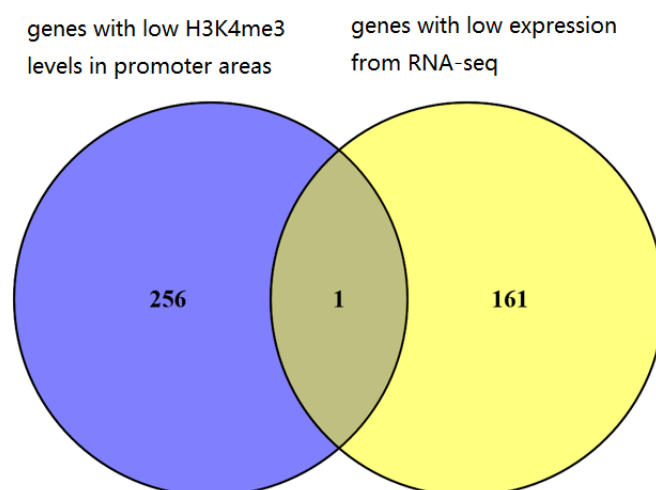


Figure 3.16. Down-regulated genes from RNA-seq and ChIP-seq in APP/PS1 mice.

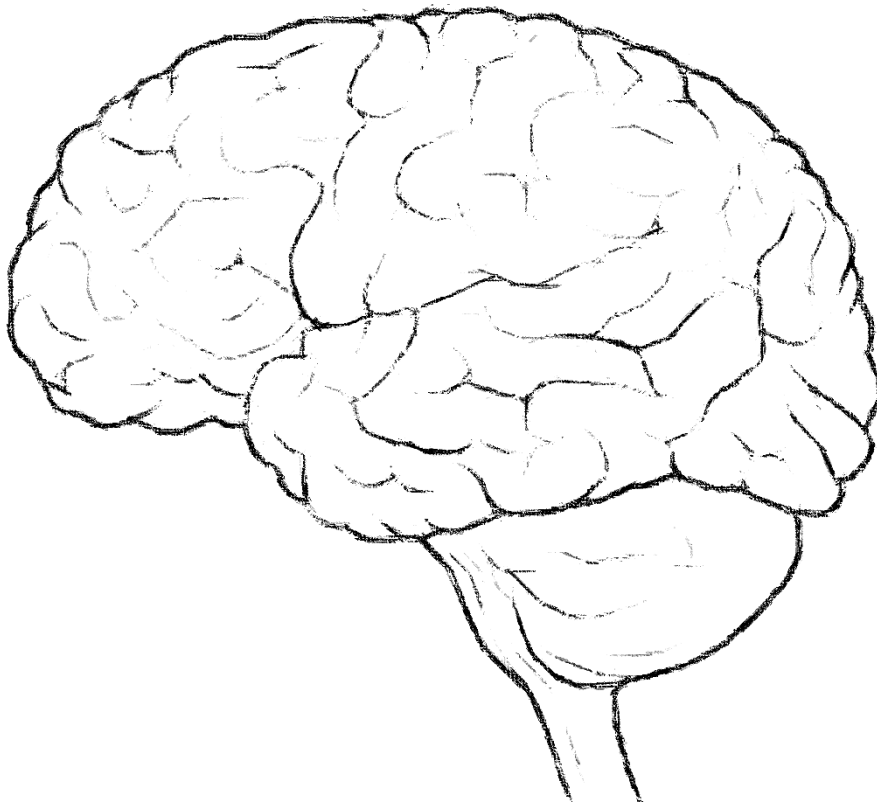
Venn diagram depicting down-regulated genes from RNA-seq (shown in yellow) and gene promoters with decreased H3K4me3 from ChIP-seq (shown in purple) and their overlap, in CA3 region of 6-month-old APP/PS1 mice. Note that RNA-seq was performed from whole CA3 tissue and ChIP-seq was performed from sorted neuronal nuclei.

A fact needs to be taken into consideration is that the RNA-seq was done from whole CA3 tissue whereas the ChIP-seq was performed from sorted CA3 neuronal nuclei. This indicates that the RNA-seq result might include a considerable portion from glia cells in CA3 region, thus can be quite different from the expression profile obtained from ChIP-seq. However, the more plausible explanation is that H3K4Me3 is only one of many epigenetic markers, and other epigenetic mechanisms may play more important role in the down-regulation of genes in early AD mice.

Nevertheless, these results confirmed that H3K4Me3 plays a key role in regulating gene expressions in neurons of hippocampal CA3 region, and H3K4Me3 level was significantly decreased at the promoter areas of many genes in 6-month male APP/PS1 mice.

CHAPTER 4

DISCUSSION



4 Discussion

4.1 CA3 circuits deficits in early AD mouse models

Growing evidence indicates that synaptic loss and dysfunction, accompanied by neural network alterations, may be the major cause of cognitive impairments in AD (Canter et al., 2016; Selkoe, 2002). Even at the early stage of AD and still free of A β plaques, the synaptic function can be already altered by abnormal amyloid metabolism (Cleary et al., 2005; Haass & Selkoe, 2007; Klyubin, Cullen, Hu, & Rowan, 2012; Lesne et al., 2006; Shankar et al., 2007; Tanzi, 2005). Therefore, it is important to explore which aspects of synaptic physiology and plasticity is particularly impaired in early AD, especially at circuits involved in memory encoding and retrieval.

The project of this thesis focused on CA3 circuits which is thought to be key for the initial stages of episodic memory encoding and recall (Kesner et al., 2016; Rebola et al., 2017). Previous work of our team has identified marked changes in synaptic plasticity at CA3-CA3 synapses in 6-month APP/PS1 mice (Viana da Silva et al., 2016). We set out to explore whether pre- and postsynaptic properties of the other major glutamatergic input to CA3 PCs, the Mf-CA3 synapses, were equally impaired in 6-month APP/PS1 mice. Additionally, we also investigated potential alterations in GABAergic synaptic transmissions onto CA3 PCs.

4.1.1 Unaltered presynaptic features and loss of LTP of NMDARs

at Mf-CA3 synapses

In line with our observation that the morphology of Mf terminals is unaltered in 6-month APP/PS1 mice, we registered no difference in presynaptic functional parameters, such as different forms of presynaptic release properties, short-term facilitation, and the characteristic presynaptic form of LTP expressed by MfB. While on the postsynaptic sites, we found no difference in the morphological features of thorny excrescences on CA3 PCs dendrites in APP/PS1 mice; likewise, glutamatergic transmission at Mf-CA3 synapses in terms of miniature and evoked EPSC amplitudes also seemed unaltered.

However, we observed that postsynaptic LTP of NMDARs was markedly impaired in 6-month APP/PS1 mice. This encouraged us to further investigate possible alterations in the number/composition/conductance of NMDARs. In contrast with some publications that describe an alteration of the ratio between NMDAR and AMPAR in models of AD (Cisse et al., 2011; Roberson et al., 2011), and some other in-vitro studies that implicate GluN2B-containing NMDARs as particular mediators of neuronal damage in AD (Cui et al., 2013; Ferreira et al., 2012; Hu et al., 2009; Ronicke et al., 2011), we found no change in either NMDAR/AMPA ratio or NMDAR composition in terms of GluN2B component in the 6 months old APP/PS1 mice at Mf-CA3 synapses. Furthermore, this form of LTP of NMDARs depends on the co-activation of postsynaptic A_{2A}Rs and mGluR5 (Rebola et al., 2008). Previous work of our group has demonstrated that abolition of A/C fiber LTP in CA3 PCs in 6-month APP/PS1 mice was caused by activation of upregulated neuronal A_{2A}Rs (Viana da Silva et al., 2016). Our current results thus may seem at odd with the notion that A_{2A}Rs are upregulated in CA3 PCs of 6-months old APP/PS1 mice. Nevertheless, we cannot rule out that changes in the signaling pathways downstream of A_{2A}R activation are responsible for the loss of LTP of NMDARs at Mf-CA3 synapses, or in other words, that the lack of LTP of NMDARs might depend on the postsynaptic function as a whole. Moreover, it will be extremely interesting to examine whether the decreased NMDAR-LTP in the MF pathway is directly responsible for any cognitive impairment of APP/PS1 mice, because this would further extend our understanding of the functional role of this circuit in behavior.

Interestingly, although we observed no impairment in MF LTP (mainly mediated by AMPAR response), some different results have been shown for Tg2576 mice. Tg2576 mice is a widely used AD model harboring the human APP^{swe695} gene, exhibits early synaptic abnormalities starting around the age of 4-6 months and displays several neuropathological features of AD later in its life (D'Amelio et al., 2011; Jacobsen et al., 2006). Jung et al. found that the MF LTP (in terms of fEPSP potentiation) is significantly enhanced in 12-month Tg2576 mice (Jung et al., 2011), while Witton et al. recorded significantly reduced MF LTP in the same model by the age of 24 months (Witton et al., 2010). We cannot explain where the discrepancies come from, but one possibility is that the PS1 transgene in APP/PS1 mice might contribute to the LTP phenotypes at MF synapses.

In addition, we found unexpectedly a marked and selective alteration of the KAR component at Mf-CA3 synapses (see below). This indicates that alteration of

glutamatergic function at early stage of AD, even at the level of a single neuron is selective for the type of input and for the type of post-synaptic receptors.

4.1.2 Decreased GABAergic transmissions onto CA3 PCs

CA3 PCs receive diverse GABAergic inputs. The interneurons involved can be categorized as parvalbumin (PV)-positive, somatostatin (SOM)-positive, cholecystinin (CCK)-positive, vasoactive intestinal polypeptide (VIP)-positive, and other incompletely characterized interneurons, each located in defined layers of CA3 and innervating different segments of CA3 PCs dendrites (Freund & Katona, 2007; Hajos et al., 2004).

These interneurons actively influence CA3 circuit activities, in that they can control the spiking of CA3 PCs by regulating neuronal excitability, firing and synaptic integration (Hajos et al., 2013; Losonczy, Biro, & Nusser, 2004; Schlinghoff, Kali, Freund, Hajos, & Gulyas, 2014; Szabo, Papp, Mate, Szabo, & Hajos, 2014). For example, it was shown in organotypic slice cultures that a single AP in a DG granule cell leads to net inhibition in CA3 PCs through feedforward inhibition, and this can be shifted to excitation when the stimulation frequency increases to the 20–40 Hz range (Mori, Abegg, Gahwiler, & Gerber, 2004). In slice preparation, feedforward inhibition potently limits postsynaptic depolarization and burst firing of CA3 PCs (Torborg, Nakashiba, Tonegawa, & McBain, 2010). Recent studies from the lab have demonstrated that CA3 interneurons control spike transfer at hippocampal Mf synapses in vivo through both GABAA and GABAB receptors, with an optimum frequency of presynaptic activity at 10 Hz (Zucca et al., 2017). Altogether, presynaptic plasticity and feedforward inhibition define the temporal rules for efficient information transfer at DG–CA3 synaptic connections in the intact circuit (Zucca et al., 2017). In this work, I report that the spontaneous but not miniature IPSC frequency was significantly decreased. Inhibitory accumulative charges were also reduced during a 20Hz train stimulation protocol in 6-month APP/PS1 mice. These results suggest that the number of GABAergic connections of CA3 PCs may not be modified in general, but the presynaptic interneurons are giving less inputs to CA3 PCs. This change may be due to either alterations in the synaptic contacts between MfBs and local interneurons, or changes in the spiking activity of presynaptic CA3 interneuron. In line with our results, some studies have reported remodeling of GABAergic neurotransmission in the human AD brain (Fuhrer et al., 2017; Limon et al., 2012) and AD transgenic mouse models (Jo

et al., 2014; Wu et al., 2014). Especially, APP/PS1 mice were shown to display spontaneous seizures, which are believed to be associated with an imbalance in the excitatory/inhibitory function in the pathology of AD (Hazra et al., 2013; Ramos et al., 2006). In APP^{swe}PS1^{dE9} mice, Minkeviciene et al. found that as early as 3.5 month there was persistently decreased resting membrane potential and firing threshold in neocortical layer 2/3 pyramidal cells and dentate granule cells, leading to increased network excitability, and bath-applied A β (proto-)fibrils achieved similar effects in juvenile rodent brain (Minkeviciene et al., 2009). Moreover, in APP/PS1-L166P mice, it was shown that there are age-dependent concomitant changes in the GABAergic pathway in the APP/PS1 mice (Oyelami et al., 2016).

However, none of these studies above has pinpointed the specific subtypes of interneurons involved or other mechanisms underlying the altered GABAergic innervations. Intriguingly, Verret et al. recorded spontaneous epileptiform discharges in hAPP mice primarily during reduced gamma oscillatory activity. Because this oscillatory rhythm is generated by inhibitory parvalbumin (PV) neurons, they suspected that this network dysfunction arised from impaired PV cells. Supporting this hypothesis, hAPP mice and AD patients showed decreased levels of the interneuron-specific and PV cell-predominant voltage-gated sodium channel subunit Nav1.1. Restoring Nav1.1 levels in hAPP mice not only increased inhibitory synaptic activity and gamma oscillations, but also reduced hypersynchrony and memory deficits. This is consistent with the results from Donato et al., demonstrating that PV neurons are highly relevant in memory encoding and memory precision in healthy rodents (Donato et al., 2013; Donato et al., 2015). Thus, it would be very interesting to further explore the intrinsic properties and/or synaptic connections of PV⁺ interneurons in hippocampal CA3 region.

4.1.3 Reduced KAR-mediated EPSCs in CA3 PCs

While AMPARs and NMDARs mediate most of basal excitatory synaptic transmission, KARs also play distinct roles in regulating the activity of CA3 circuits. KARs are abundantly present in the stratum lucidum of the CA3 region, both pre- and postsynaptically at Mf synapses (Darstein et al., 2003; Ruiz et al., 2005). The analysis of KAR knockout mice has provided us information about the potential role of KARs in hippocampus-dependent memory (Carta, Fievre, Gorlewicz, & Mulle, 2014). For instance, GluK4 KO mice exhibit moderate deficits in spatial memory acquisition and recall but not in working memory tasks (Catches, Xu, & Contractor, 2012; Lowry,

Kruyer, Norris, Cederroth, & Strickland, 2013). GluK2 KO mice were impaired in contextual fear conditioning (Ko et al., 2005), but did not show any deficits in the Morris water maze (Mulle et al., 1998).

At postsynaptic sites, KARs are present at only a subset of glutamatergic synapses in CA3 PCs and in a subpopulation of interneurons, influencing the integrative features of synaptic transmission by mediating the slow component of postsynaptic EPSCs (Castillo et al., 1997; Mulle et al., 1998; Pinheiro et al., 2013). In this work, we showed for the first time that there is a robust reduction in KAR-mediated currents at MF-CA3 synapses in any model of AD. We propose that there may be dysfunctional KARs or less KARs at postsynaptic sites of MF-CA3 synapses. Whether extrasynaptic KARs are affected or not is still unclear.

The function of KARs at Mf synapses is further complicated by the presence of presynaptic KARs. Presynaptic KARs can be activated by a single AP, resulting in the facilitation of synaptic transmission in a few milliseconds range, which can be observed during pairs or trains of stimuli as well as during spike transmission (Sachidhanandam, Blanchet, Jeantet, Cho, & Mulle, 2009). In addition, presynaptic KARs also facilitate the induction of the presynaptic LTP at Mf-CA3 synapses (Contractor, Swanson, & Heinemann, 2001; Lauri et al., 2001; Pinheiro et al., 2007; Schmitz, Mellor, & Nicoll, 2001). However, we did not observe any change in the presynaptic short-term and long-term plasticity at the Mf-C3 synapses in APP/PS1 mice. Thus, for now we do not have a reason to suspect deficits of KARs on the presynaptic sites in this AD mouse model.

Intriguingly, a reduction of KAR-mediated EPSCs were also observed in conditional PS KO mice. Presenilin (PS) is the catalytic component of the γ -secretase complex, so its mutation can alter γ -secretase cleavage and promote the production of A β ₄₂ (Guo et al., 1999; Jankowsky et al., 2004). Apart from APP, N-cadherin (NCad) is also an important substrate of γ -secretase. NCads are synaptic adhesion proteins implicated in synapse formation and maturation (Basu, Taylor, & Williams, 2015). It has been shown previously by our group, that activation of NCad recruits GluK2 subunit to cadherin/catenin complexes, stabilizing KARs at the synaptic membrane (Coussen et al., 2002). Both overexpression of a dominant-negative form of NCad and knockdown of NCad in CA3 PCs could lead to a strong reduction in the amplitude of KAR-EPSCs, while the amplitude of AMPAR currents were not significantly reduced (Fievre et al., 2016). Our findings in APP/PS1 mice and PS KO mice suggest that the lack of normal NCad resulting from dysfunctional γ -secretase might underlie impaired recruitment of stabilization of KARs at MF-CA3 synapses.

Moreover, the impaired KAR-EPSCs and reduced GABAergic inputs in CA3 PCs might not be independent events, because there is also considerable expression of KARs in GABAergic interneurons in hippocampus. It has been shown that KAR agonists can activate presynaptic KARs, regulating GABAergic transmission onto CA1 pyramidal cells (Clarke et al., 1997; Rodriguez-Moreno & Lerma, 1998). In fact, low concentrations of kainate facilitate GABA release, whereas high concentrations of KAR agonists depress GABAergic synapses in CA1 region (Jiang, Xu, Nedergaard, & Kang, 2001). Kainate also increases GABAergic transmission between CA1 interneurons (Cossart et al., 2001; Mulle et al., 2000). However, we do not see any solid evidence of KARs activation by endogenous glutamate affecting GABAergic transmission. It will be interesting to study KARs expression and function in CA3 interneurons, or in Mf synapses onto these interneurons.

Finally, trains of high-frequency stimulation (50 stimuli at 25 Hz) can induce both NMDAR LTP and KAR LTD at Mf synapses, the latter depends on the activation of adenosine A_{2A} receptors (Chamberlain, Sadowski, Teles-Grilo Ruivo, Atherton, & Mellor, 2013; Rebola et al., 2008). Since we observed a loss of NMDAR LTP in APP/PS1 mice, it might be interesting to check if KAR LTD is affected or not. However, considering the significantly reduced amplitudes of KAR-EPSCs in APP/PS1 mice, it might be difficult to register a difference.

4.2 CA3 circuits modifications after contextual learning

Being at the entry level of hippocampal circuitry, the CA3 region of hippocampus is thought to be important for episodic memory encoding, especially at the initial stage of acquisition. However, the links between the plasticity of CA3 circuits and memory encoding are not well understood (Rebola et al., 2017).

Paired recordings revealed that Mf can innervate up to four different types of CA3 interneurons through projections to different districts of the CA3 PC arborization (Szabadics & Soltesz, 2009). These interneurons in the stratum lucidum innervated by filopodial or small en passant Mf synapses are the anatomical basis for feedforward inhibition of DG-CA3 circuits (Evstratova & Toth, 2014; Galvan, Cosgrove, & Barrionuevo, 2011; McBain, 2008; Torborg et al., 2010), which is thought to be closely related to episodic memory. Within hours, one-trial contextual fear conditioning and Morris water maze learning can lead to robust and reversible outgrowth of filopodia at Mf terminals that synapse onto PV-positive fast-spiking interneurons. This plasticity

has been proved to be crucial for the precision of contextual memory (Ruediger et al., 2011). The increased number of filopodia at Mf terminals is thought to enhance DG-CA3 feedforward inhibition, possibly by enhancing the signal-to-noise ratio and building a more salient representation of the context from the DG inputs. Further work is needed, since there are still open questions about the actual time point at which the new synaptic contacts become fully functional and are integrated into the CA3 circuits for memory encoding. Plus, the involvement of other types of interneurons than PV-expressing cells is not yet fully investigated.

In line with these results, we showed that the spontaneous IPSC frequency was increased 3 hours after CFC, and this increase disappeared 24 hours after the contextual learning. This implies that the feedforward inhibition onto CA3 PCs undergoes rapid and reversible strengthening after CFC. However, unlike Ruediger et al. (Ruediger, Spirig, Donato, & Caroni, 2012; Ruediger et al., 2011) have reported, we did not discover any changes in LMT filopodia numbers after CFC, suggesting the structural plasticity of MF synapses might already be at ceiling level before the contextual learning. This could be due to many reasons, for instance, the housing conditions of our animal facility, or the way we handled the subjects. Moreover, we observed increased sIPSCs but not mIPSCs, suggesting that probably not so many new functional inhibitory synapses were formed onto CA3 PCs rapidly after CFC in our experimental conditions, but the existing GABAergic connections were more active after learning.

However, a non-neglectable factor might be complicating the scenario, i.e. the mice were single-housed for one week before experiment at the age of 7 weeks. Social deprivation/isolation is a type of stress and can lead to reduced brain BDNF levels in adult C57BL/6J mice (Barry et al., 2012), reduced neurogenesis as well as poorer learning and memory performance in rodents (Famitafreshi et al., 2015). Particularly, some studies have shown that social isolation can alter the GABAergic activities in hippocampus. For example, male adult mice socially isolated for 4 weeks showed reductions in levels of allopregnanolone in hippocampal CA3 pyramidal neurons and DG granular cells (Agís-Balboa, Pinna, Kadriu, Costa, & Guidotti, 2007; Nin et al., 2011), while allopregnanolone being a GABA_A receptor active neurosteroid that facilitates the inhibitory actions of GABA and up-regulates BDNF in the adult mouse (Nin et al., 2011; Pinna, 2010). Although in our study, the mice were only single-housed for one week, we could not exclude the possibility that social isolation and stress might mask or exaggerate some changes in GABAergic circuits.

In addition, expression of immediate early genes in CA3 PCs can provide a link between behavioral experience and the molecular events that are necessary for memory encoding (Kubik, Miyashita, & Guzowski, 2007). We showed in this work that the C-Fos positive CA3 PCs were increased rapidly after CFC. However, other immediate early genes may serve as better labels for memory traces. For example, it has been shown that the activity-dependent transcription factor NPAS4 is selectively expressed in CA3 PCs after presentation of a novel context, and selective deletion of the gene encoding NPAS4 in CA3 impairs contextual fear conditioning (Ramamoorthi et al., 2011). Moreover, NPAS4 is also shown to be involved in the activity-dependent regulation of inhibitory synapse development (Lin et al., 2008). Therefore, it will be interesting to express fluorescent proteins or even channelrhodopsins under NPAS4 promoter, so that we can identify memory-related CA3 PCs to record from or manipulate. In this way, we may be able to deepen our understanding of CA3 circuits modifications after contextual learning.

4.3 Transcriptome changes in CA3 region in early AD

As we know, epigenetic markers are actively regulating gene expressions on a genomic level, both during learning in healthy subjects and in neuropathological situations. For example, histone-methyltransferase MLL2 (KMT2B) is shown to be essential for memory formation in mice (Kerimoglu et al., 2013); histone modification profile can be altered in AD mouse models, and systemic application of histone deacetylase inhibitor (HDACi) can rescue the memory deficits in these mice (Kilgore et al., 2010). In the same direction, we first performed RNA-seq with dissected CA3 tissue from APP/PS1 mice to screen for changes on a transcriptome level, and found a list of up- and down-regulated genes at this early stage of AD. Then we carried out ChIP-seq for a histone modification marker: H3K4me3, which has been shown to be directly related to one-trial contextual memory (Gupta et al., 2010), and we found that there was a concrete decrease in H3K4me3 levels at the promoter areas of various genes in CA3 PCs, especially those involved in neuronal proliferation. Adult neurogenesis is known to be very important for encoding new information (Leuner et al., 2006; Aimone et al., 2006). Our finding is yet another piece of evidence among reports of altered neurogenesis in various models of AD (Haughey et al., 2002; Jin et al., 2004; Dong et al., 2004; Donovan et al., 2006; Zhang et al., 2007). Especially, one study using the same AD model as our group showed that these mice have diminished new-born

neuronal survival in hippocampus but no change in overall cell proliferation, resulting in decreased number of newborn neurons in DG (Verret et al., 2007).

However, the down-regulated genes with low H3K4me3 marker are not overlapping much with the down-regulated genes from RNA-seq result, suggesting that other epigenetic mechanisms might play more important roles in expressing early deficits in this AD mouse model.

4.4 Perspectives

Our work mainly explored the pre- and postsynaptic features of hippocampal CA3 synapses in an AD mouse model. We showed that LTP of NMDARs is abolished at the Mf-CA3 synapses, GABAergic innervations of CA3 PCs is slightly reduced, and postsynaptic KARs in CA3 PCs shows a marked decrease in 6-months old APP/PS1 mice. Moreover, we showed that in CA3, at this early stage of AD, many transcriptional regulations are already taking place across the whole genome. Last but not least, we showed changes of GABAergic synaptic transmission in CA3 circuits rapidly after contextual fear conditioning, confirming its role in memory encoding.

As a next step, we would like to further explore the phenomenon of reduced KAR-mediated EPSCs at Mf-CA3 synapses. For example, it is important to know whether the reduced conductance of KARs is due to reduced number of functional KARs at the postsynaptic sites, or less KARs are present on cell membrane in general. To this end we can for instance wash in Kainate in the aCSF while record the KAR events from CA3 PCs. This can also be accompanied by immunohistochemistry staining of KARs in CA3 region as a confirmation.

In another direction, it will be also interesting to explore which subtypes of interneurons are mediating modifications in CA3 GABAergic transmission in AD models as well as in healthy subjects after learning. For this we might need genetically encoded fluorescent markers for interneurons, so that we can register their properties and connections with CA3 PCs. Of course, with all these data being collected from in vitro acute hippocampal slices, we would be interested to see some confirmation by in vivo electrophysiology studies from rather intact CA3 circuits.

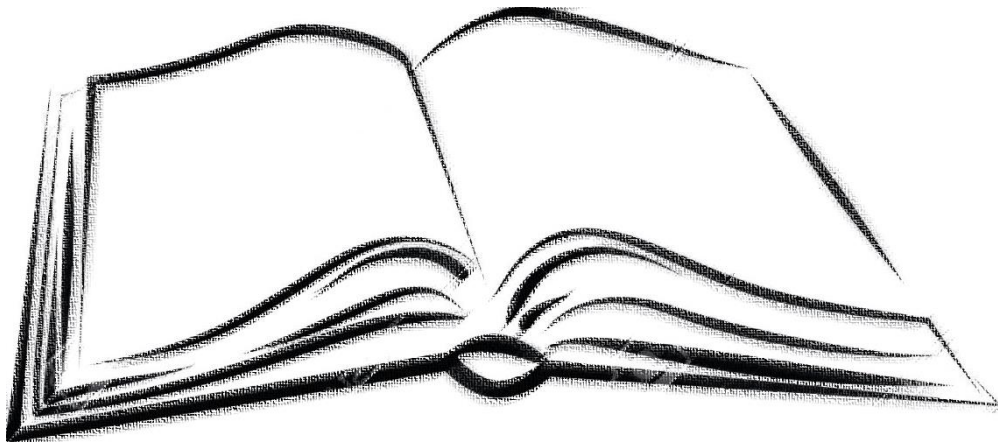
Overall, CA3 circuits are worth studying in that they have all the anatomical and functional attributes to serve in the rapid encoding of episodic memory, and are also among the first targets to be impaired when early AD pathologies occur. Hopefully these experiments provide novel insights into synaptic dysfunction differentially

Discussion

expressed at specific inputs onto a single CA3 PC at an early stage of AD, and contribute to the understanding of the circuits and mechanisms underlying contextual memory encoding.

CHAPTER 5

BIBLIOGRAPHY



5 Bibliography

5.1 Books

Alberts, B., Johnson, A., Lewis, J., Raff, M., Roberts, K., Walter, P. (2002). *Molecular Biology of the Cell* (4th ed.). New York: Garland Science. ISBN 978-0-8153-3218-3.

Anderson, P., Morris, R., Amaral, D., Bliss, T., O'Keefe, J. (2007) *The hippocampus book* (first ed.). New York: Oxford University Press. ISBN 978-0-19-510027-3.

Finger, S. (2005) *Minds Behind the Brain: A history of the pioneers and their discoveries*. Oxford Scholarship Online. ISBN-13: 9780195181821.

Hebb, D. O. (1949). *The Organization of Behavior: A Neuropsychological Theory*. New York: Wiley and Sons. ISBN 9780471367277.

Kazdin, A. E. (2000) *Encyclopedia of Psychology*. American Psychological Association. ISBN: 978-1-55798-187-5.

O'Keefe, J. & Nadel, L. (1978). *The Hippocampus as a Cognitive Map*. Oxford Univ. Press. ISBN 13: 9780198572060.

Ramón y Cajal S. (1899). *Textura del Sistema Nervioso del Hombre y de los Vertebrados*. Madrid: Moya. ISBN: 9788477539254.

Sherwood, L. (2015). *Human Physiology: From Cells to Systems*. Cengage Learning. ISBN 978-1-305-44551-2.

Spence, K.W., Spence, J.T. (1968). *The psychology of learning and motivation* (Volume 2). New York: Academic Press. ISBN 9780125433020.

Waddington, C. H. (1953). *The Epigenetics of Birds*. Cambridge University Press. (2014 edition). ISBN 978-1-107-44047-0.

5.2 References

- Acsady, L., Kamondi, A., Sik, A., Freund, T., & Buzsaki, G. (1998). GABAergic cells are the major postsynaptic targets of mossy fibers in the rat hippocampus. *J Neurosci*, *18*(9), 3386-3403.
- Aggleton, J. P., & Brown, M. W. (1999). Episodic memory, amnesia, and the hippocampal-anterior thalamic axis. *Behav Brain Sci*, *22*(3), 425-444; discussion 444-489.
- Agís-Balboa RC, Pinna G, Pibiri F, Kadriu B, Costa E, Guidotti A. (2007). Down-regulation of neurosteroid biosynthesis in corticolimbic circuits mediates social isolation-induced behavior in mice. *Proc Natl Acad Sci*, Nov 20;104(47):18736-41.
- Aimone JB, Wiles J, Gage FH. Potential role for adult neurogenesis in the encoding of time in new memories. *Nat Neurosci*. 2006; 9:723–727.
- Allinson, T. M., Parkin, E. T., Turner, A. J., & Hooper, N. M. (2003). ADAMs family members as amyloid precursor protein alpha-secretases. *J Neurosci Res*, *74*(3), 342-352. doi:10.1002/jnr.10737
- Amaral, D. G. (1978). A Golgi study of cell types in the hilar region of the hippocampus in the rat. *J Comp Neurol*, *182*(4 Pt 2), 851-914.
- Amaral, D. G., Ishizuka, N., & Claiborne, B. (1990). Neurons, numbers and the hippocampal network. *Prog Brain Res*, *83*, 1-11.
- Amaral, D. G., Scharfman, H. E., & Lavenex, P. (2007). The dentate gyrus: fundamental neuroanatomical organization (dentate gyrus for dummies). *Prog Brain Res*, *163*, 3-22. doi:10.1016/s0079-6123(07)63001-5
- Bagot, R. C., Zhang, T. Y., Wen, X., Nguyen, T. T., Nguyen, H. B., Diorio, J., . . . Meaney, M. J. (2012). Variations in postnatal maternal care and the epigenetic regulation of metabotropic glutamate receptor 1 expression and hippocampal function in the rat. *Proc Natl Acad Sci U S A*, *109* Suppl 2, 17200-17207. doi:10.1073/pnas.1204599109
- Ballard, C., Gauthier, S., Corbett, A., Brayne, C., Aarsland, D., & Jones, E. (2011). Alzheimer's disease. *Lancet*, *377*(9770), 1019-1031. doi:10.1016/s0140-6736(10)61349-9
- Barage, S. H., & Sonawane, K. D. (2015). Amyloid cascade hypothesis: Pathogenesis and therapeutic strategies in Alzheimer's disease. *Neuropeptides*, *52*, 1-18. doi:10.1016/j.npep.2015.06.008

- Barrera, L. O., Li, Z., Smith, A. D., Arden, K. C., Cavenee, W. K., Zhang, M. Q., . . . Ren, B. (2008). Genome-wide mapping and analysis of active promoters in mouse embryonic stem cells and adult organs. *Genome Res*, *18*(1), 46-59. doi:10.1101/gr.6654808
- Barski, A., Cuddapah, S., Cui, K., Roh, T. Y., Schones, D. E., Wang, Z., . . . Zhao, K. (2007). High-resolution profiling of histone methylations in the human genome. *Cell*, *129*(4), 823-837. doi:10.1016/j.cell.2007.05.009
- Basu, R., Taylor, M. R., & Williams, M. E. (2015). The classic cadherins in synaptic specificity. *Cell Adh Migr*, *9*(3), 193-201. doi:10.1080/19336918.2014.1000072
- Bauer, U. M., Daujat, S., Nielsen, S. J., Nightingale, K., & Kouzarides, T. (2002). Methylation at arginine 17 of histone H3 is linked to gene activation. *EMBO Rep*, *3*(1), 39-44. doi:10.1093/embo-reports/kvf013
- Ben-Ari, Y. (2002). Excitatory actions of gaba during development: the nature of the nurture. *Nat Rev Neurosci*, *3*(9), 728-739. doi:10.1038/nrn920
- Benjamin, J. S., Pilarowski, G. O., Carosso, G. A., Zhang, L., Huso, D. L., Goff, L. A., . . . Bjornsson, H. T. (2017). A ketogenic diet rescues hippocampal memory defects in a mouse model of Kabuki syndrome. *Proc Natl Acad Sci U S A*, *114*(1), 125-130. doi:10.1073/pnas.1611431114
- Bennett, M. V. (2000). Electrical synapses, a personal perspective (or history). *Brain Res Brain Res Rev*, *32*(1), 16-28.
- Berchtold, N. C., & Cotman, C. W. (1998). Evolution in the conceptualization of dementia and Alzheimer's disease: Greco-Roman period to the 1960s. *Neurobiol Aging*, *19*(3), 173-189.
- Bernander, O., Douglas, R. J., Martin, K. A., & Koch, C. (1991). Synaptic background activity influences spatiotemporal integration in single pyramidal cells. *Proc Natl Acad Sci U S A*, *88*(24), 11569-11573.
- Bernardo, A., Harrison, F. E., McCord, M., Zhao, J., Bruchey, A., Davies, S. S., . . . McDonald, M. P. (2009). Elimination of GD3 synthase improves memory and reduces amyloid-beta plaque load in transgenic mice. *Neurobiol Aging*, *30*(11), 1777-1791. doi:10.1016/j.neurobiolaging.2007.12.022
- Berridge, M. J. (1998). Neuronal calcium signaling. *Neuron*, *21*(1), 13-26.
- Berry A, Bellisario V, Capoccia S, Tirassa P, Calza A, Alleva E, Cirulli F. (2012). Social deprivation stress is a triggering factor for the emergence of anxiety- and depression-like behaviours and leads to reduced brain BDNF levels in C57BL/6J mice. *Psychoneuroendocrinology*, *37*:762–772. DOI: 10.1016/j.psyneuen.2011.09.007

Bibliography

- Bird, C. M., & Burgess, N. (2008). The hippocampus and memory: insights from spatial processing. *Nat Rev Neurosci*, 9(3), 182-194. doi:10.1038/nrn2335
- Blackstad, T. W. (1956). Commissural connections of the hippocampal region in the rat, with special reference to their mode of termination. *J Comp Neurol*, 105(3), 417-537.
- Blackstad, T. W., Brink, K., Hem, J., & Jeune, B. (1970). Distribution of hippocampal mossy fibers in the rat. An experimental study with silver impregnation methods. *J Comp Neurol*, 138(4), 433-449. doi:10.1002/cne.901380404
- Blackstad, T. W., & Kjaerheim, A. (1961). Special axo-dendritic synapses in the hippocampal cortex: electron and light microscopic studies on the layer of mossy fibers. *J Comp Neurol*, 117, 133-159.
- Bleakman, D., & Lodge, D. (1998). Neuropharmacology of AMPA and kainate receptors. *Neuropharmacology*, 37(10-11), 1187-1204.
- Blennow, K., de Leon, M. J., & Zetterberg, H. (2006). Alzheimer's disease. *Lancet*, 368(9533), 387-403. doi:10.1016/s0140-6736(06)69113-7
- Borchelt, D. R., Davis, J., Fischer, M., Lee, M. K., Slunt, H. H., Ratovitsky, T., . . . Price, D. L. (1996). A vector for expressing foreign genes in the brains and hearts of transgenic mice. *Genet Anal*, 13(6), 159-163.
- Borchelt, D. R., Ratovitski, T., van Lare, J., Lee, M. K., Gonzales, V., Jenkins, N. A., . . . Sisodia, S. S. (1997). Accelerated amyloid deposition in the brains of transgenic mice coexpressing mutant presenilin 1 and amyloid precursor proteins. *Neuron*, 19(4), 939-945.
- Bragin A, Csicsvari J, Penttonen M, Buzsaki G. (1997). Epileptic afterdischarge in the hippocampal-entorhinal system: current source density and unit studies. *Neuroscience*, 76:1187–1203.
- Bruzzone, R., Hormuzdi, S. G., Barbe, M. T., Herb, A., & Monyer, H. (2003). Pannexins, a family of gap junction proteins expressed in brain. *Proc Natl Acad Sci U S A*, 100(23), 13644-13649. doi:10.1073/pnas.2233464100
- Burns, A. (1992). Psychiatric phenomena in dementia of the Alzheimer type. *Int Psychogeriatr*, 4 Suppl 1, 43-54.
- Burns, A., & Iliffe, S. (2009). Alzheimer's disease. *Bmj*, 338, b158. doi:10.1136/bmj.b158
- Buxbaum, J. D., Christensen, J. L., Ruefli, A. A., Greengard, P., & Loring, J. F. (1993). Expression of APP in brains of transgenic mice containing the entire human APP gene. *Biochem Biophys Res Commun*, 197(2), 639-645.

doi:10.1006/bbrc.1993.2527

- Cabrejo, L., Guyant-Marechal, L., Laquerriere, A., Vercelletto, M., De la Fourniere, F., Thomas-Anterion, C., . . . Hannequin, D. (2006). Phenotype associated with APP duplication in five families. *Brain*, *129*(Pt 11), 2966-2976. doi:10.1093/brain/awl237
- Canter, R. G., Penney, J., & Tsai, L. H. (2016). The road to restoring neural circuits for the treatment of Alzheimer's disease. *Nature*, *539*(7628), 187-196. doi:10.1038/nature20412
- Cao, D., Lu, H., Lewis, T. L., & Li, L. (2007). Intake of sucrose-sweetened water induces insulin resistance and exacerbates memory deficits and amyloidosis in a transgenic mouse model of Alzheimer disease. *J Biol Chem*, *282*(50), 36275-36282. doi:10.1074/jbc.M703561200
- Caporale, N., & Dan, Y. (2008). Spike timing-dependent plasticity: a Hebbian learning rule. *Annu Rev Neurosci*, *31*, 25-46. doi:10.1146/annurev.neuro.31.060407.125639
- Carta, M., Fievre, S., Gorlewicz, A., & Mulle, C. (2014). Kainate receptors in the hippocampus. *Eur J Neurosci*, *39*(11), 1835-1844. doi:10.1111/ejn.12590
- Carta, M., Lanore, F., Rebola, N., Szabo, Z., Da Silva, S. V., Lourenco, J., . . . Mulle, C. (2014). Membrane lipids tune synaptic transmission by direct modulation of presynaptic potassium channels. *Neuron*, *81*(4), 787-799. doi:10.1016/j.neuron.2013.12.028
- Castillo, P. E., Malenka, R. C., & Nicoll, R. A. (1997). Kainate receptors mediate a slow postsynaptic current in hippocampal CA3 neurons. *Nature*, *388*(6638), 182-186. doi:10.1038/40645
- Catches, J. S., Xu, J., & Contractor, A. (2012). Genetic ablation of the GluK4 kainate receptor subunit causes anxiolytic and antidepressant-like behavior in mice. *Behav Brain Res*, *228*(2), 406-414. doi:10.1016/j.bbr.2011.12.026
- Chamberlain, S. E., Sadowski, J. H., Teles-Grilo Ruivo, L. M., Atherton, L. A., & Mellor, J. R. (2013). Long-term depression of synaptic kainate receptors reduces excitability by relieving inhibition of the slow afterhyperpolarization. *J Neurosci*, *33*(22), 9536-9545. doi:10.1523/jneurosci.0034-13.2013
- Chawla, M. K., Guzowski, J. F., Ramirez-Amaya, V., Lipa, P., Hoffman, K. L., Marriott, L. K., . . . Barnes, C. A. (2005). Sparse, environmentally selective expression of Arc RNA in the upper blade of the rodent fascia dentata by brief spatial experience. *Hippocampus*, *15*(5), 579-586. doi:10.1002/hipo.20091
- Chen, D., Ma, H., Hong, H., Koh, S. S., Huang, S. M., Schurter, B. T., . . . Stallcup, M.

Bibliography

- R. (1999). Regulation of transcription by a protein methyltransferase. *Science*, 284(5423), 2174-2177.
- Cheung, I., Shulha, H. P., Jiang, Y., Matevossian, A., Wang, J., Weng, Z., & Akbarian, S. (2010). Developmental regulation and individual differences of neuronal H3K4me3 epigenomes in the prefrontal cortex. *Proc Natl Acad Sci U S A*, 107(19), 8824-8829. doi:10.1073/pnas.1001702107
- Cisse, M., Halabisky, B., Harris, J., Devidze, N., Dubal, D. B., Sun, B., . . . Mucke, L. (2011). Reversing EphB2 depletion rescues cognitive functions in Alzheimer model. *Nature*, 469(7328), 47-52. doi:10.1038/nature09635
- Claiborne, B. J., Amaral, D. G., & Cowan, W. M. (1986). A light and electron microscopic analysis of the mossy fibers of the rat dentate gyrus. *J Comp Neurol*, 246(4), 435-458. doi:10.1002/cne.902460403
- Clarke, V. R., Ballyk, B. A., Hoo, K. H., Mandelzys, A., Pellizzari, A., Bath, C. P., . . . Bleakman, D. (1997). A hippocampal GluR5 kainate receptor regulating inhibitory synaptic transmission. *Nature*, 389(6651), 599-603. doi:10.1038/39315
- Clayton, N. S., & Russell, J. (2009). Looking for episodic memory in animals and young children: prospects for a new minimalism. *Neuropsychologia*, 47(11), 2330-2340. doi:10.1016/j.neuropsychologia.2008.10.011
- Cleary, J. P., Walsh, D. M., Hofmeister, J. J., Shankar, G. M., Kuskowski, M. A., Selkoe, D. J., & Ashe, K. H. (2005). Natural oligomers of the amyloid-beta protein specifically disrupt cognitive function. *Nat Neurosci*, 8(1), 79-84. doi:10.1038/nn1372
- Cohen, N. J., Poldrack, R. A., & Eichenbaum, H. (1997). Memory for items and memory for relations in the procedural/declarative memory framework. *Memory*, 5(1-2), 131-178. doi:10.1080/741941149
- Collingridge, G. L., Peineau, S., Howland, J. G., & Wang, Y. T. (2010). Long-term depression in the CNS. *Nat Rev Neurosci*, 11(7), 459-473. doi:10.1038/nrn2867
- Conn, P. J., & Pin, J. P. (1997). Pharmacology and functions of metabotropic glutamate receptors. *Annu Rev Pharmacol Toxicol*, 37, 205-237. doi:10.1146/annurev.pharmtox.37.1.205
- Contractor, A., Swanson, G., & Heinemann, S. F. (2001). Kainate receptors are involved in short- and long-term plasticity at mossy fiber synapses in the hippocampus. *Neuron*, 29(1), 209-216.
- Cossart, R., Tyzio, R., Dinocourt, C., Esclapez, M., Hirsch, J. C., Ben-Ari, Y., & Bernard, C. (2001). Presynaptic kainate receptors that enhance the release of

- GABA on CA1 hippocampal interneurons. *Neuron*, 29(2), 497-508.
- Coussen, F., Normand, E., Marchal, C., Costet, P., Choquet, D., Lambert, M., . . . Mulle, C. (2002). Recruitment of the kainate receptor subunit glutamate receptor 6 by cadherin/catenin complexes. *J Neurosci*, 22(15), 6426-6436. doi:20026623
- Cramer, P. E., Cirrito, J. R., Wesson, D. W., Lee, C. Y., Karlo, J. C., Zinn, A. E., . . . Landreth, G. E. (2012). ApoE-directed therapeutics rapidly clear beta-amyloid and reverse deficits in AD mouse models. *Science*, 335(6075), 1503-1506. doi:10.1126/science.1217697
- Crusio, W. E., Genthner-Grimm, G., & Schwegler, H. (2007). A quantitative-genetic analysis of hippocampal variation in the mouse. *J Neurogenet*, 21(4), 197-208. doi:10.1080/01677060701715827
- Crusio, W. E., & Schwegler, H. (2005). Learning spatial orientation tasks in the radial-maze and structural variation in the hippocampus in inbred mice. *Behav Brain Funct*, 1(1), 3. doi:10.1186/1744-9081-1-3
- Cui, Z., Feng, R., Jacobs, S., Duan, Y., Wang, H., Cao, X., & Tsien, J. Z. (2013). Increased NR2A:NR2B ratio compresses long-term depression range and constrains long-term memory. *Sci Rep*, 3, 1036. doi:10.1038/srep01036
- D'Amelio M, Cavallucci V, Middei S, Marchetti C, Pacioni S, Ferri A, Diamantini A, De Zio D, Carrara P, Battistini L, Moreno S, Bacci A, Ammassari-Teule M, Marie H, Cecconi F. (2011). Caspase-3 triggers early synaptic dysfunction in a mouse model of Alzheimer's disease. *Nat Neurosci*, Jan;14(1):69-76. doi: 10.1038/nn.2709.
- Dan, Y., & Poo, M. M. (2006). Spike timing-dependent plasticity: from synapse to perception. *Physiol Rev*, 86(3), 1033-1048. doi:10.1152/physrev.00030.2005
- Darstein, M., Petralia, R. S., Swanson, G. T., Wenthold, R. J., & Heinemann, S. F. (2003). Distribution of kainate receptor subunits at hippocampal mossy fiber synapses. *J Neurosci*, 23(22), 8013-8019.
- Daumas, S., Ceccom, J., Halley, H., Frances, B., & Lassalle, J. M. (2009). Activation of metabotropic glutamate receptor type 2/3 supports the involvement of the hippocampal mossy fiber pathway on contextual fear memory consolidation. *Learn Mem*, 16(8), 504-507. doi:10.1101/lm.1418309
- de Jong, A. P., Schmitz, S. K., Toonen, R. F., & Verhage, M. (2012). Dendritic position is a major determinant of presynaptic strength. *J Cell Biol*, 197(2), 327-337. doi:10.1083/jcb.201112135
- Di Lorenzo, A., & Bedford, M. T. (2011). Histone arginine methylation. *FEBS Lett*, 585(13), 2024-2031. doi:10.1016/j.febslet.2010.11.010

Bibliography

- Diana, R. A., Yonelinas, A. P., & Ranganath, C. (2007). Imaging recollection and familiarity in the medial temporal lobe: a three-component model. *Trends Cogn Sci, 11*(9), 379-386. doi:10.1016/j.tics.2007.08.001
- Ding, Y., Qiao, A., Wang, Z., Goodwin, J. S., Lee, E. S., Block, M. L., . . . Fan, G. H. (2008). Retinoic acid attenuates beta-amyloid deposition and rescues memory deficits in an Alzheimer's disease transgenic mouse model. *J Neurosci, 28*(45), 11622-11634. doi:10.1523/jneurosci.3153-08.2008
- Dingledine, R., Borges, K., Bowie, D., & Traynelis, S. F. (1999). The glutamate receptor ion channels. *Pharmacol Rev, 51*(1), 7-61.
- Dingledine, R., & Conn, P. J. (2000). Peripheral glutamate receptors: molecular biology and role in taste sensation. *J Nutr, 130*(4S Suppl), 1039s-1042s.
- Donato F, Chowdhury A, Lahr M, Caroni P. (2015). Early- and late-born parvalbumin basket cell subpopulations exhibiting distinct regulation and roles in learning. *Neuron, Feb 18;85*(4):770-86. doi: 10.1016/j.neuron.2015.01.011.
- Donato F, Rompani SB, Caroni P. (2013). Parvalbumin-expressing basket-cell network plasticity induced by experience regulates adult learning. *Nature, Dec 12;504*(7479):272-6. doi: 10.1038/nature12866.
- Dong H, Goico B, Martin M, Csernansky CA, Bertchume A, Csernansky JG. Modulation of hippocampal cell proliferation, memory, and amyloid plaque deposition in APPsw (Tg2576) mutant mice by isolation stress. *Neuroscience. 2004; 127*:601–609.
- Donovan MH, Yazdani U, Norris RD, Games D, German DC, Eisch AJ. Decreased adult hippocampal neurogenesis in the PDAPP mouse model of Alzheimer's disease. *J Comp Neurol. 2006; 495*:70–83.
- Dyrks, T., Dyrks, E., Masters, C. L., & Beyreuther, K. (1993). Amyloidogenicity of rodent and human beta A4 sequences. *FEBS Lett, 324*(2), 231-236.
- Eichenbaum, H. (1997). Declarative memory: insights from cognitive neurobiology. *Annu Rev Psychol, 48*, 547-572. doi:10.1146/annurev.psych.48.1.547
- Eichenbaum, H., Yonelinas, A. P., & Ranganath, C. (2007). The medial temporal lobe and recognition memory. *Annu Rev Neurosci, 30*, 123-152. doi:10.1146/annurev.neuro.30.051606.094328
- Evstratova, A., & Toth, K. (2014). Information processing and synaptic plasticity at hippocampal mossy fiber terminals. *Front Cell Neurosci, 8*, 28. doi:10.3389/fncel.2014.00028
- Famitafreshi H., Karimian M., Fanaei H., Attari F., Fatima S. (2015). Social isolation

- is associated with reduced neurogenesis, impaired spatial working memory performance and altered anxiety levels in male rats. *Open Access Anim. Physiol.* 7, 87–95. doi:10.2147/oaap.s84327
- Feldman, D. E. (2012). The spike-timing dependence of plasticity. *Neuron*, 75(4), 556-571. doi:10.1016/j.neuron.2012.08.001
- Fernandes, D., & Carvalho, A. L. (2016). Mechanisms of homeostatic plasticity in the excitatory synapse. *J Neurochem*, 139(6), 973-996. doi:10.1111/jnc.13687
- Ferreira, I. L., Bajouco, L. M., Mota, S. I., Auberson, Y. P., Oliveira, C. R., & Rego, A. C. (2012). Amyloid beta peptide 1-42 disturbs intracellular calcium homeostasis through activation of GluN2B-containing N-methyl-d-aspartate receptors in cortical cultures. *Cell Calcium*, 51(2), 95-106. doi:10.1016/j.ceca.2011.11.008
- Ferri, C. P., Prince, M., Brayne, C., Brodaty, H., Fratiglioni, L., Ganguli, M., . . . Sczufca, M. (2005). Global prevalence of dementia: a Delphi consensus study. *Lancet*, 366(9503), 2112-2117. doi:10.1016/s0140-6736(05)67889-0
- Fievre, S., Carta, M., Chamma, I., Labrousse, V., Thoumine, O., & Mulle, C. (2016). Molecular determinants for the strictly compartmentalized expression of kainate receptors in CA3 pyramidal cells. *Nat Commun*, 7, 12738. doi:10.1038/ncomms12738
- Fioravante, D., & Regehr, W. G. (2011). Short-term forms of presynaptic plasticity. *Curr Opin Neurobiol*, 21(2), 269-274. doi:10.1016/j.conb.2011.02.003
- Fisahn, A., Heinemann, S. F., & McBain, C. J. (2005). The kainate receptor subunit GluR6 mediates metabotropic regulation of the slow and medium AHP currents in mouse hippocampal neurones. *J Physiol*, 562(Pt 1), 199-203. doi:10.1113/jphysiol.2004.077412
- Fitts, P. M. (1992). The information capacity of the human motor system in controlling the amplitude of movement. 1954. *J Exp Psychol Gen*, 121(3), 262-269.
- Fortune, E. S., & Rose, G. J. (2001). Short-term synaptic plasticity as a temporal filter. *Trends Neurosci*, 24(7), 381-385.
- Franberg, J., Svensson, A. I., Winblad, B., Karlstrom, H., & Frykman, S. (2011). Minor contribution of presenilin 2 for gamma-secretase activity in mouse embryonic fibroblasts and adult mouse brain. *Biochem Biophys Res Commun*, 404(1), 564-568. doi:10.1016/j.bbrc.2010.12.029
- Francis, R., McGrath, G., Zhang, J., Ruddy, D. A., Sym, M., Apfeld, J., . . . Curtis, D. (2002). *aph-1* and *pen-2* are required for Notch pathway signaling, gamma-secretase cleavage of betaAPP, and presenilin protein accumulation. *Dev Cell*, 3(1), 85-97.

Bibliography

- Freund, T. F., & Katona, I. (2007). Perisomatic inhibition. *Neuron*, *56*(1), 33-42. doi:10.1016/j.neuron.2007.09.012
- Fuhrer, T. E., Palpagama, T. H., Waldvogel, H. J., Synek, B. J. L., Turner, C., Faull, R. L., & Kwakowsky, A. (2017). Impaired expression of GABA transporters in the human Alzheimer's disease hippocampus, subiculum, entorhinal cortex and superior temporal gyrus. *Neuroscience*, *351*, 108-118. doi:10.1016/j.neuroscience.2017.03.041
- Galvan, E. J., Cosgrove, K. E., & Barrionuevo, G. (2011). Multiple forms of long-term synaptic plasticity at hippocampal mossy fiber synapses on interneurons. *Neuropharmacology*, *60*(5), 740-747. doi:10.1016/j.neuropharm.2010.11.008
- Games, D., Adams, D., Alessandrini, R., Barbour, R., Berthelette, P., Blackwell, C., . . . et al. (1995). Alzheimer-type neuropathology in transgenic mice overexpressing V717F beta-amyloid precursor protein. *Nature*, *373*(6514), 523-527. doi:10.1038/373523a0
- Gewaltig, M. O., Diesmann, M., & Aertsen, A. (2001). Propagation of cortical synfire activity: survival probability in single trials and stability in the mean. *Neural Netw*, *14*(6-7), 657-673.
- Gloor, P., Salanova, V., Olivier, A., & Quesney, L. F. (1993). The human dorsal hippocampal commissure. An anatomically identifiable and functional pathway. *Brain*, *116* (Pt 5), 1249-1273.
- Gluck, M. A., & Granger, R. (1993). Computational models of the neural bases of learning and memory. *Annu Rev Neurosci*, *16*, 667-706. doi:10.1146/annurev.ne.16.030193.003315
- Gonzales, R. B., DeLeon Galvan, C. J., Rangel, Y. M., & Claiborne, B. J. (2001). Distribution of thorny excrescences on CA3 pyramidal neurons in the rat hippocampus. *J Comp Neurol*, *430*(3), 357-368.
- Goyal, R. K., & Chaudhury, A. (2013). Structure activity relationship of synaptic and junctional neurotransmission. *Auton Neurosci*, *176*(1-2), 11-31. doi:10.1016/j.autneu.2013.02.012
- Grabs D, Bergmann M, Schuster T, Fox PA, Brich M, Gratz M. (1994). Differential expression of synaptophysin and synaptoporin during pre- and postnatal development of the rat hippocampal network. *Eur J Neurosci*, *6*(11):1765-71.
- Granger, A. J., & Nicoll, R. A. (2014). Expression mechanisms underlying long-term potentiation: a postsynaptic view, 10 years on. *Philos Trans R Soc Lond B Biol Sci*, *369*(1633), 20130136. doi:10.1098/rstb.2013.0136
- Grewal, S. I., & Moazed, D. (2003). Heterochromatin and epigenetic control of gene

- expression. *Science*, 301(5634), 798-802. doi:10.1126/science.1086887
- Grilli, M. D., & Verfaellie, M. (2014). Personal semantic memory: insights from neuropsychological research on amnesia. *Neuropsychologia*, 61, 56-64. doi:10.1016/j.neuropsychologia.2014.06.012
- Guenther, M. G., Levine, S. S., Boyer, L. A., Jaenisch, R., & Young, R. A. (2007). A chromatin landmark and transcription initiation at most promoters in human cells. *Cell*, 130(1), 77-88. doi:10.1016/j.cell.2007.05.042
- Gundlfinger, A., Breustedt, J., Sullivan, D., & Schmitz, D. (2010). Natural spike trains trigger short- and long-lasting dynamics at hippocampal mossy fiber synapses in rodents. *PLoS One*, 5(4), e9961. doi:10.1371/journal.pone.0009961
- Guo, Q., Fu, W., Sopher, B. L., Miller, M. W., Ware, C. B., Martin, G. M., & Mattson, M. P. (1999). Increased vulnerability of hippocampal neurons to excitotoxic necrosis in presenilin-1 mutant knock-in mice. *Nat Med*, 5(1), 101-106. doi:10.1038/4789
- Gupta, S., Kim, S. Y., Artis, S., Molfese, D. L., Schumacher, A., Sweatt, J. D., . . . Lubin, F. D. (2010). Histone methylation regulates memory formation. *J Neurosci*, 30(10), 3589-3599. doi:10.1523/JNEUROSCI.3732-09.2010
- Haass, C., Hung, A. Y., Schlossmacher, M. G., Teplow, D. B., & Selkoe, D. J. (1993). beta-Amyloid peptide and a 3-kDa fragment are derived by distinct cellular mechanisms. *J Biol Chem*, 268(5), 3021-3024.
- Haass, C., Lemere, C. A., Capell, A., Citron, M., Seubert, P., Schenk, D., . . . Selkoe, D. J. (1995). The Swedish mutation causes early-onset Alzheimer's disease by beta-secretase cleavage within the secretory pathway. *Nat Med*, 1(12), 1291-1296.
- Haass, C., & Selkoe, D. J. (2007). Soluble protein oligomers in neurodegeneration: lessons from the Alzheimer's amyloid beta-peptide. *Nat Rev Mol Cell Biol*, 8(2), 101-112. doi:10.1038/nrm2101
- Hagena, H., & Manahan-Vaughan, D. (2011). Learning-facilitated synaptic plasticity at CA3 mossy fiber and commissural-associational synapses reveals different roles in information processing. *Cereb Cortex*, 21(11), 2442-2449. doi:10.1093/cercor/bhq271
- Hajos, N., Karlocai, M. R., Nemeth, B., Ulbert, I., Monyer, H., Szabo, G., . . . Gulyas, A. I. (2013). Input-output features of anatomically identified CA3 neurons during hippocampal sharp wave/ripple oscillation in vitro. *J Neurosci*, 33(28), 11677-11691. doi:10.1523/jneurosci.5729-12.2013
- Hajos, N., Palhalmi, J., Mann, E. O., Nemeth, B., Paulsen, O., & Freund, T. F. (2004). Spike timing of distinct types of GABAergic interneuron during hippocampal

- gamma oscillations in vitro. *J Neurosci*, 24(41), 9127-9137. doi:10.1523/jneurosci.2113-04.2004
- Harris, E. W., & Cotman, C. W. (1986). Long-term potentiation of guinea pig mossy fiber responses is not blocked by N-methyl D-aspartate antagonists. *Neurosci Lett*, 70(1), 132-137.
- Hasselmo, M. E., Wyble, B. P., & Wallenstein, G. V. (1996). Encoding and retrieval of episodic memories: role of cholinergic and GABAergic modulation in the hippocampus. *Hippocampus*, 6(6), 693-708. doi:10.1002/(SICI)1098-1063(1996)6:6<693::AID-HIPO12>3.0.CO;2-W
- Haughey NJ, Nath A, Chan SL, Borchard AC, Rao MS, Mattson MP. Disruption of neurogenesis by amyloid beta-peptide, and perturbed neural progenitor cell homeostasis, in models of Alzheimer's disease. *J Neurochem*. 2002; 83:1509–1524.
- Hazra, A., Gu, F., Aulakh, A., Berridge, C., Eriksen, J. L., & Ziburkus, J. (2013). Inhibitory neuron and hippocampal circuit dysfunction in an aged mouse model of Alzheimer's disease. *PLoS One*, 8(5), e64318. doi:10.1371/journal.pone.0064318
- Hendry, S. H., Schwark, H. D., Jones, E. G., & Yan, J. (1987). Numbers and proportions of GABA-immunoreactive neurons in different areas of monkey cerebral cortex. *J Neurosci*, 7(5), 1503-1519.
- Herreman, A., Hartmann, D., Annaert, W., Saftig, P., Craessaerts, K., Serneels, L., . . . De Strooper, B. (1999). Presenilin 2 deficiency causes a mild pulmonary phenotype and no changes in amyloid precursor protein processing but enhances the embryonic lethal phenotype of presenilin 1 deficiency. *Proc Natl Acad Sci U S A*, 96(21), 11872-11877.
- Hiratani, N., Teramae, J. N., & Fukai, T. (2012). Associative memory model with long-tail-distributed Hebbian synaptic connections. *Front Comput Neurosci*, 6, 102. doi:10.3389/fncom.2012.00102
- Hnasko, T. S., & Edwards, R. H. (2012). Neurotransmitter corelease: mechanism and physiological role. *Annu Rev Physiol*, 74, 225-243. doi:10.1146/annurev-physiol-020911-153315
- Holahan, M. R., Rekart, J. L., Sandoval, J., & Routtenberg, A. (2006). Spatial learning induces presynaptic structural remodeling in the hippocampal mossy fiber system of two rat strains. *Hippocampus*, 16(6), 560-570. doi:10.1002/hipo.20185
- Holcomb, L., Gordon, M. N., McGowan, E., Yu, X., Benkovic, S., Jantzen, P., . . . Duff,

- K. (1998). Accelerated Alzheimer-type phenotype in transgenic mice carrying both mutant amyloid precursor protein and presenilin 1 transgenes. *Nat Med*, 4(1), 97-100.
- Hollmann, M., & Heinemann, S. (1994). Cloned glutamate receptors. *Annu Rev Neurosci*, 17, 31-108. doi:10.1146/annurev.ne.17.030194.000335
- Holtmaat, A., Randall, J., & Cane, M. (2013). Optical imaging of structural and functional synaptic plasticity in vivo. *Eur J Pharmacol*, 719(1-3), 128-136. doi:10.1016/j.ejphar.2013.07.020
- Hsia, A. Y., Masliah, E., McConlogue, L., Yu, G. Q., Tatsuno, G., Hu, K., . . . Mucke, L. (1999). Plaque-independent disruption of neural circuits in Alzheimer's disease mouse models. *Proc Natl Acad Sci U S A*, 96(6), 3228-3233.
- Hsiao, K., Chapman, P., Nilsen, S., Eckman, C., Harigaya, Y., Younkin, S., . . . Cole, G. (1996). Correlative memory deficits, Abeta elevation, and amyloid plaques in transgenic mice. *Science*, 274(5284), 99-102.
- Hu, N. W., Klyubin, I., Anwyl, R., & Rowan, M. J. (2009). GluN2B subunit-containing NMDA receptor antagonists prevent Abeta-mediated synaptic plasticity disruption in vivo. *Proc Natl Acad Sci U S A*, 106(48), 20504-20509. doi:10.1073/pnas.0908083106
- Huijgen, J., & Samson, S. (2015). The hippocampus: A central node in a large-scale brain network for memory. *Rev Neurol (Paris)*, 171(3), 204-216. doi:10.1016/j.neurol.2015.01.557
- Hulme, S. R., Jones, O. D., & Abraham, W. C. (2013). Emerging roles of metaplasticity in behaviour and disease. *Trends Neurosci*, 36(6), 353-362. doi:10.1016/j.tins.2013.03.007
- Hunt, D. L., Puente, N., Grandes, P., & Castillo, P. E. (2013). Bidirectional NMDA receptor plasticity controls CA3 output and heterosynaptic metaplasticity. *Nat Neurosci*, 16(8), 1049-1059. doi:10.1038/nn.3461
- Iwase, S., Brookes, E., Agarwal, S., Badeaux, A. I., Ito, H., Vallianatos, C. N., . . . Shi, Y. (2016). A Mouse Model of X-linked Intellectual Disability Associated with Impaired Removal of Histone Methylation. *Cell Rep*, 14(5), 1000-1009. doi:10.1016/j.celrep.2015.12.091
- Jacobsen JS, Wu CC, Redwine JM, Comery TA, Arias R, Bowlby M, Martone R, Morrison JH, Pangalos MN, Reinhart PH, Bloom FE. (2006). Early-onset behavioral and synaptic deficits in a mouse model of Alzheimer's disease. *Proc Natl Acad Sci*, Mar 28;103(13):5161-6.
- Jang, H. J., & Kwag, J. (2012). GABAA receptor-mediated feedforward and feedback

- inhibition differentially modulate hippocampal spike timing-dependent plasticity. *Biochem Biophys Res Commun*, 427(3), 466-472. doi:10.1016/j.bbrc.2012.08.081
- Jankowsky, J. L., Fadale, D. J., Anderson, J., Xu, G. M., Gonzales, V., Jenkins, N. A., . . . Borchelt, D. R. (2004). Mutant presenilins specifically elevate the levels of the 42 residue beta-amyloid peptide in vivo: evidence for augmentation of a 42-specific gamma secretase. *Hum Mol Genet*, 13(2), 159-170. doi:10.1093/hmg/ddh019
- Jankowsky, J. L., Slunt, H. H., Ratovitski, T., Jenkins, N. A., Copeland, N. G., & Borchelt, D. R. (2001). Co-expression of multiple transgenes in mouse CNS: a comparison of strategies. *Biomol Eng*, 17(6), 157-165.
- Jarrett, J. T., Berger, E. P., & Lansbury, P. T., Jr. (1993). The carboxy terminus of the beta amyloid protein is critical for the seeding of amyloid formation: implications for the pathogenesis of Alzheimer's disease. *Biochemistry*, 32(18), 4693-4697.
- Jiang, L., Xu, J., Nedergaard, M., & Kang, J. (2001). A kainate receptor increases the efficacy of GABAergic synapses. *Neuron*, 30(2), 503-513.
- Jin K, Galvan V, Xie L, Mao XO, Gorostiza OF, Bredesen DE, Greenberg DA. Enhanced neurogenesis in Alzheimer's disease transgenic (PDGF-APP^{Sw}, Ind) mice. *Proc Natl Acad Sci USA*. 2004b; 101:13363–13367.
- Jo, S., Yarishkin, O., Hwang, Y. J., Chun, Y. E., Park, M., Woo, D. H., . . . Lee, C. J. (2014). GABA from reactive astrocytes impairs memory in mouse models of Alzheimer's disease. *Nat Med*, 20(8), 886-896. doi:10.1038/nm.3639
- Jung JH, An K, Kwon OB, Kim HS, Kim JH. (2011). Pathway-specific alteration of synaptic plasticity in Tg2576 mice. *Mol Cells*, Aug;32(2):197-201. doi: 10.1007/s10059-011-0077-8.
- Justin, N., De Marco, V., Aasland, R., & Gamblin, S. J. (2010). Reading, writing and editing methylated lysines on histone tails: new insights from recent structural studies. *Curr Opin Struct Biol*, 20(6), 730-738. doi:10.1016/j.sbi.2010.09.012
- Kaifosh, P., & Losonczy, A. (2016). Mnemonic Functions for Nonlinear Dendritic Integration in Hippocampal Pyramidal Circuits. *Neuron*, 90(3), 622-634. doi:10.1016/j.neuron.2016.03.019
- Kano, S., Colantuoni, C., Han, F., Zhou, Z., Yuan, Q., Wilson, A., . . . Sawa, A. (2013). Genome-wide profiling of multiple histone methylations in olfactory cells: further implications for cellular susceptibility to oxidative stress in schizophrenia. *Mol Psychiatry*, 18(7), 740-742. doi:10.1038/mp.2012.120

- Kauer, J. A., & Malenka, R. C. (2007). Synaptic plasticity and addiction. *Nat Rev Neurosci*, 8(11), 844-858. doi:10.1038/nrn2234
- Kerimoglu, C., Agis-Balboa, R. C., Kranz, A., Stilling, R., Bahari-Javan, S., Benito-Garagorri, E., . . . Fischer, A. (2013). Histone-methyltransferase MLL2 (KMT2B) is required for memory formation in mice. *J Neurosci*, 33(8), 3452-3464. doi:10.1523/jneurosci.3356-12.2013
- Kesner, R. P., Kirk, R. A., Yu, Z., Polansky, C., & Musso, N. D. (2016). Dentate gyrus supports slope recognition memory, shades of grey-context pattern separation and recognition memory, and CA3 supports pattern completion for object memory. *Neurobiol Learn Mem*, 129, 29-37. doi:10.1016/j.nlm.2015.08.010
- Kilgore, M., Miller, C. A., Fass, D. M., Hennig, K. M., Haggarty, S. J., Sweatt, J. D., & Rumbaugh, G. (2010). Inhibitors of class 1 histone deacetylases reverse contextual memory deficits in a mouse model of Alzheimer's disease. *Neuropsychopharmacology*, 35(4), 870-880. doi:10.1038/npp.2009.197
- Kim, T. K., Lee, J. E., Park, S. K., Lee, K. W., Seo, J. S., Im, J. Y., . . . Han, P. L. (2012). Analysis of differential plaque depositions in the brains of Tg2576 and Tg-APP^{swe}/PS1^{dE9} transgenic mouse models of Alzheimer disease. *Exp Mol Med*, 44(8), 492-502. doi:10.3858/emm.2012.44.8.056
- Kitazawa, M., Medeiros, R., & Laferla, F. M. (2012). Transgenic mouse models of Alzheimer disease: developing a better model as a tool for therapeutic interventions. *Curr Pharm Des*, 18(8), 1131-1147.
- Kleckner, N. W., & Dingledine, R. (1988). Requirement for glycine in activation of NMDA-receptors expressed in *Xenopus* oocytes. *Science*, 241(4867), 835-837.
- Klyubin, I., Cullen, W. K., Hu, N. W., & Rowan, M. J. (2012). Alzheimer's disease Abeta assemblies mediating rapid disruption of synaptic plasticity and memory. *Mol Brain*, 5, 25. doi:10.1186/1756-6606-5-25
- Knafo, S., Venero, C., Merino-Serrais, P., Feraud-Espinosa, I., Gonzalez-Soriano, J., Ferrer, I., . . . DeFelipe, J. (2009). Morphological alterations to neurons of the amygdala and impaired fear conditioning in a transgenic mouse model of Alzheimer's disease. *J Pathol*, 219(1), 41-51. doi:10.1002/path.2565
- Ko, S., Zhao, M. G., Toyoda, H., Qiu, C. S., & Zhuo, M. (2005). Altered behavioral responses to noxious stimuli and fear in glutamate receptor 5 (GluR5)- or GluR6-deficient mice. *J Neurosci*, 25(4), 977-984. doi:10.1523/jneurosci.4059-04.2005
- Kobayashi, K., & Poo, M. M. (2004). Spike train timing-dependent associative modification of hippocampal CA3 recurrent synapses by mossy fibers. *Neuron*,

41(3), 445-454.

- Kojro, E., & Fahrenholz, F. (2005). The non-amyloidogenic pathway: structure and function of alpha-secretases. *Subcell Biochem*, 38, 105-127.
- Korol, D. L., Abel, T. W., Church, L. T., Barnes, C. A., & McNaughton, B. L. (1993). Hippocampal synaptic enhancement and spatial learning in the Morris swim task. *Hippocampus*, 3(2), 127-132. doi:10.1002/hipo.450030204
- Kouzarides, T. (2007). Chromatin modifications and their function. *Cell*, 128(4), 693-705. doi:10.1016/j.cell.2007.02.005
- Kubik, S., Miyashita, T., & Guzowski, J. F. (2007). Using immediate-early genes to map hippocampal subregional functions. *Learn Mem*, 14(11), 758-770. doi:10.1101/lm.698107
- Kwon, H. B., & Castillo, P. E. (2008). Role of glutamate autoreceptors at hippocampal mossy fiber synapses. *Neuron*, 60(6), 1082-1094. doi:10.1016/j.neuron.2008.10.045
- Laatsch, R. H., & Cowan, W. M. (1966). Electron microscopic studies of the dentate gyrus of the rat. I. Normal structure with special reference to synaptic organization. *J Comp Neurol*, 128(3), 359-395. doi:10.1002/cne.901280305
- Lamb, B. T., Sisodia, S. S., Lawler, A. M., Slunt, H. H., Kitt, C. A., Kearns, W. G., . . . Gearhart, J. D. (1993). Introduction and expression of the 400 kilobase amyloid precursor protein gene in transgenic mice [corrected]. *Nat Genet*, 5(1), 22-30. doi:10.1038/ng0993-22
- Lassalle, J. M., Bataille, T., & Halley, H. (2000). Reversible inactivation of the hippocampal mossy fiber synapses in mice impairs spatial learning, but neither consolidation nor memory retrieval, in the Morris navigation task. *Neurobiol Learn Mem*, 73(3), 243-257. doi:10.1006/nlme.1999.3931
- Lauri, S. E., Delany, C., VR, J. C., Bortolotto, Z. A., Ornstein, P. L., J, T. R. I., & Collingridge, G. L. (2001). Synaptic activation of a presynaptic kainate receptor facilitates AMPA receptor-mediated synaptic transmission at hippocampal mossy fibre synapses. *Neuropharmacology*, 41(8), 907-915.
- Lawrence JJ, McBain CJ. (2003). Interneuron diversity series: containing the detonation--feedforward inhibition in the CA3 hippocampus. *Trends Neurosci.*, 26:631-640.
- Le Duigou, C., Simonnet, J., Telenczuk, M. T., Fricker, D., & Miles, R. (2014). Recurrent synapses and circuits in the CA3 region of the hippocampus: an associative network. *Front Cell Neurosci*, 7, 262. doi:10.3389/fncel.2013.00262

- Lee, K. J., Queenan, B. N., Rozeboom, A. M., Bellmore, R., Lim, S. T., Vicini, S., & Pak, D. T. (2013). Mossy fiber-CA3 synapses mediate homeostatic plasticity in mature hippocampal neurons. *Neuron*, 77(1), 99-114. doi:10.1016/j.neuron.2012.10.033
- Lee, M. K., Borchelt, D. R., Kim, G., Thinakaran, G., Slunt, H. H., Ratovitski, T., . . . Sisodia, S. S. (1997). Hyperaccumulation of FAD-linked presenilin 1 variants in vivo. *Nat Med*, 3(7), 756-760.
- Lerma, J. (2003). Roles and rules of kainate receptors in synaptic transmission. *Nat Rev Neurosci*, 4(6), 481-495. doi:10.1038/nrn1118
- Lesne, S., Koh, M. T., Kotilinek, L., Kaye, R., Glabe, C. G., Yang, A., . . . Ashe, K. H. (2006). A specific amyloid-beta protein assembly in the brain impairs memory. *Nature*, 440(7082), 352-357. doi:10.1038/nature04533
- Leuner B, Gould E, Shors TJ. Is there a link between adult neurogenesis and learning? *Hippocampus*. 2006; 16:216–224.
- Levitan, D., Lee, J., Song, L., Manning, R., Wong, G., Parker, E., & Zhang, L. (2001). PS1 N- and C-terminal fragments form a complex that functions in APP processing and Notch signaling. *Proc Natl Acad Sci U S A*, 98(21), 12186-12190. doi:10.1073/pnas.211321898
- Levy, W. B. (1996). A sequence predicting CA3 is a flexible associator that learns and uses context to solve hippocampal-like tasks. *Hippocampus*, 6(6), 579-590. doi:10.1002/(SICI)1098-1063(1996)6:6<579::AID-HIPO3>3.0.CO;2-C
- Li, B., Carey, M., & Workman, J. L. (2007). The role of chromatin during transcription. *Cell*, 128(4), 707-719. doi:10.1016/j.cell.2007.01.015
- Li, X. G., Somogyi, P., Ylinen, A., & Buzsáki, G. (1994). The hippocampal CA3 network: an in vivo intracellular labeling study. *J Comp Neurol*, 339(2), 181-208. doi:10.1002/cne.903390204
- Liaw, J. S., & Berger, T. W. (1996). Dynamic synapse: a new concept of neural representation and computation. *Hippocampus*, 6(6), 591-600. doi:10.1002/(SICI)1098-1063(1996)6:6<591::AID-HIPO4>3.0.CO;2-K
- Lieberman, D. N., & Mody, I. (1999). Properties of single NMDA receptor channels in human dentate gyrus granule cells. *J Physiol*, 518(Pt 1), 55-70.
- Limon, A., Reyes-Ruiz, J. M., & Miledi, R. (2012). Loss of functional GABA(A) receptors in the Alzheimer diseased brain. *Proc Natl Acad Sci U S A*, 109(25), 10071-10076. doi:10.1073/pnas.1204606109
- Lin, Y., Bloodgood, B. L., Hauser, J. L., Lapan, A. D., Koon, A. C., Kim, T. K., . . .

Bibliography

- Greenberg, M. E. (2008). Activity-dependent regulation of inhibitory synapse development by Npas4. *Nature*, 455(7217), 1198-1204. doi:10.1038/nature07319
- Ling, Y., Morgan, K., & Kalsheker, N. (2003). Amyloid precursor protein (APP) and the biology of proteolytic processing: relevance to Alzheimer's disease. *Int J Biochem Cell Biol*, 35(11), 1505-1535.
- Losonczy, A., Biro, A. A., & Nusser, Z. (2004). Persistently active cannabinoid receptors mute a subpopulation of hippocampal interneurons. *Proc Natl Acad Sci U S A*, 101(5), 1362-1367. doi:10.1073/pnas.0304752101
- Lowry, E. R., Kruyer, A., Norris, E. H., Cederroth, C. R., & Strickland, S. (2013). The GluK4 kainate receptor subunit regulates memory, mood, and excitotoxic neurodegeneration. *Neuroscience*, 235, 215-225. doi:10.1016/j.neuroscience.2013.01.029
- Lu, W., Shi, Y., Jackson, A. C., Bjorgan, K., During, M. J., Sprengel, R., . . . Nicoll, R. A. (2009). Subunit composition of synaptic AMPA receptors revealed by a single-cell genetic approach. *Neuron*, 62(2), 254-268. doi:10.1016/j.neuron.2009.02.027
- Luger, K., Mader, A. W., Richmond, R. K., Sargent, D. F., & Richmond, T. J. (1997). Crystal structure of the nucleosome core particle at 2.8 Å resolution. *Nature*, 389(6648), 251-260. doi:10.1038/38444
- Mansour, M., Nagarajan, N., Nehring, R. B., Clements, J. D., & Rosenmund, C. (2001). Heteromeric AMPA receptors assemble with a preferred subunit stoichiometry and spatial arrangement. *Neuron*, 32(5), 841-853.
- Marchetti C, Marie H. (2011). Hippocampal synaptic plasticity in Alzheimer's disease: what have we learned so far from transgenic models? *Rev Neurosci*, 22(4):373-402. doi: 10.1515/RNS.2011.035
- Marr, D. (1971). Simple memory: a theory for archicortex. *Philos Trans R Soc Lond B Biol Sci*, 262(841), 23-81.
- Maston, G. A., Landt, S. G., Snyder, M., & Green, M. R. (2012). Characterization of enhancer function from genome-wide analyses. *Annu Rev Genomics Hum Genet*, 13, 29-57. doi:10.1146/annurev-genom-090711-163723
- Mayer, M. L., & Westbrook, G. L. (1987). Permeation and block of N-methyl-D-aspartic acid receptor channels by divalent cations in mouse cultured central neurones. *J Physiol*, 394, 501-527.
- McBain, C. J. (2008). Differential mechanisms of transmission and plasticity at mossy fiber synapses. *Prog Brain Res*, 169, 225-240. doi:10.1016/s0079-

6123(07)00013-1

- Meffin, H., Burkitt, A. N., & Grayden, D. B. (2004). An analytical model for the "large, fluctuating synaptic conductance state" typical of neocortical neurons in vivo. *J Comput Neurosci*, *16*(2), 159-175. doi:10.1023/B:JCNS.0000014108.03012.81
- Melyan, Z., Lancaster, B., & Wheal, H. V. (2004). Metabotropic regulation of intrinsic excitability by synaptic activation of kainate receptors. *J Neurosci*, *24*(19), 4530-4534. doi:10.1523/JNEUROSCI.5356-03.2004
- Melyan, Z., Wheal, H. V., & Lancaster, B. (2002). Metabotropic-mediated kainate receptor regulation of IsAHP and excitability in pyramidal cells. *Neuron*, *34*(1), 107-114.
- Menzel, R. (2012). The honeybee as a model for understanding the basis of cognition. *Nat Rev Neurosci*, *13*(11), 758-768. doi:10.1038/nrn3357
- Minkeviciene R, Rheims S, Dobszay MB, Zilberter M, Hartikainen J, Fülöp L, Penke B, Zilberter Y, Harkany T, Pitkänen A, Tanila H. (2009). Amyloid beta-induced neuronal hyperexcitability triggers progressive epilepsy. *J Neurosci*, Mar 18;29(11):3453-62. doi: 10.1523/JNEUROSCI.5215-08.2009.
- Mori, M., Abegg, M. H., Gähwiler, B. H., & Gerber, U. (2004). A frequency-dependent switch from inhibition to excitation in a hippocampal unitary circuit. *Nature*, *431*(7007), 453-456. doi:10.1038/nature02854
- Morris, R. G. (2001). Episodic-like memory in animals: psychological criteria, neural mechanisms and the value of episodic-like tasks to investigate animal models of neurodegenerative disease. *Philos Trans R Soc Lond B Biol Sci*, *356*(1413), 1453-1465. doi:10.1098/rstb.2001.0945
- Morrisette, D. A., Parachikova, A., Green, K. N., & LaFerla, F. M. (2009). Relevance of transgenic mouse models to human Alzheimer disease. *J Biol Chem*, *284*(10), 6033-6037. doi:10.1074/jbc.R800030200
- Morse, S. J., Butler, A. A., Davis, R. L., Soller, I. J., & Lubin, F. D. (2015). Environmental enrichment reverses histone methylation changes in the aged hippocampus and restores age-related memory deficits. *Biology (Basel)*, *4*(2), 298-313. doi:10.3390/biology4020298
- Mosammaparast, N., & Shi, Y. (2010). Reversal of histone methylation: biochemical and molecular mechanisms of histone demethylases. *Annu Rev Biochem*, *79*, 155-179. doi:10.1146/annurev.biochem.78.070907.103946
- Mucke, L., Masliah, E., Yu, G. Q., Mallory, M., Rockenstein, E. M., Tatsuno, G., . . . McConlogue, L. (2000). High-level neuronal expression of abeta 1-42 in wild-type human amyloid protein precursor transgenic mice: synaptotoxicity without

- plaque formation. *J Neurosci*, 20(11), 4050-4058.
- Mullan, M., Crawford, F., Axelman, K., Houlden, H., Lilius, L., Winblad, B., & Lannfelt, L. (1992). A pathogenic mutation for probable Alzheimer's disease in the APP gene at the N-terminus of beta-amyloid. *Nat Genet*, 1(5), 345-347. doi:10.1038/ng0892-345
- Mulle, C., Sailer, A., Perez-Otano, I., Dickinson-Anson, H., Castillo, P. E., Bureau, I., . . . Heinemann, S. F. (1998). Altered synaptic physiology and reduced susceptibility to kainate-induced seizures in GluR6-deficient mice. *Nature*, 392(6676), 601-605. doi:10.1038/33408
- Mulle, C., Sailer, A., Swanson, G. T., Brana, C., O'Gorman, S., Bettler, B., & Heinemann, S. F. (2000). Subunit composition of kainate receptors in hippocampal interneurons. *Neuron*, 28(2), 475-484.
- Myers, C. E., & Scharfman, H. E. (2009). A role for hilar cells in pattern separation in the dentate gyrus: a computational approach. *Hippocampus*, 19(4), 321-337. doi:10.1002/hipo.20516
- Myers, C. E., & Scharfman, H. E. (2011). Pattern separation in the dentate gyrus: a role for the CA3 backprojection. *Hippocampus*, 21(11), 1190-1215. doi:10.1002/hipo.20828
- Nadel, L., & Moscovitch, M. (1997). Memory consolidation, retrograde amnesia and the hippocampal complex. *Curr Opin Neurobiol*, 7(2), 217-227.
- Nadim, F., & Bucher, D. (2014). Neuromodulation of neurons and synapses. *Curr Opin Neurobiol*, 29, 48-56. doi:10.1016/j.conb.2014.05.003
- Nakashiba, T., Cushman, J. D., Pelkey, K. A., Renaudineau, S., Buhl, D. L., McHugh, T. J., . . . Tonegawa, S. (2012). Young dentate granule cells mediate pattern separation, whereas old granule cells facilitate pattern completion. *Cell*, 149(1), 188-201. doi:10.1016/j.cell.2012.01.046
- Nicolas, M., & Hassan, B. A. (2014). Amyloid precursor protein and neural development. *Development*, 141(13), 2543-2548. doi:10.1242/dev.108712
- Nicoll, R. A., & Schmitz, D. (2005). Synaptic plasticity at hippocampal mossy fibre synapses. *Nat Rev Neurosci*, 6(11), 863-876. doi:10.1038/nrn1786
- Nilsberth, C., Westlind-Danielsson, A., Eckman, C. B., Condron, M. M., Axelman, K., Forsell, C., . . . Lannfelt, L. (2001). The 'Arctic' APP mutation (E693G) causes Alzheimer's disease by enhanced Abeta protofibril formation. *Nat Neurosci*, 4(9), 887-893. doi:10.1038/nn0901-887
- Nin MS, Martinez LA, Pibiri F, Nelson M, Pinna G. (2011). Neurosteroids reduce social

- isolation-induced behavioral deficits: a proposed link with neurosteroid-mediated upregulation of BDNF expression. *Front Endocrinol (Lausanne)*, Nov 21;2:73. doi: 10.3389/fendo.2011.00073.
- Nishioka, K., Rice, J. C., Sarma, K., Erdjument-Bromage, H., Werner, J., Wang, Y., . . . Reinberg, D. (2002). PR-Set7 is a nucleosome-specific methyltransferase that modifies lysine 20 of histone H4 and is associated with silent chromatin. *Mol Cell*, 9(6), 1201-1213.
- Norman, K. A., & O'Reilly, R. C. (2003). Modeling hippocampal and neocortical contributions to recognition memory: a complementary-learning-systems approach. *Psychol Rev*, 110(4), 611-646. doi:10.1037/0033-295x.110.4.611
- O'Leary, T. P., & Brown, R. E. (2009). Visuo-spatial learning and memory deficits on the Barnes maze in the 16-month-old APP^{swe}/PS1^{dE9} mouse model of Alzheimer's disease. *Behav Brain Res*, 201(1), 120-127. doi:10.1016/j.bbr.2009.01.039
- O'Reilly, R. C., & McClelland, J. L. (1994). Hippocampal conjunctive encoding, storage, and recall: avoiding a trade-off. *Hippocampus*, 4(6), 661-682. doi:10.1002/hipo.450040605
- Orth, A., Tapken, D., & Hollmann, M. (2013). The delta subfamily of glutamate receptors: characterization of receptor chimeras and mutants. *Eur J Neurosci*, 37(10), 1620-1630. doi:10.1111/ejn.12193
- Ostrowski, D., Kahsai, L., Kramer, E. F., Knutson, P., & Zars, T. (2015). Place memory retention in *Drosophila*. *Neurobiol Learn Mem*, 123, 217-224. doi:10.1016/j.nlm.2015.06.015
- Otto, C., Kovalchuk, Y., Wolfer, D. P., Gass, P., Martin, M., Zuschratter, W., . . . Schutz, G. (2001). Impairment of mossy fiber long-term potentiation and associative learning in pituitary adenylate cyclase activating polypeptide type I receptor-deficient mice. *J Neurosci*, 21(15), 5520-5527.
- Oyelami, T., Bondt, A., den Wyngaert, I. V., Hoorde, K. V., Hoskens, L., Shaban, H., . . . Drinkenburg, W. H. (2016). Age-dependent concomitant changes in synaptic dysfunction and GABAergic pathway in the APP/PS1 mouse model. *Acta Neurobiol Exp (Wars)*, 76(4), 282-293.
- Penttonen M, Kamondi A, Sik A, Acsady L, Buzsaki G. (1997). Feed-forward and feedback activation of the dentate gyrus in vivo during dentate spikes and sharp wave bursts. *Hippocampus*, 7:437– 450.
- Perea, G., Navarrete, M., & Araque, A. (2009). Tripartite synapses: astrocytes process and control synaptic information. *Trends Neurosci*, 32(8), 421-431.

doi:10.1016/j.tins.2009.05.001

Pereda, A. E. (2014). Electrical synapses and their functional interactions with chemical synapses. *Nat Rev Neurosci*, *15*(4), 250-263. doi:10.1038/nrn3708

Pinheiro, P. S., Lanore, F., Veran, J., Artinian, J., Blanchet, C., Crepel, V., . . . Mulle, C. (2013). Selective block of postsynaptic kainate receptors reveals their function at hippocampal mossy fiber synapses. *Cereb Cortex*, *23*(2), 323-331. doi:10.1093/cercor/bhs022

Pinheiro, P. S., Perrais, D., Coussen, F., Barhanin, J., Bettler, B., Mann, J. R., . . . Mulle, C. (2007). GluR7 is an essential subunit of presynaptic kainate autoreceptors at hippocampal mossy fiber synapses. *Proc Natl Acad Sci U S A*, *104*(29), 12181-12186. doi:10.1073/pnas.0608891104

Pinna G. (2010). In a mouse model relevant for post-traumatic stress disorder, selective brain steroidogenic stimulants (SBSS) improve behavioral deficits by normalizing allopregnanolone biosynthesis. *Behav Pharmacol*, Sep;21(5-6):438-50. doi: 10.1097/FBP.0b013e32833d8ba0.

Querfurth, H. W., & LaFerla, F. M. (2010). Alzheimer's disease. *N Engl J Med*, *362*(4), 329-344. doi:10.1056/NEJMra0909142

Ramamoorthi, K., Fropf, R., Belfort, G. M., Fitzmaurice, H. L., McKinney, R. M., Neve, R. L., . . . Lin, Y. (2011). Npas4 regulates a transcriptional program in CA3 required for contextual memory formation. *Science*, *334*(6063), 1669-1675. doi:10.1126/science.1208049

Ramos, B., Baglietto-Vargas, D., del Rio, J. C., Moreno-Gonzalez, I., Santa-Maria, C., Jimenez, S., . . . Vitorica, J. (2006). Early neuropathology of somatostatin/NPY GABAergic cells in the hippocampus of a PS1xAPP transgenic model of Alzheimer's disease. *Neurobiol Aging*, *27*(11), 1658-1672. doi:10.1016/j.neurobiolaging.2005.09.022

Rea, S., Eisenhaber, F., O'Carroll, D., Strahl, B. D., Sun, Z. W., Schmid, M., . . . Jenuwein, T. (2000). Regulation of chromatin structure by site-specific histone H3 methyltransferases. *Nature*, *406*(6796), 593-599. doi:10.1038/35020506

Rebola, N., Carta, M., Lanore, F., Blanchet, C., & Mulle, C. (2011). NMDA receptor-dependent metaplasticity at hippocampal mossy fiber synapses. *Nat Neurosci*, *14*(6), 691-693. doi:10.1038/nn.2809

Rebola, N., Carta, M., & Mulle, C. (2017). Operation and plasticity of hippocampal CA3 circuits: implications for memory encoding. *Nat Rev Neurosci*, *18*(4), 208-220. doi:10.1038/nrn.2017.10

Rebola, N., Lujan, R., Cunha, R. A., & Mulle, C. (2008). Adenosine A2A receptors are

- essential for long-term potentiation of NMDA-EPSCs at hippocampal mossy fiber synapses. *Neuron*, 57(1), 121-134. doi:10.1016/j.neuron.2007.11.023
- Regehr, W. G., Carey, M. R., & Best, A. R. (2009). Activity-dependent regulation of synapses by retrograde messengers. *Neuron*, 63(2), 154-170. doi:10.1016/j.neuron.2009.06.021
- Reiserer, R. S., Harrison, F. E., Syverud, D. C., & McDonald, M. P. (2007). Impaired spatial learning in the APPSwe + PSEN1DeltaE9 bigenic mouse model of Alzheimer's disease. *Genes Brain Behav*, 6(1), 54-65. doi:10.1111/j.1601-183X.2006.00221.x
- Reitz, C., & Mayeux, R. (2014). Alzheimer disease: epidemiology, diagnostic criteria, risk factors and biomarkers. *Biochem Pharmacol*, 88(4), 640-651. doi:10.1016/j.bcp.2013.12.024
- Roberson, E. D., Halabisky, B., Yoo, J. W., Yao, J., Chin, J., Yan, F., . . . Mucke, L. (2011). Amyloid-beta/Fyn-induced synaptic, network, and cognitive impairments depend on tau levels in multiple mouse models of Alzheimer's disease. *J Neurosci*, 31(2), 700-711. doi:10.1523/jneurosci.4152-10.2011
- Roberts, E. (1986). What do GABA neurons really do? They make possible variability generation in relation to demand. *Exp Neurol*, 93(2), 279-290.
- Rodriguez-Moreno, A., & Lerma, J. (1998). Kainate receptor modulation of GABA release involves a metabotropic function. *Neuron*, 20(6), 1211-1218.
- Roguev, A., Schaft, D., Shevchenko, A., Pijnappel, W. W., Wilm, M., Aasland, R., & Stewart, A. F. (2001). The *Saccharomyces cerevisiae* Set1 complex includes an Ash2 homologue and methylates histone 3 lysine 4. *Embo j*, 20(24), 7137-7148. doi:10.1093/emboj/20.24.7137
- Rolls, E. T. (2013). A quantitative theory of the functions of the hippocampal CA3 network in memory. *Front Cell Neurosci*, 7, 98. doi:10.3389/fncel.2013.00098
- Ronicke, R., Mikhaylova, M., Ronicke, S., Meinhardt, J., Schroder, U. H., Fandrich, M., . . . Reymann, K. G. (2011). Early neuronal dysfunction by amyloid beta oligomers depends on activation of NR2B-containing NMDA receptors. *Neurobiol Aging*, 32(12), 2219-2228. doi:10.1016/j.neurobiolaging.2010.01.011
- Rotter, S., & Diesmann, M. (1999). Exact digital simulation of time-invariant linear systems with applications to neuronal modeling. *Biol Cybern*, 81(5-6), 381-402. doi:10.1007/s004220050570
- Routtenberg, A. (2010). Adult learning and remodeling of hippocampal mossy fibers: unheralded participant in circuitry for long-lasting spatial memory.

Hippocampus, 20(1), 44-45. doi:10.1002/hipo.20664

Rovelet-Lecrux, A., Hannequin, D., Raux, G., Le Meur, N., Laquerriere, A., Vital, A., . . . Champion, D. (2006). APP locus duplication causes autosomal dominant early-onset Alzheimer disease with cerebral amyloid angiopathy. *Nat Genet*, 38(1), 24-26. doi:10.1038/ng1718

Ruediger, S., Spirig, D., Donato, F., & Caroni, P. (2012). Goal-oriented searching mediated by ventral hippocampus early in trial-and-error learning. *Nat Neurosci*, 15(11), 1563-1571. doi:10.1038/nn.3224

Ruediger, S., Vittori, C., Bednarek, E., Genoud, C., Strata, P., Sacchetti, B., & Caroni, P. (2011). Learning-related feedforward inhibitory connectivity growth required for memory precision. *Nature*, 473(7348), 514-518. doi:10.1038/nature09946

Rugg, M. D., & Yonelinas, A. P. (2003). Human recognition memory: a cognitive neuroscience perspective. *Trends Cogn Sci*, 7(7), 313-319.

Ruiz, A., Sachidhanandam, S., Utvik, J. K., Coussen, F., & Mulle, C. (2005). Distinct subunits in heteromeric kainate receptors mediate ionotropic and metabotropic function at hippocampal mossy fiber synapses. *J Neurosci*, 25(50), 11710-11718. doi:10.1523/JNEUROSCI.4041-05.2005

Sachidhanandam, S., Blanchet, C., Jeantet, Y., Cho, Y. H., & Mulle, C. (2009). Kainate receptors act as conditional amplifiers of spike transmission at hippocampal mossy fiber synapses. *J Neurosci*, 29(15), 5000-5008. doi:10.1523/jneurosci.5807-08.2009

Salin, P. A., Scanziani, M., Malenka, R. C., & Nicoll, R. A. (1996). Distinct short-term plasticity at two excitatory synapses in the hippocampus. *Proc Natl Acad Sci U S A*, 93(23), 13304-13309.

Santos-Rosa, H., Schneider, R., Bannister, A. J., Sherriff, J., Bernstein, B. E., Emre, N. C., . . . Kouzarides, T. (2002). Active genes are tri-methylated at K4 of histone H3. *Nature*, 419(6905), 407-411. doi:10.1038/nature01080

Savonenko, A. V., Xu, G. M., Price, D. L., Borchelt, D. R., & Markowska, A. L. (2003). Normal cognitive behavior in two distinct congenic lines of transgenic mice hyperexpressing mutant APP SWE. *Neurobiol Dis*, 12(3), 194-211.

Schacter, D. L., Addis, D. R., & Buckner, R. L. (2007). Remembering the past to imagine the future: the prospective brain. *Nat Rev Neurosci*, 8(9), 657-661. doi:10.1038/nrn2213

Scharf, A. N., & Imhof, A. (2011). Every methyl counts--epigenetic calculus. *FEBS Lett*, 585(13), 2001-2007. doi:10.1016/j.febslet.2010.11.029

- Scharfman, H. E., & Myers, C. E. (2012). Hilar mossy cells of the dentate gyrus: a historical perspective. *Front Neural Circuits*, 6, 106. doi:10.3389/fncir.2012.00106
- Schlingloff, D., Kali, S., Freund, T. F., Hajos, N., & Gulyas, A. I. (2014). Mechanisms of sharp wave initiation and ripple generation. *J Neurosci*, 34(34), 11385-11398. doi:10.1523/jneurosci.0867-14.2014
- Schmid, S. M., & Hollmann, M. (2008). To gate or not to gate: are the delta subunits in the glutamate receptor family functional ion channels? *Mol Neurobiol*, 37(2-3), 126-141. doi:10.1007/s12035-008-8025-0
- Schmitz, D., Mellor, J., & Nicoll, R. A. (2001). Presynaptic kainate receptor mediation of frequency facilitation at hippocampal mossy fiber synapses. *Science*, 291(5510), 1972-1976. doi:10.1126/science.1057105
- Schneider, J., Wood, A., Lee, J. S., Schuster, R., Dueker, J., Maguire, C., . . . Shilatifard, A. (2005). Molecular regulation of histone H3 trimethylation by COMPASS and the regulation of gene expression. *Mol Cell*, 19(6), 849-856. doi:10.1016/j.molcel.2005.07.024
- Schoepfer, R., Monyer, H., Sommer, B., Wisden, W., Sprengel, R., Kuner, T., . . . et al. (1994). Molecular biology of glutamate receptors. *Prog Neurobiol*, 42(2), 353-357.
- Schoepp, D. D., Jane, D. E., & Monn, J. A. (1999). Pharmacological agents acting at subtypes of metabotropic glutamate receptors. *Neuropharmacology*, 38(10), 1431-1476.
- Schotta, G., Lachner, M., Sarma, K., Ebert, A., Sengupta, R., Reuter, G., . . . Jenuwein, T. (2004). A silencing pathway to induce H3-K9 and H4-K20 trimethylation at constitutive heterochromatin. *Genes Dev*, 18(11), 1251-1262. doi:10.1101/gad.300704
- Scoville, W. B., & Milner, B. (1957). Loss of recent memory after bilateral hippocampal lesions. *J Neurol Neurosurg Psychiatry*, 20(1), 11-21.
- Scoville, W. B., & Milner, B. (2000). Loss of recent memory after bilateral hippocampal lesions. 1957. *J Neuropsychiatry Clin Neurosci*, 12(1), 103-113. doi:10.1176/jnp.12.1.103
- Seeburg, P. H., Higuchi, M., & Sprengel, R. (1998). RNA editing of brain glutamate receptor channels: mechanism and physiology. *Brain Res Brain Res Rev*, 26(2-3), 217-229.
- Selkoe, D. J. (2002). Alzheimer's disease is a synaptic failure. *Science*, 298(5594), 789-791. doi:10.1126/science.1074069

Bibliography

- Seo, J. S., Lee, K. W., Kim, T. K., Baek, I. S., Im, J. Y., & Han, P. L. (2011). Behavioral stress causes mitochondrial dysfunction via ABAD up-regulation and aggravates plaque pathology in the brain of a mouse model of Alzheimer disease. *Free Radic Biol Med*, 50(11), 1526-1535. doi:10.1016/j.freeradbiomed.2011.02.035
- Shankar, G. M., Bloodgood, B. L., Townsend, M., Walsh, D. M., Selkoe, D. J., & Sabatini, B. L. (2007). Natural oligomers of the Alzheimer amyloid-beta protein induce reversible synapse loss by modulating an NMDA-type glutamate receptor-dependent signaling pathway. *J Neurosci*, 27(11), 2866-2875. doi:10.1523/jneurosci.4970-06.2007
- Shen, J., Bronson, R. T., Chen, D. F., Xia, W., Selkoe, D. J., & Tonegawa, S. (1997). Skeletal and CNS defects in Presenilin-1-deficient mice. *Cell*, 89(4), 629-639.
- Shi, Y., & Whetstine, J. R. (2007). Dynamic regulation of histone lysine methylation by demethylases. *Mol Cell*, 25(1), 1-14. doi:10.1016/j.molcel.2006.12.010
- Shilatifard, A. (2008). Molecular implementation and physiological roles for histone H3 lysine 4 (H3K4) methylation. *Curr Opin Cell Biol*, 20(3), 341-348. doi:10.1016/j.ceb.2008.03.019
- Shilatifard, A. (2012). The COMPASS family of histone H3K4 methylases: mechanisms of regulation in development and disease pathogenesis. *Annu Rev Biochem*, 81, 65-95. doi:10.1146/annurev-biochem-051710-134100
- Shulha, H. P., Cheung, I., Whittle, C., Wang, J., Virgil, D., Lin, C. L., . . . Weng, Z. (2012). Epigenetic signatures of autism: trimethylated H3K4 landscapes in prefrontal neurons. *Arch Gen Psychiatry*, 69(3), 314-324. doi:10.1001/archgenpsychiatry.2011.151
- Shulha, H. P., Crisci, J. L., Reshetov, D., Tushir, J. S., Cheung, I., Bharadwaj, R., . . . Akbarian, S. (2012). Human-specific histone methylation signatures at transcription start sites in prefrontal neurons. *PLoS Biol*, 10(11), e1001427. doi:10.1371/journal.pbio.1001427
- Singec I, Knoth R, Ditter M, Hagemeyer CE, Rosenbrock H, Frotscher M, Volk B. (2002). Synaptic vesicle protein synaptoporin is differently expressed by subpopulations of mouse hippocampal neurons. *J Comp Neurol*. 452(2):139-53. doi: 10.1002/cne.10371
- Sinha, S., Anderson, J. P., Barbour, R., Basi, G. S., Caccavello, R., Davis, D., . . . John, V. (1999). Purification and cloning of amyloid precursor protein beta-secretase from human brain. *Nature*, 402(6761), 537-540. doi:10.1038/990114
- Snowdon, D. A., Greiner, L. H., Mortimer, J. A., Riley, K. P., Greiner, P. A., &

- Markesbery, W. R. (1997). Brain infarction and the clinical expression of Alzheimer disease. The Nun Study. *Jama*, 277(10), 813-817.
- Sperling, R. (2007). Functional MRI studies of associative encoding in normal aging, mild cognitive impairment, and Alzheimer's disease. *Ann N Y Acad Sci*, 1097, 146-155. doi:10.1196/annals.1379.009
- Squire, L. R. (1986). Mechanisms of memory. *Science*, 232(4758), 1612-1619.
- Squire, L. R., & Dede, A. J. (2015). Conscious and unconscious memory systems. *Cold Spring Harb Perspect Biol*, 7(3), a021667. doi:10.1101/cshperspect.a021667
- Squire, L. R., Stark, C. E., & Clark, R. E. (2004). The medial temporal lobe. *Annu Rev Neurosci*, 27, 279-306. doi:10.1146/annurev.neuro.27.070203.144130
- St George-Hyslop, P. H., & Petit, A. (2005). Molecular biology and genetics of Alzheimer's disease. *C R Biol*, 328(2), 119-130.
- Steiner, H., Winkler, E., Edbauer, D., Prokop, S., Basset, G., Yamasaki, A., . . . Haass, C. (2002). PEN-2 is an integral component of the gamma-secretase complex required for coordinated expression of presenilin and nicastrin. *J Biol Chem*, 277(42), 39062-39065. doi:10.1074/jbc.C200469200
- Stern, P., Behe, P., Schoepfer, R., & Colquhoun, D. (1992). Single-channel conductances of NMDA receptors expressed from cloned cDNAs: comparison with native receptors. *Proc Biol Sci*, 250(1329), 271-277. doi:10.1098/rspb.1992.0159
- Strahl, B. D., & Allis, C. D. (2000). The language of covalent histone modifications. *Nature*, 403(6765), 41-45. doi:10.1038/47412
- Strahl, B. D., Ohba, R., Cook, R. G., & Allis, C. D. (1999). Methylation of histone H3 at lysine 4 is highly conserved and correlates with transcriptionally active nuclei in Tetrahymena. *Proc Natl Acad Sci U S A*, 96(26), 14967-14972.
- Strange, B. A., Witter, M. P., Lein, E. S., & Moser, E. I. (2014). Functional organization of the hippocampal longitudinal axis. *Nat Rev Neurosci*, 15(10), 655-669. doi:10.1038/nrn3785
- Sturchler-Pierrat, C., Abramowski, D., Duke, M., Wiederhold, K. H., Mistl, C., Rothacher, S., . . . Sommer, B. (1997). Two amyloid precursor protein transgenic mouse models with Alzheimer disease-like pathology. *Proc Natl Acad Sci U S A*, 94(24), 13287-13292.
- Swanson, L. W., Wyss, J. M., & Cowan, W. M. (1978). An autoradiographic study of the organization of intrahippocampal association pathways in the rat. *J Comp*

- Neurol*, 181(4), 681-715. doi:10.1002/cne.901810402
- Sykova, E., & Nicholson, C. (2008). Diffusion in brain extracellular space. *Physiol Rev*, 88(4), 1277-1340. doi:10.1152/physrev.00027.2007
- Szabadics, J., & Soltesz, I. (2009). Functional specificity of mossy fiber innervation of GABAergic cells in the hippocampus. *J Neurosci*, 29(13), 4239-4251. doi:10.1523/jneurosci.5390-08.2009
- Szabo, G. G., Papp, O. I., Mate, Z., Szabo, G., & Hajos, N. (2014). Anatomically heterogeneous populations of CB1 cannabinoid receptor-expressing interneurons in the CA3 region of the hippocampus show homogeneous input-output characteristics. *Hippocampus*, 24(12), 1506-1523. doi:10.1002/hipo.22330
- Szpunar, K. K. (2010). Episodic Future Thought: An Emerging Concept. *Perspect Psychol Sci*, 5(2), 142-162. doi:10.1177/1745691610362350
- Tanzi, R. E. (2005). The synaptic Abeta hypothesis of Alzheimer disease. *Nat Neurosci*, 8(8), 977-979. doi:10.1038/nn0805-977
- Tarawneh, R., & Holtzman, D. M. (2012). The clinical problem of symptomatic Alzheimer disease and mild cognitive impairment. *Cold Spring Harb Perspect Med*, 2(5), a006148. doi:10.1101/cshperspect.a006148
- Todd, S., Barr, S., Roberts, M., & Passmore, A. P. (2013). Survival in dementia and predictors of mortality: a review. *Int J Geriatr Psychiatry*, 28(11), 1109-1124. doi:10.1002/gps.3946
- Torborg, C. L., Nakashiba, T., Tonegawa, S., & McBain, C. J. (2010). Control of CA3 output by feedforward inhibition despite developmental changes in the excitation-inhibition balance. *J Neurosci*, 30(46), 15628-15637. doi:10.1523/jneurosci.3099-10.2010
- Traynelis, S. F., Wollmuth, L. P., McBain, C. J., Menniti, F. S., Vance, K. M., Ogden, K. K., . . . Dingledine, R. (2010). Glutamate receptor ion channels: structure, regulation, and function. *Pharmacol Rev*, 62(3), 405-496. doi:10.1124/pr.109.002451
- Trudeau, L. E., & Gutierrez, R. (2007). On cotransmission & neurotransmitter phenotype plasticity. *Mol Interv*, 7(3), 138-146. doi:10.1124/mi.7.3.5
- Tulving, E., & Schacter, D. L. (1990). Priming and human memory systems. *Science*, 247(4940), 301-306.
- Ullman, M. T. (2001). A neurocognitive perspective on language: the declarative/procedural model. *Nat Rev Neurosci*, 2(10), 717-726.

doi:10.1038/35094573

- Vallianatos, C. N., & Iwase, S. (2015). Disrupted intricacy of histone H3K4 methylation in neurodevelopmental disorders. *Epigenomics*, 7(3), 503-519. doi:10.2217/epi.15.1
- van Strien, N. M., Cappaert, N. L., & Witter, M. P. (2009). The anatomy of memory: an interactive overview of the parahippocampal-hippocampal network. *Nat Rev Neurosci*, 10(4), 272-282. doi:10.1038/nrn2614
- Vaquero, A., Loyola, A., & Reinberg, D. (2003). The constantly changing face of chromatin. *Sci Aging Knowledge Environ*, 2003(14), Re4.
- Vashishtha, M., Ng, C. W., Yildirim, F., Gipson, T. A., Kratter, I. H., Bodai, L., . . . Thompson, L. M. (2013). Targeting H3K4 trimethylation in Huntington disease. *Proc Natl Acad Sci U S A*, 110(32), E3027-3036. doi:10.1073/pnas.1311323110
- Vassar, R., Bennett, B. D., Babu-Khan, S., Kahn, S., Mendiaz, E. A., Denis, P., . . . Citron, M. (1999). Beta-secretase cleavage of Alzheimer's amyloid precursor protein by the transmembrane aspartic protease BACE. *Science*, 286(5440), 735-741.
- Verkhatsky, A., & Kirchhoff, F. (2007). NMDA Receptors in glia. *Neuroscientist*, 13(1), 28-37. doi:10.1177/1073858406294270
- Verret L, Jankowsky JL, Xu GM, Borchelt DR, Rampon C. (2007). Alzheimer's-type amyloidosis in transgenic mice impairs survival of newborn neurons derived from adult hippocampal neurogenesis. *J Neurosci*, Jun 20;27(25):6771-80.
- Verret L, Mann EO, Hang GB, Barth AM, Cobos I, Ho K, Devidze N, Masliah E, Kreitzer AC, Mody I, Mucke L, Palop JJ. (2012). Inhibitory interneuron deficit links altered network activity and cognitive dysfunction in Alzheimer model. *Cell*, Apr 27;149(3):708-21. doi: 10.1016/j.cell.2012.02.046.
- Viana da Silva, S., Haberl, M. G., Zhang, P., Bethge, P., Lemos, C., Goncalves, N., . . . Mulle, C. (2016). Early synaptic deficits in the APP/PS1 mouse model of Alzheimer's disease involve neuronal adenosine A2A receptors. *Nat Commun*, 7, 11915. doi:10.1038/ncomms11915
- Volianskis, A., Kostner, R., Molgaard, M., Hass, S., & Jensen, M. S. (2010). Episodic memory deficits are not related to altered glutamatergic synaptic transmission and plasticity in the CA1 hippocampus of the APP^{swe}/PS1^{deltaE9}-deleted transgenic mice model of ss-amyloidosis. *Neurobiol Aging*, 31(7), 1173-1187. doi:10.1016/j.neurobiolaging.2008.08.005
- Vyleta, N. P., Borges-Merjane, C., & Jonas, P. (2016). Plasticity-dependent, full detonation at hippocampal mossy fiber-CA3 pyramidal neuron synapses. *Elife*,

5. doi:10.7554/eLife.17977

- Wang, H., Huang, Z. Q., Xia, L., Feng, Q., Erdjument-Bromage, H., Strahl, B. D., . . . Zhang, Y. (2001). Methylation of histone H4 at arginine 3 facilitating transcriptional activation by nuclear hormone receptor. *Science*, *293*(5531), 853-857. doi:10.1126/science.1060781
- Waring, S. C., & Rosenberg, R. N. (2008). Genome-wide association studies in Alzheimer disease. *Arch Neurol*, *65*(3), 329-334. doi:10.1001/archneur.65.3.329
- Webb, W. M., Sanchez, R. G., Perez, G., Butler, A. A., Hauser, R. M., Rich, M. C., . . . Lubin, F. D. (2017). Dynamic association of epigenetic H3K4me3 and DNA 5hmC marks in the dorsal hippocampus and anterior cingulate cortex following reactivation of a fear memory. *Neurobiol Learn Mem*. doi:10.1016/j.nlm.2017.02.010
- Webster, S. J., Bachstetter, A. D., Nelson, P. T., Schmitt, F. A., & Van Eldik, L. J. (2014). Using mice to model Alzheimer's dementia: an overview of the clinical disease and the preclinical behavioral changes in 10 mouse models. *Front Genet*, *5*, 88. doi:10.3389/fgene.2014.00088
- Weisskopf, M. G., & Nicoll, R. A. (1995). Presynaptic changes during mossy fibre LTP revealed by NMDA receptor-mediated synaptic responses. *Nature*, *376*(6537), 256-259. doi:10.1038/376256a0
- Wenthold, R. J., Petralia, R. S., Blahos, J., II, & Niedzielski, A. S. (1996). Evidence for multiple AMPA receptor complexes in hippocampal CA1/CA2 neurons. *J Neurosci*, *16*(6), 1982-1989.
- Wilke, S. A., Antonios, J. K., Bushong, E. A., Badkoobehi, A., Malek, E., Hwang, M., . . . Ghosh, A. (2013). Deconstructing complexity: serial block-face electron microscopic analysis of the hippocampal mossy fiber synapse. *J Neurosci*, *33*(2), 507-522. doi:10.1523/JNEUROSCI.1600-12.2013
- Wilson, R. I., & Nicoll, R. A. (2002). Endocannabinoid signaling in the brain. *Science*, *296*(5568), 678-682. doi:10.1126/science.1063545
- Wisden, W., & Seeburg, P. H. (1993). Mammalian ionotropic glutamate receptors. *Curr Opin Neurobiol*, *3*(3), 291-298.
- Witter, M. P. (1993). Organization of the entorhinal-hippocampal system: a review of current anatomical data. *Hippocampus*, *3 Spec No*, 33-44.
- Witter, M. P., Canto, C. B., Couey, J. J., Koganezawa, N., & O'Reilly, K. C. (2014). Architecture of spatial circuits in the hippocampal region. *Philos Trans R Soc Lond B Biol Sci*, *369*(1635), 20120515. doi:10.1098/rstb.2012.0515

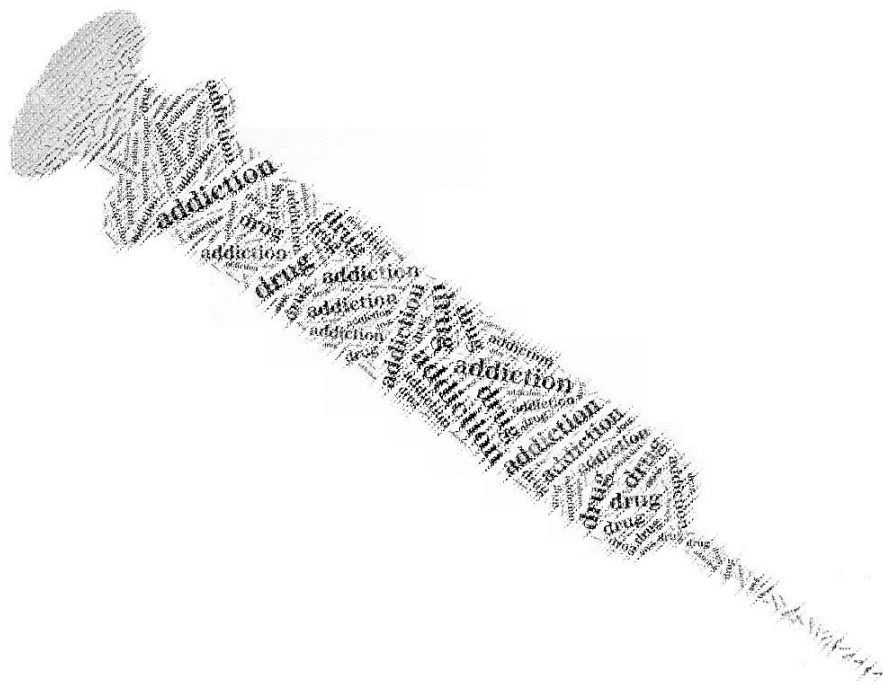
- Witton J, Brown JT, Jones MW, Randall AD. (2012). Altered synaptic plasticity in the mossy fibre pathway of transgenic mice expressing mutant amyloid precursor protein. *Mol Brain*, Nov 1;3:32. doi: 10.1186/1756-6606-3-32.
- Wolfe, M. S., Xia, W., Ostaszewski, B. L., Diehl, T. S., Kimberly, W. T., & Selkoe, D. J. (1999). Two transmembrane aspartates in presenilin-1 required for presenilin endoproteolysis and gamma-secretase activity. *Nature*, 398(6727), 513-517. doi:10.1038/19077
- Wong, P. C., Zheng, H., Chen, H., Becher, M. W., Sirinathsinghji, D. J., Trumbauer, M. E., . . . Sisodia, S. S. (1997). Presenilin 1 is required for Notch1 and DII1 expression in the paraxial mesoderm. *Nature*, 387(6630), 288-292. doi:10.1038/387288a0
- Wu, Z., Guo, Z., Gearing, M., & Chen, G. (2014). Tonic inhibition in dentate gyrus impairs long-term potentiation and memory in an Alzheimer's [corrected] disease model. *Nat Commun*, 5, 4159. doi:10.1038/ncomms5159
- Yamakura, T., & Shimoji, K. (1999). Subunit- and site-specific pharmacology of the NMDA receptor channel. *Prog Neurobiol*, 59(3), 279-298.
- Yoshiike, Y., Kimura, T., Yamashita, S., Furudate, H., Mizoroki, T., Murayama, M., & Takashima, A. (2008). GABA(A) receptor-mediated acceleration of aging-associated memory decline in APP/PS1 mice and its pharmacological treatment by picrotoxin. *PLoS One*, 3(8), e3029. doi:10.1371/journal.pone.0003029
- Younkin, S. G. (1998). The role of A beta 42 in Alzheimer's disease. *J Physiol Paris*, 92(3-4), 289-292.
- Yu, G., Nishimura, M., Arawaka, S., Levitan, D., Zhang, L., Tandon, A., . . . St George-Hyslop, P. (2000). Nicastrin modulates presenilin-mediated notch/glp-1 signal transduction and betaAPP processing. *Nature*, 407(6800), 48-54. doi:10.1038/35024009
- Zhang C, McNeil E, Dressler L, Siman R. Long-lasting impairment in hippocampal neurogenesis associated with amyloid deposition in a knock-in mouse model of familial Alzheimer's disease. *Exp Neurol*. 2007; 204:77-87.
- Zhang, K., Tang, H., Huang, L., Blankenship, J. W., Jones, P. R., Xiang, F., . . . Burlingame, A. L. (2002). Identification of acetylation and methylation sites of histone H3 from chicken erythrocytes by high-accuracy matrix-assisted laser desorption ionization-time-of-flight, matrix-assisted laser desorption ionization-postsource decay, and nanoelectrospray ionization tandem mass spectrometry. *Anal Biochem*, 306(2), 259-269.
- Zhang, W., Hao, J., Liu, R., Zhang, Z., Lei, G., Su, C., . . . Li, Z. (2011). Soluble Abeta

Bibliography

- levels correlate with cognitive deficits in the 12-month-old APPswe/PS1dE9 mouse model of Alzheimer's disease. *Behav Brain Res*, 222(2), 342-350. doi:10.1016/j.bbr.2011.03.072
- Zhou, Z., Yuan, Q., Mash, D. C., & Goldman, D. (2011). Substance-specific and shared transcription and epigenetic changes in the human hippocampus chronically exposed to cocaine and alcohol. *Proc Natl Acad Sci U S A*, 108(16), 6626-6631. doi:10.1073/pnas.1018514108
- Zhu, J. J., Esteban, J. A., Hayashi, Y., & Malinow, R. (2000). Postnatal synaptic potentiation: delivery of GluR4-containing AMPA receptors by spontaneous activity. *Nat Neurosci*, 3(11), 1098-1106. doi:10.1038/80614
- Zucca, S., Griguoli, M., Malezieux, M., Grosjean, N., Carta, M., & Mulle, C. (2017). Control of Spike Transfer at Hippocampal Mossy Fiber Synapses In Vivo by GABAA and GABAB Receptor-Mediated Inhibition. *J Neurosci*, 37(3), 587-598. doi:10.1523/jneurosci.2057-16.2017
- Zucker, R. S., & Regehr, W. G. (2002). Short-term synaptic plasticity. *Annu Rev Physiol*, 64, 355-405. doi:10.1146/annurev.physiol.64.092501.114547

CHAPTER 6

ANNEXES



6 Annexes

6.1 Computational modeling of hippocampal DG-CA3 networks

6.1.1 Single pyramidal neuron model

The modeling of hippocampal DG-CA3 networks was performed with a Python-based software NEST, in Oracle VM VirtualBox environment.

At the hub of all connection, a multi-compartment conductance-based leaky integrate-and-fire neuron model (`iaf_cond_alpha_mc`) was used for CA3 pyramidal cells (Bernander, Douglas, Martin, & Koch, 1991; Meffin, Burkitt, & Grayden, 2004) (Figure 6.1), and for DG granular cells and interneurons a simpler leaky integrate-and-fire neuron model was used (Gewaltig, Diesmann, & Aertsen, 2001; Rotter & Diesmann, 1999).

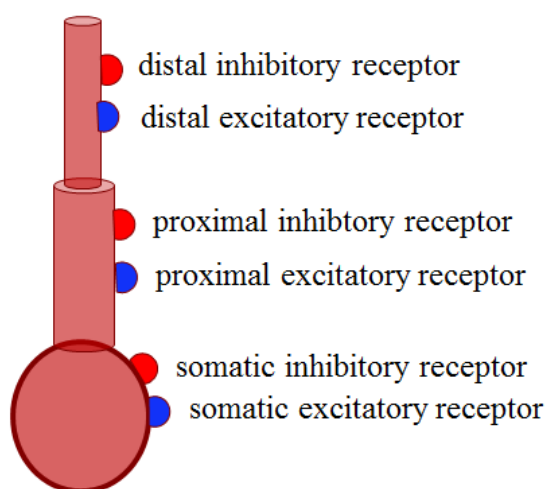


Figure 6.1. A simplified illustration of a multi-compartment conductance-based leaky integrate-and-fire neuron.

The model `iaf_cond_alpha_mc` contains three compartments: soma, proximal dendrite, and distal dendrite. An action potential is generated when somatic membrane potential exceeds the threshold, and there's a refractory period after a spike. However, the dendritic membrane potentials are not manipulated in this case.

We set excitatory or inhibitory conductance-based synapses onto each

compartment with alpha-function time course. Each compartment also received current input from a current generator (e.g. to create noise). We also set synaptic weights for each type of connection.

6.1.2 Network design of DG-CA3 circuits

Four types of neurons were taken into consideration in this model: DG granular cells, CA3 pyramidal cells, interneurons for feedforward inhibition, and interneurons for feedback inhibition.

A matrix of 40×40 neurons was created for DG granular cell layer, and also a matrix of 40×40 was created as the CA3 pyramidal layer. Each DG cell was innervating neurons in the CA3 layer in a circular area (radius: 0.6, kernel: 0.9) with somatic excitatory synapses. Apart from this input, the CA3 layer also received input from EC (created by a Poisson spike generator) and CA3-CA3 recurrent input. The recurrent input was designed as each CA3 neuron was connecting a 10×10 grid of CA3 PCs in the vicinity, and the strength of connection followed Gaussian distribution (Figure 6.2).

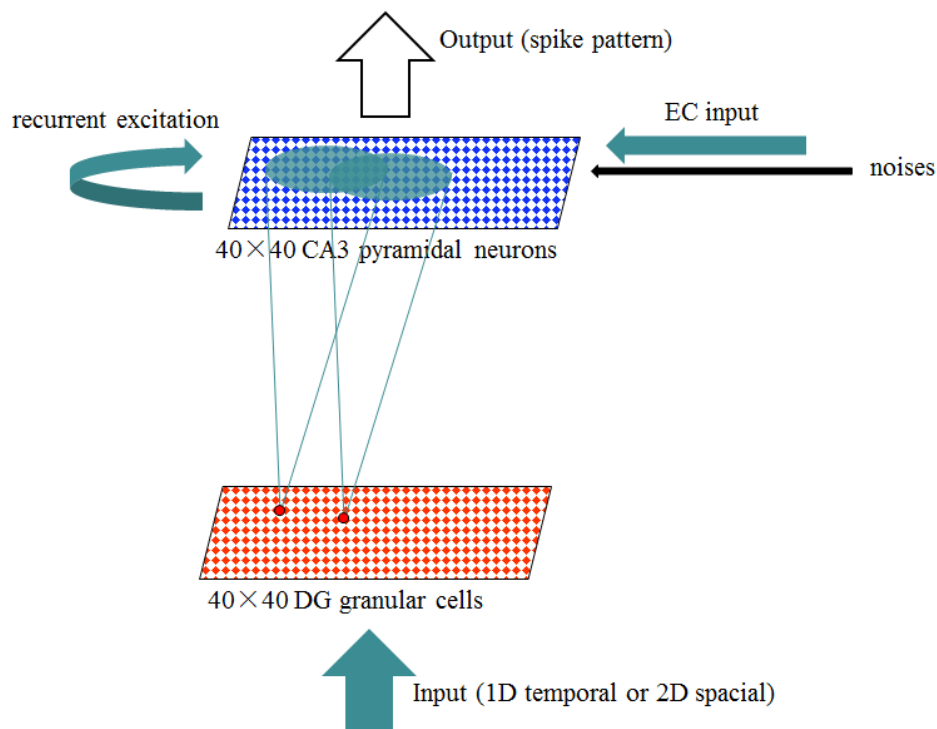


Figure 6.2. Illustration of DG granular cell layer and CA3 pyramidal cell layer and the connecting pattern between them.

Moreover, 400 interneurons for feedforward inhibition (FFI interneuron) and 200 interneurons for feedback inhibition (FBI interneuron) was added to the system. Each FFI interneuron received inputs from a circular area (radius: 0.8, kernel: 0.9, weights=5) of cells in DG layer, and projected onto the CA3 layer in a donut manner (inner radius: 0.2, outer radius: 0.8, kernel: 0.8) through proximal inhibitory synapses. While the FBI interneurons received general input from CA3 layer (followed pairwise Bernoulli distribution with a probability of 0.9, weights: 1), and projects back to CA3 layer in a similar manner through proximal inhibitory synapses. Noise was introduced with 2 Poisson spike generators (at 9700Hz and 14300Hz respectively) (Figure 6.3).

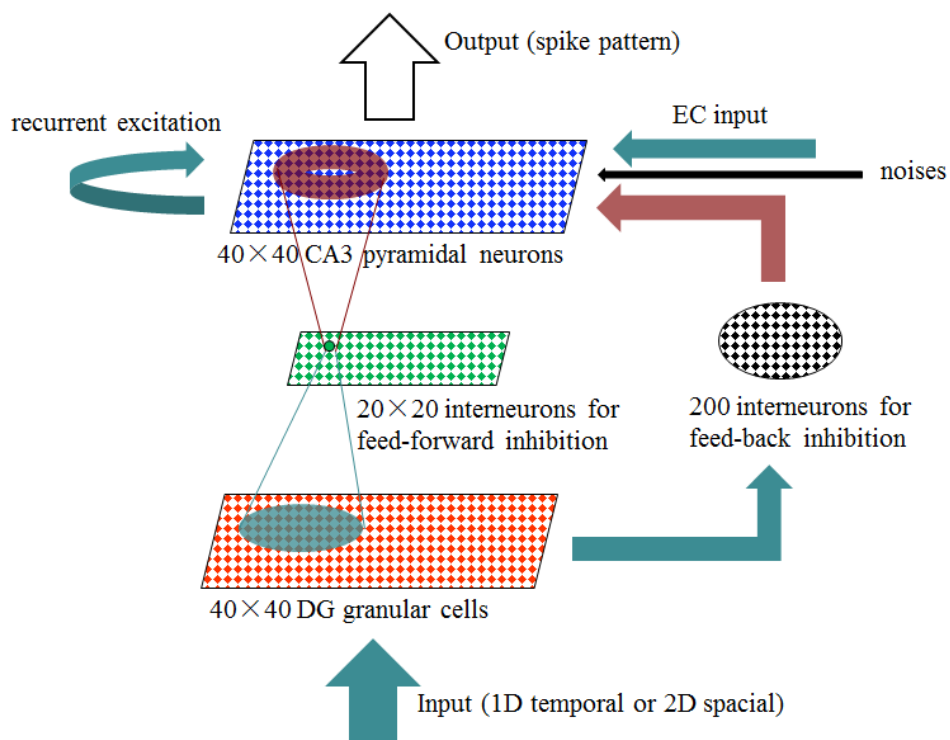


Figure 6.3. A more complete illustration with two types of interneurons for FFI and FBI respectively in the network.

Six different binary input sequences were designed. When run through the network, an output spike pattern was generated for each input signal (Figure 6.4). Parameters of the network were adjusted to achieve a more physiological activity pattern for the 4 groups of neurons. In the end, the average firing rate of each population was calculated: DG 14.3 Hz, CA3 15.2 Hz, FFI interneuron 19.2 Hz, and FBI interneuron 25.3 Hz.

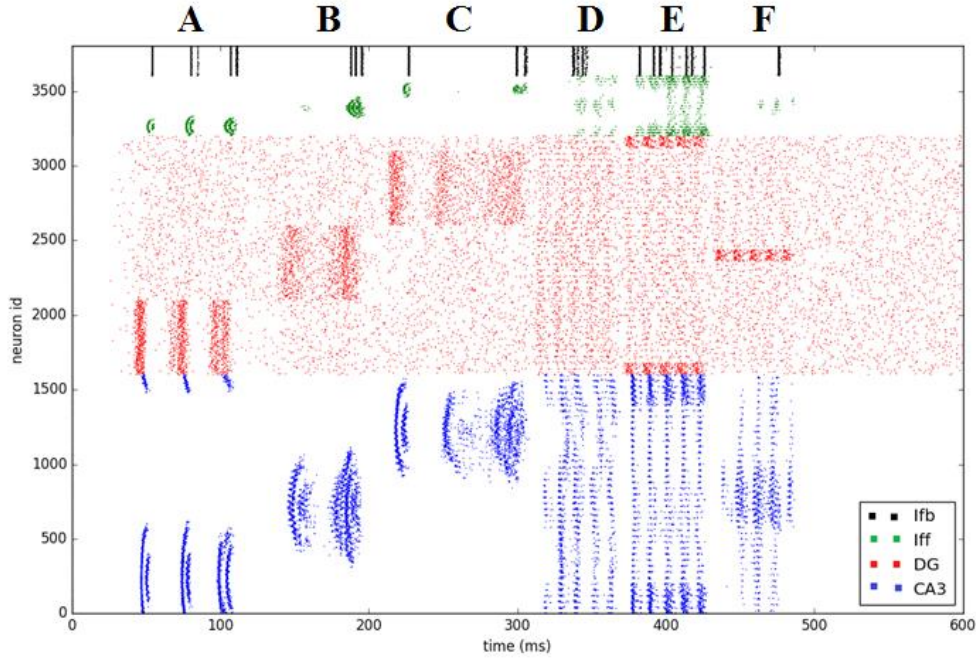


Figure 6.4. Spike patterns of four distinctive populations of neurons.

Scatter plot illustrating spikes of each population of neurons. CA3 layer was represented in blue, DG in red, FFI interneurons in green and FBI interneurons in black. 6 distinctive inputs were delivered sequentially, with interactions of multiple factors in the network, each resulted in a unique spike pattern.

6.1.3 Test of the model with input/output correlation

The fidelity of this artificial network was tested using an input/output correlation equation as follows:

$$M^\mu(t) = \frac{\eta^\mu \cdot X^{\Delta t}(t)}{\|\eta^\mu\| \|X^{\Delta t}(t)\|}$$

Where η^μ was the binary input vector, and $X^{\Delta t}(t)$ was the binarized output spike pattern.

The test was carried out multiple times with different FFI and FBI weights to optimize the fidelity of the network (Figure 6.5). After being fit to a curve, we could see that both too high and too low inhibition weights decreased the I/O correlation. Another thing to note is that as the I/O correlation was increasing together synaptic weights before reaching the plateau on the curve, the computational burden for each neuron was also increasing, resulting in unnaturally high firing rate in the neuron. Therefore, a slightly conservative inhibitory synaptic weight should be picked for the interneurons in order to have a more physiological network model.

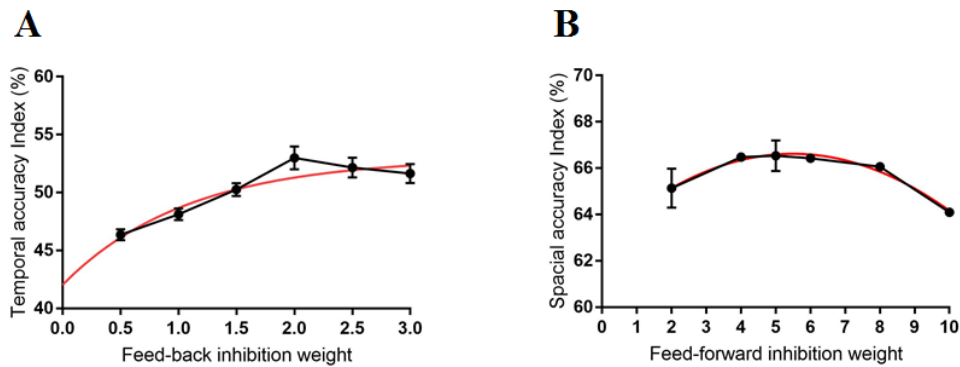


Figure 6.5. Relations between inhibitory synaptic weight and I/O correlation index for FFI and FBI interneurons.

A. Line chart of FBI weights plotted against the I/O correlation index, with an exponential curve fit. The firing frequency of the FBI interneurons were: 3.1Hz at weight = 0.5, 35.5Hz at weight = 1.0, 57.2Hz at weight = 1.5, 76.2Hz at weight = 2.0, 91.4Hz at weight = 2.5, 105 Hz at weight = 3.0. **B.** Line chart of FFI weights plotted against the I/O correlation index, with an exponential curve fit. The firing frequency of the FFI interneurons were: 1.2Hz at weight = 2, 3.5Hz at weight = 4, 9.6Hz at weight = 5, 19.2Hz at weight = 6, 42.8Hz at weight = 8, 67.3 Hz at weight = 10.

Overall, we built this over-simplified computational model of the DG-CA3 neuronal networks, to investigate if and to what extent the local interneurons in CA3 region contribute to memory encoding precision. This model can be further improved by implementing the spike timing-dependent plasticity (STDP) rule at the synapses (Dan & Poo, 2006; Kobayashi & Poo, 2004). STDP happens when the pre- and postsynaptic sides are excited within a specific time window, e.g. normally LTP is induced when stimulation of presynaptic fibers happens before the postsynaptic cell fires. This protocol is called STDP and LTP is normally induced when stimulation of presynaptic fibers happens before the postsynaptic cell fires (Caporale & Dan, 2008; Feldman, 2012). For example, in a CA3-CA1 computational model, Jang et al. especially applied STDP rule to two groups of interneurons for feedforward and feedback inhibition, and found that the two pathways differentially modulate synaptic activity, and inhibitory synaptic weight and synaptic location influenced the STDP profile, suggesting a role of inhibitory network of STDP and in memory processing of hippocampal circuits (Jang & Kwag, 2012). Moreover, Zalay et al. simulated the hippocampal Mf-CA3 network with both di-synaptic inhibition and monosynaptic

excitation, and found that feedforward inhibition is crucial for the high-pass filter function of Mf-CA3 circuits (Fortune & Rose, 2001).

Taken together, this is only a very primitive model of DG-CA3 neuronal networks, and the reality is much more complicated than the constructed model. However, it might serve some purposes in neuroscience research. With more improvement, such models could be potentially used for generating disease models where the behavior of a certain type of neurons was altered. It could also be used for predicting, for example, interneuron subtypes in certain circuits by fine-tuning properties of the neuronal population.


```

223
224 import nest
225 import numpy as np
226 import nest.raster_plot
227 import pylab
228 import matplotlib.pyplot as plt
229 import nest.topology as tp
230
231 aa=np.asarray(a)
232 aaa=aa.ravel()
233 a0=[]
234 for i in range(0,len(aaa)):
235     if (i+301.)/10*aaa[i] !=0:
236         a0.append((i+301.)/10*aaa[i])
237
238 bb=np.asarray(b)
239 bbb=bb.ravel()
240 b0=[]
241 for i in range(0,len(bbb)):
242     if (i+1201.)/10*bbb[i] !=0:
243         b0.append((i+1201.)/10*bbb[i])
244
245 cc=np.asarray(c)
246 ccc=cc.ravel()
247 c0=[]
248 for i in range(0,len(ccc)):
249     if (i+2101.)/10*ccc[i] !=0:
250         c0.append((i+2101.)/10*ccc[i])
251
252 dd=np.asarray(d)
253 ddd=dd.ravel()
254 d1=[]
255 for i in range(0,len(ddd)):
256     if ddd[i] !=0:
257         d1.append(i)
258
259 ee=np.asarray(e)
260 eee=ee.ravel()
261 e1=[]
262 for i in range(0,len(eee)):
263     if eee[i] !=0:
264         e1.append(i)
265
266 ff=np.asarray(f)
267 fff=ff.ravel()
268 f1=[]
269 for i in range(0,len(fff)):
270     if fff[i] !=0:
271         f1.append(i)
272
273 nest.ResetKernel()
274
275 T = 600. # simulation time (ms)
276 dt = 0.1 # simulation resolution (ms)
277
278 pyr = 1600 # number of CA3 pyramidal neurons
279 Ifb = 400 # number of interneurons for feedforward inhibition
280 Ifb = 200 # number of interneurons for feedback inhibition
281 dg = 1600 # number of DG granular cells
282
283 conn_dict2 = {'rule': 'pairwise_bernoulli', 'p': 0.2} # set connection probability
284 conn_dict5 = {'rule': 'pairwise_bernoulli', 'p': 0.5}
285 conn_dict9 = {'rule': 'pairwise_bernoulli', 'p': 0.9}
286
287 # nest.SetKernelStatus({'resolution':dt,'local_num_threads':4})
288
289 syns = nest.GetDefaults('iaf_cond_alpha_mc')['receptor_types']
290 rqs = nest.GetDefaults('iaf_cond_alpha_mc')['recordables']
291 nest.CopyModel('static_synapse', 'prex', {'receptor_type': syns['proximal_exc']})
292 nest.CopyModel('static_synapse', 'soe', {'receptor_type': syns['soma_exc']})
293 conn_dict_dgpyr = {'connection_type': 'divergent', 'mask': {'circular': {'radius': 0.6}, 'kernel': 0.9, 'synapse_model': 'soe'}}
294 nest.CopyModel('static_synapse', 'iffpyr', {'weight': 3.0, 'receptor_type': syns['proximal_inh']})
295 conn_dict_dgiff = {'connection_type': 'convergent', 'mask': {'circular': {'radius': 0.8}, 'kernel': 0.9, 'weights': 5.}}
296 conn_dict_iffpyr = {'connection_type': 'divergent', 'mask': {'doughnut': {'inner_radius': 0.2, 'outer_radius': 0.8}, 'kernel': 0.8, 'synapse_model': 'iffpyr'}}
297 conn_dict_pyrpyr = {'connection_type': 'convergent', 'mask': {'grid': {'rows': 10, 'columns': 10}, 'kernel': 0.5, 'synapse_model': 'prex', 'weights': {'p_center': 1., 'sigma': 5.}}}
298
299 pop_pyr = tp.CreateLayer({'extent': [4.,4.], 'rows': 40, 'columns': 40, 'elements': 'iaf_cond_alpha_mc', 'edge_wrap': True})
300 pop_pyr=nest.GetLeaves(pop_pyr)[0]
301 dVms = [{'soma': {'V_m': -70+16*np.random.rand()}}, {'V_reset': -65.0} for x in pop_pyr]
302 nest.SetStatus(pop_pyr, dVms)
303 pop_dg = tp.CreateLayer({'extent': [4.,4.], 'rows': 40, 'columns': 40, 'elements': 'iaf_neuron', 'edge_wrap': True})
304 pop_dgs=nest.GetLeaves(pop_dg)[0]
305 nest.SetStatus(pop_dgs, [{'tau_m': 20.0, 'V_th': -45.0, 'C_m': 60.0} for x in pop_dgs])
306 nest.SetStatus(pop_dgs, [{'V_m': -70+26*np.random.rand()} for x in pop_dgs])
307 pop_Ifb = tp.CreateLayer({'extent': [4.,4.], 'rows': 20, 'columns': 20, 'elements': 'iaf_neuron', 'edge_wrap': True})
308 pop_Ifbs = nest.GetLeaves(pop_Ifb)[0]
309 nest.SetStatus(pop_Ifbs, [{'tau_m': 15.0, 'V_th': -48.0, 'C_m': 100.0, 'V_m': -50.0, 'V_reset': -50.0} for x in pop_Ifbs])
310 nest.SetStatus(pop_Ifbs, [{'V_m': -50+6*np.random.rand()} for x in pop_Ifbs])
311 pop_Ifb = nest.Create('iaf_neuron', Ifb)
312 nest.SetStatus(pop_Ifb, [{'tau_m': 15.0, 'V_th': -45.0, 'C_m': 100.0, 'V_m': -50.0, 'V_reset': -50.0} for x in pop_Ifb])
313 nest.SetStatus(pop_Ifb, [{'V_m': -50+6*np.random.rand()} for x in pop_Ifb])
314
315 spikeEC=nest.Create('poisson_generator')
316 nest.SetStatus(spikeEC, {'rate': 5000.0}) # input from Entorhinal Cortex
317 spikeDG=nest.Create('poisson_generator')
318 nest.SetStatus(spikeDG, {'rate': 6700.0}) # input from DG
319
320 Tinput=nest.Create('spike_generator',3)
321 nest.SetStatus(Tinput, [{'spike_times':a0}, {'spike_times':b0}, {'spike_times':c0}])
322
323 Sinput=nest.Create('poisson_generator',3)
324 nest.SetStatus(Sinput, [{'rate': 8000.0, 'start': 310.0, 'stop': 360.0}, {'rate': 8000.0, 'start': 370.0, 'stop': 420.0}, {'rate': 8000.0, 'start': 430.0, 'stop': 480.0}])
325
326 noise = nest.Create('poisson_generator', 2)
327 nest.SetStatus(noise, [{'rate': 9700.0}, {'rate': 14300.0}])
328
329 nest.CopyModel('static_synapse', 'soex', {'receptor_type': syns['soma_exc']})
330

```

```

330
331 nest.Connect(spikeDG, pop_dgs, syn_spec={"weight": 2.0})
332 nest.Connect(spikeEC, pop_pyrs, syn_spec = {'receptor_type': syns['distal_exc']})
333 tp.ConnectLayers(pop_dg, pop_pyr, conn_dict_dgpyr)
334 tp.ConnectLayers(pop_dg, pop_Ifb, conn_dict_dgiff)
335 tp.ConnectLayers(pop_Ifb, pop_pyr, conn_dict_Ifbpyr)
336 tp.ConnectLayers(pop_pyr, pop_pyr, conn_dict_pyrpyr)
337 nest.Connect(pop_pyrs, pop_Ifb, conn_dict9, syn_spec = {'model': 'static_synapse', 'weight': 1.})
338 nest.Connect(pop_Ifb, pop_pyrs, conn_dict9, syn_spec = {'receptor_type': syns['proximal_inh'], 'model': 'static_synapse'})
339
340 nest.Connect([Tinput[0]], pop_dgs[0:499], syn_spec={"weight": 3.0})
341 nest.Connect([Tinput[1]], pop_dgs[500:999], syn_spec={"weight": 3.0})
342 nest.Connect([Tinput[2]], pop_dgs[1000:1499], syn_spec={"weight": 3.0})
343
344 p1=np.array(nest.GetLeaves(pop_dg)[0])[np.array(d1)].tolist()
345 nest.Connect([Sinput[0]], p1, syn_spec={"weight": 3.0})
346 p2=np.array(nest.GetLeaves(pop_dg)[0])[np.array(e1)].tolist()
347 nest.Connect([Sinput[1]], p2, syn_spec={"weight": 3.0})
348 p3=np.array(nest.GetLeaves(pop_dg)[0])[np.array(f1)].tolist()
349 nest.Connect([Sinput[2]], p3, syn_spec={"weight": 3.0})
350
351 nest.Connect([noise[0]], pop_pyrs, syn_spec={"weight": 0.15, 'receptor_type': syns['sona_exc']})
352 nest.Connect([noise[1]], pop_pyrs, syn_spec={"weight": -0.1, 'receptor_type': syns['sona_exc']})
353
354 multimeter = nest.Create('multimeter', params = {'record_from': rqs, 'interval': 0.1})
355 spikedetector = nest.Create("spike_detector", params={'withgid': True, 'withtime': True})
356 nest.Connect(multimeter, pop_pyrs[14:18])
357 nest.Connect(pop_pyrs,spikedetector)
358 voltmeterDG=nest.Create('voltmeter')
359 nest.Connect(voltmeterDG, pop_dgs[14:18])
360 voltmeterIff=nest.Create('voltmeter')
361 nest.Connect(voltmeterIff, pop_Ifbs[14:18])
362 voltmeterIfb=nest.Create('voltmeter')
363 nest.Connect(voltmeterIfb, pop_Ifb[14:18])
364 spikedetectorDG = nest.Create('spike_detector')
365 nest.Connect(pop_dgs,spikedetectorDG)
366 spikedetectorIff = nest.Create('spike_detector')
367 nest.Connect(pop_Ifbs,spikedetectorIff)
368 spikedetectorIfb = nest.Create('spike_detector')
369 nest.Connect(pop_Ifb,spikedetectorIfb)
370
371 nest.Simulate(T)
372
373 dnm = nest.GetStatus(multimeter)[0]
374 Vms = dnm["events"]["V_m.s"]
375 ts = dnm["events"]["times"]
376 voltageDG = nest.GetStatus(voltmeterDG)[0]["events"]["V_m"]
377 tsDG = nest.GetStatus(voltmeterDG)[0]["events"]["times"]
378 voltageIff = nest.GetStatus(voltmeterIff)[0]["events"]["V_m"]
379 tsIff = nest.GetStatus(voltmeterIff)[0]["events"]["times"]
380 voltageIfb = nest.GetStatus(voltmeterIfb)[0]["events"]["V_m"]
381 tsIfb = nest.GetStatus(voltmeterIfb)[0]["events"]["times"]
382
383 plt.subplots()
384 plt.plot(tsDG,voltageDG,'r',tsIff,voltageIff,'g',tsIfb,voltageIfb,'k',ts,Vms,'b')
385 plt.legend(('DG', 'Iff', 'Ifb','CA3'),loc='lower right')
386 plt.axis([0, T, -72, -42])
387 plt.ylabel('Membrane potential (mV)')
388 plt.xlabel('time (ms)')
389 plt.title('Responses of iaf_cond_alpha_nc neuron')
390
391 dSD = nest.GetStatus(spikedetector,keys='events')[0]
392 evs = dSD["senders"]
393 ts = dSD["times"]
394 sdDG = nest.GetStatus(spikedetectorDG,keys='events')[0]
395 evsDG = sdDG["senders"]
396 tsDG = sdDG["times"]
397 sdIff = nest.GetStatus(spikedetectorIff,keys='events')[0]
398 evsIff = sdIff["senders"]
399 tsIff = sdIff["times"]
400 sdIfb = nest.GetStatus(spikedetectorIfb,keys='events')[0]
401 evsIfb = sdIfb["senders"]
402 tsIfb = sdIfb["times"]
403
404 fig,ax=plt.subplots()
405 ax.plot(tsDG, evsDG, 'r.', markersize=1, label='DG')
406 ax.plot(tsIff, evsIff, 'g.', markersize=1, label='Iff')
407 ax.plot(tsIfb, evsIfb, 'k.', markersize=1, label='Ifb')
408 ax.plot(ts, evs, 'b.', markersize=1, label='CA3')
409 ax.set_xlim(0,T)
410 ax.set_ylim(pop_pyrs[0], pop_Ifb[-1],pop_Ifbs[-2],pop_dgs[-3])
411 ax.set_xlabel('time (ms)')
412 ax.set_ylabel('neuron id')
413 plt.legend(('Ifb', 'Iff', 'DG','CA3'),loc='lower right')
414

```

```

414
415 rate_DG = float(nest.GetStatus(spikedetectorDG)[0]['n_events']) / T * 1e3 / dg
416 print "\nFiring rate DG = %.1f spikes/s" % (rate_DG)
417 rate_Iff = float(nest.GetStatus(spikedetectorIff)[0]['n_events']) / T * 1e3 / Iff
418 print "\nFiring rate Iff = %.1f spikes/s" % (rate_Iff)
419 rate_Ifb = float(nest.GetStatus(spikedetectorIfb)[0]['n_events']) / T * 1e3 / Ifb
420 print "\nFiring rate Ifb = %.1f spikes/s" % (rate_Ifb)
421 rate_pyr = float(nest.GetStatus(spikedetector)[0]['n_events']) / T * 1e3 / pyr
422 print "\nFiring rate CA3 = %.1f spikes/s" % (rate_pyr)
423
424 plt.subplots()
425 plt.hist(ts, bins=np.arange(0,300,0.1))
426
427 plt.show()
428
429 x1,y1,_=plt.hist(ts, bins=np.arange(29.9,120,0.1))
430 x2,y2,_=plt.hist(ts, bins=np.arange(119.9,210,0.1))
431 x3,y3,_=plt.hist(ts, bins=np.arange(209.9,300,0.1))
432
433 def GetCorr(v,w):
434     u=float(sum(p*q for p,q in zip(v, w)))/float((np.linalg.norm(v)))/float((np.linalg.norm(w)))
435     return u
436
437 u11=GetCorr(x1,aaa)
438 u21=GetCorr(x1,bbb)
439 u31=GetCorr(x1,ccc)
440 u22=GetCorr(x2,bbb)
441 u12=GetCorr(x2,aaa)
442 u32=GetCorr(x2,ccc)
443 u33=GetCorr(x3,ccc)
444 u13=GetCorr(x3,aaa)
445 u23=GetCorr(x3,bbb)
446
447 print u11,u21,u31
448 print u22,u12,u32
449 print u33,u13,u23
450 print 'temporal accuracy:', ((u11-u21)/u11+(u11-u31)/u11+(u22-u12)/u22+(u22-u32)/u22+(u33-u13)/u33+(u33-u23)/u33)/6*100, '%'
451
452 index1=[]
453 for i in range(0,len(ts)):
454     if (ts[i]>=310.0) and (ts[i]<360.0):
455         index1.append(i)
456
457 index2=[]
458 for i in range(0,len(ts)):
459     if (ts[i]>=370.0) and (ts[i]<420.0):
460         index2.append(i)
461
462 index3=[]
463 for i in range(0,len(ts)):
464     if (ts[i]>=430.0) and (ts[i]<480.0):
465         index3.append(i)
466
467 k0=np.unique(evs[index1], return_counts=True)[0]
468 k1=np.unique(evs[index1], return_counts=True)[1]
469
470 for i in range(0,pyr):
471     if not (i in k0):
472         k1=np.insert(k1,i,0)
473
474 m0=np.unique(evs[index2], return_counts=True)[0]
475 m1=np.unique(evs[index2], return_counts=True)[1]
476 for i in range(0,pyr):
477     if not (i in m0):
478         m1=np.insert(m1,i,0)
479
480 n0=np.unique(evs[index3], return_counts=True)[0]
481 n1=np.unique(evs[index3], return_counts=True)[1]
482 for i in range(0,pyr):
483     if not (i in n0):
484         n1=np.insert(n1,i,0)
485
486 k11=k1[2::]
487 m11=m1[2::]
488 n11=n1[2::]
489
490 z11=GetCorr(ddd,k11)
491 z21=GetCorr(eee,k11)
492 z31=GetCorr(fff,k11)
493 z22=GetCorr(eee,m11)
494 z12=GetCorr(ddd,m11)
495 z32=GetCorr(fff,m11)
496 z33=GetCorr(fff,n11)
497 z13=GetCorr(ddd,n11)
498 z23=GetCorr(eee,n11)
499
500 print z11,z21,z31
501 print z22,z12,z32
502 print z33,z12,z23
503 print 'spacial accuracy:', ((z11-z21)/z11+(z11-z31)/z11+(z22-z12)/z22+(z22-z32)/z22+(z33-z13)/z33+(z33-z23)/z33)/6*100, '%'

```

ARTICLE

Received 29 Feb 2016 | Accepted 12 May 2016 | Published 17 Jun 2016

DOI: 10.1038/ncomms11915

OPEN

Early synaptic deficits in the APP/PS1 mouse model of Alzheimer's disease involve neuronal adenosine A_{2A} receptors

Silvia Viana da Silva^{1,2}, Matthias Georg Haber^{3,*}, Pei Zhang^{1,*}, Philipp Bethge¹, Cristina Lemos⁴, Nélio Gonçalves⁴, Adam Gorlewicz¹, Meryl Malezieux¹, Francisco Q. Gonçalves⁴, Noëlle Grosjean¹, Christophe Blanchet¹, Andreas Frick³, U Valentin Nägerl¹, Rodrigo A. Cunha^{4,5} & Christophe Mulle¹

Synaptic plasticity in the autoassociative network of recurrent connections among hippocampal CA3 pyramidal cells is thought to enable the storage of episodic memory. Impaired episodic memory is an early manifestation of cognitive deficits in Alzheimer's disease (AD). In the APP/PS1 mouse model of AD amyloidosis, we show that associative long-term synaptic potentiation (LTP) is abolished in CA3 pyramidal cells at an early stage. This is caused by activation of upregulated neuronal adenosine A_{2A} receptors (A_{2A}R) rather than by dysregulation of NMDAR signalling or altered dendritic spine morphology. Neutralization of A_{2A}R by acute pharmacological inhibition, or downregulation driven by shRNA interference in a single postsynaptic neuron restore associative CA3 LTP. Accordingly, treatment with A_{2A}R antagonists reverts one-trial memory deficits. These results provide mechanistic support to encourage testing the therapeutic efficacy of A_{2A}R antagonists in early AD patients.

¹Interdisciplinary Institute for Neuroscience, University of Bordeaux, CNRS UMR 5297, F-33000 Bordeaux, France. ²BEB PhD program CNC Coimbra, 3004-517 Coimbra, Portugal. ³University of Bordeaux, Neurocentre Magendie, INSERM U862, F-33000 Bordeaux, France. ⁴CNC-Center for Neuroscience and Cell Biology, University of Coimbra, 3004-517 Coimbra, Portugal. ⁵Faculty of Medicine, University of Coimbra, 3004-504 Coimbra, Portugal. * These authors contributed equally to this work. Correspondence and requests for materials should be addressed to C.M. (email: christophe.mulle@u-bordeaux.fr).

Loss of episodic hippocampal-dependent memory is the earliest clinical sign of Alzheimer's disease (AD), consistent with reduced activation of hippocampal regions during memory encoding tasks in patients with mild cognitive impairment¹. Synaptic loss is the best morphological correlate of cognitive impairment in early AD, rather than amyloid-beta plaques, tangle formation or neuronal loss². The CA3 subregion of the hippocampus encodes episodic memories, particularly at the earliest stage of acquisition, presumably by developing instant representations of a context³. The autoassociative network of recurrent connections among CA3 pyramidal cells (PCs) is thought to enable the storage of episodic memories through synaptic plasticity of these associative/commissural (A/C) inputs^{4,5}. In mouse models of AD, synaptic dysfunction has been mostly studied in the CA1 region or dentate gyrus with very few studies addressing deficits in CA3 (ref. 6). Long-term potentiation (LTP) of synaptic transmission at Schaffer collateral-CA1 synapses is generally impaired in mouse models of AD (refs 6,7). Whether synaptic plasticity is affected in the recurrent CA3 network in AD mouse models has not yet been addressed.

Dysregulation of NMDA receptors (NMDAR) has been proposed as a link between A β accumulation and disruption of LTP (ref. 8) although neuromodulation systems may also be impaired. Epidemiologic studies indicate that regular caffeine intake attenuates memory decline during aging⁹ and reduces the risk to develop AD (ref. 10). In animal models of AD, chronic caffeine intake prevents memory deterioration, an effect mimicked by the selective inhibition of A_{2A} receptors (A_{2A}R), which are a main target of caffeine¹¹. Conversely, the overactivation of hippocampal A_{2A}R is sufficient to disrupt memory performance¹². A_{2A}R are upregulated in cortical areas of AD patients¹³ including in the hippocampal formation¹⁴, but the mechanisms by which the blockade of A_{2A}R restores memory impairment are not understood. The impact of A_{2A}R may depend on the stage of progression of the disease, with a role for astrocytic A_{2A}R at late stages¹⁴. Here we provide evidence for early synaptic dysfunction in CA3 PCs in a mouse model of AD, and we explore the implication of NMDAR and A_{2A}R.

Results

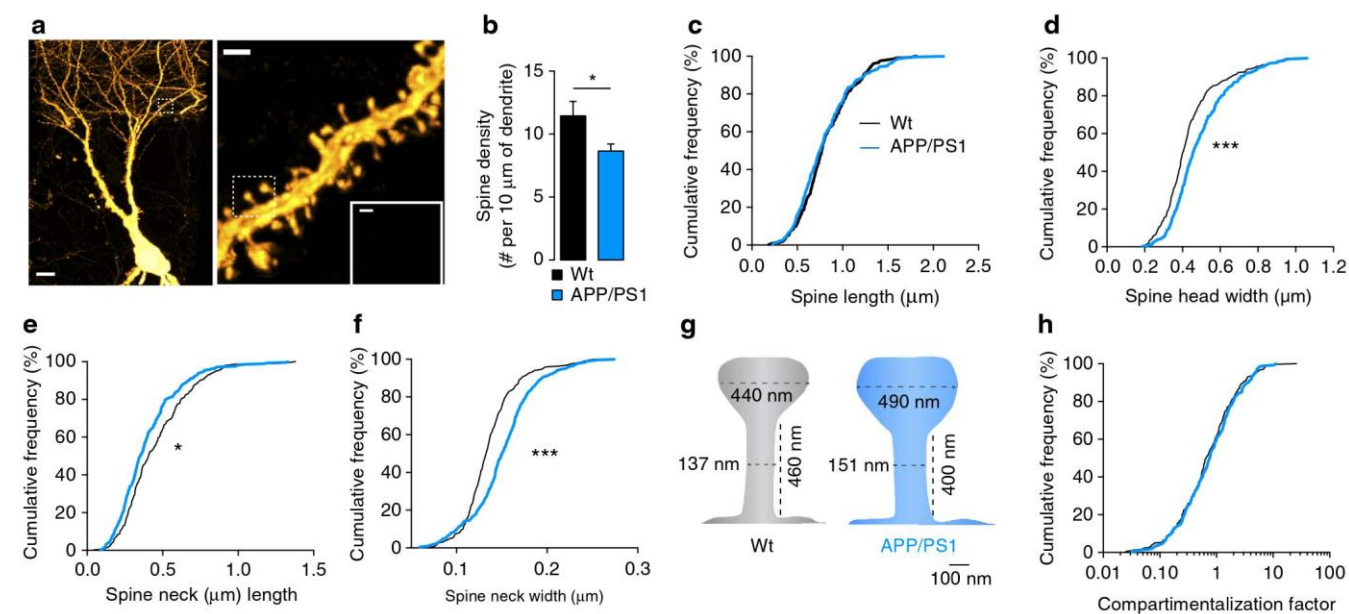
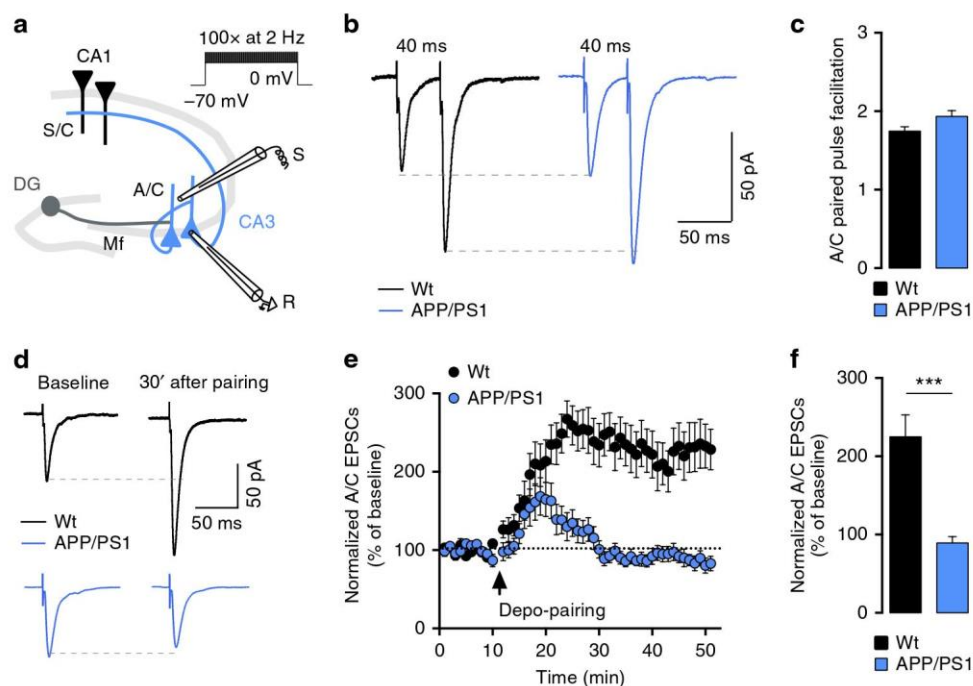
Impaired A/C synaptic plasticity in CA3 in APP/PS1 mice. We performed whole-cell patch clamp recordings of CA3 PCs to characterize the synaptic properties of A/C inputs in 6-month-old male APP/PS1 (Amyloid precursor protein (APP) gene with Swedish mutation and presenilin 1 gene (PS1) with deletion of exon 9) mice at early stages of amyloid-beta deposition¹⁵ when the CA3 region appears largely spared (Supplementary Fig. 1a). We initially recorded excitatory postsynaptic current (mEPSCs), which arise from the different types of glutamatergic synapses impinging on CA3 PCs. The average amplitude of mEPSCs was significantly decreased in APP/PS1 compared with wild-type (wt) mice (wt: 29 ± 2 pA, APP/PS1: 23 ± 1 pA, $P = 0.007$), whereas mEPSC frequency, measured by the inter event interval (IEI), was only minimally affected (wt: 0.7 ± 0.2 s, APP/PS1: 0.9 ± 0.1 s; Supplementary Fig. 2a,b). The decreased amplitude was mainly attributed to mEPSCs with amplitudes < 50 pA, suggesting that large amplitude mEPSCs arising from mossy fibre-CA3 synapses¹⁶ were not affected (Supplementary Fig. 2b). We further found that the paired-pulse ratio (PPR) of A/C synaptic responses was not different between APP/PS1 (1.9 ± 0.1) and wt mice (1.8 ± 0.1), arguing against presynaptic alterations (Fig. 1a–c). Pairing of presynaptic activation and postsynaptic depolarization induces an NMDAR-dependent

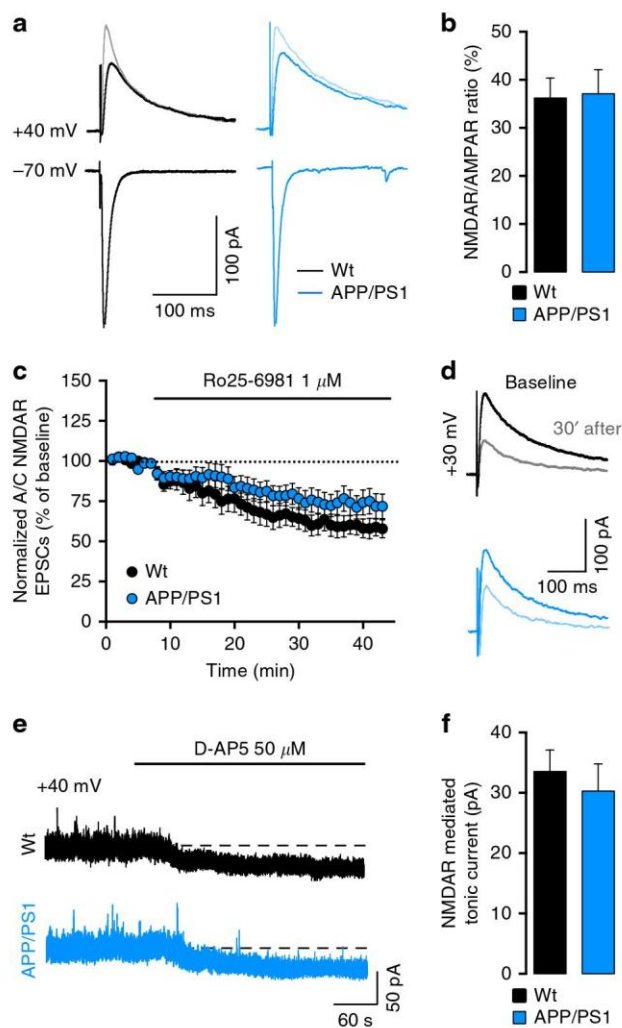
LTP of A/C inputs in CA3 PCs (ref. 17). Pairing A/C stimulation (100 stimuli at 2 Hz) with a depolarization to 0 mV (Fig. 1a) induced a robust LTP of AMPA-EPSCs in wt mice ($218 \pm 38\%$), which was absent in APP/PS1 mice ($93 \pm 12\%$, $P < 0.0001$; Fig. 1d–f).

To explore the mechanisms underlying the abolition of LTP of A/C inputs in APP/PS1 mice, we first tested whether this loss was correlated with morphological alterations of CA3 dendritic spines. Bilateral stereotaxic injections of retrograde rabies virus expressing green fluorescent protein (GFP; RABV)¹⁸ into CA1 were performed to specifically label CA3 PCs. We quantified spine density and morphology in these neurons using stimulated emission depletion (STED) microscopy. We found a decrease in the density of spines in the *stratum radiatum* of APP/PS1 mice (wt: 11.5 ± 1.1 spines per $10 \mu\text{m}$, APP/PS1: 8.7 ± 0.6 spines per $10 \mu\text{m}$, $P = 0.037$; Fig. 2a,b). STED microscopy allowed us to examine traditionally neglected key nanoscale features of spine morphology (Supplementary Table 2). Although spine length was similar in both genotypes (wt: $0.82 \pm 0.02 \mu\text{m}$, APP/PS1: $0.81 \pm 0.02 \mu\text{m}$, Fig. 2c), we found a marked shift to larger spine heads in APP/PS1 mice (wt: $0.44 \pm 0.01 \mu\text{m}$, APP/PS1: $0.49 \pm 0.01 \mu\text{m}$, $P < 0.0001$, Fig. 3d), in parallel with shorter and wider spine necks (Fig. 2e,f and Supplementary Table 2). As synapse compartmentalization is strongly shaped by spine morphology¹⁹, these changes (Fig. 2g) could potentially explain the decreased ability of the pairing protocol to induce LTP. However, the compartmentalization factor, which is a measure of biochemical compartmentalization of spine synapses (see definition in the Methods section), was preserved because the effects of the structural changes cancelled each other out (Fig. 2h). Thus the morphological phenotype seems insufficient to explain the absence of LTP observed at A/C synapses in APP/PS1 mice.

Loss of A/C LTP is not associated with alterations of NMDAR.

We tested whether dysregulation of NMDAR function, which has been implicated in impaired synaptic plasticity in models of AD (ref. 8), may be causally related to the loss of LTP in APP/PS1 mice. Insufficient membrane potential depolarization can be ruled out as a possible cause for the loss of A/C LTP in APP/PS1 mice as our LTP protocol controls for postsynaptic membrane potential. We found no difference in synaptic NMDAR/AMPA ratio between wt ($36 \pm 4\%$) and APP/PS1 mice ($37 \pm 5\%$; Fig. 3a,b). However, the relative expression of different GluN2 NMDAR subunits at synapses may strongly modulate plasticity²⁰, and the toxic effects of amyloid-beta oligomers applied in cultured neurons and acute slices is thought to involve the GluN2B subunit^{21,22}. We found no difference in the inhibition of NMDAR EPSC amplitude by Ro25-6981 ($1 \mu\text{M}$), a selective antagonist of GluN2B-containing NMDAR (wt: $59.0 \pm 5.9\%$, APP/PS1: $73.6 \pm 7.6\%$; Fig. 3c,d) or in NMDAR EPSC decay time (Supplementary Fig. 3a,b), ruling out a major change in GluN2 subunit composition of synaptic NMDAR in CA3 PCs in APP/PS1 mice. The subcellular localization of NMDAR (synaptic versus extrasynaptic) leads to the activation of different intracellular signalling pathways; importantly, extrasynaptic NMDAR were shown to be essential for amyloid-beta mediated toxicity^{23,24}. We evaluated extrasynaptic NMDAR by measuring the amplitude of tonic NMDAR-mediated currents recorded at $+40$ mV. Tonic currents were blocked to the same extent by the NMDAR antagonist D-AP5 ($50 \mu\text{M}$) in both genotypes (wt: 34 ± 4 pA and APP/PS1: 30 ± 5 pA; Fig. 3e,f). In addition, the blockade of tonic currents by Ro25-6981 ($1 \mu\text{M}$) did not indicate any change in GluN2B content (Supplementary Fig. 3c,d). Finally, we reasoned that if dysregulation of NMDAR was responsible for





the loss of A/C LTP in APP/PS1 mice, then the selective potentiation of synaptic NMDAR by D-serine²⁵ may rescue plasticity. Enhancement of synaptic NMDAR by bath application of 10 μ M D-serine (~20% increase in current amplitude,

Supplementary Fig. 3e–g) did not rescue A/C LTP in APP/PS1 mice ($109.0 \pm 9.5\%$, Supplementary Fig. 3h–j and Supplementary Table 1) or alter A/C LTP in wt mice. Hence, the complete loss of A/C LTP in 6-month-old APP/PS1 mice does not appear to correlate with alterations in the function or GluN2B content of neither synaptic nor extrasynaptic NMDAR.

Inhibition of A_{2A}R rescues A/C LTP in APP/PS1 mice. A_{2A}R control synaptic plasticity¹², are involved in memory impairment^{11,26} and are upregulated in the brain of AD patients^{13,14} and animal models of AD^{27,28}. We used a binding assay on isolated CA3 synaptic membranes and showed a robust increase of A_{2A}R density in 6-month-old APP/PS1 mice (wt: 38 ± 7 fmol per mg protein; APP/PS1: 75 ± 6 fmol per mg protein, $P=0.002$; Fig. 4a). Based on these results, we investigated if a short incubation of the slices for 10 min with the selective A_{2A}R antagonist SCH58261 (50 nM) could affect synaptic plasticity at A/C synapses. Strikingly, SCH58261 rescued in large part A/C LTP in APP/PS1 synapses ($160 \pm 16\%$), in comparison with APP/PS1 slices treated with vehicle solution ($98 \pm 9\%$, Fig. 4b–d). ZM241385 (50 nM), a chemically distinct and selective A_{2A}R antagonist was equally effective in rescuing A/C LTP (wt: $165.9 \pm 20.8\%$, $P=0.063$; Fig. 4d and Supplementary Table 1). The difference in mEPSCs amplitude observed between APP/PS1 and wt littermates (wt: 25.2 ± 1.5 pA; APP/PS1: 19.5 ± 1.1 pA) was not rescued by a short incubation with SCH58261 (wt_{SCH}: 24.0 ± 1.5 pA; APP/PS1_{SCH}: 19.6 ± 0.8 pA; $P=0.006$ for genotype effect; $P=0.173$ for drug effect, Supplementary Fig. 4a–c). Similarly, the distribution of mEPSCs amplitudes in both genotypes was not altered by SCH58261 (Supplementary Fig. 4b). Although SCH58261 incubation caused a small alteration in the distribution of IEIs between mEPSCs (Supplementary Fig. 4d), it did not cause any significant effect on the mean IEI values (wt_{Baseline}: 0.4 ± 0.1 s; wt_{SCH58261}: 0.6 ± 0.2 s; APP/PS1_{Baseline}: 0.6 ± 0.2 s; APP/PS1_{SCH58261}: 0.8 ± 0.2 s, Supplementary Fig. 4e).

A_{2A}R act synergistically with mGluR5 in hippocampal neurons²⁹, and mGluR5 antagonists rescue contextual fear conditioning in APP/PS1 mice³⁰. Accordingly, we found that a selective antagonist of mGluR5 (MTEP, 10 μ M) also rescued A/C LTP levels in APP/PS1 mice to values similar to those obtained with the A_{2A}R antagonist SCH58261 ($164 \pm 28\%$, Fig. 5a–c). A combined incubation with both MTEP and SCH58261 did not further increase A/C LTP levels in 6-month-old APP/PS1 mice ($163 \pm 18\%$, $P=0.008$, Fig. 5a–c and Supplementary Table 1), suggesting that A_{2A}R and mGluR5 operate through a common pathway to impair LTP. Importantly, these antagonists did not further increase the level of A/C LTP in wt mice (Supplementary Fig. 5a–c and Supplementary Table 1). Pharmacological inhibition of either A_{2A}R or mGluR5 did not fully rescue A/C LTP, possibly because the antagonists attenuate LTP in wt mice (Supplementary Fig. 4e,f). Adenosine neuromodulation depends on a balanced activation of inhibitory A₁R and A_{2A}R. We tested whether adenosine A₁R levels were comparatively affected by using a binding assay on purified CA3 synaptic membranes and observed a modest increase of A₁R density in 6-month-old APP/PS1 mice (wt: 938.2 ± 27.2 fmol per mg protein; APP/PS1: 1044.0 ± 19.0 fmol per mg protein, $P=0.002$; Supplementary Fig. 6a). To test if this alteration in A₁R density affected A/C synapses, we recorded evoked AMPAR EPSCs and bath applied 100 nM DCPCX (a selective A₁R antagonist). DCPCX equally increased the amplitude of AMPAR EPSCs in APP/PS1 ($134.0 \pm 11.0\%$) and wt mice ($143.3 \pm 17.8\%$, Supplementary Fig. 6b–d), arguing for similar levels of A₁R at those synapses.

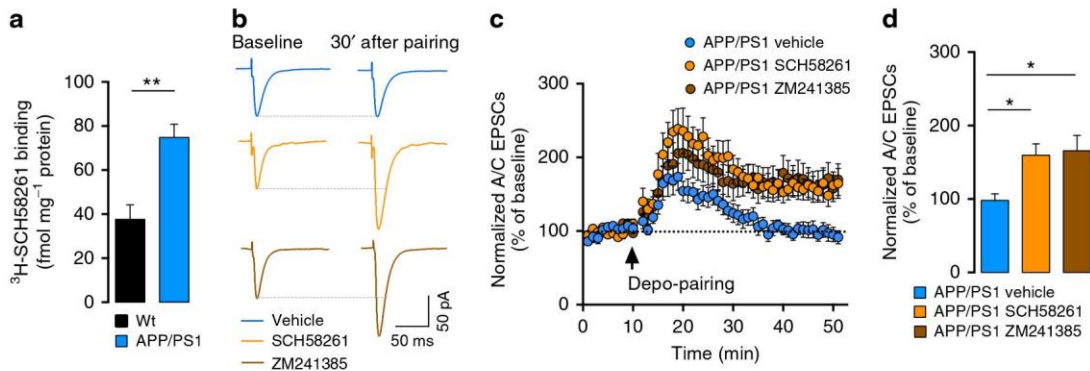


Figure 4 | Blockade of neuronal $A_{2A}R$ restores synaptic plasticity in CA3 PCs. (a) The density of $A_{2A}R$ is increased in synaptic membranes prepared from the CA3 region of APP/PS1 mice compared with wt littermates ($n = 6$, $**P = 0.002$, Mann-Whitney test). (b) Example traces representing a 10 min average of A/C-EPSCs before and 30 min after depo-pairing LTP protocol in the presence of SCH58261 (50 nM) or ZM241385 (50 nM). (c) Summary time course of normalized A/C-EPSCs recorded from APP/PS1 mice during LTP protocol performed in the presence of the two different $A_{2A}R$ antagonists or in control conditions. (d) Bar graph representing mean LTP amplitude recorded at 30–40 min after depo-pairing protocol represented in c. A 10-min incubation period with two different classes of $A_{2A}R$ antagonists, SCH58261 ($n = 11$) and ZM241385 ($n = 12$, $P = 0.006$ Kruskal-Wallis test with Dunn's multiple comparison test), rescued the LTP of A/C synapses in APP/PS1 mice ($n = 11$ for vehicle, Supplementary Table 1). Electrophysiology recordings were performed in the presence of 10 μM bicuculline and 3 μM CGP55845.

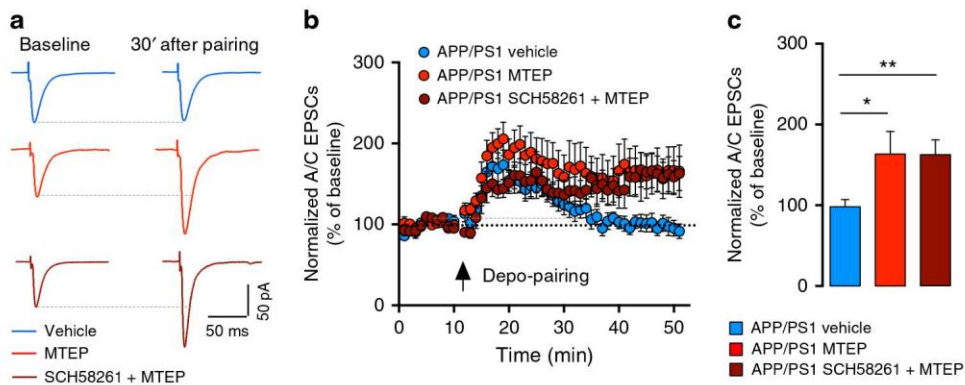


Figure 5 | $A_{2A}R$ and mGluR5 are involved in the loss of A/C LTP in APP/PS1 mice. (a) Example traces representing the average of A/C-EPSCs 10 min before and 30 min after depo-pairing LTP protocol. Recordings were performed in the presence of 10 μM bicuculline and 3 μM CGP55845. (b) Summary time course of normalized A/C-EPSCs recorded from APP/PS1 mice during LTP protocol performed in the presence of MTEP (10 μM) and MTEP + SCH58261 (50 nM). (c) Bar graph representing mean LTP amplitude recorded at 30–40 min after depo-pairing protocol represented in b. A 10-min incubation with MTEP ($n = 12$) or MTEP + SCH58261 ($n = 11$, $P = 0.008$ Kruskal-Wallis test with Dunn's multiple comparison test) rescued the LTP of A/C synapses in APP/PS1 mice ($n = 11$ for vehicle group, Supplementary Table 1).

$A_{2A}R$ antagonists can prevent $A\beta$ -induced memory impairment in mice²⁶. We thus tested whether SCH58261 (intraperitoneal injection, 0.1 mg per kg, for 6–7 days) could revert deficits in one-trial memory tasks, which depend on CA3 circuits^{3,4}, in a different group of 6-month-old APP/PS1 mice. When tested in the object displacement paradigm (30 min inter-trial interval), APP/PS1 mice showed impaired recognition of a displaced object, which was rescued on $A_{2A}R$ inhibition (Fig. 6a–c). Wt mice treated with saline displayed a higher displacement index ($68.2 \pm 4.0\%$), whereas APP/PS1 mice did not show any preference for the displaced object ($54.9 \pm 4.1\%$, $P = 0.034$ for genotype effect, Fig. 6b). This difference between genotypes was abrogated by SCH58261 treatment (wt_{SCH58261}: $63.5 \pm 3.3\%$; APP/PS1_{SCH58261}: $60.0 \pm 3.7\%$). Likewise, $A_{2A}R$ inhibition rescued the performance of APP/PS1 mice in a modified Y-maze task (30 min inter-trial interval), as shown by the increase in the percentage of time exploring the novel arm (wt_{Saline}: 40.5 ± 2.4 and APP/PS1_{Saline}: $34.6 \pm 2.8\%$, $P = 0.024$ for genotype effect, Fig. 6d–f). APP/PS1 mice treated with SCH58261 showed no difference in the time spent in the novel arm ($42.7 \pm 4.1\%$) when compared with wt mice treated with SCH58261 ($46.9 \pm 2.7\%$, Fig. 6e).

$A_{2A}R$ expressed in CA3 PCs are involved in A/C LTP deficits. Since both neuronal¹² and astrocytic $A_{2A}R$ (ref. 14) may control memory performance, we sought to understand if the pharmacological rescue of plasticity at early stages of AD is either due to an action on neurons or glia. For this purpose, we employed a knockdown approach of $A_{2A}R$ in neurons using a VSV-G-coated lentivirus expressing shRNA against $A_{2A}R$ and a fluorescent marker (sh $A_{2A}R$, see validation in Supplementary Information). One month after stereotaxic infection in the CA3 region of 5-month-old APP/PS1 mice, a few GFP-positive CA3 PCs (sh $A_{2A}R^+$, expressing the shRNA) could be identified in hippocampal slices (Fig. 7a). To check for neuronal tropism of the lentiviral construct, we injected eGFP-sh $A_{2A}R$ lentivirus in the CA3 region of wt mice and performed immunohistochemistry on hippocampal sections. We observed a near exclusive co-localization with the neuronal marker NeuN for virally injected eGFP-positive cells, whereas no co-localization was observed with the astrocytic marker glial fibrillary acidic protein (GFAP) (Supplementary Fig. 7).

We found that genetic silencing of $A_{2A}R$ in individual CA3 PCs rescued LTP of A/C synapses in these cells in 6-month-old APP/

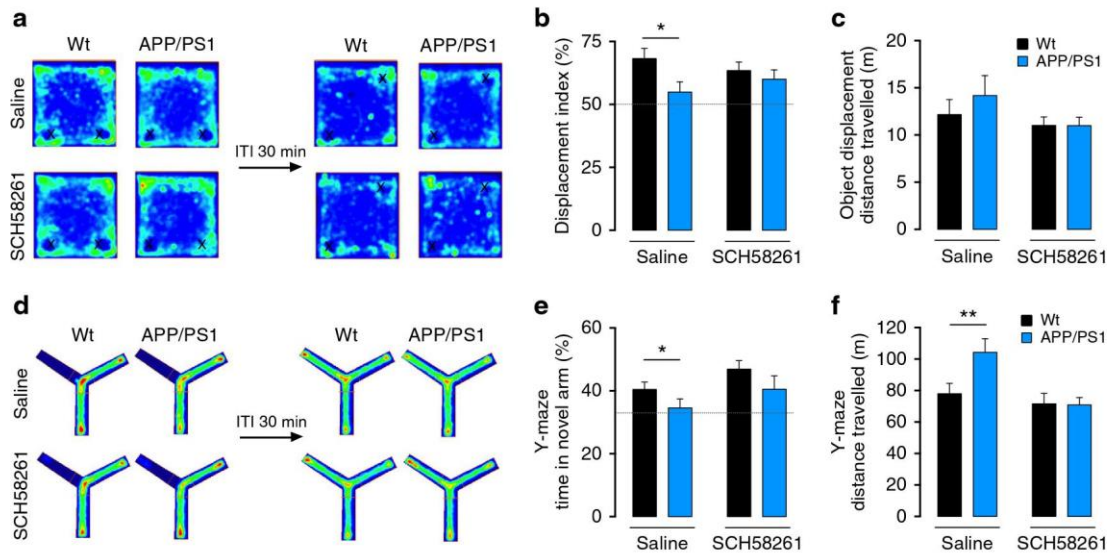


Figure 6 | Treatment with $A_{2A}R$ blockers restores one-trial memory impairment in APP/PS1 mice. (a) Average occupation plot representing the pattern of exploration of the mice in the object displacement test. Mice were treated with SCH58261 or saline for 6 days (b) Bar graph representing the percentage of time spent by mice exploring the displaced object. The displacement index is higher in $w_{t_{saline}}$ ($n = 12$) when compared with $APP/PS1_{saline}$ ($n = 9$, $*P = 0.034$, two-way ANOVA, genotype effect; Sidak's multiple comparisons test $w_{t_{saline}}$ versus $APP/PS1_{saline}$, $*P = 0.0374$). By contrast, whereas SCH58261 is devoid of effects in wt ($n = 11$, Sidak's multiple comparisons test $w_{t_{saline}}$ Saline versus $w_{t_{SCH58261}}$, $P = 0.594$), it reverted the lower percentage of time that APP/PS1 mice interacted with the novel object ($n = 10$, Sidak's multiple comparisons test $APP/PS1_{saline}$ versus $APP/PS1_{SCH58261}$, $P = 0.6047$). (c) No alterations were found in the average distance travelled by mice ($w_{t_{saline}}$: 12.2 ± 1.6 m, $n = 12$, $APP/PS1_{saline}$: 14.5 ± 1.9 m, $n = 9$, $P = 0.405$; $w_{t_{SCH58261}}$: 11.0 ± 0.9 m, $n = 11$, $APP/PS1_{SCH58261}$: 11.0 ± 0.9 m, $n = 10$, $P = 0.096$, two-way ANOVA). (d) Average occupation plot of exploration in the Y-maze task. (e) Bar graph representing the percentage of time spent in the novel arm by wt and APP/PS1 mice treated with SCH58261 or saline for 7 days. When comparing APP/PS1 ($n = 9$) and wt ($n = 12$) mice in the saline groups, we observed a difference in the percentage of time spent in the novel arm ($*P = 0.024$, two-way ANOVA, genotype effect; Sidak's multiple comparisons test $w_{t_{saline}}$ versus $w_{t_{SCH58261}}$, $*P = 0.0347$). SCH58261 treatment had no effect in wt groups ($n = 11$, Sidak's multiple comparisons test $w_{t_{saline}}$ versus $w_{t_{SCH58261}}$, $P = 0.901$), but reverted the memory deficit in APP/PS1 mice ($n = 10$, Sidak's multiple comparisons test $APP/PS1_{saline}$ versus $APP/PS1_{SCH58261}$, $P = 0.410$) (f) Distance travelled in the test phase of the modified Y-maze ($w_{t_{saline}}$: 77.9 ± 6.7 m, $n = 12$, $APP/PS1_{saline}$: 104.2 ± 8.6 m, $n = 9$; $w_{t_{SCH58261}}$: 71.5 ± 6.7 m, $n = 11$, $APP/PS1_{SCH58261}$: 70.8 ± 4.8 m, $n = 10$, $**P = 0.006$, two-way ANOVA with Sidak's multiple comparisons test). Horizontal dashed lines in b and e represent the random displacement values for better visualization.

PS1 mice. LTP of A/C synapses did not recover in uninfected neighbouring $sh-A_{2A}R^{-/-}$ CA3 PCs ($shA_{2A}R^{+}$: $174 \pm 20\%$, $shA_{2A}R^{-}$ cells: $92 \pm 9\%$, $P = 0.001$; Fig. 7a–c) or in cells infected with scramble RNA ($scrRNA^{+}$: $105 \pm 8\%$, Fig. 7d–f). A/C LTP could be rescued in $scrRNA^{+}$ cells with a short SCH58261 incubation as in control APP/PS1 CA3 PCs ($168 \pm 6\%$, $P = 0.0014$, Fig. 7d–f). Furthermore, the extent of A/C LTP following SCH58261 incubation was not different between $scrRNA^{+}$ and $shRNA^{+}$ cells ($173 \pm 15\%$), indicating that the $A_{2A}R$ shRNA occludes the effect of SCH58261 in $shRNA^{+}$ cells and not in control neurons (Supplementary Table 1 and Fig. 7f). This strongly suggests that the loss of A/C LTP is caused by gain of function of $A_{2A}R$ specifically in neurons and not glial cells at this early stage of AD. In addition, removal of $A_{2A}R$ from a single postsynaptic CA3 PC is sufficient to rescue A/C LTP, strongly suggesting a pathological function of postsynaptic $A_{2A}R$.

Discussion

This study provides the first characterization of AD-related synaptic impairment in the autoassociative network of recurrent connections between CA3 PCs which is crucially involved in the initial encoding of memory^{3,5}. At early stages of AD pathology in APP/PS1 mice, we found no major alteration of basal AMPAR or NMDAR-mediated transmission. However, we show that associative pairing between presynaptic A/C stimulation and postsynaptic spiking failed to induce LTP in single CA3 PCs.

Studies of LTP in mouse models of AD have often provided contradictory results⁶, possibly depending on the age and on the

experimental conditions to induce plasticity. In CA1, LTP of field EPSPs induced by high-frequency stimulation is attenuated—but not abolished—in an age-dependent manner in 4–6-month-old APP/PS1 mice³¹. Spine shape may determine the ability of synapses to undergo LTP by tuning biochemical and electrophysiological compartmentalization¹⁹. We observed a moderate decrease of spine density, which may correlate with subtle differences in the frequency of mEPSCs but cannot explain the abolition of LTP. Using STED microscopy, we unravelled subtle changes in spine necks and spine heads in 6-month-old APP/PS1 mice. However, as the morphological changes are predicted to leave biochemical synapse compartmentalization intact, it is unlikely that differences in synapse morphology can account for the LTP defect in APP/PS1 mice.

Associative LTP of A/C synapses depends on the activation of NMDAR during the induction phase^{17,32}. Many studies have proposed NMDAR and in particular GluN2B-containing NMDAR as targets for A β peptides⁸. GluN2B is thought to be important for induction of LTP, due to the direct physical interaction of its C-terminal tail with CaMKII (ref. 33). Our electrophysiological results indicate that the loss of A/C LTP in APP/PS1 mice cannot be attributed to decreased function of synaptic NMDAR or to a major change of GluN2B-containing NMDAR. We found no change in tonically activated extrasynaptic NMDAR, which were proposed to participate in the inhibition of LTP by soluble A β oligomers²³. In line with our data, chronic blockade of GluN2B-containing NMDAR does not rescue behaviour or spine morphology in PS2APP mice³⁴. We do not exclude the possibility that NMDAR

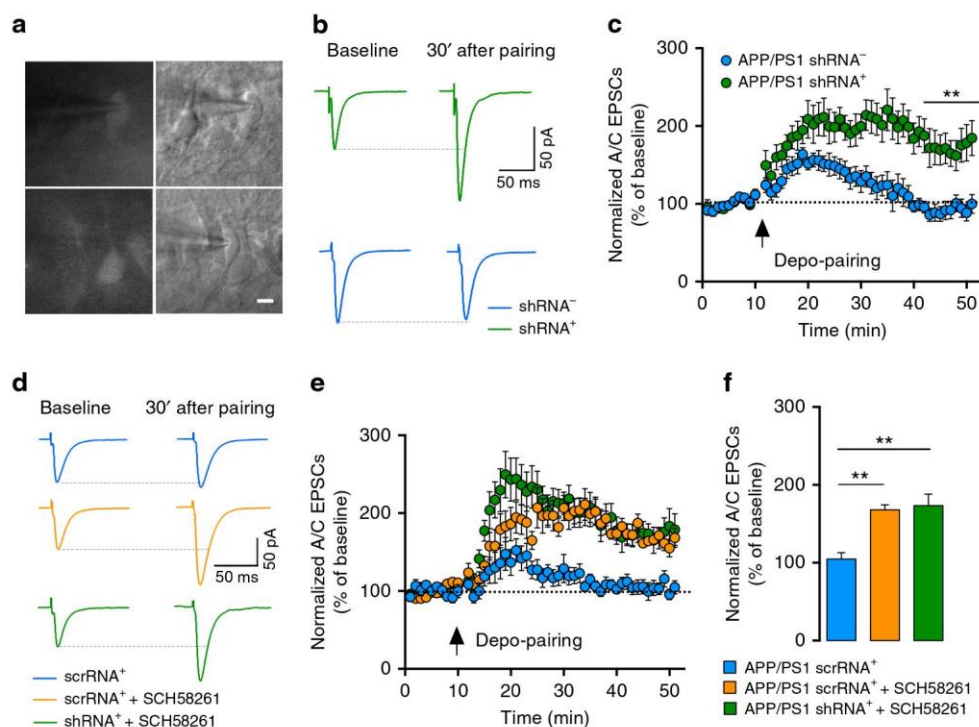


Figure 7 | Genetic silencing of neuronal $A_{2A}R$ restores A/C LTP. (a) Example pictures of CA3 PCs infected with shRNA lentivirus. Infected cells (shRNA⁺) and non-infected cells (shRNA⁻) in the proximity of infected cells were patched for the experiments in (b). Scale bar represents 10 μ m. (b) Example traces representing average A/C-EPSCs 10 min before and 30 min after LTP protocol in infected and non-infected cells. (c) Summary time course of normalized A/C-EPSCs during depo-pairing LTP protocol, recorded from APP/PS1 mice injected with $A_{2A}R$ shRNA; in shRNA⁺ cells there was a rescue of the A/C LTP ($n = 7$) that was absent in shRNA⁻ cells ($n = 7$, $**P = 0.001$, Mann-Whitney test, Supplementary Table 1). (d) Example traces representing the average of A/C-EPSCs 10 min before and 30 min after depo-pairing LTP protocol in infected cells with $A_{2A}R$ shRNA or scrRNA lentivirus. (e) Summary time course of normalized A/C-EPSCs recorded from APP/PS1 mice during LTP protocol performed in scrRNA⁺ cells ($n = 9$) in the absence and scrRNA⁺ ($n = 7$) or shRNA⁺ cells ($n = 9$) in the presence of SCH58261 (50 nM). (f) Bar graph representing mean LTP amplitude recorded at 30–40 min after depo-pairing protocol represented in e. APP/PS1 cells infected with scrRNA virus (scrRNA⁺) do not sustain LTP (Supplementary Table 1). A 10-min incubation period with SCH58261 increased LTP amplitude of scrRNA⁺ cells to levels similar to the genetic silencing of $A_{2A}R$ (Supplementary Table 1). In shRNA⁺ cells, SCH58261 did not further increase the LTP levels ($**P = 0.0014$, Kruskal-Wallis test with Dunn's multiple comparison test between groups). All electrophysiology recordings were performed in the presence of 10 μ M bicuculline and 3 μ M CGP55845.

signalling may be strongly compromised at later stages of AD. However our study suggests that NMDAR may not be a valid target to restore hippocampal synaptic plasticity and the moderate cognitive deficits at early stage of AD pathology, in support of the lack of clinical efficiency of memantine in mild AD (ref. 35).

Strikingly, we found that the acute inhibition of $A_{2A}R$ by two different antagonists rescued LTP of A/C synapses, strongly suggesting that activation of $A_{2A}R$ by ambient adenosine or by adenosine produced during the LTP induction protocol disrupts synaptic plasticity in APP/PS1 mice. This raises several questions with regards to the source of adenosine, the cellular localization of $A_{2A}R$ and the signalling mechanism engaged to compromise LTP. On brain injury, $A_{2A}R$ undergo increased expression in both neurons and glia^{14,36}; their conditional removal from astrocytes ameliorates spatial memory selectively at later stages of AD (ref. 14). Our pharmacological experiments do not allow distinguishing effects of the antagonists on glial cells, pyramidal neurons or interneurons. However, we found that $A_{2A}R$ are upregulated in CA3 synapses at early stages of AD. Moreover, silencing $A_{2A}R$ selectively in an individual CA3 PC is sufficient to restore A/C LTP. Thus, the increase of $A_{2A}R$ in postsynaptic CA3 PCs can by itself explain the abolition of LTP. Although we cannot rule out an increased expression of astrocytic $A_{2A}R$ at this stage, this is not required for impaired plasticity. Interestingly, the

prevention of synaptic plasticity can be relieved by acute antagonism of $A_{2A}R$, providing some potential therapeutic strategies for early cognitive dysfunction in AD. Accordingly, the treatment of APP/PS1 mice with SCH58261 improved their one-trial spatial memory performance in both an object displacement and a modified Y-maze task, which is thought to depend on the activity of CA3 circuits³. More work is necessary to establish clear links between impaired A/C LTP and rapid acquisition of memory. Systemic administration of SCH58261 did not affect recall in one-trial memory tasks in wt mice, although it partly inhibited A/C LTP. Conversely, in APP/PS1 mice, behavioural deficits were markedly improved by SCH58261 administration, although A/C LTP deficit was only partly reverted.

The mechanism by which activation of upregulated $A_{2A}R$ compromises LTP is unknown. Because silencing $A_{2A}R$ in an individual CA3 PC rescues LTP, postsynaptic $A_{2A}R$ are likely at play. $A_{2A}R$ are pleiotropic receptors activating multiple G proteins and transducing pathways; the extended C-terminal domain of $A_{2A}R$ engages several proteins other than those canonically involved in signalling by G-protein coupled receptors³⁷. Furthermore, the signalling pathways of upregulated $A_{2A}R$ in disease-like conditions may be altered³⁸. Which of these multiple transducing systems is associated with the control by $A_{2A}R$ of synaptic plasticity is still unknown.

The ability of both A_{2A}R and mGluR5 to disrupt A/C LTP is intriguing and may provide a clue to the underlying mechanism²⁹. Interestingly, A_{2A}R and mGluR5 are both also necessary for the expression of LTP of NMDARs in CA3 PCs (ref. 39). The molecular mechanisms by which the amount of A_{2A}R is increased at early stages in neurons and at later (neuroinflammatory) stages in astrocytes still remains to be deciphered, in view of the complexity of the A_{2A}R gene promoter⁴⁰. Upregulation of A_{2A}R at early stages may not be restricted to CA3 PCs and may include interneurons and interneuronal connections to regulate the overall excitability of CA3 circuits⁴¹. Nevertheless, postsynaptic A_{2A}R in CA3 PCs, rather than such possible alterations account for deficits in A/C CA3 LTP.

Overall, the present study shows that at the early onset of AD-like features in APP/PS1 mice, associative long-term synaptic plasticity is abolished in CA3 PCs due to the activation of upregulated A_{2A}R in the postsynaptic compartment rather than to modifications of synaptic structure or NMDAR function. Our results are based on one-mouse model of AD, and it would certainly be important in the near future to extend this to other experimental models of cognitive deficits. Nonetheless, the exquisite ability of A_{2A}R blockade to restore the defective A/C CA3 LTP in APP/PS1 mice, in parallel to studies linking A_{2A}R to cognitive deficits^{11,12}, provides an additional mechanistic support to encourage testing the therapeutic efficacy of A_{2A}R antagonists in early AD patients.

Methods

Mice. APP/PS1 mice were obtained from Jackson's Lab and used according to regulations of the University of Bordeaux/CNRS Animal Care and Use Committee. The colony was maintained in a hemizygote state by crossing transgenic female mice to B6C3F1/J male mice. Throughout all their life, littermate wt and APP/PS1 male mice were housed in groups ranging from 4 to 10 animals per cage with free access to water and food. The large transparent plexiglas cages were kept in a temperature-regulated room on a 12-h light/dark cycle, and protected from exterior pathogens by a filter. All experiments were performed in the light phase of the circadian cycle in 6 months APP/PS1 and age-matched wt littermates.

Electrophysiology. Mice were anaesthetized with a ketamine (75 mg kg⁻¹) and xylazine (10 mg kg⁻¹) mix and intracardially perfused with ice-cold oxygenated cutting solution composed of 200 mM of sucrose, 20 mM glucose, 0.4 mM CaCl₂, 8 mM MgCl₂, 2 mM KCl, 1.3 mM NaH₂PO₄, 26 mM NaHCO₃, 1.3 mM ascorbate, 0.4 mM pyruvate and 3 mM kynurenic acid (pH 7.3). When the solution coming out of the heart was free of blood, mice were decapitated and the head immersed in ice-cold cutting buffer. The brain was quickly dissected and parasagittal slices (350 μm thick) were cut using a Leica vibratome (Leica VT 1200S) in the same solution. The slices were kept for 20 min in an oxygenated resting artificial cerebrospinal fluid (aCSF) containing 110 mM NaCl, 2.5 mM KCl, 0.8 mM CaCl₂, 8 mM MgCl₂, 1.25 mM NaH₂PO₄, 26 mM NaHCO₃, 0.4 mM ascorbate, 3 mM pyruvate and 14 mM glucose (pH 7.3) at 33 °C in the presence of kynurenic acid (2 mM). The slices were then transferred into another resting aCSF, now without kynurenic acid and left at room temperature for a maximum of 6 h after cutting. All drugs from Sigma-Aldrich, unless otherwise stated (see Supplementary Table 3 for details).

Cells were identified by differential interference contrast microscopy using an Olympus fixed stage upright microscope (BX51WI) equipped with a ×40 magnification immersion objective. Once at the electrophysiology set-up, slices were superfused with oxygenated (95% O₂, 5% CO₂) aCSF composed by 125 mM NaCl, 2.5 mM KCl, 2.3 mM CaCl₂, 1.3 mM MgCl₂, 1.25 mM NaH₂PO₄, 26 mM NaHCO₃ and 14 mM glucose (pH 7.4) and with 10 μM bicuculline. A period of 10 min was allowed for slice stabilization and removal of the excess Mg²⁺ from the resting solution. Whole-cell recordings were made at room temperature from visually identified CA3 PCs with borosilicate glass capillaries with 3–5 MΩ resistance filled with 140 mM CsMSO₃, 2 mM MgCl₂, 4 mM NaCl, 0.2 mM EGTA, 5 mM phosphocreatine, 3 mM ATPNa₂, 0.4 mM GTP and 10 mM HEPES (pH 7.2). The access resistance was <20 MΩ and the experiment was discarded if it changed by >20%. EPSCs were evoked using a patch pipette (~5 MΩ) filled with aCSF positioned in the CA3 stratum radiatum. The identification of the A/C synaptic currents was performed according to the following criteria: (1) frequency facilitation not >1.2 when switching stimulation from 0.1 to 1 Hz, (2) paired-pulse facilitation ratio <3 and (3) EPSCs decays free of a secondary peak that might indicate the presence of polysynaptic contamination. No liquid-junction potential correction was used. Recordings were made using an EPC10.0 amplifier (HEKA

Elektronik), filtered at 0.5–1 kHz and analysed using IGOR Pro and Neuromatic V2.6 softwares.

Stereotaxic injections and viral vectors. A small hairpin (sh) RNA was engineered to target the mouse A_{2A}R (shA_{2A}RNA), with the following sequence: 5'-CTA GTT TCC AAA AAG AAC AAC TGC AGT CAG AAA TCT CTT GAA TTT CTG ACT GCA GTT GTT-3' and 5'-CGG GGA TCT GTG GTC TCA TAC AGA AC-3'. These oligomers and the H1 forward primer 5'-CAC CGA ACG CTG ACG TCA TCA ACC CG-3' were used for PCR with the pBC-H1 plasmid (pBC; Stratagene, Amsterdam, The Netherlands) containing the H1 promoter (GenBank: X16612, nucleotides 146–366) as a template. The silencing H1-shRNA cassettes were inserted into the lentivector plasmid SIN-cPPT-PGK-EGFP-WHV-LTR-TRE-RFA together with an EGFP reporter gene. As a control, we engineered a lentivector expressing a scrambled sequence of the RNA targeting A_{2A}R (scrRNA). Both the shA_{2A}RNA and scrRNA were packaged in VSV-G-coated lentiviral vectors. Lentivectors were produced in HEK293T cells, with a four-plasmid system, as previously described⁴² and the lentiviral particles content was determined by assessing HIV-1 p24 antigen levels (Gentaur, Spain). Viral stocks were stored at -80 °C until use and were thawed on ice before their *in vivo* administration. For control experiments, the lentivectors were administered to mice anaesthetized with avertin (240 μg g⁻¹, i.p.) and placed in a stereotaxic frame (Stoelting, Wood Dale, USA). To test the *in vivo* efficiency of the shA_{2A}RNA, we first injected the lentivector (286,000 ng of p24 antigen per ml) unilaterally into the mouse striatum, where the high density of A_{2A}R allows a faithful quantification of A_{2A}R downregulation. Mice received 1.4 μl of shA_{2A}RNA or scrRNA (0.2 μl per min) with an automatic injector (Stoelting) in the following coordinates: antero-posterior: +0.6 mm; medio-lateral: ±1.8 mm; and ventral: -3.3 mm. After 3 weeks, an immunohistochemical analysis of the percentage striatal area labelled with eGFP (ref. 43) showed that the lentivectors transfected 27.2 ± 2.7% (n = 4) of the volume of dorsal striatum. This caused a 68 ± 8% (n = 4) decrease of A_{2A}R mRNA expression, evaluated by quantitative PCR (ref. 44) and a 55 ± 6% (n = 4) decrease of A_{2A}R protein density in the striatum, as evaluated by Western blot analysis⁴⁵. Mice were kept in their home cages for 4 weeks before being killed for preparation of slices and recording of transfected and non-transfected neurons, identified by the presence or absence of eGFP. The estimated amount of cells transfected varied from experiments to experiments and was ~15 cells per slice and 600 cells per infection (similar profile to Supplementary Fig. 6).

The GFP expressing RABV were stereotaxically injected as previously described⁴⁶ in CA1 stratum radiatum and the cellular CA3 morphology was analysed after 6 days. For STED microscopy, we performed immunohistochemistry (anti-GFP Alexa 488) on 60 μm brain sections to further increase the signal to background ratio.

Immunohistochemistry. (a) For immunolabelling performed on RABV infected brains, coronal sections (60 μm) were washed three times with 0.5% Triton-X100 (TX) in 1 × PBS (20 min each) and pre-incubated 1 h in a serum solution (goat serum 10% + 0.5% TX in 1 × PBS). The sections were washed three times with 1 × PBS and immersed in the primary antibody solution (rabbit anti-GFP antibody A11122, Invitrogen; 1/1,000 in 0.5% TX in 1 × PBS) for 24 h at 4 °C on a shaker. After washing four times with 1 × PBS, the sections were incubated with the secondary antibody (goat anti-rabbit Alexa Fluor 488 antibody, A11008 from Invitrogen; 1/1,000 diluted in 1 × PBS + 0.5% TX) for 2 h at room temperature. The brain sections were mounted in ProLong Gold Antifade mounting medium (Invitrogen/Molecular Probes) and covered by individual round glass coverslips of 18-mm diameter (0.17 ± 0.01 mm thick). (b) Immunolabelling for detection of amyloid plaques was performed as described above, using a primary antibody raised against human amyloid-beta peptides (polyclonal rabbit antibody, 1/500; ABCAM ab2539) and goat anti-rabbit secondary antibody coupled with Alexa Fluor 488. (c) Immunohistochemistry to determine the cell types infected in the hippocampal CA3 area was performed on sections from lentivirus-infected mice as described above, using following antibodies: anti-NeuN (mouse Millipore MAB377, 1/400), anti-GFAP (rabbit Millipore AB5804, 1/1,000), donkey anti-mouse secondary antibody coupled Alexa Fluor 594 (1/200) and donkey anti-rabbit secondary antibody coupled Alexa Fluor 594 (1:200).

STED microscopy and morphometric analysis. Super-resolved images of spine morphology were obtained with a custom-built STED microscope with a nominal spatial resolution of 50 nm. All images were acquired in the stratum radiatum above the CA3b region as stacks of 10 z-sections with a step size of 192 nm and a pixel size of 40 nm × 40 nm. For spine counts and density calculations over large field-of-views (image from Fig. 2a left and data Fig. 2b), a home-built two-photon microscope, (λ_{exc} = 920 nm) equipped with a water-immersion objective (60X LUMFI, 1.1 NA, Olympus) was used as previously described⁴⁷. For more detailed analyses of spine morphology we used a home-built STED microscope. It was based on an inverted microscope (DMI 6000 CS Trino, Leica), using a pulsed-laser diode (PDL 800-D, Picoquant) for excitation (λ_{exc} = 485 nm, ~90 ps) and a Ti:Sa-OPO system (Chameleon, Coherent; OPO, APE) for fluorescence quenching (λ_{STED} = 595 nm, ~200 ps), as described previously⁴⁸. The pulses of originally 200 fs duration were stretched to ~300 ps by dispersion via a 100-m-long

polarization-preserving fiber (Schäfer + Kirchhoff, Hamburg, Germany). To create the STED focal doughnut, a polymeric phase plate (RPC Photonics, Rochester, NY) was introduced into the path of the expanded STED beam, imprinting a helical phase ramp onto the wavefront. The STED and excitation pulses were synchronized via external triggering of the laser diode, and the delay was adjusted with a custom-built electronic delay generator. Both beams were overlapped with a dichroic mirror (AHF Analytentechnik, Tübingen, Germany), and focused onto the fixed sample by an oil objective (HCX PL APO, 1.47 NA, $\times 100$; Leica, Wetzlar, Germany). A telecentric beam scanner (Yanus IV, TILL Photonics, Gräfelfing, Germany) with scan and tube lenses from the microscope manufacturer was used to steer the beam. Focusing by the objective was controlled via a piezo actuator (P-721 PIFOC, PI Physik Instrumente, Karlsruhe, Germany). The fluorescence was collected episcopically using a dichroic mirror and a 525/50 band-pass filter, and imaged onto a multimode optical fiber connected to an avalanche photodiode (SPCM-AQR-13-FC, PerkinElmer, Waltham, MA). Images were acquired using ImSpector software (courtesy of A. Schönle, Max Planck Institute for Biophysical Chemistry, Göttingen, Germany). All morphological measurements were done using a custom-made plug-in for ImageJ where the spine length was measured from the base of the dendrite to the edge of the head, following the curvature of the spine neck. Spine neck width is reported as the average from multiple spine neck profiles, drawn orthogonal to the spine neck curvature. Spine head width was measured orthogonal to the axis of the spine neck. The length and width of each spine neck was determined by measuring the full width at half-maximum of a Gaussian fit applied to line profiles across the spine neck.

To evaluate the impact of nanoscale alterations in spine morphology on diffusional coupling, we calculated the compartmentalization factor, which is defined as:

$$CF = \frac{V * L}{A}$$

where V is the spine head volume, L the spine neck length and A the cross-sectional area of the spine neck. compartmentalization factor corresponds to the time constant τ of diffusional recovery ($\tau = \frac{V * L}{A * D}$) after a step change in concentration of a molecule with a diffusion coefficient D , serving as a quantitative measure of the degree of biochemical compartmentalization of a synapse⁴⁹.

Binding assays. On collection, the two hippocampi from each mouse were stored at -80°C . The hippocampi were then frozen in ice-cold Krebs solution (140 mM NaCl, 5 mM KCl, 25 mM HEPES, 1 mM EDTA, 10 mM glucose and pH 7.4) and sliced in a McIlwain chopper (800 μm). Each individual slice was then placed on a rubber surface, over a drop of ice-cold Krebs solution, and CA3 subslices were manually dissected under microscope magnification⁵⁰. To purify synaptic membranes, the CA3 subslices from each animal were placed in an eppendorf with 500 μl of ice-cold sucrose solution (0.32 M) containing 50 mM Tris-HCl, 2 mM EGTA and 1 mM dithiothreitol, pH 7.6, homogenized with a micro-Potter-Elvehjem and centrifuged at 3,000g for 10 min at 4°C . The supernatants were collected, centrifuged at 14,000g for 20 min at 4°C and the pellet was resuspended in 500 μl of a 45% (v/v) Percoll solution made up in a Krebs solution. After centrifugation at 14,000g for 2 min at 4°C , the top layer was removed (synaptosomal fraction), washed in 500 μl of Krebs solution and vigorously resuspended in 500 μl of Tris/Mg solution (50 mM Tris and 10 mM MgCl_2 , pH 7.4). The mixtures were centrifuged at 30,000g for 30 min to pull-down synaptic membranes and resuspended in 500 μl of Tris/Mg solution with 4 U ml^{-1} adenosine deaminase (Sigma), to remove endogenous adenosine. We have previously shown that the synaptic membranes provide an enrichment of markers of nerve terminals (SNAP-25, syntaxin-1) and of the postsynaptic density (PSD-95), which display a $<2\%$ contamination with astrocytic material, as gauged by the western blot evaluation of GFAP in the purified synaptosomes used to prepare synaptic membranes⁵¹.

To evaluate the binding density of $A_{2A}R$, we used ^3H -SCH58261 {2-(2-Furanyl)-7-(2-phenylethyl)-7H-pyrazolo[4,3-e][1,2,4]triazolo[1,5-c]pyrimidin-5-amine}, which binds selectively cortical $A_{2A}R$ (ref. 52), whereas the binding density of $A_{1}R$ was determined using ^3H -1,3-dipropyl-8-cyclopentylxanthine (DPCPX). Binding of ^3H -SCH58261 (specific activity of 77 Ci mmol^{-1} ; prepared by Amersham and generously offered by Dr Ennio Ongini, Shering-Plough, Milan, Italy) or of ^3H -DPCPX (specific activity of 102.1 Ci mmol^{-1} ; DuPont NEN, Boston, MA, USA) was for 2 h at room temperature with 6.5–13.5 $\mu\text{g ml}^{-1}$ of synaptosomal protein in a final volume of 200 μl in Tris/Mg solution containing 4 U ml^{-1} adenosine deaminase with a single supra-maximal and selective concentration of ^3H -DPCPX (10 nM) or of ^3H -SCH58261 (6 nM). Specific binding was determined by subtraction of the non-specific binding, which was measured in the presence of 1 μM 8-[4-[(2-aminoethyl)amino]carbonylmethyl-oxypheyl]xanthine (XAC), a mixed $A_1/A_{2A}R$ antagonist. Each binding assay data point was performed in duplicate. The binding reactions were stopped by vacuum filtration through glass fibre filters (B filters) using a 12-wells-Millipore harvester. The filters were then placed in scintillation vials and 4 ml of scintillation liquid cocktail (AquaSafe 500 Plus Ready Safe) was added. Radioactivity was determined after at least 12 h with a counting efficiency of 55–60% using a Tricarb 2900TR liquid scintillation analyser (Perkin Elmer). After subtraction of the non-specific from the total binding, the disintegration per min values corresponding to the specific binding were converted into absolute amounts fmol of bound ^3H -

SCH58261 or ^3H -DPCPX, which was normalized per mg of protein, quantified with the BCA method.

Behavioural experiments. The behavioural tasks, namely the modified Y-maze and object location tasks, were performed as a measurement of short-term spatial memory (to focus on CA3 region) and based on the innate preference of rodents to explore novelty. All the behavioural tests were performed during the light phase of the circadian cycle (between 08:30–02:00 hours), under red/low light (12lx). The intraperitoneal injection of SCH58261 was performed around 06:00 hours, to avoid the repercussion of the acute effect of the drug in the behavioural tasks and in the animal sleeping cycle. Between each trial the apparatus was cleaned with a 10% ethanol solution to avoid odour cues. At the end of the training trial, the mice were removed from the apparatus and kept in an individual cage during the inter-trial intervals. Mice were first tested in the object displacement test and then tested 12 h later in the modified Y-maze test, based on our previous validation that there is no influence of the object displacement test on the modified Y-maze test with this temporal interval either in control mice or in mice with memory deficits (Rial *et al.*⁵³). All experimental data was analysed using the ANY-maze video tracking system, Stoelting, US.

Modified Y-maze. The Y-maze apparatus consisted of three arms (42 cm long, 15 cm height and 8 cm large) made from impermeable black formica with a brown floor and was placed at the ground level. During the training phase, one arm was blocked by a removable door. In this phase the mice were positioned in the start arm, facing the center of the maze and allowed to explore only two arms (start and other) for 8 min. The test was performed 30 min later (with the door blocking the novel arm removed) and the animal were placed again in the start arm and allowed to explore the three arms during 8 min. The number of entries and the time spent in each arm was measured, as previously described^{53,54}.

Object displacement/object location. The object displacement protocol used was carried out as previously described^{53,54}. Briefly, the mice were first habituated for a 10-min period in the empty apparatus, a box composed by transparent plexiglass walls and brown floor (50 cm wide, 50 cm deep and 40 cm high), placed at the ground level. In the training phase, performed 24 h after the habituation phase, two identical plastic 50 ml Falcon tubes filled with dyed sterile water were placed 15 cm away from the walls of the arena. The mice were placed at the center of the apparatus and allowed to explore these two identical objects for 10 min, and we recorded the time spent sniffing/whisking or looking (≤ 1 cm) at the objects. The test was performed 30 min later, where one of the objects was moved creating a different spatial combination for the animal to explore during 5 min; again the time spent exploring the objects in the novel and familiar locations was recorded. All locations for the objects were counterbalanced among the groups. The displacement index was determined by the percentage of the time spent exploring the displaced object (T_{novel}) over the time spent exploring both objects. Displacement index is defined as $(T_{\text{novel}} \times 100)/(T_{\text{novel}} + T_{\text{familiar}})$.

SCH58261 injections (0.1 mg kg^{-1} , i.p.) were done each day, for 7 consecutive days before behavioural evaluation. Electrophysiological experiments were not carried out on animals used for behavioural experiments.

Statistical analysis. All statistical analyses were performed with Prism6 GraphPad Software. Values are presented as mean \pm s.e.m. in the text and figure legends. The data normality was tested using the D'Agostino & Pearson omnibus normality test. If data was normally distributed, a Student's t -test or one-way and two-way analysis of variance (ANOVA; to compare more than two independent groups) was performed; otherwise, a Mann-Whitney test was used (to compare two groups) and Kruskal-Wallis test followed by a Dunn's multiple comparison test (to compare more than two groups). Within-cell comparisons were made with Wilcoxon matched pairs test using non-normalized values. Data distributions were analysed using the Kolmogorov-Smirnov test with the data from wt mice as reference. Statistical differences were considered significant at $P < 0.05$.

Data availability. The data that support the findings of this study are available from the corresponding author on request.

References

- Sperling, R. Functional MRI studies of associative encoding in normal aging, mild cognitive impairment, and Alzheimer's disease. *Ann. N. Y. Acad. Sci.* **1097**, 146–155 (2007).
- Selkoe, D. J. Alzheimer's disease is a synaptic failure. *Science* **298**, 789–791 (2002).
- Kesner, R. P. A process analysis of the CA3 subregion of the hippocampus. *Front. Cell. Neurosci.* **7**, 78 (2013).
- Nakazawa, K. *et al.* Hippocampal CA3 NMDA receptors are crucial for memory acquisition of one-time experience. *Neuron* **38**, 305–315 (2003).
- Rolls, E. T. & Treves, A. The neuronal encoding of information in the brain. *Prog. Neurobiol.* **95**, 448–490 (2011).
- Marchetti, C. & Marie, H. Hippocampal synaptic plasticity in Alzheimer's disease: what have we learned so far from transgenic models? *Rev. Neurosci.* **22**, 373–402 (2011).

7. Sheng, M., Sabatini, B. L. & Südhof, T. C. Synapses and Alzheimer's disease. *Cold Spring Harb. Perspect. Biol.* **4** (2012).
8. Malinow, R. New developments on the role of NMDA receptors in Alzheimer's disease. *Curr. Opin. Neurobiol.* **22**, 559–563 (2012).
9. Ritchie, K. *et al.* The neuroprotective effects of caffeine: a prospective population study (the Three City Study). *Neurology* **69**, 536–545 (2007).
10. Cao, C. *et al.* High Blood caffeine levels in MCI linked to lack of progression to dementia. *J. Alzheimers Dis.* **30**, 559–572 (2012).
11. Dall'Igna, O. P. *et al.* Caffeine and adenosine A2a receptor antagonists prevent β -amyloid (25–35)-induced cognitive deficits in mice. *Exp. Neurol.* **203**, 241–245 (2007).
12. Li, P. *et al.* Optogenetic activation of intracellular adenosine A2A receptor signaling in the hippocampus is sufficient to trigger CREB phosphorylation and impair memory. *Mol. Psychiatry* **20**, 1339–1349 (2015).
13. Albasanz, J. L., Perez, S., Barrachina, M., Ferrer, I. & Martín, M. Up-regulation of adenosine receptors in the frontal cortex in Alzheimer's disease. *Brain Pathol.* **18**, 211–219 (2008).
14. Orr, A. G. *et al.* Astrocytic adenosine receptor A2A and Gs-coupled signaling regulate memory. *Nat. Neurosci.* **18**, 423–434 (2015).
15. Garcia-Alloza, M. *et al.* Characterization of amyloid deposition in the APPsw/PS1E9 mouse model of Alzheimer disease. *Neurobiol. Dis.* **24**, 516–524 (2006).
16. Henze, D. A., Card, J. P., Barrionuevo, G. & Ben-Ari, Y. Large amplitude miniature excitatory postsynaptic currents in hippocampal CA3 pyramidal neurons are of mossy fiber origin. *J. Neurophysiol.* **77**, 1075–1086 (1997).
17. Debanne, D., Gähwiler, B. H. & Thompson, S. M. Long-term synaptic plasticity between pairs of individual CA3 pyramidal cells in rat hippocampal slice cultures. *J. Physiol. (Lond)* **507**(Pt 1): 237–247 (1998).
18. Wickersham, I. R., Finke, S., Conzelmann, K.-K. & Callaway, E. M. Retrograde neuronal tracing with a deletion-mutant rabies virus. *Nat. Methods* **4**, 47–49 (2006).
19. Tønnesen, J., Katona, G., Rózsa, B. & Nägerl, U. V. Spine neck plasticity regulates compartmentalization of synapses. *Nat. Neurosci.* **17**, 678–685 (2014).
20. Paoletti, P., Bellone, C. & Zhou, Q. NMDA receptor subunit diversity: impact on receptor properties, synaptic plasticity and disease. *Nat. Rev. Neurosci.* **14**, 383–400 (2013).
21. Hu, N.-W., Klyubin, I., Anwyl, R., Anwyl, R. & Rowan, M. J. GluN2B subunit-containing NMDA receptor antagonists prevent Abeta-mediated synaptic plasticity disruption *in vivo*. *Proc. Natl Acad. Sci. USA* **106**, 20504–20509 (2009).
22. Rönicke, R. *et al.* Early neuronal dysfunction by amyloid β oligomers depends on activation of NR2B-containing NMDA receptors. *Neurobiol. Aging* **32**, 2219–2228 (2011).
23. Li, S. *et al.* Soluble A oligomers inhibit long-term potentiation through a mechanism involving excessive activation of extrasynaptic nr2b-containing nmda receptors. *J. Neurosci.* **31**, 6627–6638 (2011).
24. Talantova, M. *et al.* A β induces astrocytic glutamate release, extrasynaptic NMDA receptor activation, and synaptic loss. *Proc. Natl Acad. Sci. USA* **110**, E2518–E2527 (2013).
25. Papouin, T. *et al.* Synaptic and extrasynaptic NMDA receptors are gated by different endogenous coagonists. *Cell* **150**, 633–646 (2012).
26. Canas, P. M. *et al.* Adenosine A2A receptor blockade prevents synaptotoxicity and memory dysfunction caused by β -amyloid peptides via p38 mitogen-activated protein kinase pathway. *J. Neurosci.* **29**, 14741–14751 (2009).
27. Arendash, G. W. *et al.* Caffeine protects Alzheimer's mice against cognitive impairment and reduces brain β -amyloid production. *Neuroscience* **142**, 941–952 (2006).
28. Espinosa, J. *et al.* Caffeine consumption prevents memory impairment, neuronal damage, and adenosine A2A receptors upregulation in the hippocampus of a rat model of sporadic dementia. *J. Alzheimers Dis.* **34**, 509–518 (2013).
29. Tebano, M. T. *et al.* Adenosine A2A receptors and metabotropic glutamate 5 receptors are co-localized and functionally interact in the hippocampus: a possible key mechanism in the modulation of N-methyl-D-aspartate effects. *J. Neurochem.* **95**, 1188–1200 (2005).
30. Um, J. W. *et al.* Metabotropic glutamate receptor 5Is a Coreceptor for Alzheimer Ab oligomer bound to cellular prion protein. *Neuron* **79**, 887–902 (2013).
31. Trinchese, F. *et al.* Progressive age-related development of Alzheimer-like pathology in APP/PS1 mice. *Ann. Neurol.* **55**, 801–814 (2004).
32. Rebola, N., Carta, M., Lanore, F., Blanchet, C. & Mulle, C. NMDA receptor-dependent metaplasticity at hippocampal mossy fiber synapses. *Nat. Neurosci.* **14**, 691–693 (2011).
33. Barria, A. & Malinow, R. NMDA receptor subunit composition controls synaptic plasticity by regulating binding to CaMKII. *Neuron* **48**, 289–301 (2005).
34. Hanson, J. E., Pare, J.-F., Deng, L., Smith, Y. & Zhou, Q. Altered GluN2B NMDA receptor function and synaptic plasticity during early pathology in the PS2APP mouse model of Alzheimer's disease. *Neurobiol. Dis.* **74**, 254–262 (2015).
35. Schneider, L. S., Dagerman, K. S., Higgins, J. P. T. & McShane, R. Lack of evidence for the efficacy of memantine in mild Alzheimer disease. *Arch. Neurol.* **68**, 991–998 (2011).
36. Cunha, R. A. & Agostinho, P. M. Chronic caffeine consumption prevents memory disturbance in different animal models of memory decline. *J. Alzheimers Dis.* **20**(Suppl 1): S95–S116 (2010).
37. Zezula, J. & Freissmuth, M. The A2A-adenosine receptor: a GPCR with unique features? *Br. J. Pharmacol.* **153**(Suppl 1): S184–S190 (2008).
38. Dai, S. S. *et al.* Local glutamate level dictates adenosine A2A receptor regulation of neuroinflammation and traumatic brain injury. *J. Neurosci.* **30**, 5802–5810 (2010).
39. Rebola, N., Lujan, R., Cunha, R. A. & Mulle, C. Adenosine A2A receptors are essential for long-term potentiation of NMDA-EPSCs at hippocampal mossy fiber synapses. *Neuron* **57**, 121–134 (2008).
40. Yu, L. *et al.* Characterization of genomic organization of the adenosine A2A receptor gene by molecular and bioinformatics analyses. *Brain Res.* **1000**, 156–173 (2004).
41. Rombo, D. M. *et al.* Synaptic mechanisms of adenosine A2A receptor-mediated hyperexcitability in the hippocampus. *Hippocampus* **25**, 566–580 (2014).
42. de Almeida, L. P., Zala, D., Aebischer, P. & Déglon, N. Neuroprotective effect of a CNTF-Expressing lentiviral vector in the quinolinic acid rat model of Huntington's disease. *Neurobiol. Dis.* **8**, 433–446 (2001).
43. Gonçalves, N., Simões, A. T., Cunha, R. A. & de Almeida, L. P. Caffeine and adenosine A2A receptor inactivation decrease striatal neuropathology in a lentiviral-based model of Machado-Joseph disease. *Ann. Neurol.* **73**, 655–666 (2013).
44. Costenla, A. R. *et al.* Enhanced role of adenosine A2A receptors in the modulation of LTP in the rat hippocampus upon ageing. *Eur. J. Neurosci.* **34**, 12–21 (2011).
45. Rebola, N., Canas, P. M., Oliveira, C. R. & Cunha, R. A. Different synaptic and subsynaptic localization of adenosine A2A receptors in the hippocampus and striatum of the rat. *Neuroscience* **132**, 893–903 (2005).
46. Habler, M. G. *et al.* An anterograde rabies virus vector for high-resolution large-scale reconstruction of 3D neuron morphology. *Brain Struct. Funct.* **220**, 1369–1379 (2015).
47. Bethge, P., Chéreau, R., Avignone, E., Marsicano, G. & Nägerl, U. V. Two-photon excitation STED microscopy in two colors in acute brain slices. *Biophys. J.* **104**, 778–785 (2013).
48. Tønnesen, J., Nadrigny, F., Willig, K. I., Wedlich-Söldner, R. & Nägerl, U. V. Two-Color STED microscopy of living synapses using a single laser-beam pair. *Biophys. J.* **101**, 2545–2552 (2011).
49. Wijetunge, L. S., Angibaud, J., Frick, A., Kind, P. C. & Nägerl, U. V. Stimulated emission depletion (STED) microscopy reveals nanoscale defects in the developmental trajectory of dendritic spine morphogenesis in a mouse model of fragile X syndrome. *J. Neurosci.* **34**, 6405–6412 (2014).
50. Cunha, R. A., Milusheva, E., Vizi, E. S., Ribeiro, J. A. & Sebastião, A. M. Excitatory and inhibitory effects of A1 and A2A adenosine receptor activation on the electrically evoked [3H]acetylcholine release from different areas of the rat hippocampus. *J. Neurochem.* **63**, 207–214 (1994).
51. Quiroz, C. *et al.* Key modulatory role of presynaptic adenosine A2A receptors in cortical neurotransmission to the striatal direct pathway. *Sci. World J.* **9**, 1321–1344 (2009).
52. Lopes, L. V. *et al.* Binding of the prototypical adenosine A2A receptor agonist CGS 21680 to the cerebral cortex of adenosine A1 and A2A receptor knockout mice. *Br. J. Pharmacol.* **141**, 1006–1014 (2004).
53. Rial, D. *et al.* Behavioral phenotyping of Parkin-deficient mice: looking for early preclinical features of Parkinson's disease. *PLoS ONE* **9**, e114216 (2014).
54. Kaster, M. P. *et al.* Caffeine acts through neuronal adenosine A2A receptors to prevent mood and memory dysfunction triggered by chronic stress. *Proc. Natl Acad. Sci. USA* **112**, 7833–7838 (2015).

Acknowledgements

This work was supported by the Centre National de la Recherche Scientifique, the Fundação para a Ciência e a Tecnologia, Santa Casa da Misericórdia, the Fondation France Alzheimer, the Agence Nationale de la Recherche (contract SynflAD), the Conseil Régional d'Aquitaine and the Labex Brain. Cellular imaging was in part performed at the Bordeaux Imaging Center, a service unit of the CNRS-INSERM and Bordeaux University, member of the national infrastructure France BioImaging. We thank Nelson Rebola and Mario Carta for their help with electrophysiology and their constant scientific support, Yoon Cho for her help with behavioural analysis and Melanie Ginger for the rabies virus.

Author contributions

S.V.S. and P.Z. performed the electrophysiology recordings. S.V.S. performed all the electrophysiology analysis. S.V.S. and M.G.H. performed all stereotaxic injections and subsequent immunolabellings. P.B. and V.N. performed STED acquisitions. P.B. and M.G.H. made the imaging analysis. C.L. and N.G. performed and analysed behaviour

experiments. A.G. performed immunostaining anti amyloid-beta plaques. F.Q.G. prepared synaptic membranes. C.B. provided help with electrophysiology analysis. R.A.C. performed binding assays and analysis, and helped with discussion. N.Go. produced shRNA and scrRNA lentiviral constructs and performed expression experiments. M.G.H. and A.F. provided rabies virus. C.M. provided supervision, guided the project and wrote the manuscript together with S.V.S. All authors discussed the results and commented on the manuscript.

Additional information

Supplementary Information accompanies this paper at <http://www.nature.com/naturecommunications>

Competing financial interests: the authors declare no competing financial interests.

Reprints and permission information is available online at <http://npg.nature.com/reprintsandpermissions/>

How to cite this article: Viana da Silva, S. *et al.* Early synaptic deficits in the APP/PS1 mouse model of Alzheimer's disease involve neuronal adenosine A_{2A} receptors. *Nat. Commun.* 7:11915 doi: 10.1038/ncomms11915 (2016).



This work is licensed under a Creative Commons Attribution 4.0 International License. The images or other third party material in this article are included in the article's Creative Commons license, unless indicated otherwise in the credit line; if the material is not included under the Creative Commons license, users will need to obtain permission from the license holder to reproduce the material. To view a copy of this license, visit <http://creativecommons.org/licenses/by/4.0/>

Reduced interaction between mGluR5 and Homer alters the surface dynamics of mGluR5 leading to synaptic NMDA receptor dysfunction and cognitive defects in the mouse model of Fragile X Syndrome

Elisabetta Aloisi^{1,2}, #Katy Le Corf^{1,2}, #Pei Zhang^{3,4}, #Virginie Labrousse^{1,2,3,4}, #Julien Dupuis^{3,4}, Matthias Georg Haberl^{1,2}, Lara Costa⁵, Melanie Ginger^{1,2}, Ryuichi Shigemoto⁶, Rohini Kuner⁷, Anke Tappe Theoder⁷, Filippo Drago⁸, Pier Vincenzo Piazza^{1,2}, Christophe Mulle^{3,4}, Laurent Groc^{3,4}, Lucia Ciranna⁸, §Maria Vincenza Catania^{9,10} and §Andreas Frick^{1,2}

¹*INSERM, Neurocentre Magendie, Physiopathologie de la plasticité neuronale, U862, 33077 Bordeaux cedex, France*

²*Univ. Bordeaux, Neurocentre Magendie, Physiopathologie de la plasticité neuronale, U862, 33077 Bordeaux cedex, France*

³*Interdisciplinary Institute for Neuroscience, IINS-CNRS, UMR 5297, University of Bordeaux, 33077 Bordeaux cedex, France*

⁴*Univ. Bordeaux, Interdisciplinary Institute for Neuroscience, UMR 5297, 33077 Bordeaux cedex, France*

⁵*Department of Clinical and Experimental Medicine, University of Messina, 98125 Messina, Italy*

⁶*IST Austria, Klosterneuburg 3400, Austria*

⁷*Institute for Pharmacology, University of Heidelberg, Im Neuenheimer Feld 366, 69120 Heidelberg, Germany*

⁸*Department of Biomedical and Biotechnological Sciences, University of Catania, 95123 Catania, Italy*

⁹*Institute of Neurological Sciences, National Research Council, ISN-CNR, 95125 Catania, Italy*

¹⁰*IRCCS Oasi Maria SS, 94018 Troina (EN), Italy*

correspondence: andreas.frick@inserm.fr, mariavincenza.catania@cnr.it

#These authors contributed equally

§co-senior authors

SUMMARY

Dysfunction of the metabotropic glutamate receptor subtype 5 (mGluR5) is crucially implicated in the pathophysiology of Fragile X Syndrome (FXS), but the underlying sub-cellular mechanisms are incompletely understood. Here, we probed the consequences of the disrupted mGluR5/Homer scaffold for synaptic and behavioral phenotypes in *Fmr1* knockout (KO) mice. Using single molecule tracking, we found that the lateral mobility and confinement of mGluR5 were exaggerated at synapses in hippocampal *Fmr1* KO neurons, causing an increased synaptic surface co-clustering of mGluR5 and N-methyl-D-aspartate receptor (NMDAR). Interestingly, we detected a reduction in the amplitude of synaptic NMDAR currents and a lack of their mGluR5-activated long-term depression in the hippocampus of *Fmr1* KO mice. All these phenomena were recapitulated in wild-type neurons by peptide-based disruption of mGluR5/Homer scaffold. Importantly, knockdown of the short Homer1a isoform reversed both NMDAR dysfunction and associated cognitive deficits in *Fmr1* KO mice, unveiling novel targets for mGluR5 based therapeutics.

INTRODUCTION

Fragile X syndrome (FXS) is the most common form of inherited intellectual disability and best-known cause of autism (reviewed by (Hagerman, 2002; Abrahams and Geschwind, 2008; Bassel and Warren, 2008)). In most cases FXS is caused by transcriptional silencing of the *FMR1* gene and the ensuing lack of encoded Fragile X Mental Retardation Protein (FMRP) (Penagarikano et al., 2007), an RNA-binding protein that regulates translation and trafficking of its interacting mRNAs in dendrites and axons (Antar et al., 2004; Zalfa et al. 2007; Bassell and Warren, 2008; de Diego Otero et al., 2002; Ferrari et al., 2007; Penagarikano et al. 2007; Santoro et al., 2012). During the last decade numerous FMRP target mRNAs have been identified (Chen et al., 2003; Darnell et al., 2001, Brown et al., 2001; Darnell et al., 2011). In contrast, how these molecules contribute to different features of FXS pathology has been only partially unraveled (Gkogkas et al., 2014; Zhang et al., 2014).

Studies from *Fmr1* knockout (KO) mouse model of FXS provide compelling evidence that an increased expression of a subset of synaptic proteins — and subsequent alteration in synaptic plasticity — underlie the cognitive aspects of this disorder (reviewed by (Pfeiffer and Huber, 2009)). In particular, exaggerated group-I metabotropic glutamate receptor subtype 5 (mGluR5)/protein synthesis-dependent hippocampal long-term depression (LTD) of α -amino-3-hydroxy-5-methyl-4-isoxazole propionic acid receptor (AMPA) currents is a hallmark feature of FXS (Huber et al., 2002; Nosyreva and Huber, 2006). These findings are central to the mGluR5 theory of FXS (Bear et al., 2004). In agreement with this notion, correction of the aberrant mGluR5 signaling, through either pharmacological or genetic means, leads to the rescue of a number of disease phenotypes (Dölen et al., 2007, 2010; Michalon et al., 2012, 2014). Although much work has focused on the protein-synthesis dependent functional consequences of mGluR5 activation, other findings suggest that the intrinsic properties and signal transduction mechanisms of mGluR5 might also be altered in FXS (reviewed by (D'Antoni et al., 2014)). Indeed, previous work has demonstrated an important link between long Homer proteins and mGluR5 at the synapse. In the absence of FMRP, this interaction is reduced (Giuffrida et al., 2005), likely contributing to an altered mGluR5-mediated signaling, neocortical circuit defects and behavioral dysfunction in *Fmr1* KO mice (Ronesi et al., 2008, 2012; Tang and Alger, 2015).

Homer proteins are a family of post-synaptic density (PSD) scaffolding proteins responsible for the link between mGluR5 and other PSD proteins (Tu et al., 1998, 1999). Both long (Homer1b/c, Homer2, and Homer3 — here collectively referred to as Homer) and short (Homer1a) isoforms have been identified; the long Homer isoforms are constitutively expressed, multimerize, and link mGluR5 to signaling pathways within the PSD (reviewed by (Shiraishi-Yamaguchi and Furuichi, 2007)). Homer1a, on the other hand, is an immediate early gene inducible by synaptic activity and functions as a dominant negative regulator of group-I mGluR signaling by disrupting the binding between mGluR5 and Homer (Xiao et al., 1998). Interestingly, mGluR5 and NMDA receptor (NMDAR) are linked together in the PSD

by a Homer-containing complex (Brakeman et al., 1997; Scannevin and Huganir, 2000; Perroy et al., 2008). This organization precludes the direct mGluR5/NMDAR association but can be disrupted by Homer1a (Bertaso et al., 2010; Moutin et al., 2012). The disassembly of the synaptic multimeric mGluR5/Homer complex by Homer1a promotes physical and functional interactions between NMDAR and mGluR5, resulting in mGluR5-mediated inhibition of NMDA currents (Moutin et al., 2012).

The dynamic movement of synaptic components has emerged as a key feature of synaptic transmission and plasticity (reviewed by (Triller and Choquet, 2005, 2008; Anggono and Huganir, 2012)). Indeed, receptors on the neuronal surface constantly switch between mobile and immobile states, driven by thermal agitation and reversible binding to stable elements such as scaffolding proteins, cytoskeletal anchoring slots or extracellular anchors (reviewed by (Choquet and Triller, 2013)). The local enrichment of receptors at the PSD is thought to result from receptor immobilization by stable elements that interact in a biochemical and structural network.

Despite the prominent role of mGluR5 in the regulation of synaptic plasticity and cognition, little is known about mGluR5 surface dynamics at the synapse and how these dynamics modulate interactions with synaptic partners — both under physiological and pathological condition. Importantly, interaction of mGluR5 with Homer proteins at the postsynaptic site regulates lateral diffusion of mGluR5 (Sergè et al., 2002). Here, we explored the dynamics of mGluR5 at hippocampal synapses and the consequences of a potential disrupted interaction with Homer proteins for NMDAR function and plasticity, as well as for related cognitive deficits in *Fmr1* KO mice. We addressed this question using a powerful combination of high-resolution single molecule tracking, electrophysiological and knockdown approaches in hippocampal neurons from wild type (WT) and *Fmr1* KO mice together with behavioral analysis. We found that the lateral mobility of mGluR5 was increased specifically at the synaptic sites in *Fmr1* KO hippocampal neurons and correlated with an increased synaptic confinement and co-clustering of mGluR5 and NMDAR. These changes were most likely the result of the mGluR5/Homer disruption. This led us to investigate changes in synaptic NMDA currents and their long-term depression following mGluR5 activation. Importantly, we found that restoring the mGluR5/Homer interaction by reducing the expression of Homer1a in the hippocampus rescued abnormal NMDAR function and plasticity as well as cognitive deficits in *Fmr1* KO mice. Our data corroborate the view that the regulation of the interaction of mGluR5 with long Homer isoforms represents a promising therapeutic target for FXS.

RESULTS

Increased lateral diffusion of mGluR5 at synapses in *Fmr1* KO neurons

To better dissect the mechanism(s) by which mGluR5 dysfunction causes synaptic abnormalities in *Fmr1* KO mice, we first investigated the lateral mobility of mGluR5 within synapses of hippocampal neurons by employing a quantum dot (QD) based single-molecule tracking approach (Figure 1A). Synapses were labeled using an active mitochondria marker (MitoTracker) to distinguish them from extrasynaptic sites, as previously described (Groc et al., 2007). The analysis of the trajectories of single mGluR5 molecules revealed that their diffusion coefficient was significantly enhanced within the synaptic compartment of *Fmr1* KO as compared with WT neurons (Figure 1B and C; +38,89%; $P < 0.001$). This result indicates an increased mobility of mGluR5 within the synaptic membrane of *Fmr1* KO neurons. Accordingly, the fraction of mobile mGluR5 (diffusion coefficient $> 0.005 \mu\text{m}^2/\text{s}$) at the synapse was higher in *Fmr1* KO neurons (+15.24%; $P < 0.001$). In contrast to the synaptic sites, lateral mobility of mGluR5 at extrasynaptic sites was comparable between *Fmr1* KO and WT neurons (Figure 1D; diffusion coefficient: $P = 0.085$; mobile fraction: $P = 0.7957$).

To determine whether the observed increase in membrane mobility was specific for mGluR5, or a more general phenomenon affecting other glutamate receptors as well, we also quantified the mobility of individual AMPA-type (AMPA) and NMDA-type (NMDAR) glutamate receptors. To this end, we tracked GluA2 and GluN1 receptor subunits comprising the AMPAR and NMDAR tetramer complexes, respectively. The dynamics of these receptor subunits have

been extensively characterized previously using QD-based tracking approaches (Groc et al., 2004; Michaluk et al., 2009; Opazo et al., 2010; Ladépêche et al., 2013; Zhang et al., 2013; Hafner et al., 2015). We found no differences in the lateral diffusion and the mobile fraction of AMPAR within the synaptic compartment (diffusion coefficient: $P = 0.723$; mobile fraction: $P = 0.9094$), whereas a small but significant reduction was detected in the extrasynaptic compartment (diffusion coefficient: -4.39% , $P < 0.001$; mobile fraction: -3.44% ; $P < 0.001$) of *Fmr1* KO neurons (Figure S1). Conversely, NMDAR showed a small yet statistically significant increase in the lateral diffusion both in the synaptic (diffusion coefficient: $+12.73\%$; $P < 0.001$) and the extrasynaptic sites (diffusion coefficient: $+11.26\%$; $P < 0.001$) of *Fmr1* KO neurons, which was not sufficient to affect the fraction of mobile receptors in both compartments (synaptic sites: $P = 0.1734$; extrasynaptic sites: $P = 0.5004$; Figure S2). These data suggest that the absence of FMRP differentially impacts the mobility of mGluR5, AMPAR and NMDAR, with a major effect for mGluR5 at synaptic sites.

Increased mGluR5 lateral diffusion is caused by the disruption of the mGluR5/Homer scaffold

Since Homer isoforms function as anchoring molecules for mGluR5 at synapses (Tu et al., 1998, 1999), we hypothesized that the previously described reduction in mGluR5/Homer interaction (Giuffrida et al., 2005) leads to the exaggerated membrane mobility of mGluR5 in *Fmr1* KO neurons reported here. If our prediction was correct, then disrupting the specific mGluR5/Homer interaction in WT neurons should mimic the disease phenotype. We tested this hypothesis, using a cell-permeable peptide containing the Homer binding motif of mGluR5 (TAT-mGluR5ct; characterized previously in Mao et al 2005; Ronesi et al., 2008, Figure 2A). Indeed, pre-incubation of WT neurons with TAT-mGluR5ct caused an increase in the lateral diffusion and mobile fraction of mGluR5 in the synaptic compartment (Figure 2B-D; diffusion coefficient; $+62.63\%$, $P < 0.001$; mobile fraction $+20.23\%$, $P < 0.001$; WT TAT-mGluR5ct vs WT TAT-mGluR5mu). Importantly, both parameters were now comparable to those of *Fmr1* KO neurons without the peptide (Figure 2C and D; diffusion coefficient, $P > 0.05$; mobile fraction, $P = 0.5047$). As expected, pre-incubation of WT neurons with a peptide containing a mutated Homer binding motif (TAT-mGluR5mu; Mao et al 2005; Ronesi et al., 2008) had no effect on the lateral diffusion of mGluR5 (Figure 2C and D; diffusion coefficient, $P > 0.05$, mobile fraction $P = 0.8943$). Moreover, neither TAT-mGluR5ct nor TAT-mGluR5mu treatment had any effect on the mGluR5 mobility in *Fmr1* KO neurons (Figure 2C and D; diffusion coefficient, $P > 0.05$; mobile fraction, $P = 0.1038$; *Fmr1* KO TAT-mGluR5ct vs *Fmr1* KO TAT-mGluR5mu). Taken together, these experiments provide strong correlative evidence that changes in the lateral diffusion of mGluR5 detected in *Fmr1* KO neurons are indeed due to a disrupted link between the long Homer scaffolding proteins and mGluR5.

Disrupted mGluR5/Homer scaffold leads to an increased surface co-clustering of mGluR5 and NMDAR in *Fmr1* KO neurons

In addition to anchoring mGluR5 at synapses, Homer containing complexes also provide a physical link to NMDARs (Brakeman et al., 1997; Scannevin and Huganir, 2000). We thus explored whether the disrupted mGluR5–Homer scaffold might also alter the interaction between mGluR5 and NMDAR in *Fmr1* KO neurons. In a first set of experiments, we took advantage of the detection accuracy of single QDs (reviewed in (Groc et al, 2007; Triller and Choquet, 2008)) by measuring the synaptic fraction of mGluR5-QD and GluN1-NMDAR-QD co-localized with MitoTracker (Figure 3A). We found that the synaptic fraction of both mGluR5-QD and GluN1-QD was increased in *Fmr1* KO neurons (Figure 3B; mGluR5, $P < 0.001$; GluN1, $P < 0.01$).

This finding provides direct evidence that mGluR5 and NMDAR are more confined within the synapse in *Fmr1* KO neurons, likely increasing the probability of physical interactions between these receptors within a given time window. To examine this further, we performed a triple immunofluorescence labeling experiment for mGluR5, NMDAR and Homer1 (the latter used as a synaptic marker), together with confocal microscopy and posthoc image analysis (Figure 3C-F). Quantitative analysis of the proportion of mGluR5-/Homer1-positive or GluN1-NMDAR-/Homer1-positive intensity (expressed as a function of total mGluR5 or GluN1-NMDAR signal) suggests in increased localization of both

mGluR5 and NMDAR at the synapse in *Fmr1* KO neurons (Figure 3D and E, respectively; mGluR5 $P < 0.001$; NMDAR $P < 0.001$). In addition, combined analysis of all three markers points to a higher degree of co-clustering of mGluR5 and NMDAR at synaptic sites (Figure 3F; $P < 0.05$) further supporting a tighter association of these receptors in the absence of FMRP.

To further examine whether disrupted mGluR5/Homer scaffold might provide a causal mechanism for this increased co-clustering of mGluR5 and NMDAR in *Fmr1* KO neurons, we again exploited the interfering peptide. As expected, the pre-incubation of WT neurons with TAT-mGluR5ct resulted in a significant increase in the mGluR5/NMDAR co-localization (Figure 3G; $P < 0.05$), reflecting the increased percentage of synaptic mGluR5 and NMDAR (Figure S3). However, pre-incubation with TAT-mGluR5mu had no effect (Figure 3G; $P = 0.3426$, Figure S3). Taken together, these data provide strong correlative evidence that the disruption of the mGluR5/Homer crosstalk causes a tighter physical association between mGluR5 and NMDAR at synapses in *Fmr1* KO neurons.

Reduced NMDAR function and plasticity in *Fmr1* KO neurons

The finding that mGluR5 and NMDAR are more closely associated at synaptic sites in *Fmr1* KO neurons prompted us to probe alterations in NMDAR function. Synaptic NMDAR-mediated excitatory postsynaptic currents (EPSC_{S_{NMDA}}) induced by *Schaffer* collateral stimulation were investigated using whole-cell patch-clamp recordings from CA1 pyramidal neurons in acute hippocampal slices (Figure 4A). EPSC_{S_{NMDA}} displayed lower amplitudes in *Fmr1* KO neurons when compared with WT neurons (Figure 4B and C; 46.5 ± 8 nA vs 175 ± 24 nA; $P < 0.001$). Consistently, the NMDA/AMPA ratio was significantly lower in *Fmr1* KO neurons (Figure 4C; *Fmr1* KO: 0.86 ± 0.05 ; WT: 1.60 ± 0.29 ; $P = 0.0094$). These defects in NMDAR function were mimicked in WT neurons by application of the interfering peptide TAT-mGluR5ct (Figure 4B and C; $P < 0.01$; 4B $P < 0.05$). These data thus strongly support our hypothesis that alterations in the membrane dynamics of mGluR5 and its tighter coupling with NMDAR, as a consequence of mGluR5/Homer disruption, mediate abnormal NMDAR function in *Fmr1* KO neurons.

It is well established that the activation of group-I mGluR induces an exaggerated LTD of EPSC_{AMPA} in hippocampal *Fmr1* KO neurons (Huber et al., 2002). LTD of EPSC_{S_{NMDA}} by group-I mGluR activation (Baskys and Malenka 1991; Snyder et al. 2001; Watabe et al. 2002; Ireland and Abraham 2009; Bhouri et al., 2014), however, has not been investigated in *Fmr1* KO mice. In WT hippocampal neurons, DHPG application (100 μ M, 5 min) induced a strong and long-lasting reduction in EPSC_{S_{NMDA}} (Figure 4D). In contrast, this form of synaptic NMDAR plasticity was largely absent in *Fmr1* KO neurons (Figure 4D; $P < 0.001$). As with the enhanced mGluR5/NMDAR co-clustering, this phenotype could also be recapitulated in WT neurons by use of our peptide mimicking approach, suggesting the defective mGluR5/Homer interaction as the underlying cause (Figure 4E-F; $P < 0.01$). These data suggest that the disruption of the mGluR5/Homer scaffold compromises NMDAR function under basal conditions as well as during synaptic plasticity in *Fmr1* KO neurons.

Reduction of Homer1a expression rescues NMDAR function and plasticity

Homer1a is known to antagonize the interaction between mGluR5 and Homer. Thus, we asked whether knocking down Homer1a — an approach that fosters the mGluR5/Homer interaction by increasing the Homer1a/Homer balance (Ronesi et al., 2012) — could correct the dysfunction in NMDAR currents in *Fmr1* KO neurons. To address this question we exploited an AAV vector expressing a small interfering hairpin RNA (shRNA) targeted against the unique 3'-untranslated region of Homer1a mRNA (Tappe et al., 2006; Klugmann and Szumlinski, 2008). A similar vector expressing scrambled shRNA served as control (Tappe et al., 2006; Klugmann and Szumlinski, 2008). AAV vectors were stereotaxically injected into the CA1 area of the hippocampus of *Fmr1* KO mice, and EPSC_{S_{NMDA}} from CA1 pyramidal neurons in acute brain slices were measured four weeks later (Figure 5A). EPSC_{S_{NMDA}} displayed higher amplitudes in *Fmr1* KO neurons expressing the shRNA for Homer1a when compared to *Fmr1* KO neurons expressing the scrambled shRNA (Figure 5B; $P < 0.05$). In addition, the mGluR-dependent LTD of EPSC_{S_{NMDA}} was significantly

increased in *Fmr1* KO neurons expressing the shRNA for Homer1a (Figure 5C; $P < 0.001$). Both findings confirm our hypothesis that mGlu5/Homer disruption can cause abnormal NMDA function and plasticity in *Fmr1* KO neurons.

Reduction of Homer1a expression rescues cognitive defects in *Fmr1* KO neurons

Can the correction of the disrupted mGluR5/Homer scaffold also rescue cognitive defects linked to NMDAR dysfunction? To evaluate the effects of Homer1a reduction on hippocampus dependent memory formation, we used two behavioral procedures — an object-recognition task and contextual fear-conditioning. Both tasks induce robust hippocampus dependent learning with a single training episode, and have previously been utilized for the investigation of memory defects in *Fmr1* KO mice (Paradee et al. 2005; Ventura et al., 2004; Busquets-Garcia et al., 2013; King and Jope, 2013; Oddi et al., 2015). Consistent with the aforementioned studies employing the first-generation *Fmr1* KO mouse line, the second-generation model, used here, exhibited similar decreases in the discrimination index (DI) in the object-recognition task (Figure S5; $P < 0.001$) and in the percentage of freezing compared with WT mice (Figure S5; $P < 0.001$). We then tested whether mGluR5/Homer crosstalk modulation could correct these defects in another batch of behaviorally naive *Fmr1* KO and WT mice, stereotaxically injected with the aforementioned AAV vectors into the CA1 area of the hippocampus. Importantly, Homer1a knockdown in the hippocampus corrected defects in both the object recognition memory (Figure 5D; $P < 0.001$) and context-based fear memory (Figure 5E; $P < 0.05$) in adult *Fmr1* KO mice. Taken together with the aforementioned results, these data strongly support the idea that disruption of mGluR5/Homer scaffold contributes to impairment of hippocampal dependant cognitive function in *Fmr1* KO mice.

DISCUSSION

In spite of the widespread acceptance of the mGluR theory of FXS, the sub-cellular mechanisms underlying mGluR5-dependent alterations in synaptic function and plasticity, as well as the subsequent cognitive phenotypes remain poorly investigated. This is because most studies so far have focused on the altered translational processes and their effect on synaptic plasticity following mGluR5 activation. Recent evidence (Ronesi et al., 2012; Tang and Alger, 2015), however, suggests that certain FXS phenotypes may be mediated by a less well-characterized aspect of mGluR5 dysfunction, namely by a defective mGluR5/Homer interaction leading to a reduced physical association with intracellular signaling pathways. Such defects are suggested to be upstream of protein translation (Ronesi et al., 2012) and may represent a novel therapeutic target for the treatment of FXS.

Here we demonstrate a novel role for mGluR5/Homer interaction in the regulation of mGluR5 surface dynamics and in the mGluR5-dependent modulation of NMDA currents under normal physiological conditions, as well as their pathophysiological modification in FXS. Specifically, we found that the disruption of the mGluR5/Homer association increased the lateral diffusion of mGluR5 at synaptic-, but not extrasynaptic sites, mimicking the phenotype observed in *Fmr1* KO neurons. This increased motility (specifically at the synapse) is in coherence with previous findings showing that long Homer isoforms are enriched at synaptic sites (Xiao et al., 1998). These alterations in receptor dynamics are specific for mGluR5 because the AMPAR subunit, GluA2, which does not bind Homer proteins, did not exhibit alterations in trafficking. Furthermore, although GluN1 also exhibited a slightly higher diffusion coefficient in *Fmr1* KO neurons, this difference was observed both at synaptic and extrasynaptic sites. Other mechanisms, including higher activity of metalloproteinases 9 or CamKII, which are both increased in FXS (Janusz et al., 2013; Zalfa et al., 2003), may impact on NMDAR lateral diffusion (Michaluk et al., 2009; Dupuis et al. 2014).

In addition to the altered receptor dynamics, we observed an increased co-localization of mGluR5 and NMDAR in hippocampal synapses from both *Fmr1* KO neurons or WT neurons treated with the interfering peptide. The higher mobility of mGluR5 in *Fmr1* KO neurons (or interfering peptide-treated WT neurons) and the associated exaggerated synaptic confinement of both mGluR5 and GluN1, might increase the probability of transient interactions between these two receptor types at synapses. Similar findings have been reported following the induction of the immediate early gene

Homer1a, leading to the mGluR5-mediated inhibition of NMDA currents (Moutin et al., 2012). In accordance with these findings, we found that EPSC_{S_{NMDA}} evoked by *Schaffer* collateral stimulation showed lower amplitudes in *Fmr1* KO neurons. Once again, the *Fmr1* KO phenotype was mimicked by application of the competing peptide. Moreover, knocking down Homer1a in the hippocampus of *Fmr1* KO mice rescued the aforementioned defect in EPSC_{S_{NMDA}}. Taken together, our findings suggest that this novel defect in NMDA function in the CA1 of *Fmr1* KO mice is specifically mediated by an altered crosstalk between mGluR5 and NMDA and that this altered crosstalk is influenced by a disruption of the physical interaction between mGluR5 and long Homer isoforms (see model in Figure 6).

NMDAR function has been the subject of previous studies in *Fmr1* KO mice, yet there is little consensus concerning the type and nature of changes observed. While no change in NMDA currents was previously found in CA1 hippocampal pyramidal cells (Hu et al., 2008) and cortex (Desai et al., 2006), several studies show a reduction of synaptic NMDA currents in several brain regions of *Fmr1* KO mouse including the anterior piriform cortex (Gocel and Larson, 2012), dentate gyrus (Yun and Trommer, 2011), prefrontal cortex (Martin et al., 2015), and nucleus accumbens (Neuhofer et al., 2015). One study, conversely, reports a transient increase in NMDAR-dependent LTP in the CA1 of 2-week old animals but not in adults (Pilpel et al., 2009). These differences reported in the literature likely reflect the range of brain regions, experimental protocols and ages of mice used. Interestingly, in accordance with our suggestion that a synaptic deficit of NMDAR in FXS might be caused by a mGluR5-mediated inhibition, the mGluR5 inverse agonist MPEP acutely rescued the increased AMPA/NMDA ratio detected in *Fmr1* KO mice (Martin et al., 2015).

In line with our hypothesis that altered mGluR5 dynamics may impinge on different aspects of NMDAR function in FXS, we also found that mGluR5-mediated LTD of EPSC_{S_{NMDA}} was reduced in *Fmr1* KO neurons. Activation of group-I mGluRs is involved in the induction of NMDAR-dependent synaptic plasticity and it can induce Long Term Potentiation (LTP) or LTD depending on whether the currents are elicited by exogenous NMDA application or synaptic stimulation. Exogenous NMDAR mediated currents are transiently potentiated by group-I mGluR activation (Benquet et al., 2002; Grishin et al., 2004; Heidinger et al., 2002; Mannaioni et al., 2001; Skeberdis et al., 2001; Snyder et al., 2001). Conversely, synaptically elicited EPSC_{S_{NMDA}} undergo depression in response to group-I mGluR activation (Baskys and Malenka 1991; Snyder et al., 2001; Watabe et al. 2002 Ireland and Abraham, 2009). The reasons for this differential response and the mechanisms underlying the mGluR-induced depression of the EPSC_{S_{NMDA}} are poorly understood. Here we suggest that the dynamic remodelling of the link between mGluR5 and Homer proteins plays a key role in the induction of LTD of synaptic EPSC_{S_{NMDA}} in response to group-I mGluR activation. A possible explanation for the reduced mGluR5-dependent NMDA-LTD observed in *Fmr1* KO mice and in the presence of TAT-mGluR5ct peptide is that the increased physical interaction between NMDAR and mGluR5 might prevent NMDAR removal from the synapse, a mechanism that is believed to be responsible for depression of synaptic NMDA currents (Ireland and Abraham, 2009). In line with this interpretation, NMDAR is more confined at synapses in the *Fmr1* KO neurons and after incubation with the TAT-mGluR5ct peptide. Alternatively, mGluR5-mediated post-translational modification of NMDAR facilitated by their physical interaction may influence the ion channel properties of NMDARs. Altered synaptic plasticity of NMDAR might be associated with cognitive impairment in the *Fmr1* KO mouse. Mechanisms of LTP and LTD are believed to be the underlying cellular basis of learning and memory formations and altered mGluR-dependent NMDAR-LTD might impact on these functions in FXS. A role for a reduced Homer-mGluR5 interaction in hippocampal-dependent cognitive impairment induced by social defeat stress, has been recently documented in mice (Wagner et al., 2013). Likewise, a selective overexpression of Homer1a in the dorsal hippocampus impairs spatial working memory (Celikel et al., 2007).

Our finding that mGluR-dependent LTD of NMDA currents is reduced in *Fmr1* KO mice, and that this reduction is strongly correlated with a disruption of the mGluR5/Homer scaffold has important implications, not only for our understanding of the pathophysiology of FXS, but also for future therapeutic approaches. NMDA hypofunction has been considered significant in the context of autism and schizophrenia and its correction by means of mGluR5 positive allosteric modulators has been proposed (Gandal et al., 2012). Genetic or pharmacological reduction of mGluR5 activity

lead to a consistent amelioration of numerous disease phenotypes in the *Fmr1* KO mouse (Bear et al., 2004; De Vrij et al., 2008; Dölen et al., 2007, 2010; Michalon et al., 2012, 2014). In spite of this promise, large scale clinical trials (Hessl et al. 2008; Berry Kravis et al. 2009; Jacquemont et al., 2011; Clinicaltrials.gov) employing novel mGluR5 antagonists have recently been cancelled because of lack of efficacy of the treatment over placebo. Here we propose that new therapeutic approaches aimed at restoring the normal mGluR5/Homer interaction might be considered in FXS. In particular, modulation of mGluR5/Homer interaction might correct phenotypes that are related to NMDA dysfunction. How the loss of FMRP leads to an altered mGluR5/Homer crosstalk is still unknown. Phosphorylation of mGluR5 at the C-terminal Homer interaction domain reduces the affinity of mGluR5 for Homer (Orlando et al., 2009). Therefore, post-translational modification of mGluR5 and/or Homer in *Fmr1* KO mice may underlie the decreased interactions. Given the dynamic nature of mGluR5/Homer interaction, it is tempting to speculate that the effect of mGluR5 blockade on FXS phenotype might critically depend on the condition which exacerbates disruption of mGluR5/Homer interaction. Further studies in human specimens and elucidation of the mechanisms underlying the reduced mGluR5/Homer interaction of FXS might help to clarify this issue.

Our findings demonstrate for the first time an alteration of the mGluR5 dynamics at synapses of *Fmr1* KO neurons and provide a new cellular mechanism by which mGluR5 dysfunction disrupts normal NMDAR synaptic plasticity. This study is not only the first to show that the surface dynamics of mGluR5 at synapses are altered in FXS, but also establishes evidence of how this alteration could contribute to the pathophysiology of FXS. The discovery that an abnormal mGluR5/Homer interaction accounts for much of the complex dysfunction of mGluR5 in FXS will help to facilitate the development of alternative, targeted therapies for this disorder and its co-morbidities, and provide mechanistic links to other genetic causes of autism.

EXPERIMENTAL PROCEDURES

Animals

All experiments were conducted in strict compliance with the European Directive (2010/63/EU), and French and Italian law governing the use of laboratory animals and were approved by the Bordeaux Ethics Committee (C2EA50, authorization #5012024-A) and by the Ethics Committee of Catania University (project # 181). Mice were housed in a SPF animal facility prior to experiments, kept on a 12 h–12 h light–dark cycle and had *ad libitum* access to food and water at all times. Second generation *Fmr1* KO mice (Mijentjes et al., 2006) were used in our study. These mice are distinct from the original *Fmr1* KO mouse genetic line, because they are deficient for both *Fmr1* mRNA and FMRP protein. Mice were backcrossed six generations into a C57BL/6J (Charles River, L'Abresle, France) background and maintained in this mixed background for all experiments. For dissociated neuronal cultures WT and *Fmr1* KO embryos were generated by crossing homozygous (*Fmr1*^{+/+} X *Fmr1*^{+/-} or *Fmr1*^{-/-} X *Fmr1*^{+/-}) progenitor mice. For electrophysiology, male WT and *Fmr1* KO littermates were generated by crossing a heterozygous (*Fmr1*^{+/-}) female mouse with a wild-type (*Fmr1*^{+/+}) male mouse as described previously (Zhang et al., 2014). Mice were subsequently re-genotyped after the experiment by tail-PCR as described by Mientjes et al. (2006). Some electrophysiology experiments (see Figure 4) were carried out on first-generation *Fmr1* KO mice (FVB background; Dutch-Belgian Fragile X Consortium (1994). Genotype was assessed by tail-PCR as described previously (Musumeci et al., 2007). Only *Fmr1*^{+/-} mice were used for electrophysiology and behavior.

Primary cell cultures

Cultures of hippocampal neurons and glial cells were prepared from E18 WT and *Fmr1* KO embryos. Pregnant mice were sacrificed by decapitation after deep anaesthesia with isoflurane and the uterine horn dissected. Hippocampi were subsequently dissected from the embryos in ice-cold dissection solution and then dissociated in trypsin (Sigma, 0.25%). Briefly, cells were plated at a density of 100 to 200 x 10³ cells per milliliter on poly-L-lysine (Sigma) precoated

coverslips and kept at 37°C in 5% CO₂. The original plating Neurobasal culture medium (Gibco) supplemented with B27 (Gibco, 2%) and complemented with 5% fetal bovine serum was replaced with a serum free medium on day *in vitro* (DIV) 2. Cytosine B-D-arabinofuranoside (Sigma, 5 μM) was added on DIV 4. All the experiments were performed at DIV 12/15.

Pharmacological treatments

A cell-permeable (TAT-fused) peptide containing the proline-rich motif (PPXXF) of the mGluR5 C-terminal tail that binds the EVH1 domain of Homer, TAT-mGluR5ct (YGRKKRRQRRR-ALTPSPFR), and a control peptide with a mutated Homer binding motif, mGluR5mu (YGRKKRRQRRR-ALTPLSPRR), were synthesized at the UT Southwestern Protein Chemistry Technology Center and kindly provided by Prof. K. Huber (Department of Neuroscience, University of Texas Southwestern Medical Center, Dallas, TX 75390, USA). The peptides were dissolved in H₂O at a concentration of 5 mM, and aliquots of this stock concentration were stored at -20°C. Frozen aliquots of both TAT-fused peptides were used within 10 days and diluted to the desired final concentration. Hippocampal cultures were treated with TAT-mGluR5ct or TAT-mGluR5mu for 1 hour with a final concentration of 5 μM in serum free culture medium at 37°C. Slices were incubated during 4 hours with either TAT-mGluR5ct or TAT-mGluR5mu (each at 5 μM) in oxygenated ACSF at room temperature (21–22° C). (S)-3,5-Dihydroxyphenylglycine (DHPG) (Abcam, # ab120007, 100 μM) was dissolved in ACSF and applied by bath perfusion.

Single-Particle (Quantum Dot) Tracking and Surface Diffusion Calculation

For single-molecule tracking experiments, neurons were first exposed for 10 minutes to either mouse monoclonal anti-NH₂ mGluR5 antibody (1:20) (Mion et al., 2001), mouse monoclonal anti-GluA2 AMPA receptor (AMPA) subunit antibody (Millipore, #MAB397, 1:200), or rabbit polyclonal anti-GluN1 NMDA receptor (NMDAR) subunit antibody (Alomone Laboratories, #AGC-001, 1:200) at 37°C. Neurons were then incubated for 10 minutes in a solution containing quantum dots (QD) 655 coupled to goat anti-mouse IgG (Invitrogen, #Q11022MP) or coupled to goat anti-rabbit IgG (Invitrogen, #Q-11421MP) (final dilution 1:5000/1:10.000) at 37°C. To label synaptic sites, neurons were incubated for 40 seconds at RT (~22°C) in a solution containing the orange mitochondria marker MitoTracker (Invitrogen, #M-7510, 20 nM). A fraction of coverslips was also incubated for 1 hour with TAT-mGluR5ct or TAT-mGluR5mu (5 μM) in culture medium at 37°C before and during the incubation with the primary antibodies. For QD 655 fluorescence imaging we used an EM-CCD camera (Evolve 512, Photometrics) with a 512 x 512 imaging array together with an HXP-120 light source (Zeiss) and the appropriate filters for excitation and emission. Images were acquired at an integration time of 50 milliseconds for up to 500 consecutive frames (24 seconds) as described previously (Groc et al., 2004; Ladépêche et al., 2013; Hafner et al., 2015). QD movements were followed on randomly selected healthy looking dendritic regions for up to 20 minutes, and analyzed using Metamorph software (Universal Imaging Corporation, PA, USA). Briefly, the instantaneous diffusion coefficient, D , was calculated for each trajectory, from linear fits of the first 4 points of the mean-square-displacement versus time function using the following equation: $\langle r^2 \rangle (t) = 4Dt$. To assign synaptic localization, trajectories were sorted into extrasynaptic (i.e. MitoTracker-negative pixels) and synaptic regions (MitoTracker-positive pixels). To determine the distribution and synaptic fraction of single QD complexes, frame stacks were obtained and on each frame the receptor/QD complexes were precisely located in synaptic and extrasynaptic compartments. Then, those locations were projected on a single image, providing a high-resolution distribution of the receptor/QD complexes.

Immunocytochemistry and confocal analysis

The surface expression of mGluR5 was studied using an antibody against the NH₂ terminal of the mGluR5 in non-permeabilized neurons (see above QD tracking experiments). After removing the medium, cell cultures were incubated with the antibody (1:10) for 30 minutes at 37°C. Subsequently, cultures were fixed with a solution containing 4%

paraformaldehyde (PFA) and 4% sucrose for 10 minutes at RT, permeabilized in PBS containing 0.1% Triton-X for 10 min, incubated with blocking solution containing 4% BSA for 45 minutes at RT, followed by incubation with the rabbit monoclonal anti-GluN1- NH₂ antibody (Alomone Labs, #AGC-001, 1:200) and the Guinea pig polyclonal anti-Homer1 antibody (Synaptic Systems, #160 004, 1:500) for 1 hour at RT. After washing, cultures were incubated for 45 minutes at RT with the appropriate secondary fluorescent antibodies (Alexa Fluor 647 anti-mouse, Invitrogen, #A-21236, 1:750; Alexa Fluor 555 anti-rabbit, Invitrogen, #A-21428, 1:750; Alexa Fluor 488 anti-Guinea pig, Invitrogen, #A-11073, 1:750). A fraction of coverslips was also incubated for 1 hour with TAT-mGluR5ct or TAT-mGluR5mu (final concentration for each: 5 μ M in culture medium) at 37°C before the incubation with anti-mGluR5 antibodies.

Images were acquired to measure co-localization of mGluR5, GluN1 and Homer1, using a commercial Leica DMI6000 TCS SP5 confocal microscope with identical settings for all conditions. Ten individual confocal images per coverslip were acquired at 12 bit-depth with a pixelsize of 96.2 nm x 96.2 nm (63x objective, 1.4 NA, 2.5 digital zoom, 1024 x 1024 pixel per image, 50 Hz scanning speed, 98.41 μ m x 98.41 μ m field of view). Images were processed with AutoquantX software (MediaCybernetics) and ImageJ software. A minimum of eight randomly chosen cells per condition was acquired and analyzed. A 2D blind deconvolution algorithm was first applied to each image in order to retrieve better data from our images. Then, analysis of the co-localization of mGluR5, GluN1 and Homer1 was performed using the “Co-localization” module of ImageJ (version 1.49; Scion Image, Frederick, MD). A custom-made macro was used to analyze the dendritic part of each image by measuring the intensity of each label using fixed threshold intensities.

Virus production and titration of recombinant adeno-associated virus (AAV)

Homer1a mRNA was targeted by RNA interference-mediated silencing. The recombinant AAVs were composed of bicistronic expression of short hairpin RNA, driven by the mouse RNA polymerase III U6 promoter (oligonucleotides corresponding to Homer1a-specific shRNA (shH1a; sense strand, 5'-GGAGCAUUGAGCUAAUUAUTT-3'; antisense strand, 5'-AUAUUAGCUCAAUGCUCCTT-3'; Sigma Genosyses), and of control shRNA (sense strand, 5'-GUACUGCUUACGAUACGGTT-3'; antisense strand, 5'-CCGUAUCGUAAGCAGUACUTT-3'), combined with GFP, expressed under the control of the CBA promoter. The entire cassette was flanked by AAV2 inverted terminal repeats (ITRs). Briefly, rAAV2/1 vectors (shCtrl and shH1a) were produced by polyethylenimine (Collingridge et al.)-mediated triple transfection of HEK293 cells. HEK 293 cells were cotransfected with the AAV cis plasmid (pAAV-U6-shRNA-CBA-GFP-WPRE-bGH, control-shRNA or Homer1a-specific shRNA (Tappe et al., 2006; Klugmann and Szumlinski, 2008), the AAV1 (pH21) and AAV2 (pRV1) helper plasmids, and the adenovirus helper plasmid (pFD6). Seventy-two hours after transfection, cells were harvested and lysed by three sequential freeze–thaw cycles (–80°C/37°C). The AAV vector were purified using heparin affinity columns (GE HealthCare), concentrated using Amicon ultra-4 centrifugal filter units with a 100,000 molecular weight cutoff (Millipore) and filtered through a 13 mm diameter 0.2 μ m syringe filter. Genomic titers were determined on the basis of an AAV2 ITR sequence-specific qPCR (Aurnhammer et al, 2012), using a LightCycler® 480 Real-Time PCR System (Roche, Meylan, France).

AAV vector administration

Briefly, WT and *Fmr1* KO mice (postnatal age 21 days) were anaesthetized with an isoflurane/air mix (3% for initial induction and 1.5%-2% for maintenance), head-fixed in a stereotaxic apparatus (David Kopf Instruments), and placed on a heating pad (HP-1M, Physitemp Instruments Inc) connected to a controller (TCAT-2LV, Physitemp Instruments Inc) set to maintain the body temperature at 37°C. Three hundred nanoliters of either AAV-shScr or AAV-shH1a were injected bilaterally into the dorsal hippocampus (Paxinos and Franklin, 2001; mouse brain atlas; coordinates: –1.95 mm AP, \pm 1.25 mm ML, –1.35 mm DV from bregma). The viruses were injected at the rate of 75 nL/min. The injections were performed using a 34-gauge needle (World Precision Instruments) attached to a 10 μ L-NanoFil microsyringe (Nanofil, World Precision Instruments). The microsyringe was driven by an electronic micropump system

(UltraMicroPump, World Precision Instruments) connected to a microprocessor controller (Micro4, MicroSyringe Pump Controller). Electrophysiological experiments began 4 weeks after virus infusion when transgene protein expression had peaked to remain at stable levels (During et al., 2003). Behavioral training started 9 weeks after virus infusion.

Slice preparation and electrophysiological recordings of NMDA currents

Acute hippocampal slices were prepared from male WT and *Fmr1* KO mice (post natal age 11-15 days). The brains were removed and placed in oxygenated ice-cold artificial cerebrospinal fluid (ACSF; in mM: NaCl 124; KCl 3.0; NaH₂PO₄ 1.2; MgSO₄ 1.2; CaCl₂ 2.0; NaHCO₃ 26; D-glucose 10; pH 7.3). The two brain hemispheres were separated and transverse slices of dorsal hippocampus (300 μ m thick) were cut using a vibratome (Leica VT1200). Slices were allowed to recover for at least 3 hours at RT while continually perfused with oxygenated ACSF. Some of the slices were incubated for 4 hours with 5–10 μ M TAT-mGluR5ct or TAT-mGluR5mu in oxygenated ACSF at RT.

For electrophysiological recordings, hippocampal slices were transferred to the recording chamber and visualized using a Leica DMLFS microscope equipped with 20X/0.30 and 40X/0.80 objectives, infrared filter and differential interference contrast (Mulle et al.). A tungsten monopolar electrode (WPI) was placed in the *stratum radiatum* to stimulate Schaffer collaterals with negative current pulses (duration 0.3 milliseconds), delivered every 30 seconds by a stimulus generator (A310 Accupulser with A360 stimulus isolator unit, WPI, USA). Stimulation intensity was set to induce 80% of maximal EPSC amplitude. Evoked EPSCs were recorded at RT from CA1 pyramidal neurons in the whole-cell patch-clamp configuration at a holding potential of –60 mV using an EPC7-plus amplifier (HEKA, Germany). Current traces were filtered at 3 kHz and digitized at 10 kHz. The NMDA-to-AMPA ratio (NMDA/AMPA) of evoked EPSCs was measured following standard procedures (Myme et al., 2003). Patch pipettes (open-tip resistance of 1.5-3 M Ω) were filled with intracellular solution containing cesium (130 mM) and tetraethylammonium (TEA, 10 mM). Mixed NMDA/AMPA EPSCs were evoked in ACSF containing bicuculline (5 μ M) and glycine (10 μ M). EPSCs were evoked every 15 sec and recorded at a holding potential of –90 mV, 0 mV, and +50 mV. For NMDA/AMPA ratio measurement, at least twenty traces were averaged at holding potential (HP) of –90 and +50 mV respectively. At a HP –90 mV, EPSCs were entirely mediated by activation of AMPA receptors (EPSC_{AMPA}). The time to peak of EPSC_{AMPA} at HP of –90 mV was used to establish the time window for measuring the peak EPSC_{AMPA} at +50 mV. A complete decay to baseline of EPSC_{AMPA} at HP of –90 mV generally occurred 40 ms after the stimulus artifact. This delay was used as a time window to measure the amplitude of the current mediated by NMDA receptors (EPSC_{NMDA}) at a HP +50 mV. The amplitude of EPSC_{NMDA} at +50mV divided by the amplitude of EPSC_{AMPA} at +50mV was taken as the NMDA/AMPA ratio.

For the LTD experiments, patch pipettes were filled with intracellular solution containing (in mM): K-gluconate 140; HEPES 10; NaCl 10; MgCl₂ 2; EGTA 0.2; QX-314 1; Mg-ATP 3.5; Na-GTP 1; pH 7.3. Slices were continuously perfused with ACSF at a flow rate of 1.0 ml/min. Following whole-cell access, the slice was perfused with Mg²⁺-free ACSF containing CNQX (10 μ M), glycine (10 μ M) and bicuculline (5 μ M) to isolate EPSCs mediated by NMDA receptors (EPSC_{NMDA}). DHPG (100 μ M) was dissolved in the same ACSF and bath-applied for 5 min. Data were acquired and analyzed with Signal software (Cambridge Electronic Design, England). EPSC_{NMDA} amplitude values were measured as the difference between peak current and baseline, averaged over 1 minutes and expressed as percentage of control (calculated from EPSCs recorded during at least 15 minutes prior to DHPG application).

For the electrophysiological recordings of NMDA currents from *Fmr1* KO mice injected with AAV-sh H1a or AAV-scr, hippocampal slices were prepared four weeks following viral injection (age of mice: 7–8 weeks). The brains were removed and placed in oxygenated ice-cold cutting solution (in mM: Choline-Cl 110; KCl 2.5; NaH₂PO₄ 1.25; MgCl₂ 7; CaCl₂ 0.5; NaHCO₃ 25; D-glucose 20; Na-Ascorbate 5; Piruvate Acid 3, pH 7.3). The two brain hemispheres were separated and sagittal slices of dorsal hippocampus (350 μ m thick) were cut using a vibratome (Leica VT1200S). Slices recovered during at least 30 minutes at 34°C in with oxygenated resting solution (in mM: NaCl 110; KCl 2.5; NaH₂PO₄ 1.25; MgCl₂ 7; CaCl₂ 0.8; NaHCO₃ 25; D-glucose 20, Na-Ascorbate 1.3; Piruvate Acid 3, pH 7.3). Then the slices were

removed from the water bath and kept at RT. The slices were transferred to the recording chamber, and were continuously superfused with ACSF (in mM NaCl 125; KCl 2.5; NaH₂PO₄ 1.25; MgCl₂ 1.3; CaCl₂ 2.3; NaHCO₃ 25; D-glucose 20, pH 7.3) at a flow rate of 1.7 ml/min. The ACSF also contained NBQX (20 μM), glycine (10 μM) and bicuculline (10 μM) to isolate EPSCs mediated by NMDA receptors (EPSC_{NMDA}). Cells were visualized using a Nikon FN-S2N microscope equipped with 10X/0.30 and 60X/1.0W objectives and differential interference contrast (Mulle et al.), and fluorescent cells were selected using a LED excitation system at 490nm (CooLED, UK). A stimulating glass pipette (open-tip resistance of 3.5-5 MΩ) was placed in the *stratum radiatum* to stimulate Schaffer collaterals with positive current pulses (duration 0.2 milliseconds), delivered every 20 seconds by a stimulus generator (DS3 constant current isolated stimulator, Digitimer Ltd., England). Evoked EPSC_{NMDA} were recorded at RT from CA1 pyramidal neurons with green fluorescence (successfully infected with AAV-sh H1a or AAV-scr) in the whole-cell patch-clamp configuration at a holding potential of +40 mV using an EPC10 amplifier (HEKA, Germany). Current traces were filtered at 3 kHz and digitized at 10 kHz. The patch pipettes (open-tip resistance of 2.5-4 MΩ) were filled with intracellular solution containing (in mM): CsMeSO₃ 133; HEPES 10; NaCl 4; MgCl₂ 2; EGTA 0.2; Phosphocreatine 5; Na₂-ATP 3; Na-GTP 0.4; pH 7.25. For determining the EPSC_{NMDA} Input/Output curve (I/O curve), at least three traces were averaged for each stimulation intensity (10μA, 20μA, 30μA, 40μA, 50μA, 60μA, 70μA, 80μA respectively). For LTD experiments, DHPG (100 μM) was dissolved in the same ACSF and bath-applied for 10 min. Data were acquired using PatchMaster software (HEKA, Germany) and analyzed with Igor software (WaveMetrics Inc., USA). EPSC_{NMDA} amplitude values were measured as the difference between peak current and baseline, expressed as percentage of control (calculated from EPSCs recorded during at least 10 minutes prior to DHPG application).

Contextual fear conditioning task

Contextual fear conditioning was assayed as previously described (Oddi et al., 2014). The task took place in a plexiglas box (30 × 24 × 22 cm high) giving access to the visuo-spatial cues in the experimental room. The floor of this conditioning chamber consisted of stainless-steel rods (2 mm diameter), spaced 5 mm apart and connected to a shock generator (Imetronic, Talence, France). The four sides of the chamber and the rods of the floor were cleaned with 70% ethanol before each trial. During conditioning, mice received five 2-second-long electric shocks (0.4 mA, 50 Hz, ITI=1 minute) after 2 minutes of habituation. During the test phase (24 hours after conditioning) mice were put back in the same chambers for 6 minutes, without receiving any shock; freezing time was manually scored as the absence of any body movement beside respiration and normalized by the test session length to obtain a percent measure. All tests were conducted by an observer blinded to the treatments.

Novel object recognition task

Novel object recognition memory was assayed as described previously (Busquets-Garcia et al., 2013). Object-recognition memory was assayed in the L-maze made out of grey Plexiglas with two corridors (30 cm long × 4.5 cm wide, and 15 cm high walls) set at a 90° angle. On day 1, mice were habituated for 10 min to the maze in which the task was performed. On the second day, mice were put back in the maze for 10 min, two identical objects were presented and the time that the mice spent exploring each object was recorded. The mice were again placed in the maze 24 h later for 10 min, one of the familiar objects was replaced with a novel object and the total time spent exploring each of the two objects was computed. Object exploration was defined as the orientation of the nose to the object at a distance of less than 2 cm. In each test session, a discrimination index (DI) was calculated as the difference between the time spent exploring the novel (TN) and the familiar object (TF) divided by the total exploration time (TN+TF): $DI = [TN - TF] / [TN + TF]$. A higher discrimination index is considered to reflect greater memory retention for the familiar object.

Data representation and statistical analysis

Group values are expressed as mean \pm s.e.m. Comparisons between groups for instantaneous diffusion coefficients were performed using Mann-Whitney test (pair comparison) or Kruskal-Wallis followed by Dunn's Multiple Comparison test (group comparison). Comparisons of cumulative distribution of instantaneous diffusion coefficients were performed using Kolmogorov-Smirnov test. The comparison of the percentage of immobile and mobile receptors was performed using Chi-square test with Yates' correction. All of the other comparisons between groups were performed using parametric statistical tests, Student's t-test (pair comparison), one or two-way Anova (group comparison) followed by Tukey's or Sidak's Multiple Comparison tests when appropriate. Significance levels were defined as * $P < 0.05$, ** $P < 0.01$, and *** $P < 0.001$.

ACKNOWLEDGEMENTS

This work was supported by the International PhD Program in Neuropharmacology from the University of Catania (Italy), Labex Bordeaux BRAIN, Telethon (GGP07264), Oasi M SS Troina ("Ricerca Finalizzata" of the Italian Ministry of Health). We thank Silvia Viana da Silva, Arnau Busquets Garcia, Laurent Ladépêche, Jennifer Peterson, and Guillaume Bony for constructive discussions and scientific advice. We thank the team of Daniel Choquet for initial help with the method of quantum dot imaging and its analysis. We also thank Natalie Sans and Mireille Montcouquiol (both Neurocentre Magendie, Bordeaux), and Carmela M. Bonaccorso and Giuseppina Bonaccorso (both Oasi Maria SS, Troina) for technical assistance. Some data were acquired using equipment of the Bordeaux Imaging Center (BIC).

REFERENCES

- Anggono, V. and Huganir, R.L. (2012). Regulation of AMPA receptor trafficking and synaptic plasticity. *Current Opinion in Neurobiology*. 22, 461-9.
- Antar, L.N., Afroz, R., Dichtenberg, J.B., Carroll, R.C. and Bassell G.J. (2004). Metabotropic glutamate receptor activation regulates fragile x mental retardation protein and FMR1 mRNA localization differentially in dendrites and at synapses. *The Journal of Neuroscience*. 24, 2648-2655.
- Aurnhammer, C., Haase, M., Muether, N., Hausl, M., Rauschhuber, C., Huber, I., Nitschko, H., Busch, U., Sing, A., Ehrhardt, A. and Baiker, A. (2012). Universal real-time PCR for the detection and quantification of adeno-associated virus serotype 2-derived inverted terminal repeat sequences. *Human Gene Therapy Methods*. 23(1):18-28.
- Baskys, A. and Malenka, R.C. (1991). Agonists at metabotropic glutamate receptors presynaptically inhibit EPSCs in neonatal rat hippocampus. *Journal of Physiology*. 444, 687-701.
- Bassell, G.J. and Warren, S.T. (2008). Fragile X syndrome: loss of local mRNA regulation alters synaptic development and function. *Neuron*. 60, 201-214.
- Bear, M.F., Huber, K.M. and Warren, S.T. (2004). The mGluR theory of fragile X mental retardation. *Trends in Neuroscience*. 27, 370-377.
- Bhourri, M., Farrow, P.A., Motee, A., Yan, X., Battaglia, G., Di Menna, L., Riozzi, B., Nicoletti, F., Fitzjohn, S.M. and Bashir, Z.I. (2014). mGlu1 receptor-induced LTD of NMDA receptor transmission selectively at Schaffer collateral-CA1 synapses mediates metaplasticity. *The Journal of Neuroscience*. 34(36):12223-9.
- Busquets-Garcia, A., Gomis-González, M., Guegan, T., Agustín-Pavón, C., Pastor, A., Mato, S., et al. (2013). Targeting the endocannabinoid system in the treatment of fragile X syndrome. *Nature Medicine*, 19(5), 603–607.
- Brakeman, P.R., Lanahan, A.A., O'Brien, R., Roche, K., Barnes, C.A., Huganir, R.L., and Worley, P.F. (1997). Homer:

- A protein that selectively binds metabotropic glutamate receptors. *Nature*. 386, 284-288.
- Benquet, P., Gee, C.E. and Gerber, U. (2002). Two distinct signaling pathways upregulate NMDA receptor responses via two distinct metabotropic glutamate receptor subtypes. *The Journal of Neuroscience*. 22, 9679–9686.
- Bertaso, F., Roussignol, G., Worley, P., Bockaert, J., Fagni, L., and Ango F., (2010). Homer1a-dependent crosstalk between NMDA and metabotropic glutamate receptors in mouse neurons. *PLoS ONE*. 5, 9755.
- Celikel, T., Marx, V., Freudenberg, F., Zivkovic, A., Resnik, E., Hasan, M.T., Licznanski, P., Osten, P., Rozov, A., Seeburg, P.H. and Schwarz, M.K. (2007). Select overexpression of homer1a in dorsal hippocampus impairs spatial working memory. *Frontiers in Neuroscience*. 15;1(1):97-110.
- Choquet, D. and Triller, A. (2013). The dynamic synapse. *Neuron*. 80, 691-703.
- D'Antoni, S., Spatuzza, M., Bonaccorso, C.M., Musumeci, S.A., Ciranna, L., Nicoletti, F., Huber, K.M. and Catania, M.V. (2014). Dysregulation of group-I metabotropic glutamate (mGlu) receptor mediated signalling in disorders associated with Intellectual Disability and Autism. *Neuroscience and Biobehavioral Reviews*. 2:228-41.
- Darnell, J.C., Van Driesche, S.J., Zhang, C., Hung, K.Y., Mele, A., Fraser, C.E., Stone, E.F., Chen, C., Fak, J.J., Chi, S.W., Licatalosi, D.D., Richter, J.D. and Darnell, R.B. (2011). FMRP stalls ribosomal translocation on mRNAs linked to synaptic function and autism. *Cell*. 146(Bernardo et al.):247-61.
- de Diego-Otero, Y., Severijnen, L.A., Van Cappellen, G., Schrier, M., Oostra, B.A. and Willemsen, R. (2002). Transport of fragile X mental retardation protein via granules in neurites of PC12 cells. *Molecular and Cellular Biology*. 22, 8332–8341.
- de Vrij, F.M., Levenga, J., van der Linde, H.C., Koekkoek, S.K., De Zeeuw, C.I., Nelson, D.L., Oostra, B.A. and Willemsen, R. (2008). Rescue of behavioral phenotype and neuronal protrusion morphology in *Fmr1* KO mice. *Neurobiology of Disease*. 31, 127–132.
- Dölen, G., Osterweil, E., Rao, B.S., Smith, G.B., Auerbach, B.D., Chattarji, S. and Bear, M.F. (2007). Correction of fragile X syndrome in mice. *Neuron*. 56, 955-962.
- Dölen, G., Carpenter, R.L., O'Carroll, T.D. and Bear, M.F. (2010). Mechanism-based approaches to treating fragile X. *Pharmacology. Ther.* 127, 78-93.
- Dupuis, J.P., Ladépêche, L., Seth, H., Bard, L., Varela, J., Mikasova, L., Bouchet, D., Rogemond, V., Honnorat, J., Hanse, E. and Groc, L. (2014). Surface dynamics of GluN2B-NMDA receptors controls plasticity of maturing glutamate synapses. *EMBO Journal*. 16;33(8):842-61.
- Dutch-Belgian Fragile X Consortium (1994) *Fmr1* knockout mice: a model to study fragile X mental retardation. *Cell* 78:23–33.
- Ferrari, F., Mercaldo, V., Piccoli, G., Sala, C., Cannata, S., Achsel, T. and Bagni, C. (2007). The fragile X mental retardation protein-RNP granules show an mGluR-dependent localization in the post-synaptic spines. *Molecular and Cellular Neuroscience*. 34, 343–354.
- Gandal, M.J., Anderson, R.L., Billingslea, E.N., Carlson, G.C., Roberts, T.P. and Siegel, S.J. (2012). Mice with reduced NMDA receptor expression: more consistent with autism than schizophrenia? *Genes, Brain and Behavior*. 11(6):740-50.
- Giuffrida, R., Musumeci, S., D'Antoni, S., Bonaccorso, C.M., Giuffrida-Stella, A.M., Oostra, B.A. and Catania, M.V. (2005). A reduced number of metabotropic glutamate subtype 5 receptors are associated with constitutive homer proteins in a mouse model of fragile X syndrome. *The Journal of Neuroscience*. 25, 8909-8916.
- Gkogkas, C.G., Khoutorsky, A., Cao, R., Jafarnejad, S.M., Prager-Khoutorsky, M., Giannakas, N., Kaminari, A.,

- Fragkouli, A., Nader, K., Price, T.J., Konicek, B.W., Graff, J.R., Tzinia, A.K., Lacaille, J.C. and Sonenberg, N. (2014). Pharmacogenetic inhibition of eIF4E-dependent Mmp9 mRNA translation reverses fragile X syndrome-like phenotypes. *Cell Reports*. 11;9(5):1742-55.
- Gocel, J. and Larson, J. (2012). Synaptic NMDA receptor-mediated currents in anterior piriform cortex are reduced in the adult fragile X mouse. *Neuroscience*. 27;221:170-81.
- Grishin, A.A., Gee, C.E., Gerber, U. and Benquet, P. (2004). Differential calcium-dependent modulation of NMDA currents in CA1 and CA3 hippocampal pyramidal cells. *The Journal of Neuroscience*. 24, 350–355.
- Groc, L., Heine, M., Cognet, L., Brickley, K., Stephenson, F.A., Lounis, B. and Choquet, D. (2004). Differential activity-dependent regulation of the lateral mobilities of AMPA and NMDA receptors. *Nature Neuroscience*. 7(7):695-6.
- Groc, L., Lafourcade, M., Heine, M., Renner, M., Racine, V., Sibarita, J.B., Lounis, B., Choquet, D. and Cognet, L. (2007). Surface trafficking of neurotransmitter receptor: comparison between single-molecule/quantum dot strategies. *The Journal of Neuroscience*. 27, 2433-7.
- Hafner, A.S., Penn, A.C., Grillo-Bosch, D., Retailleau, N., Poujol, C., Philippat, A., Coussen, F., Sainlos, M., Opazo, P., Choquet, D. (2015). Lengthening of the Stargazin Cytoplasmic Tail Increases Synaptic Transmission by Promoting Interaction to Deeper Domains of PSD-95. *Neuron*. 86(Bernardo et al.):475-89.
- Hagerman, R.J. (2002). The physical and behavioural phenotype. In: *Fragile X Syndrome: Diagnosis, Treatment, and Research*. (Hagerman RJ, Hagerman PJ editors), The Johns Hopkins University Press, Baltimore, MD, pp. 3-109.
- Heidinger, V., Manzerra, P., Wang, X.Q., Strasser, U., Yu, S.P., Choi, D.W. and Behrens, M.M. (2002). Metabotropic glutamate receptor 1-induced upregulation of NMDA receptor current: mediation through the Pyk2/Src-family kinase pathway in cortical neurons. *The Journal of Neuroscience*. 22, 5452–5461.
- Huber, K.M., Gallagher, S.M. Warren S.T. and Bear, M.F. (2002). Altered synaptic plasticity in a mouse model of fragile X mental retardation. *Proceedings of the National Academy of Sciences of the United States of America*. 99, 7746-50.
- Ireland, D.R. and Abraham, W.C. (2009). Mechanisms of group I mGluR-dependent long-term depression of NMDA receptor-mediated transmission at Schaffer collateral-CA1 synapses. *The Journal of Neurophysiology*. 101,1375-85.
- Janusz, A., Milek, J., Perycz, M., Pacini, L., Bagni, C., Kaczmarek, L., Dziembowska, M. (2013). The Fragile X mental retardation protein regulates matrix metalloproteinase 9 mRNA at synapses. *The Journal of Neuroscience*. 33(46):18234-41.
- King, M.K. and Jope, R.S. (2013). Lithium treatment alleviates impaired cognition in a mouse model of fragile X syndrome. *Genes, Brain and Behavior*. 12(7):723-31.
- Klugmann, M., Szumlinski, K.K. (2008) Targeting Homer genes using adeno-associated viral vector: lessons learned from behavioural and neurochemical studies. *Behavioral Pharmacology*. 19(5-6):485-500.
- Martin, H.G., Lassalle, O., Brown, J.T. and Manzoni, O.J. (2015). Age-Dependent Long-Term Potentiation Deficits in the Prefrontal Cortex of the Fmr1 Knockout Mouse Model of Fragile X Syndrome. *Cerebral Cortex*. pii: bhv031.
- Mannaioni, G., Marino, M.J., Valenti, O., Traynelis, S.F. and Conn, P.J. (2001). Metabotropic glutamate receptors 1 and 5 differentially regulate CA1 pyramidal cell function. *The Journal of Neuroscience*. 21, 5925–5934.
- Mao, L. Yang, L., Tang, Q., Samdani, S., Zhang G. and Wang, J.Q. (2005). The scaffold protein Homer1b/c links metabotropic glutamate receptor 5 to extracellular signal-regulated protein kinase cascades in neurons. *The*

Journal of Neuroscience. 25, 2741-2752.

- Michalou, A., Sidorov, M., Ballard, T.M., Ozmen, L., Spooren, W., Wettstein, J.G., Jaeschke, G., Bear, M.F. and Lindemann, L. (2012). Chronic pharmacological mGlu5 inhibition corrects Fragile X in adult mice. *Neuron*. 74, 49-56.
- Michalou, A., Bruns, A., Risterucci, C., Honer, M., Ballard, T.M., Ozmen, L., Jaeschke, G., Wettstein, J.G., von Kienlin, M., Künnecke, B. and Lindemann, L. (2014). Chronic metabotropic glutamate receptor 5 inhibition corrects local alterations of brain activity and improves cognitive performance in fragile X mice. *Biological Psychiatry*. 75, 189-97.
- Michaluk, P., Mikasova, L., Groc, L., Frischknecht, R., Choquet, D., Kaczmarek, L. (2009). Matrix metalloproteinase-9 controls NMDA receptor surface diffusion through integrin beta1 signaling. *The Journal of Neuroscience*. 29(18):6007-12.
- Mientjes, E.J., Nieuwenhuizen, I., Kirkpatrick, L., Zu, T., Hoogeveen-Westerveld, M., Severijnen, L., Rifé M., Willemsen, R., Nelson, D.L. and Oostra, B.A. (2006). The generation of a conditional Fmr1 knock out mouse model to study Fmrp function in vivo. *Neurobiology of Disease*. 21:549-55.
- Mion, S., Corti, C., Neki, A., Shigemoto, R., Corsi, M., Fumagalli, G. and Ferraguti, F. (2001). Bidirectional regulation of neurite elaboration by alternatively spliced metabotropic glutamate receptor 5 (mGluR5) isoforms. *Molecular and Cellular Neuroscience*. 17(6):957-72.
- Moutin, E., Raynaud, F., Roger, J., Pellegrino, E., Homburger, V., Bertaso, F., Ollendorff, V., Bockaert, J., Fagni, L. and Perroy, J. (2012). Dynamic remodeling of scaffold interactions in dendritic spines controls synaptic excitability. *The Journal of Cell Biology*. 198, 251-63.
- Musumeci, S.A., Calabrese, G., Bonaccorso, C.M., D'Antoni, S., Brouwer, J.R., Bakker, C.E., Elia, M., Ferri, R., Nelson, D.L., Oostra, B.A. and Catania, M.V. (2007). Audiogenic seizure susceptibility is reduced in fragile X knockout mice after introduction of FMR1 transgenes. *Experimental Neurology*. 203(1):233-40.
- Myme, C.I., Sugino, K., Turrigiano, G.G. and Nelson, S.B. (2003) The NMDA-to-AMPA ratio at synapses onto layer 2/3 pyramidal neurons is conserved across prefrontal and visual cortices. *Journal of Neurophysiology*, 90, 771-779.
- Neuhof, D., Henstridge, C.M., Dudok, B., Sepers, M., Lassalle, O., Katona, I. and Manzoni OJ. (2015). Functional and structural deficits at accumbens synapses in a mouse model of Fragile X. *Frontiers in Cellular Neuroscience*. 26:9:100.
- Nosyreva, E.D. and Huber, K.M. (2006). Metabotropic receptor-dependent long-term depression persists in the absence of protein synthesis in the mouse model of fragile X syndrome. *The Journal of Neurophysiology*. 95, 3291-5.
- Oddi, D., Subashi, E., Middei, S., Bellocchio, L., Lemaire-Mayo, V., Guzmán, M., Crusio, W.E., D'Amato, F.R. and Pietropaolo, S. (2015). Early social enrichment rescues adult behavioral and brain abnormalities in a mouse model of fragile X syndrome. *Neuropsychopharmacology*. 3;40(5):1113-22.
- Opazo, P., Labrecque, S., Tigaret, C.M., Frouin, A., Wiseman, P.W., De Koninck, P., Choquet, D. (2010). CaMKII triggers the diffusional trapping of surface AMPARs through phosphorylation of stargazin. *Neuron*. 67(Bernardo et al.):239-52.
- Orlando, L. R., Ayala, R., Kett, L. R., Curley, A. A., Duffner, J., Bragg, D. C., et al. (2009). Phosphorylation of the homer-binding domain of group I metabotropic glutamate receptors by cyclin-dependent kinase 5. *Journal of*

- Neurochemistry. 110(Bernardo et al.), 557–569.
- Paradee, W., Melikian, H. E., Rasmussen, D. L., Kenneson, A., Conn, P. J., & Warren, S. T. (1999). Fragile X mouse: strain effects of knockout phenotype and evidence suggesting deficient amygdala function. *Neuroscience*. 94(1), 185–192.
- Penagarikano, O., Mulle, J.G. and Warren, S.T. (2007). The pathophysiology of fragile x syndrome. *The Annual Review of Genomics and Human Genetics*. 8:109-29.
- Pfeiffer, B.E. and Huber, K.M. The state of synapses in fragile X syndrome. *The Neuroscientist*. 15, 549-67 (2009).
- Perroy, J., F. Raynaud, V. Homburger, M.C. Rousset, L. Telley, J. Bockaert, and L. Fagni. (2008). Direct interaction enables cross-talk between ionotropic and group I metabotropic glutamate receptors. *Journal Of Biological Chemistry*. 283, 6799-6805.
- Ronesi, J.A. and Huber, K.M. (2008). Homer interactions are necessary for metabotropic glutamate receptor-induced long-term depression and translational activation. *The Journal of Neuroscience*. 28, 543-547.
- Ronesi, J.A., Collins, K.A., Hays, S.A., Tsai, N.P., Guo, W., Birnbaum, S.G., Hu, J.H., Worley, P.F., Gibson, J.R., Huber, K.M. (2012). Disrupted Homer scaffolds mediate abnormal mGluR5 function in a mouse model of fragile X syndrome. *Nature Neuroscience*. 15, 431-440.
- Santoro, M.R., Bray, S.M. and Warren, S.T. (2012). Molecular mechanisms of fragile X syndrome: a twenty-year perspective. *Annual Review of Pathology*. 7:219-45.
- Scannevin, R.H., and Huganir, R.L. (2000). Postsynaptic organization and regulation of excitatory synapses. *Nature Reviews Neuroscience*. 1, 133-141.
- Sergé, A., Fargeaud, L., He´mar, A. and Choquet, D. (2002). Receptor activation and Homer differentially control the lateral mobility of metabotropic glutamate receptor 5 in the neuronal membrane. *The Journal of Neuroscience*. 22, 3910-3920.
- Shiraishi-Yamaguchi, Y. and Furuichi, T. (2007). The Homer family proteins. *Genome Biology*. 8, 206.
- Skeberdis, V.A., Lan, J., Opitz, T., Zheng, X., Bennett, M.V. and Zukin, R.S. (2001). mGluR1-mediated potentiation of NMDA receptors involves a rise in intracellular calcium and activation of protein kinase C. *Neuropharmacology*. 40, 856–865.
- Snyder, E.M., Philpot, B.D., Huber, K.M., Dong, X., Fallon, J.R. and Bear, M.F. (2001). Internalization of ionotropic glutamate receptors in response to mGluR activation. *Nature Neuroscience*. 4, 1079-85.
- Tang, A.H. and Alger, B.E. (2015). Homer protein-metabotropic glutamate receptor binding regulates endocannabinoid signaling and affects hyperexcitability in a mouse model of fragile x syndrome. *The Journal of Neuroscience*. 35(9):3938-45.
- Tappe, A., Klugmann, M., Luo, C., Hirlinger, D., Agarwal, N., Benrath, J., Ehrenguber, M.U., Doring, M.J., Kuner, R. (2006). Synaptic scaffolding protein Homer1a protects against chronic inflammatory pain. *Nature Medicine*. 12(6):677-81.
- Triller, A. and Choquet, D. (2003). Synaptic structure and diffusion dynamics of synaptic receptors. *Biology of the Cell*. 95, 465-76.
- Triller, A. and Choquet, D. (2008). New concepts in synaptic biology derived from single-molecule imaging. *Neuron*. 59, 359-74.
- Tu, J.C., Xiao, B., Yuan, J.P., Lanahan, A.A., Leoffert, K., Li, M., Linden, D.J. and Worley, P.F. (1998). Homer binds a

- novel proline-rich motif and links group 1 metabotropic glutamate receptors with IP3 receptors. *Neuron*. 21, 717-726.
- Tu, J.C., Xiao, B., Naisbitt, S., Yuan, J.P., Petralia, R.S., Brakeman, P., Doan, A., Aakalu, V.K., Lanahan, A.A., Sheng, M. and Worley, P.F. (1999). Coupling of mGluR/Homer and PSD-95 complexes by the Shank family of postsynaptic density proteins. *Neuron*. 23, 583-592.
- Ventura, R., Pascucci, T., Catania, M.V., Musumeci, S.A. and Puglisi-Allegra, S. (2004). Object recognition impairment in Fmr1 knockout mice is reversed by amphetamine: involvement of dopamine in the medial prefrontal cortex. *Behavioural Pharmacology*.15(5-6):433-42.
- Wagner, K.V., Hartmann, J., Mangold, K., Wang, X.D., Labermaier, C., Liebl, C., Wolf, M., Gassen, N.C., Holsboer, F., Rein, T., Müller, M.B. and Schmidt, M.V. (2013). Homer1 mediates acute stress-induced cognitive deficits in the dorsal hippocampus. *Journal of Neuroscience*. 27;33(9):3857-64.
- Watabe, A.M., Carlisle, H.J. and O'Dell, T.J. (2002). Postsynaptic induction and presynaptic expression of group 1 mGluR-dependent LTD in the hippocampal CA1 region. *The Journal of Neurophysiology*. 87, 1395-403.
- Xiao, B., Tu, J.C., Petralia, R.S., Yuan, J.P., Doan, A., Breder, C.D., Ruggiero, A., Lanahan, A.A., Wenthold, R.J. and Worley, P.F. (1998). Homer regulates the association of group 1 metabotropic glutamate receptors with multivalent complexes of homer-related, synaptic proteins. *Neuron*. 21, 707-716.
- Yun, S.H. and Trommer, B.L. (2011). Fragile X mice: reduced long-term potentiation and N-Methyl-D-Aspartate receptor-mediated neurotransmission in dentate gyrus. *Journal of Neuroscience Research*. 89(Bernardo et al.):176-82.
- Zalfa, F., Giorgi, M., Primerano, B., Moro, A., Di Penta, A., Reis, S., Oostra, B. and Bagni, C. (2003). The fragile X syndrome protein FMRP associates with BC1 RNA and regulates the translation of specific mRNAs at synapses. *Cell*. 112(3):317-27.
- Zalfa, F., Eleuteri, B., Dickson, K.S., Mercaldo, V., De Rubeis, S., di Penta, A., Tabolacci, E., Chiurazzi, P., Neri, G., Grant, S.G. and Bagni, C. (2007). A new function for the fragile X mental retardation protein in regulation of PSD-95 mRNA stability. *Nature Neuroscience*. 10, 578–587.
- Zhang, H., Etherington, L.A., Hafner, A.S., Belevi, D., Coussen, F., Delagrè, P., Chaouloff, F., Spedding, M., Lambert, J.J., Choquet, D., Groc, L. (2013). Regulation of AMPA receptor surface trafficking and synaptic plasticity by a cognitive enhancer and antidepressant molecule. *Molecular Psychiatry*. 18(4):471-84.
- Zhang, Y., Bonnan, A., Bony G., Ferezou, I., Pietropaolo, S., Ginger, M., Sans, N., Rossier, J., Oostra, B., LeMasson, G. and Frick, A. (2014). Dendritic channelopathies contribute to neocortical and sensory hyperexcitability in Fmr1(-/y) mice. *Nature Neuroscience*. 17(12):1701-9.

FIGURES

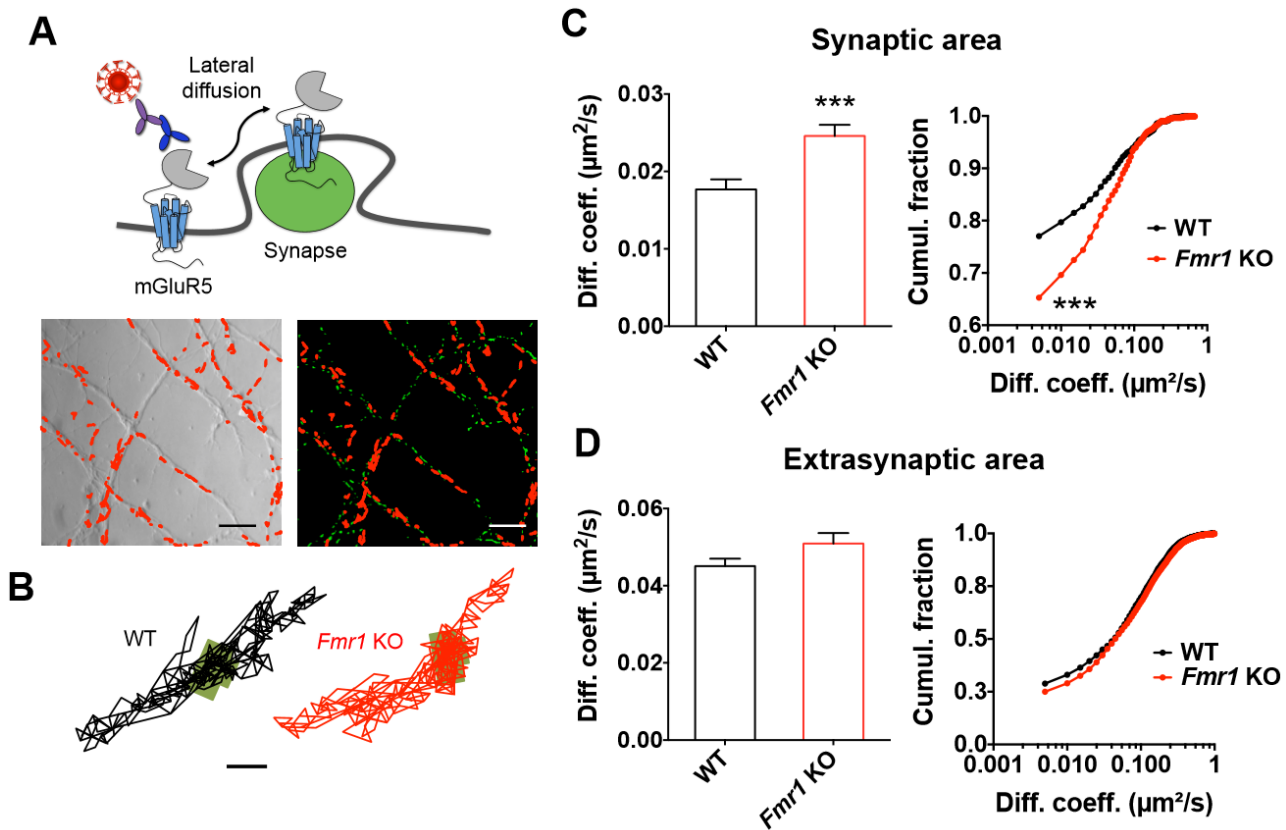


Figure 1. Membranous mGluR5 displays an increased lateral diffusion rate within the synaptic compartment of hippocampal *Fmr1* KO neurons. (A) Experimental setup. *Upper panel*: schematic drawing of the endogenous mGluR5 in the dendritic membrane labeled with a QD-antibody complex targeting the extracellular domain of the receptor. *Lower panel*: reconstructed trajectories of surface mGluR5-QD complexes in the dendritic membrane of hippocampal neurons are depicted in red and shown on a phase contrast (*left*) and epifluorescence image showing MitoTracker labeling of synaptic sites in green (Holcomb et al.). Scale bar = 5 μm . (B) Representative trajectories of single surface mGluR5-QD in WT and *Fmr1* KO neurons. The synaptic sites are represented by the green shapes. Scale bar = 1 μm . (C) Mean distribution (*left panel*) and cumulative distribution (*right panel*) of the instantaneous diffusion coefficient of mGluR5-QDs in the synaptic compartment. The lateral diffusion is significantly higher in *Fmr1* KO neurons (WT, 0.018 ± 0.001 , $n = 1633$ trajectories; *Fmr1* KO, 0.025 ± 0.001 , $n = 1451$ trajectories; $P < 0.001$ by Mann-Whitney test on plot distribution; $P < 0.001$ by Kolmogorov-Smirnov test on cumulative distribution). (D) Mean distribution (*left panel*) and cumulative distribution (*right panel*) of the instantaneous diffusion coefficient of mGluR5-QDs in the extrasynaptic area of WT and *Fmr1* KO neurons (WT, 0.045 ± 0.002 , $n = 1907$ trajectories; *Fmr1* KO, 0.051 ± 0.003 , $n = 1350$ trajectories; $P = 0.085$ by Mann-Whitney test on plot distribution; $P = 0.057$ by Kolmogorov-Smirnov test on cumulative distribution). Data are shown as mean \pm s.e.m. *** $P < 0.001$.

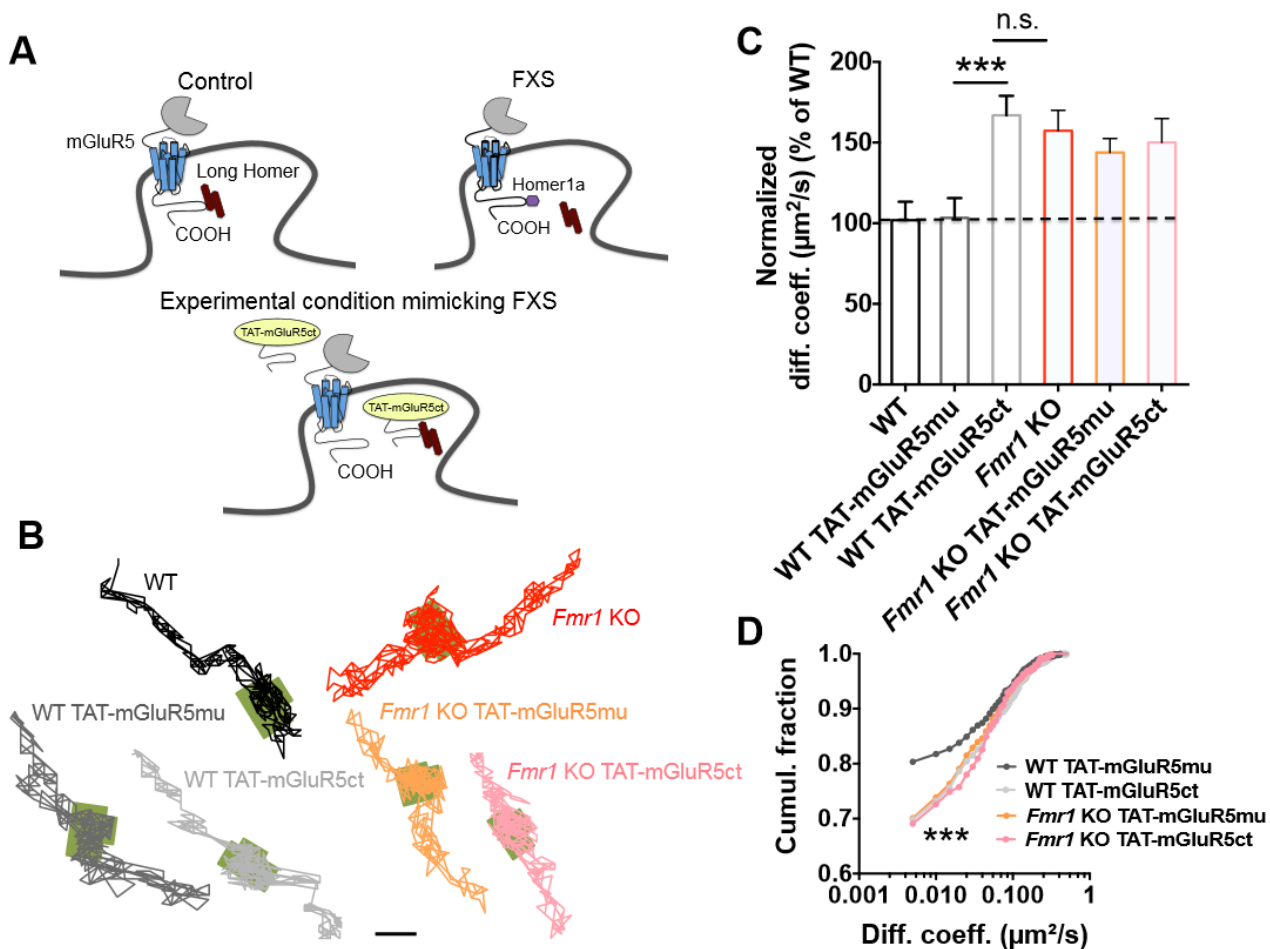


Figure 2. Disruption of the link between mGluR5 and Homer in WT neurons mimics the *Fmr1* KO phenotype. (A) Schematic illustration of the effect of the cell permeable TAT-mGluR5ct peptide. This peptide disrupts the mGluR5/Homer link, mimicking the situation in *Fmr1* KO neurons. (B) Representative trajectories of single surface mGluR5-QD in WT and *Fmr1* KO neurons treated with TAT-mGluR5ct and its mutated TAT-mGluR5mu control peptide (both peptides 5 μM , 1h). The synaptic sites are represented by the green shapes. Scale bar = 1 μm . (C) Normalized instantaneous diffusion coefficient of mGluR5-QDs in the synaptic area of WT and *Fmr1* KO neurons treated with TAT-mGluR5mu and TAT-mGluR5ct. The lateral diffusion rate of mGluR5-QDs in WT neurons treated with TAT-mGluR5ct peptide is comparable to that in *Fmr1* KO neurons under basal conditions (WT, 0.016 ± 0.002 , $n = 636$ trajectories; WT TAT-mGluR5mu, 0.016 ± 0.002 , $n = 1798$ trajectories; WT TAT-mGluR5ct, 0.027 ± 0.002 , $n = 1444$ trajectories; *Fmr1* KO, 0.025 ± 0.002 , $n = 793$ trajectories; *Fmr1* KO TAT-mGluR5mu, 0.023 ± 0.001 , $n = 1419$ trajectories; *Fmr1* KO TAT-mGluR5ct, 0.022 ± 0.003 , $n = 489$ trajectories; $P < 0.001$ by Kruskal Wallis test). (D) Cumulative distribution of the instantaneous diffusion coefficient of mGluR5-QDs within the synaptic area of WT and *Fmr1* KO neurons treated with TAT-mGluR5mu and TAT-mGluR5ct ($P < 0.001$ by Kolmogorov-Smirnov test). Data are shown as mean \pm s.e.m. *** $P < 0.001$.

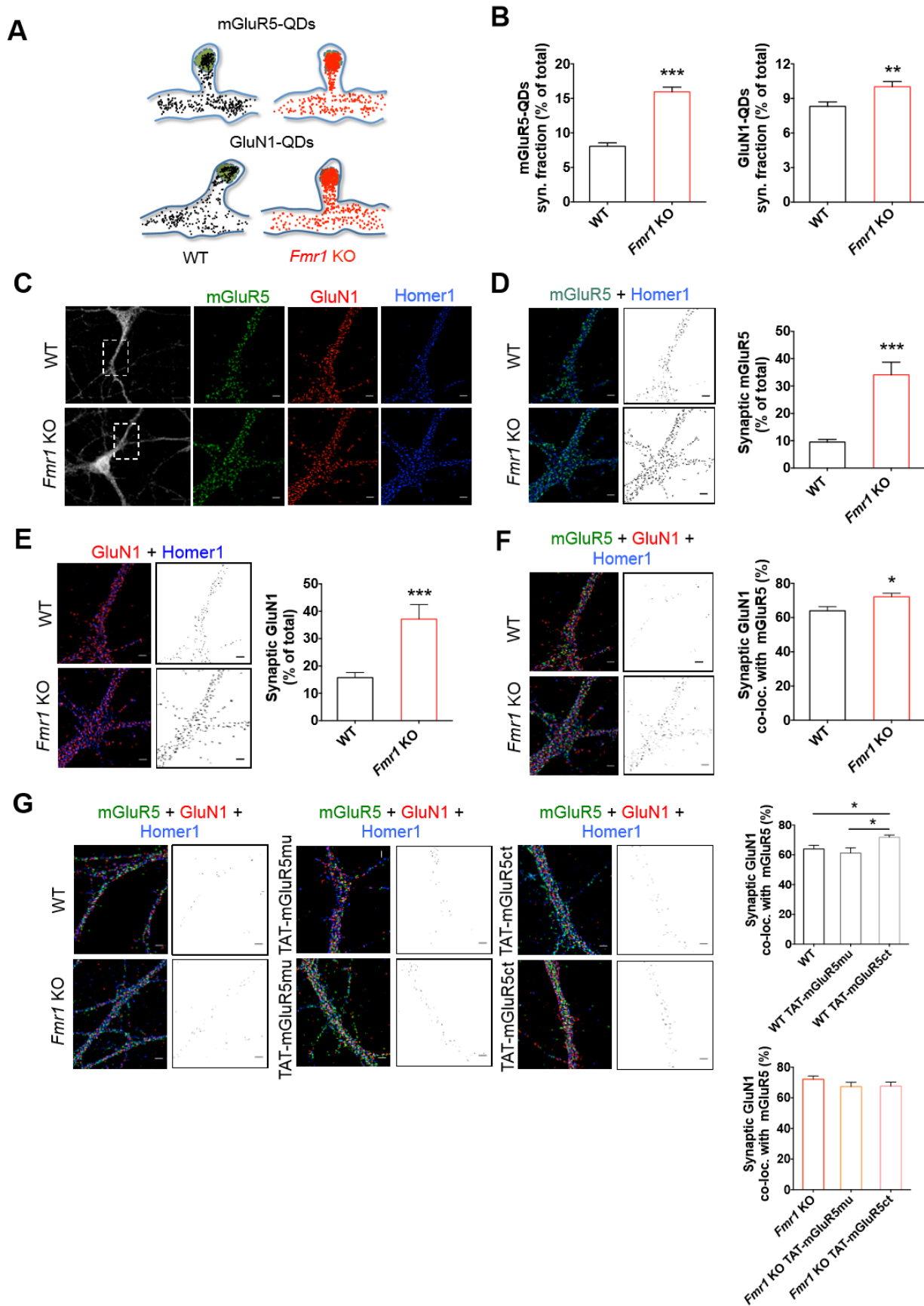


Figure 3. mGluR5 and GluN1 are more confined within the synaptic compartment in *Fmr1* KO neurons. (A) Representative surface distribution of mGluR5-QD (*upper panel*) and GluN1-QD (*lower panel*) clusters (each dot

represents the detection of a single receptor during 1-sec acquisition time), revealing the synaptic site as a trapping zone (green). (B) Relative fractions of synaptic mGluR5-QD (*left panel*) and GluN1-QD (*right panel*) particles. These values are increased in *Fmr1* KO neurons (mGluR5-QD, WT, 8.053 ± 0.504 %, n= 16 dendritic fields; *Fmr1* KO, 15.95 ± 0.685 %, n = 14 dendritic fields; $P < 0.001$ by unpaired Student's t-test; GluN1-QD, WT, 8.318 ± 0.382 %, n = 63 dendritic fields; *Fmr1* KO, 10.02 ± 0.446 %, n = 51 dendritic fields; $P < 0.01$ by unpaired Student's t-test). (C) Representative images of cultured hippocampal neurons from WT and *Fmr1* KO mice that were triple-labeled with the primary antibodies anti-mGlu5-NH₂, anti-GluN1-NH₂ and anti-Homer1. (D and E). Group data show a significant increase in the expression of mGluR5 and GluN1 in the synaptic area of *Fmr1* KO neurons calculated as percentage of mGluR5/Homer1 or GluN1/Homer1 co-labeled area over total mGluR5 or GluN1 labeled area/field (mGluR5, WT, 9.527 ± 0.959 %, n = 27 dendritic fields; *Fmr1* KO, 35.62 ± 4.618 %, n = 21 dendritic fields; $P < 0.001$ by unpaired Student's t-test; GluN1, WT, 15.75 ± 1.841 %, n = 29 dendritic fields; *Fmr1* KO 37.15 ± 5.324 %, n = 18 dendritic fields; $P < 0.001$ by unpaired Student's t-test). (F) Group data show a significant increase in the percentage of synaptic GluN1 co-localized with mGluR5 in *Fmr1* KO neurons (WT, 63.97 ± 2.414 %, n = 26 dendritic fields; *Fmr1* KO, 72.14 ± 2.081 %, n = 23 dendritic fields; $P < 0.05$ by unpaired Student's t-test). (G) Pretreatment with TAT-mGluR5ct peptide (5 μ M, 1h) leads to a significant increase in mGluR5 and GluN1 co-localization in the synaptic area of WT neurons (WT, 63.97 ± 2.414 %, n = 26 dendritic fields; WT TAT-mGluR5mu, 61.19 ± 3.489 %, n = 10 dendritic fields; WT TAT-mGluR5ct, 71.79 ± 1.528 %, n = 27 dendritic fields; $P < 0.05$ by one way Anova test). No differences were observed for co-localization in *Fmr1* KO neurons treated with either TAT-mGluR5mu or TAT-mGluR5ct (both 5 μ M, 1h) (*Fmr1* KO, 72.14 ± 2.081 %, n = 23 dendritic fields; *Fmr1* KO TAT-mGluR5mu, 67.32 ± 2.832 %, n = 20 dendritic fields; *Fmr1* KO TAT-mGluR5ct, 67.58 ± 2.69 %, n = 15 dendritic fields; $P = 0.343$ by one way Anova test). Data are shown as mean \pm s.e.m. *** $P < 0.001$, ** $P < 0.01$, * $P < 0.05$. Scale bar = 2 μ m (except panel C for low magnification scale bar = 10 μ m).

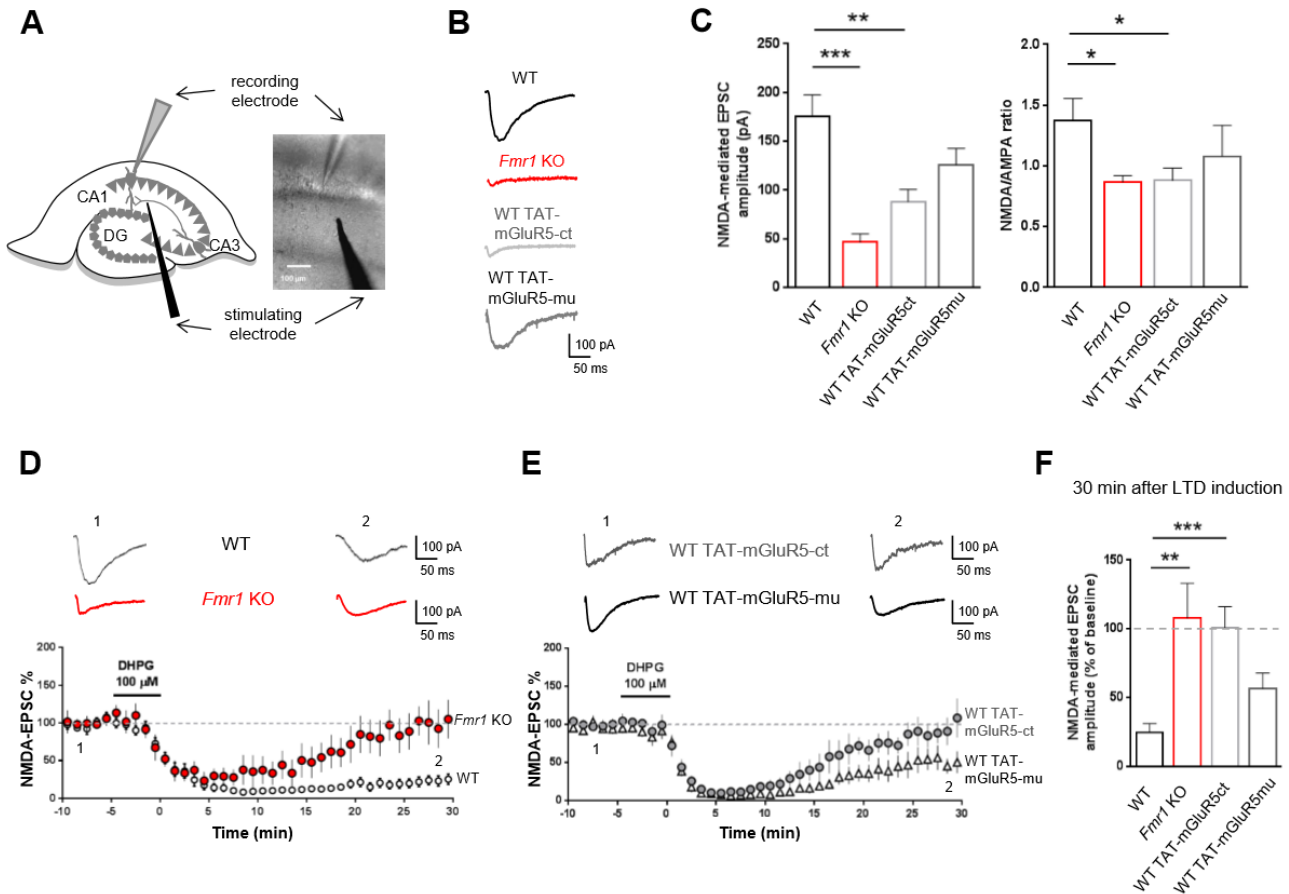


Figure 4. Disruption of mGluR5/Homer coupling alters synaptic NMDAR function and plasticity in *Fmr1* KO neurons. (A) NMDA receptor-mediated excitatory post-synaptic currents (EPSC_{SNMDA}) were recorded under whole-cell patch clamp from CA1 pyramidal neurons in hippocampal slices following stimulation of *Schaffer* collaterals. (B) Representative traces of EPSC_{SNMDA} recorded from CA1 neurons in slices from WT, *Fmr1* KO, WT treated with TAT-mGluR5-ct and TAT-mGluR5-mu (both peptides 5 μ M, 4 hours). (C) Left panel: the amplitude of EPSC_{SNMDA} in CA1 neurons from *Fmr1* KO slices (46.4 ± 8.4 pA, $n = 7$) was significantly lower than in WT (175.7 ± 21.9 pA, $n = 11$, $P = 0.0004$ by unpaired Student's t-test). In a similar manner, in WT slices treated with TAT-mGluR5-ct, the amplitude of EPSC_{SNMDA} was significantly lower than in control conditions (88.1 ± 12.7 pA, $n = 13$, $P = 0.0016$ by unpaired Student's t-test). In neurons from WT slices incubated with TAT-mGluR5-mu, the amplitude of EPSC_{SNMDA} was comparable to control (125.9 ± 16.8 pA $n = 8$, $P = 0.11$ by unpaired Student's t-test). Right panel: mixed AMPA- and NMDA-EPSCs were recorded at a holding potential of +50 mV to evaluate the NMDA/AMPA ratio. The NMDA/AMPA ratio in *Fmr1* KO slices (0.86 ± 0.05 , $n = 8$) was significantly lower than in WT (1.60 ± 0.29 , $n = 5$, $P = 0.0094$ by unpaired Student's t-test). A reduction in NMDA/AMPA ratio was also observed in slices treated with TAT-mGluR5-ct (1.14 ± 0.03 , $n = 4$). (D, F) EPSC_{SNMDA} were recorded from CA1 pyramidal neurons at a HP -60 mV, in the presence of bicuculline and CNQX. Bath application of the group-I mGluR agonist DHPG (100 μ M, 5 min) induced a long-term depression (mGluR-LTD) of EPSC_{SNMDA} recorded in WT slices (EPSC_{SNMDA} amplitude 30 min after LTD induction: 24.9 ± 2 % of control, $n = 8$). mGluR-LTD of EPSC_{SNMDA} was not observed in *Fmr1* KO neurons (EPSC_{SNMDA} amplitude: 107.8 ± 25 %

of control, $n = 6$, a value significantly different from WT, $P = 0.004$ by unpaired Student's t -test). (E, F) The lack of mGluR-mediated plasticity of EPSC_{NMDA} could be mimicked in WT slices after pretreatment with TAT-mGluR5-ct peptide (EPSC_{NMDA} amplitude: 100.6 ± 15 % of baseline, $n = 8$, a value significantly different from WT, $P = 0.0006$ by unpaired Student's t -test) but not with its control peptide TAT-mGluR5-mu (EPSC_{NMDA} amplitude: 56.6 ± 11 % of control, $n = 7$). Data are shown as mean \pm s.e.m. *** $P < 0.001$, ** $P < 0.01$, * $P < 0.05$.

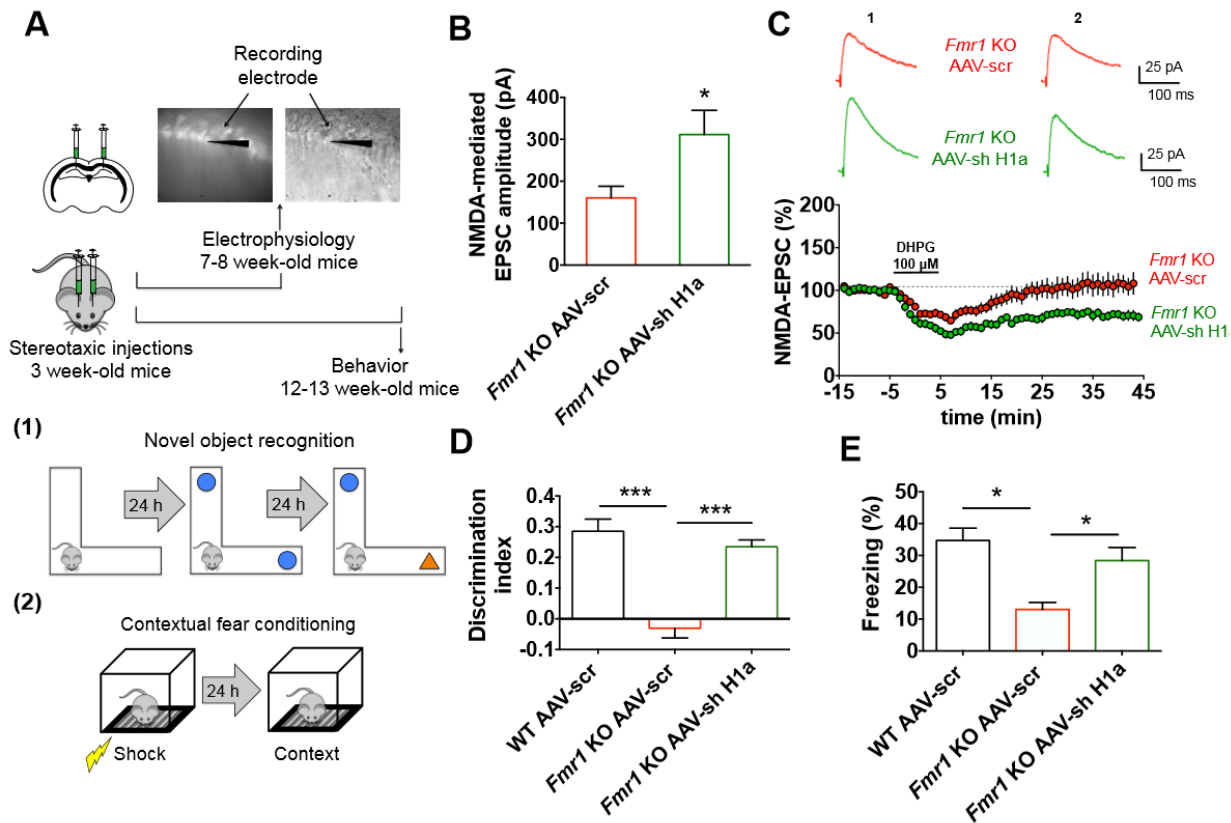


Figure 5. Reduction of Homer1a expression rescues synaptic NMDAR dysfunction and cognitive defects in *Fmr1* KO mice. (A) Schematic representation of the experimental procedure. WT and *Fmr1* KO mice (postnatal age 21 days) were bilaterally injected into the dorsal hippocampus with either AAV-shH1a or AAV-Scr. Experiments were performed four weeks (electrophysiology, B and C) or nine weeks (behavioral training, D and E) following virus injection. Object-recognition memory was assayed in the L-maze. On day 1, mice were habituated for 10 min to the maze in which the task was performed. On the second day, mice were put back in the maze for 10 min, and two identical objects were presented. The mice were again placed in the maze 24 h later for 10 min, one of the familiar objects was replaced with a novel object and the total time spent exploring each of the two objects was computed. During the fear conditioning task, mice received five 2-second electric shocks (0.4 mA, 50 Hz, ITI=1 minute) after 2 minutes of habituation. During the test phase (24 hours after conditioning) mice were put back in the same chambers for 6 minutes, without receiving any shock. (B) The EPSC_{NMDA} amplitude of AAV-sh H1a injected *Fmr1* KO mice was significantly larger than that of AAV-scr injected *Fmr1* KO mice (*Fmr1* KO AAV-scr, EPSC_{NMDA} amp. = 160.4 ± 27.8 , $n = 12$; *Fmr1* KO AAV-sh H1a, EPSC_{NMDA} amp. = 311.3 ± 58 , $n = 12$; $P < 0.05$, unpaired Student's t -test). (C) AAV-sh H1a infection of CA1 pyramidal neurons in *Fmr1* KO mice rescues normal long-term depression of EPSC_{NMDA} induced by bath application of the group-I mGluR agonist DHPG (100 μ M, 10 min) (EPSC_{NMDA} amplitude 40 min after LTD induction: 70.4 ± 6 % of control, $n = 6$). mGluR dependent LTD of EPSC_{NMDA} was not observed in *Fmr1* KO mice injected with AAV-scr (EPSC_{NMDA} amplitude: 106.8 ± 7 % of control, $n = 7$, $P < 0.001$, by unpaired Student's t -test). (D) Discrimination index values in the object recognition test of mice after bilateral intra-hippocampal microinjection of AAV-sh H1a (300 nl per side) or AAV-scr (WT AAV-scr, 0.244 ± 0.042 , $n = 10$; *Fmr1* KO AAV-scr, -0.030 ± 0.032 , $n = 9$; *Fmr1* KO AAV-sh H1a, 0.235

± 0.022 , $n = 8$). The reduction of Homer1a expression showed an improvement of cognitive function in *Fmr1* KO mice after AAV-sh H1a injections ($P < 0.001$, two-way Anova test). (E) Percentage of freezing time in the context recognition test after bilateral intra-hippocampal microinjection of AAV-sh H1a (300 nl per side) or AAV-scr (WT AAV-scr, $32.623 \pm 3.637\%$, $n = 9$; *Fmr1* KO AAV-scr, $12.163 \pm 1.773\%$, $n = 9$; *Fmr1* KO AAV-sh H1a, $30.444 \pm 3.918\%$, $n = 8$). The reduction of Homer1a expression showed an improvement of cognitive function in *Fmr1* KO mice after AAV-sh H1a injections ($P < 0.05$ by two way Anova test). Data are shown as mean \pm s.e.m. *** $P < 0.001$, * $P < 0.05$.

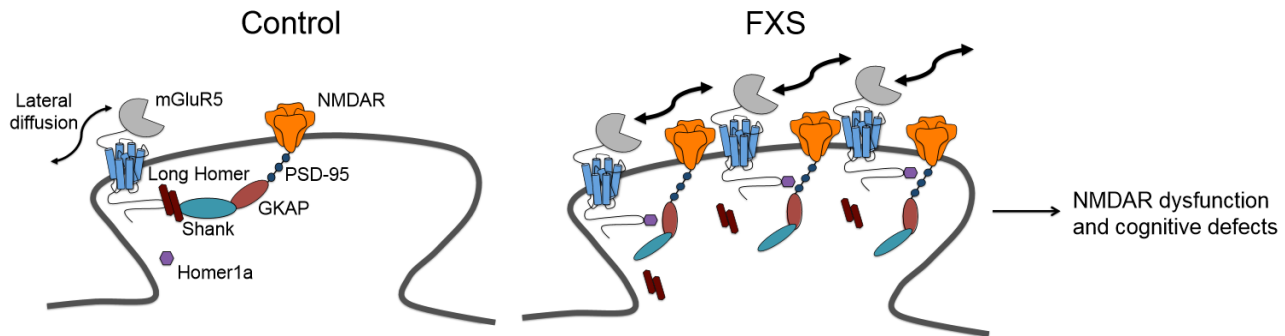


Figure 6. Model for dysfunction of the NMDAR/mGluR5 crosstalk in *Fmr1* KO neurons. In WT neurons, long Homer proteins anchor mGluR5 to a chain of PSD proteins in the synapse and prevent a direct interaction with NMDAR. Under those conditions, a co-clustering of mGluR5 and NMDAR is prevented. In *Fmr1* KO neurons, however, mGluR5 is less associated with the long Homer proteins and more associated with the short isoform, Homer1a. This disengagement from the long Homer protein-containing complex increases the lateral diffusion of mGluR5 and promotes the interaction with synaptic NMDAR. This constellation prevents boosting of NMDAR currents under control conditions and their LTD following mGluR5 stimulation.

The Yin–Yang Dynamics of DNA Methylation Is the Key Regulator for Smooth Muscle Cell Phenotype Switch and Vascular Remodeling

Jianhui Zhuang, Peipei Luan, Hailing Li, Kai Wang, Pei Zhang, Yawei Xu, Wenhui Peng

Objective—DNA methylation plays an important role in chronic diseases such as atherosclerosis, yet the mechanisms are poorly understood. The objective of our study is to indicate the regulatory mechanisms of DNA methylation in vascular smooth muscle cells (VSMCs) and its roles in atherosclerosis.

Approach and Results—In ApoE^{-/-} mice fed a Western diet, DNA methyltransferase inhibitor, 5-aza-2'-deoxycytidine, significantly attenuated atherosclerotic lesions (20.1±2.2% versus 30.8±7.5%; *P*=0.016) and suppressed DNA methyltransferase activity and concomitantly decreased global 5-methylcytosine content in atherosclerotic lesions of ApoE^{-/-} mice. Using a carotid ligation model, we found that 5-aza-2'-deoxycytidine also dramatically inhibited neointimal formation (intimal area: 2.25±0.14×10⁴ versus 4.07±0.22×10⁴ μm²; *P*<0.01). Abnormal methylation status at the promoter of ten–eleven translocation 2, one of the key demethylation enzymes in mammals, was ameliorated after 5-aza-2'-deoxycytidine treatment, which in turn caused an increase in global DNA hydroxymethylation and 5-hydroxymethylcytosine enrichment at the promoter of Myocardin. In vitro, 5-aza-2'-deoxycytidine treatment or DNA methyltransferase 1 knockdown decreased global 5-methylcytosine content and restored Myocardin expression in VSMCs induced by platelet-derived growth factor, thus preventing excessive VSMCs dedifferentiation, proliferation, and migration. Furthermore, DNA methyltransferase 1 binds to ten–eleven translocation 2 promoter and is required for ten–eleven translocation 2 methylation in VSMCs.

Conclusions—The inhibitory effects of DNA demethylation on global 5-methylcytosine content and ten–eleven translocation 2 hypermethylation in atherosclerotic aorta can recover 5-hydroxymethylcytosine enrichment at the Myocardin promoter and prevent VSMC dedifferentiation and vascular remodeling.

(*Arterioscler Thromb Vasc Biol.* 2017;37:84-97. DOI: 10.1161/ATVBAHA.116.307923.)

Key Words: aorta ■ atherosclerosis ■ DNA methylation ■ platelet-derived growth factor ■ vascular remodeling

Atherosclerosis is a chronic and multifactorial disease mediated by complex interplay between resident endothelial cells, vascular smooth muscle cells (VSMCs), and infiltrating macrophages. Environmental exposure to risk factors such as hyperlipidemia throughout the development of atherosclerosis causes vascular remodeling and in turn reduces arterial compliance. Although many drugs inhibiting vascular remodeling and metabolic disorder offer an effective therapeutic strategy for preventing atherosclerotic progression, none of these drugs are found to totally reverse atherosclerotic plaque in animal experiments.^{1,2} Furthermore, clinical trials have revealed that intensive lipid-lowering treatment with rosuvastatin or atorvastatin only leads to limited plaque regression (1.22% and 0.99%, respectively),^{3,4} although routine statin treatments can significantly reduce >30% of the risk of major adverse cardiac events such as myocardial infarction.⁵⁻⁹ The

memory effects of atherosclerosis imply that the mechanisms for atherogenesis are partially independent of the risk factors. It seems that atherosclerosis would progress at its own pace, once the atherosclerotic plaques are formed.

Epigenetic modifications refer to heritable changes in gene expression that are not coded in the DNA sequence itself. Studies demonstrate that epigenomic changes in tissues and cells play important roles in vascular remodeling and atherosclerosis.¹⁰ DNA methylation is the most understood epigenetic modification. The effect of DNA methylation on gene expression can persist even if the risk factors are removed. In eukaryotic genomes, DNA methyltransferases (DNMTs) catalyze the conversion of cytosines, predominantly in cytidine phosphate guanosine (CpG) dinucleotides, to 5-methylcytosine (5-mC), and then silence gene expression. The DNMT inhibitor 5-aza-2'-deoxycytidine (5-aza) is

Received on: November 11, 2015; final version accepted on: October 31, 2016.

From the Department of Cardiology, Shanghai Tenth People's Hospital, Tongji University School of Medicine, China (J.Z., H.L., K.W., Y.X., W.P.); Department of Endocrinology, Xinhua Hospital, Shanghai Jiaotong University School of Medicine, China (P.L.); and Interdisciplinary Institute for Neuroscience, University of Bordeaux, France (P.Z.).

The online-only Data Supplement is available with this article at <http://atvb.ahajournals.org/lookup/suppl/doi:10.1161/ATVBAHA.116.307923/-/DC1>.

Correspondence to Wenhui Peng, MD, PhD, or Yawei Xu, MD, PhD, Department of Cardiology, Shanghai Tenth People's Hospital, Tongji University School of Medicine, 301 Middle Yanchang Rd, Shanghai 200072, China. E-mail pwenhui@tongji.edu.cn or xuyawei@tongji.edu.cn

© 2016 American Heart Association, Inc.

Arterioscler Thromb Vasc Biol is available at <http://atvb.ahajournals.org>

DOI: 10.1161/ATVBAHA.116.307923

Nonstandard Abbreviations and Acronyms	
5-aza	5-aza-2'-deoxycytidine
5-hmC	5-hydroxymethylcytosine
5-mC	5-methylcytosine
DNMT	DNA methyltransferase
PDGF	platelet-derived growth factor
RASMC	rat aortic smooth muscle cell
siRNA	small interfering RNA
SRF	serum response factor
Tet	ten-eleven translocation
VSMC	vascular smooth muscle cell

proven to counteract the depressed expression of methylation genes and is currently approved for treatment of myelodysplastic syndrome.^{11–14} Interestingly, physiological demethylation also exists *in vivo* to balance the silencing effect on gene expression by DNA methylation. Even though no direct DNA demethyltransferases were identified, current studies showed that 5-mC can be oxidized to 5-hydroxymethylcytosine (5-hmC) by ten-eleven translocation (Tet) family of enzymes.^{15,16} Through the base excision repair pathway, 5-hmC is then converted to unmethylated cytosine, leading to demethylation and gene reactivation.^{17–19}

Previous studies had demonstrated that atherosclerosis occurred in familial aggregation, suggesting the role of genetic factors in atherogenesis.²⁰ Recent evidence supported an association between DNA methylation and cardiovascular diseases, such as atherosclerosis and vascular remodeling.^{20–22} Dunn et al²³ uncovered that inhibition of DNA methylation attenuated atherosclerotic burden through ameliorating endothelial dysfunction and restoring mechanosensitive endothelial gene expression induced by oscillatory shear stress. On the other hand, several studies suggested that DNA methylation might participate in regulating VSMC phenotype and vascular remodeling.²⁴ Liu et al²⁵ reported a significant reduction in Tet2 expression in the neointima or coronary atherosclerotic plaques. Loss of Tet2 suppressed 5-hmC enrichment and affected the expression of VSMC differentiation marker genes, which in turn aggravated vascular remodeling. It is, thus, important to determine the role of DNA methylation changes in VSMCs and vascular remodeling.

In this study, we sought to study the DNA methylation state in different stages of atherosclerosis. We found that DNA methylation balance regulated by DNMT1 and Tet2 influenced VSMCs phenotype and vascular remodeling.

Materials and Methods

Materials and Methods are available in the [online-only Data Supplement](#).

Results

DNMT Inhibitor Attenuated Atherosclerosis in ApoE^{-/-} Mice

Because 5-aza has been proven to inhibit DNA methylation, we administrated 5-aza to ApoE^{-/-} mice to confirm the effect of DNA demethylation on atherosclerosis. At first, we found

that body weights were comparable at the indicated time points between vehicle- and 5-aza-treated group, indicating that drug treatment was well tolerated (Figure I in the [online-only Data Supplement](#)). In addition, 5-aza treatment for 12 weeks had no remarkable effect on the plasma levels of lipid profiles and fasting glucose (Figure II in the [online-only Data Supplement](#)). We then examined the effect of 5-aza on atherosclerosis. After 18 weeks exposure of 5-aza, atherosclerotic lesion area was significantly attenuated when compared with that in vehicle-treated ApoE^{-/-} mice as demonstrated by en face Oil red O-positive area (20.1±2.2% versus 30.8±7.5%; $P=0.016$; Figure 1A and 1B) and by quantification of lesion area at the aortic root (Figure 1C and 1D).

We further examined whether 5-aza affected plaque composition. Masson staining demonstrated that necrotic core was smaller in 5-aza-treated ApoE^{-/-} mice compared with vehicle-treated ApoE^{-/-} mice (22.0±4.2% versus 50.8±4.5%; $P<0.01$; Figure 1E through 1G). As shown in Figure 1E and 1F, 5-aza significantly reduced plaque macrophage content by >50% compared with vehicle-treated group (1.1±0.1% versus 2.8±0.2%; $P<0.01$). The relative contents of α -smooth muscle actin were similar between vehicle- and 5-aza-treated groups (Figure 1H and 1I). However, the distribution of α -smooth muscle actin staining was diffuse in vehicle-treated ApoE^{-/-} mice, which was restored in 5-aza-treated ApoE^{-/-} mice (Figure 1J and 1K).

DNMT Inhibition Dynamically Regulated DNA Methylation and Tet2 Expression in Atherosclerotic Aorta

Because epigenetic drift occurred during aging of certain tissue types, we next evaluated global methylation and hydroxymethylation levels in the aorta of ApoE^{-/-} mice at different ages. In line with the findings derived from other tissues, we found that global DNA methylation, as opposed to global DNA hydroxymethylation, was gradually decreased with age both in aorta DNA of wild-type and ApoE^{-/-} mice, which were fed with Western diet (Figure 2A and 2B).

Because DNMT1, DNMT3a, and DNMT3b are the principal mediators of DNA methylation in mammalian cells,^{26,27} we determined the expression of DNMT proteins in atherosclerotic plaques. In the serial sections of aortic sinus stained with α -smooth muscle actin or F4/80 and immunofluorescence images, we found that DNMT1 was predominantly expressed in VSMCs, rather than in macrophages, in the plaque of ApoE^{-/-} mice (Figure 2C and 2D). DNMT3a was equivalently expressed in VSMCs and macrophages in plaque, whereas DNMT3b was undetectable in the cross sections from wild-type and ApoE^{-/-} mice (Figure 2C).

The inhibitory function of 5-aza depends on trapping DNMT1 in a covalent complex with DNA and also preferentially targets DNMT1 via ubiquitin-dependent proteasomal degradation.¹¹ The protein expression of DNMT1 and DNMT3a was higher in vehicle-treated ApoE^{-/-} mice when compared with wild-type mice but was not affected by 5-aza treatment (Figure 2E and 2F). However, DNMT3b was expressed in low level in 3 groups but rich in mouse heart (Figure 2E). This intriguing phenomenon prompted us to investigate the consequence of the enzyme activity of DNMT

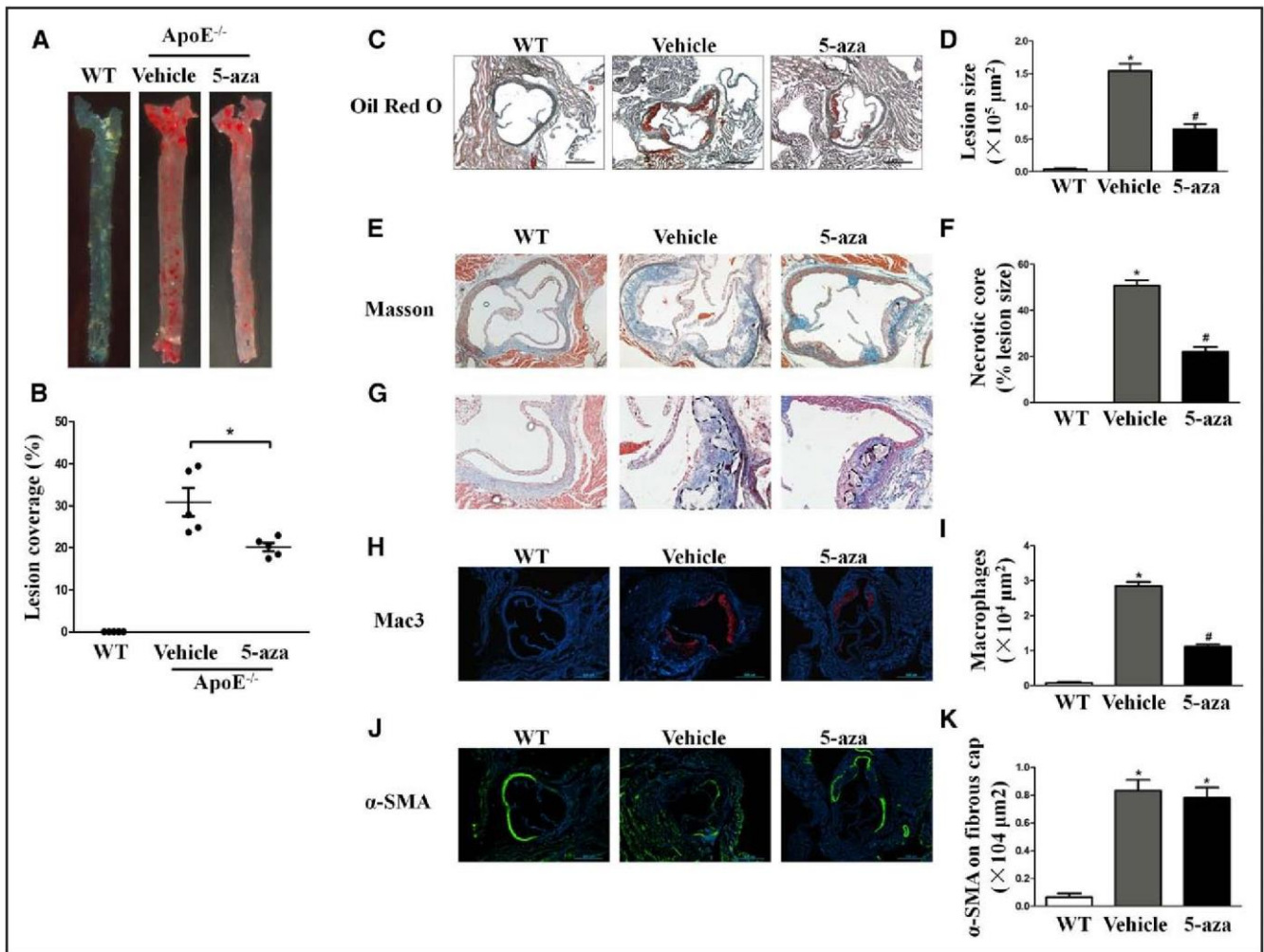


Figure 1. DNA methyltransferase (DNMT) inhibitor 5-aza-2'-deoxycytidine (5-aza) suppresses atherosclerosis. **A** and **B**, En face plaque quantification of aortic arch and thoracic aorta stained with Oil red O. Values are mean \pm SD from 5 animals in each group. **C** and **D**, Sections and quantification of aortic sinus stained by Oil red O. Scale bar=500 μm . Values are mean \pm SD from 4 animals in each group. **E–G**, Representative images of Masson staining and quantification of the percentage of necrotic core in the plaques with and without 5-aza treatment. Values are mean \pm SD from 4 animals in each group. **H** and **I**, Representative images and quantification of macrophage immunostaining of the aortic roots with and without 5-aza treatment. Scale bar=500 μm . Values are mean \pm SD from 4 animals in each group. **J** and **K**, Representative images and quantification of α -smooth muscle actin (α -SMA) immunostaining of the aortic roots with and without 5-aza treatment. Scale bar=500 μm . Values are mean \pm SD from 4 animals in each group. * P <0.05 vs wild-type (WT) group; # P <0.05 vs vehicle group.

after 5-aza treatment. As shown in Figure 2G, the aortas dissected from vehicle-treated ApoE^{-/-} mice had higher enzyme activities than the wild-type samples. Administration of 5-aza in turn suppressed the excessive DNMT activity by 2.76-fold. In keeping with the changes of DNMT activity, 5-mC content was significantly increased in vehicle-treated ApoE^{-/-} mice but declined close to normal level when treated with 5-aza (Figure 2H). Collectively, these results suggested that the effect of 5-aza on DNA demethylation of the aorta containing atherosclerotic plaques was mediated via suppression of DNMT enzyme activity.

Given that Tet2 was the predominant DNA demethylation enzyme in arteries,²⁴ we firstly investigated the expression of Tet2 among 3 groups. Using our panel of mouse aorta samples, we tested the abundance of RNA transcripts and protein. As shown in Figure 2I and 2J, the expression of Tet2 was significantly reduced in the aorta of vehicle-treated ApoE^{-/-} mice compared with wild-type group and restored after administration of 5-aza, which was inversely associated with DNMT activity.

Decreased Expression of Tet2 Attributed to Excessive Promoter Methylation

To clarify the underlying mechanisms of Tet2 expression, we applied methylation-specific polymerase chain reaction and pyrosequence to quantify methylation percentage at target CpG sites in the promoter of Tet2. The locations of Tet2 promoter and CpG islands were shown in Figure 3A. It was reported that the fragment containing high-density CpG sites within the promoter significantly correlated with transcription repression of downstream genes. Thus, we first screened the promoter region of Tet2. Within these fragments, we performed methylation-specific polymerase chain reaction to determine the methylation status and found that the methylation level of fragment 2 was higher in the aorta of vehicle-treated ApoE^{-/-} mice than other 2 groups (Figure 3B). Using pyrosequencing, we further confirmed that the single methylation percentages at 7 of 8 target CpG sites, as well as the average methylation percentages of all sequencing CpG sites, were markedly elevated in vehicle-treated ApoE^{-/-} group than those in wild-type and 5-aza-treated

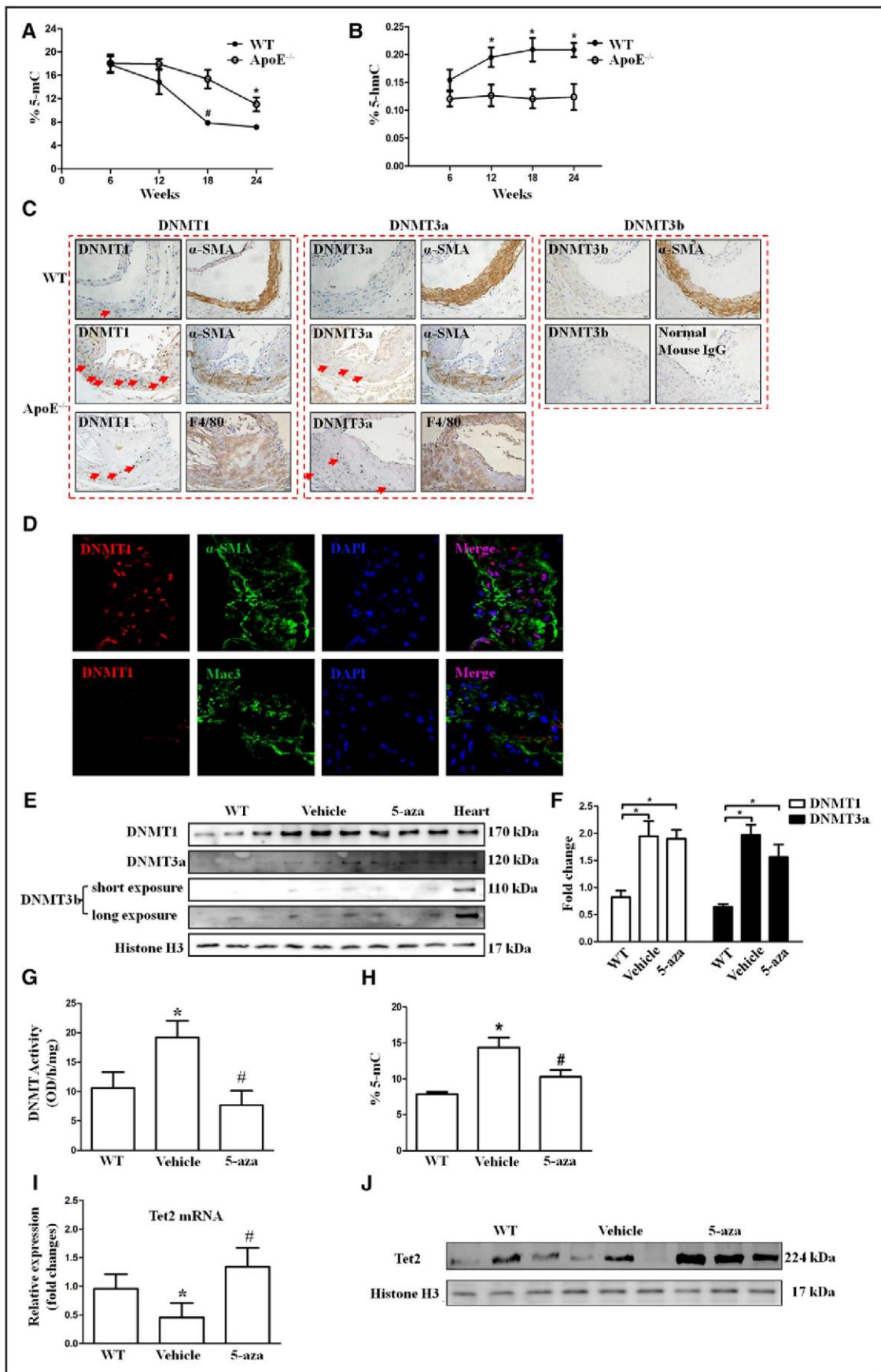


Figure 2. Dynamic changes in global DNA methylation and hydroxymethylation and 5-aza-2'-deoxycytidine (5-aza) inhibit DNA methyltransferase (DNMT) enzyme activity and global 5-methylcytosine (5-mC) content. **A**, Quantification of 5-mC content in aortas at indicated ages of wild-type (WT) and ApoE^{-/-} mice. ApoE^{-/-} mice were fed a high-fat diet containing 16.6% fat, 10.6% sucrose, and (Continued)

Figure 2 Continued. 1.3% cholesterol. WT mice were fed a normal chow diet containing 20.5% protein and 4.6% fat. Values are mean \pm SD from 4 animals in each group. * P <0.05 vs 6 weeks in each group. # P <0.05 vs WT group at the same stage. **B**, Quantification of 5-hydroxymethylcytosine (5-hmC) content in aortas at indicated ages of WT and ApoE^{-/-} mice. Values are mean \pm SD from 4 animals in each group. * P <0.05 vs 6 weeks in each group. # P <0.05 vs WT group at the same stage. **C**, Series sections of aortic sinus allow colocalization of DNMTs with α -smooth muscle actin (α -SMA) and F4/80 in WT and ApoE^{-/-} mice. Arrowheads show strong expression of DNMT1 and DNMT3a located in the α -SMA and F4/80 positive areas of atherosclerosis. Immunohistochemical staining of normal IgG is presented as negative control experiments. Scale bars=20 μ m. Values are mean \pm SD from 4 animals in each group. **D**, Representative immunofluorescence images of DNMT1, α -SMA, and Mac3 costaining within the aortic roots. **E** and **F**, Western blot analyses show the expression of DNMT1, DNMT3a, and DNMT3b in aortas among 3 groups and quantitative results of Western blot. Heart lysates are used as positive controls. * P <0.05. **G**, Quantification of enzyme activities of DNMT in aortas among 3 groups. Values are mean \pm SD from 4 animals in each group. * P <0.05 vs WT group. # P <0.05 vs vehicle group. **H**, Quantification of 5-mC content in aortas among 3 groups. Values are mean \pm SD from 4 animals in each group. * P <0.05 vs WT group. # P <0.05 vs vehicle group. **I**, Relative mRNA expression levels of ten-eleven translocation 2 (Tet2) in aortas among 3 groups are determined by quantitative polymerase chain reaction (PCR). Values are mean \pm SD from 4 animals in each group. * P <0.05 vs WT group. # P <0.05 vs vehicle group. **J**, Western blot analyses show the expression of Tet2 in aortas among 3 groups. DAPI indicates 4',6-diamidino-2-phenylindole; and OD, optical density.

groups (Figure 3C and 3D; Figure III in the online-only Data Supplement). Moreover, compared with unmethylated vector, the methylated vector containing the fragment of Tet2 promoter suppressed luciferase activity by 56.5% in A7r5 which is a rat smooth muscle cell line (Figure 3E), reflecting that abnormal methylation status of Tet2 would repress its promoter activity and mRNA expression.

DNMT Inhibitor Resulted in 5-hmC Enrichment at the Myocardin Promoter

Given that Tet2 was required for conversion from 5-mC to 5-hmC, the interim cytosine to unmethylated cytosine, so we analyzed global 5-hmC content and gene-specific hydroxymethylation. As shown in Figure 4A, global hydroxymethylation level was dramatically lower in vehicle-treated mice compared with other 2 groups. Because Liu et al²⁵ reported that knockdown of Tet2 caused a cascade of epigenetic changes in VSMC phenotypic genes, we wished to address the issue of whether demethylation of Tet2 promoter after 5-aza treatment mediated the methylation and hydroxymethylation status at the promoters of these genes. Gene-specific measurement of hydroxymethylation was determined by quantitative polymerase chain reaction using primers pre-designed to the promoter region of Myocardin, Krüppel-like factor 4, and serum response factor (SRF). Compared with vehicle group, 5-aza treatment inhibited the methylation level at the Myocardin promoter with concomitant recruitment of 5-hmC in the corresponding region of Myocardin promoter (Figure 4B and 4C). Accordingly, the mRNA expression of Myocardin was repressed in the aorta of vehicle-treated ApoE^{-/-} mice but significantly reversed by 5-aza (Figure 4D). On the contrary, the 5-mC and 5-hmC contents at the indicated regions of Krüppel-like factor 4 and SRF promoters were not altered among 3 groups (Figure IV in the online-only Data Supplement). In agreement with the methylation and hydroxymethylation status of Krüppel-like factor 4 and SRF promoter, the mRNA expression of Krüppel-like factor 4 and SRF remained unchanged among 3 groups (Figure IV in the online-only Data Supplement).

DNMT1 Regulated VSMCs Proliferation, Migration, and Phenotype Switching

The altered Myocardin methylation in plaque implied that DNA hypermethylation may affect VSMC marker genes expression

and impair VSMC function during atherosclerotic development. Inspired by the finding and hypothesis, we then determined the role of 5-aza on VSMC function in vitro. It was known that VSMCs proliferation and migration into the intima were imperative steps for atherosclerosis and restenosis.²⁸ As an initial step, we examined the effect of 5-aza on DNMT activity and global 5-mC content in rat aortic smooth muscle cells (RASMCs). RASMCs were treated with 1 and 5 μ mol/L of 5-aza, which did not affect cell viability (Figure V in the online-only Data Supplement). Although administration of 5-aza did not affect the expression of DNMT1 and DNMT3a stimulated by platelet-derived growth factor (PDGF), the DNMT activity was profoundly repressed by 5-aza treatment (Figure 5A through 5D). Accordingly, incremental 5-mC content induced by PDGF was decreased after 5-aza treatment (Figure 5E). We next determined the role of 5-aza in the proliferation and migration of RASMCs. Scratch assays were performed to evaluate the role of 5-aza in SMCs migration. As shown in Figure 5F and 5G, administration of 5-aza for 3 days significantly suppressed PDGF-induced migration of RASMCs. As shown in Figure 5H, treatment of RASMCs with 5-aza significantly inhibited PDGF-induced proliferation in a time- and dose-dependent manner.

Our in vivo observation had displayed a significant reduction of Myocardin expression in the aortas of ApoE^{-/-} mice after 5-aza treatment. Thus, we next studied the effect of 5-aza on VSMC phenotype modulation. After treatment of RASMCs with 5-aza for \leq 5 days, the mRNA expression of VSMC differentiation marker genes, such as smooth muscle α -actin, smooth muscle-myosin heavy chain, and Myocardin, was markedly reversed 1.5-fold to 4-fold when compared with the decreased expression levels induced by PDGF (Figure 5I). Accordingly, the protein expression of these genes was restored by 5-aza treatment (Figure 5J). Moreover, the morphological analysis demonstrated that PDGF induced a flattened shape and a moderately larger size that reflected a dedifferentiated state of VSMCs. In contrast, administration of 5-aza kept VSMCs in a spindle-like shape that reflected a differentiated state (Figure 5K). We then measured the cell surface area among 3 groups, finding that much larger VSMCs in PDGF-treated group compared with vehicle group and smaller VSMCs in 5-aza-treated group compared with PDGF-treated group, respectively (Figure 5L). Together, these data demonstrated that inhibition of DNA methylation retarded VSMCs proliferation and migration through suppression of VSMC plasticity.

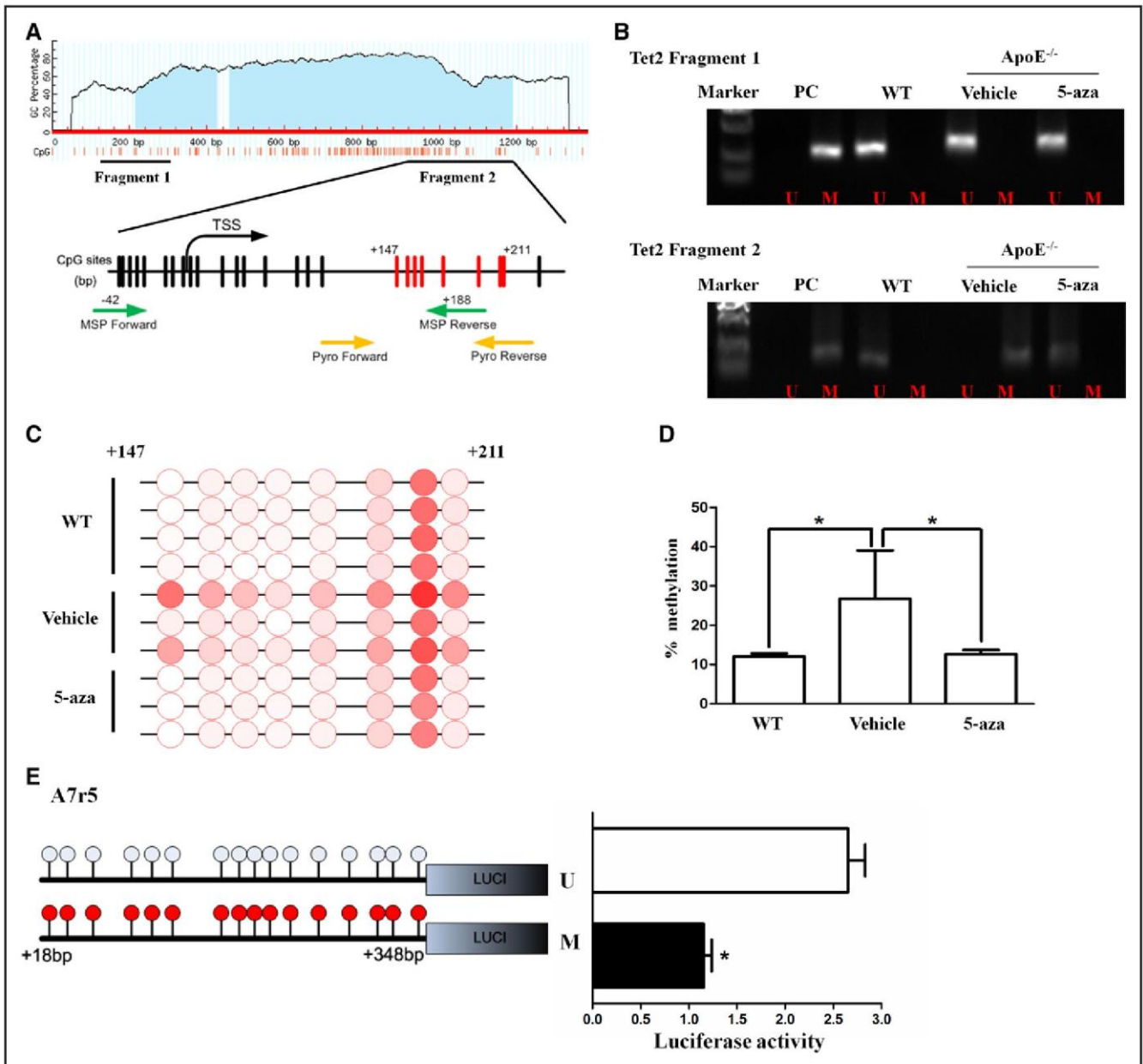


Figure 3. 5-aza-2'-deoxycytidine (5-aza) reverses ten-eleven translocation 2 (Tet2) hypermethylation and recovers its expression in atherosclerotic aorta. **A**, Schematic diagram of Tet2 promoter. **Upper**, CG percentages within the target region of Tet2 promoter. Blue area shows cytidine phosphate guanosine (CpG) island coverage within this region. Black pillars show CpG sites detected by methylation-specific polymerase chain reaction (MSP), whereas red pillars show CpG sites detected by pyrosequencing. Green and yellow arrows indicate the primer pairs of MSP and pyrosequencing spanning fragment 2, respectively. **B**, The methylation status of fragment 1 and fragment 2 within Tet2 promoter in aorta among 3 groups is determined by MSP. Normal aorta DNA was treated with methylase SssI as a positive control (PC). The methylation status of PCs (2 lanes) and samples are represented. **C**, Illustrative CpG site methylation levels for 3 groups at the target Tet2 promoter measured by pyrosequencing. Fully methylated CpG site is colored by red, whereas unmethylated CpG site is colored by white. **D**, Quantification of methylation percentages from all measured CpG sites by pyrosequencing. Data are mean \pm SD. * P <0.05. **E**, Relative luciferase activity of pGL3-basic containing Ethylated (M) Tet2 fragments. Each experiment was performed in triplicate. M or unmethylated (U) Tet2 fragments is measured by dual-luciferase reporter assay and normalized with an internal pGL-TK Renilla activity. * P <0.05. TSS indicates transcription start site; and WT, wild type.

Effects of DNMT Inhibitor on Neointimal Formation

Even though 5-aza could inhibit VSMC proliferation, migration, and dedifferentiation in vitro, it was still required to validate the effect of 5-aza on VSMC functions and vascular remodeling in vivo. For this purpose, complete ligation of common carotid artery was performed to induce extensive neointimal formation in the presence of an intact endothelial

lining. First and foremost, we determined the expression levels of DNMT1 and DNMT3a in vitro. DNMT1 was highly expressed in RASMC but almost undetectable in macrophages, whereas DNMT3a was comparably expressed in RASMC and macrophages (Figure 6A). We then characterized the pattern of expression of DNMT1 and DNMT3a in mouse neointimal formation model at 21 days after carotid artery ligation. Immunohistochemistry analysis showed that

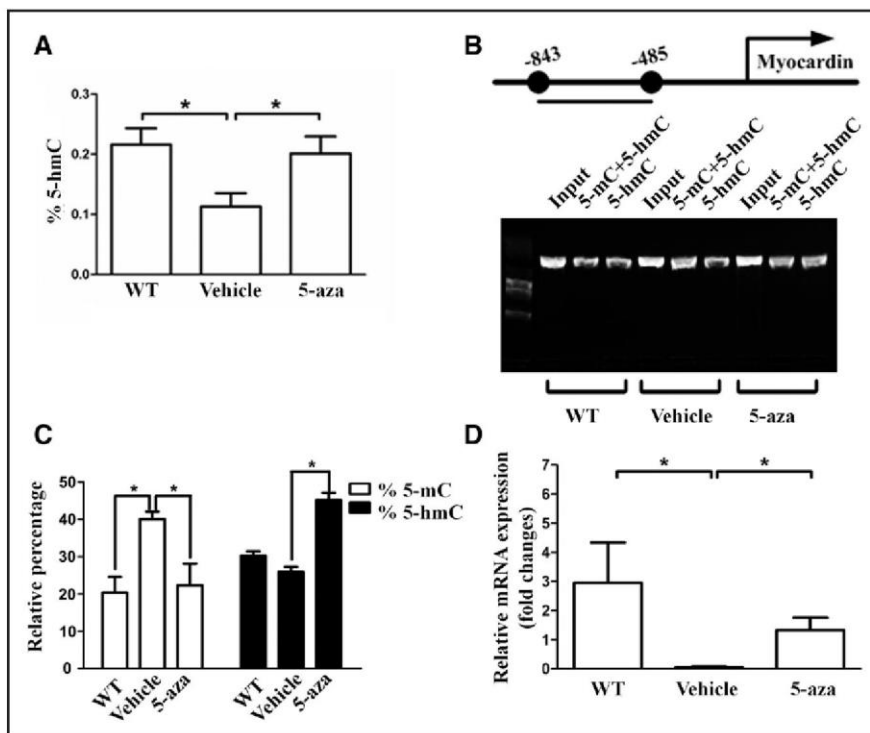


Figure 4. 5-aza-2'-deoxycytidine (5-aza) increases global 5-hydroxymethylcytosine (5-hmC) content and enhances 5-hmC enrichment at Myocardin promoter. **A**, Quantification of 5-hmC content in aortas among 3 groups. Values are mean±SD from 4 animals in each group. * $P<0.05$. **B**, Representative images of glycosylation-coupled methylation-sensitivity polymerase chain reaction (PCR) showing promoter-specific 5-methylcytosine (5-mC) and 5-hmC levels at Myocardin promoter. **C**, The percentages of promoter-specific 5-mC and 5-hmC levels at Myocardin promoter relative to input DNA content are quantified by quantitative PCR. Values are mean±SD from 4 animals in each group. * $P<0.05$. **D**, Relative mRNA expression levels of Myocardin in aortas among 3 groups are determined by quantitative PCR. Values are mean±SD from 4 animals in each group. * $P<0.05$. WT indicates wild type.

DNMT1 was widely expressed in the medial and neointimal layers, whereas DNMT3a was predominantly localized in the neointimal layer (Figure 6B). In contrast, DNMT1 and DNMT3a were not yet observed in the sham arteries.

The stimulation of DNMT1 and DNMT3a in response to vascular injury promoted us to gain further insight into the effect of DNA demethylation in neointimal formation. Vehicle or 5-aza (1 mg/kg) was intraperitoneally injected daily for 3 weeks after carotid ligation. We did not find any death in 5-aza-treated group. The body weights between saline- and 5-aza-treated groups were also comparable (19.2 ± 0.8 versus 18.6 ± 0.9 g; $P=0.39$). After harvesting the carotid arteries, we found that 5-aza substantially inhibited neointima formation (Figure 6C), which was associated with a decrease in both neointimal area ($2.25\pm 0.14\times 10^4$ versus $4.07\pm 0.22\times 10^4$ μm^2 ; $P<0.01$; Figure 6D) and the intima-to-media ratio (0.20 ± 0.02 versus 0.44 ± 0.03 ; $P<0.01$; Figure 6E). Likewise, immunohistochemistry staining and quantitative analysis showed a 4-fold increase in the proportion of Tet2-positive cells within the neointimal layer of 5-aza-treated group (Figure 6F and 6G).

Knockdown of DNMT1 Suppressed VSMCs Proliferation, Migration, and Dedifferentiation

We next sought to determine which isoforms of DNMT enzymes were involved in VSMC differentiation, proliferation, and migration. First, we confirmed the small interfering RNA (siRNA) inhibitory efficiency because the expression of DNMT1 and DNMT3a were downregulated by 63.4% and 59.9%, respectively, in protein level (Figure 7A). Indeed, when compared with DNMT3a, the knockdown of DNMT1 more efficiently abolished DNMT enzyme activities along with 5-mC content ($5.6\pm 2.7\%$ versus $13.6\pm 5.7\%$; $P=0.042$; Figure VI in the online-only Data Supplement). We then examined whether DNMT1 or DNMT3a specifically

mediated VSMC proliferation and migration. PDGF-induced proliferation was significantly inhibited by siDNMT1 but not siDNMT3a (Figure 7B; Figure VIIA in the online-only Data Supplement). Likewise, DNMT1 knockdown dramatically attenuated VSMCs migration stimulated by PDGF (Figure 7C and 7D). Nevertheless, no significant changes were observed in VSMC migration when treated by DNMT3a siRNA (Figure VII B and VII C in the online-only Data Supplement). Furthermore, the elevated expression levels of VSMCs dedifferentiation marker genes induced by PDGF were decreased after transfection with DNMT1-specific siRNA for 48 hours (Figure 7E). Nonetheless, DNMT3a siRNA had no impact on PDGF-induced VSMCs differentiation (Figure VII D in the online-only Data Supplement).

Depletion of DNMT1 Restored Tet2 Expression and Suppressed Tet2 Methylation

We further investigate the effect of 5-aza and DNMT1 on Tet2 observed in mice model. Although PDGF inhibited Tet2 expression in a time-dependent manner, the administration of 5-aza for 3 and 5 days significantly restored Tet2 expression in RASMCs ($P=0.013$ and $P=0.004$, respectively; Figure 8A). The methylation levels of Tet2 promoter in RASMCs were then evaluated by quantitative methylation-specific polymerase chain reaction. Consistent with increased Tet2 expression after incubation with 5-aza, the methylation levels of Tet2 promoter were suppressed by 5-day treatment of 5-aza (Figure 8B).

Inspired by the role of 5-aza on the inhibition of 5-mC content and Tet2 expression, we further discussed the reciprocal effect between DNMT1 and Tet2. Although depletion of DNMT1 increased Tet2 expression (Figure 8C), knockdown of Tet2 did not conversely affected DNMT1 expression (Figure 8D). Likewise, when compared with control siRNA,

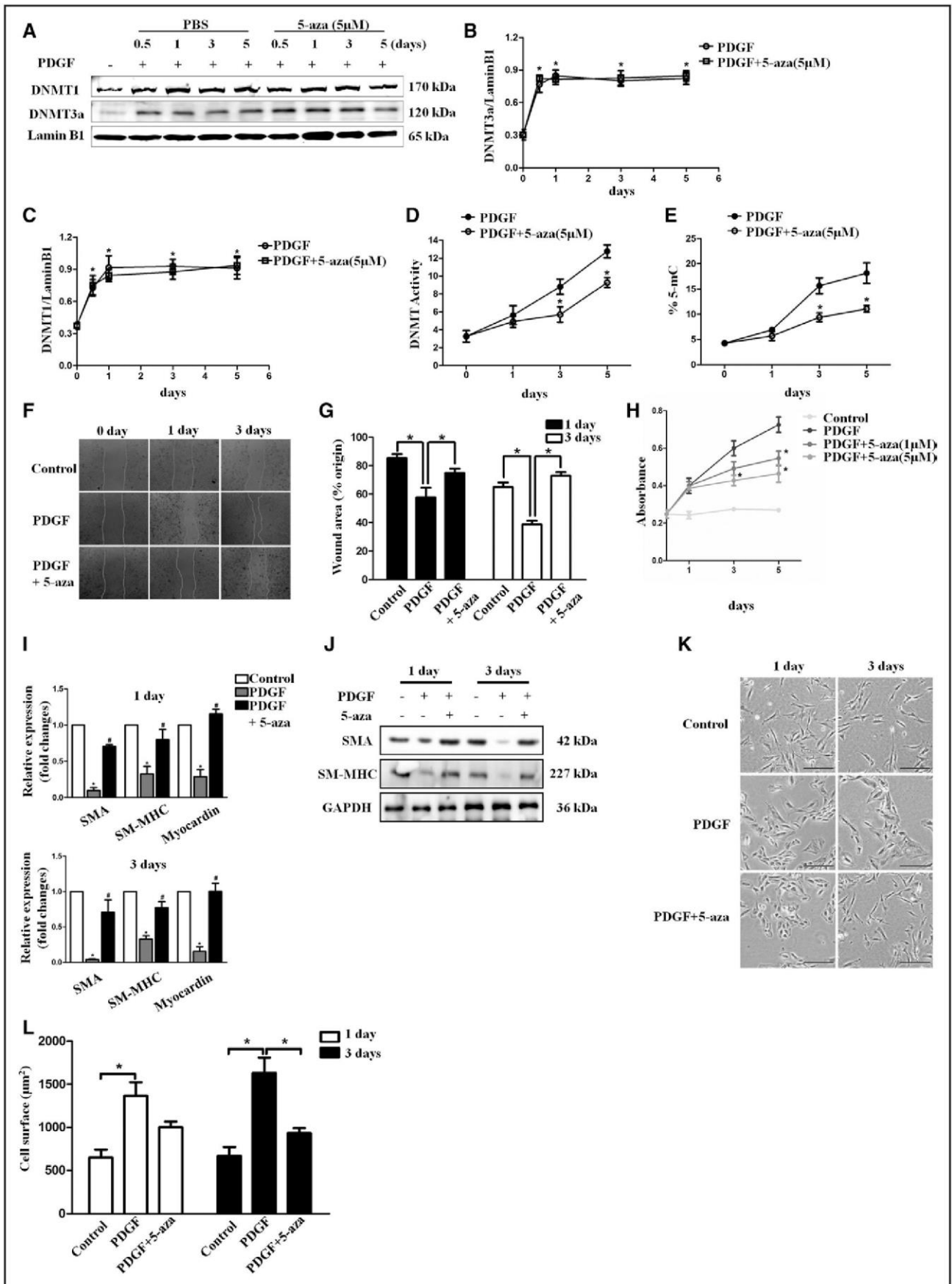


Figure 5. 5-aza-2'-deoxycytidine (5-aza) decreases vascular smooth muscle cell (VSMC) proliferation, migration, and dedifferentiation. **A**, Rat aortic smooth muscle cells (RASMCs) were cultured in serum-free medium for 24 h, then pretreated with 5-aza (5 μmol/L) for 24 h, and followed with platelet-derived growth factor (PDGF; 20 ng/mL) incubation for 0.5, 1, 3, and 5 d. Western blot analyses (*Continued*)

Figure 5 Continued. and quantitative results (**B** and **C**) showed the expression of DNA methyltransferase 1 (DNMT1) and DNMT3a in RASMCs at indicated time points. **D**, Quantification of enzyme activities of DNMT in RASMCs treated with PDGF (20 ng/mL) and 5-aza (5 μ mol/L) at indicated time points. * P <0.05 vs PDGF treatment group at the same time point. **E**, Quantification of 5-methylcytosine (5-mC) content in RASMCs pretreated with 5-aza (5 μ mol/L) and followed with PDGF (20 ng/mL) incubation at indicated time points. * P <0.05 vs PDGF treatment group at the same time point. **F**, Representative images of wound healing assay. **G**, The extent of wound healing was calculated as the percentage of remaining cell-free area compared with the original wound area. * P <0.05. **H**, RASMCs were stimulated with PDGF (20 ng/mL) in the presence or absence of 5-aza, and cell proliferation was assayed by CellTiter 96 aqueous one solution cell proliferation assay. * P <0.05 vs PDGF treatment group at the same time point. **I**, The mRNA expression levels of smooth muscle actin (SMA), smooth muscle-myosin heavy chain (SM-MHC), and Myocardin in RASMCs pretreated with 5-aza (5 μ mol/L) for 24 h and followed with PDGF (20 ng/mL) incubation for 1 and 3 d were measured by quantitative polymerase chain reaction (PCR). * P <0.05 vs control group. # P <0.05 vs PDGF treatment group. **J**, The protein expression of SMA and SM-MHC in RASMCs pretreated with 5-aza (5 μ mol/L) for 24 h and followed with PDGF (20 ng/mL) incubation for 1 and 3 d were measured by Western blots. **K**, Representative morphological images of the RASMCs pretreated with 5-aza (5 μ mol/L) for 24 h and followed with PDGF (20 ng/mL) incubation for 1 and 3 d. Each experimental data point was performed in triplicate. **L**, Bar graphs of calculated cell surface area in the indicated groups after 1- and 3-d treatment with phosphate buffer saline or 5-aza (5 μ mol/L). * P <0.05.

DNMT1 siRNA significantly repressed the methylation levels of Tet2 promoter induced by PDGF for 5 days in RASMCs (Figure 8E). Considering the effect of DNMT1 on Tet2 expression, we applied chromatin immunoprecipitation assays to test whether DNMT1 binds to Tet2 promoter and found that DNMT1 recognized and bound to the second fragment at Tet2 promoter (Figure 8F and 8G). More importantly, PDGF incubation for 3 days promoted DNMT1 binding to Tet2 promoter when compared with phosphate buffer saline group ($P=0.017$; Figure 8H and 8I). Compared with pretreatment with control siRNA, the 5-aza-induced suppression of RASMC proliferation and migration was partly counteracted by pretreatment with Tet2 siRNA (Figure VIII A through VIII C in the [online-only Data Supplement](#)). Accordingly, knockdown of Tet2 also activated the suppression of RASMC dedifferentiation obtained from 5-aza treatment (Figure VIII D in the [online-only Data Supplement](#)).

Discussion

In this study, we showed that DNA methylation was increased, whereas DNA hydroxymethylation, 1 intermediate form for demethylation, was decreased in atherosclerotic aorta. The increased global methylation could be explained by the enhanced activity of DNMT1 and reduced expression of Tet2. However, administration with 5-aza would restore aberrant hypermethylation both in global level and within the promoter of Tet2. As a consequence, 5-hmC was recaptured within the promoter of Myocardin, which promoted differentiation of VSMCs and inhibited the vascular remodeling (Figure IX in the [online-only Data Supplement](#)).

The clinical relevance of DNA methylation firstly became apparent in relation to cancer.²⁹ Then the abnormal DNA methylation was also found associated with other diseases such as Rett syndrome, immune deficiency, and so on.^{30,31} Some changes of DNA methylation can be a physiological response to environmental changes, whereas others might be associated with a pathological process such as cell phenotype change or even malignant transformation.¹⁶ VSMCs can revert to a synthetic phenotype featuring highly proliferative and migratory activity and increased synthesis of inflammatory factors. We find that DNMT activities differ along with atherosclerotic progression, although DNMT1 and Tet2 influence the DNA methylation equilibrium and SMC phenotype. Furthermore, to preclude other confounding factors, we apply a carotid artery ligation model in which abnormalities in VSMCs are

primarily responsible for vascular remodeling. The observation that 5-aza treatment inhibits neointimal formation confirms our assumption that 5-aza inhibits vascular remodeling via DNA demethylation in VSMCs.

As reviewed elsewhere, 2 pathways involve the DNA demethylation.^{30–32} One is passive demethylation, which is largely acquired by the inhibition of DNMTs activity. On the other side, the process of active conversion and removal of 5-mC is referred to as active demethylation. About the latter, mounting evidence has accumulated that Tet enzyme family serves as keys for the conversion of 5-mC to 5-hmC. Together with the established pharmacological action of 5-aza and our current finding, the effect of 5-aza on Tet2 expression could be explained by the mechanism that 5-aza is recruited into the hypermethylated fragments, forming covalent bonds with DNMT1 and causing DNMT1 enzyme inactivation. As a consequence of 5-aza incorporation, DNMT1 fails to combine with Tet2 promoter and maintain Tet2 methylation, eventually resulting in the recovery of Tet2 expression and the elevation of global 5-hmC levels. These results suggest that DNMT inhibitor, 5-aza, reverses DNA hypermethylation in atherosclerotic aorta of ApoE^{-/-} mice not only through inhibition of DNMT activity and traditional passive demethylation but also indirectly through recovery of Tet2 expression and active demethylation. However, based on analyses of recent evidence from our and other laboratories, we could not postulate which pathway predominates after 5-aza treatment.

DNA demethylation regulated by the Tet family is important for physiology and pathology.¹⁵ The decreased expression of Tet2 has been shown in human atherosclerosis.²⁵ The Tet2 hypermethylation observed in our study emerges as another acceptable mechanism to explain persistently reduced Tet2 expression in atherosclerosis. In addition, Liu et al²⁵ documents that induction of Tet2 in VSMCs is capable of converting 5-mC to 5-hmC at promoters of smooth muscle-myosin heavy chain, SRF, and Myocardin and lifts the repression of gene expression. Conversely, our study finds that the Myocardin is the major transcription factor regulated by DNA methylation in vivo because we only observe that a decrease in 5-mC is concomitant with an increase in 5-hmC at promoter of Myocardin after 5-aza treatment, although smooth muscle-myosin heavy chain and SRF are not found similar changes in atherosclerotic aorta.

Another goal of our study is to identify specific DNMT enzyme involved in atherosclerosis for subsequent functional analysis. In mammalian cells, DNMTs have 3

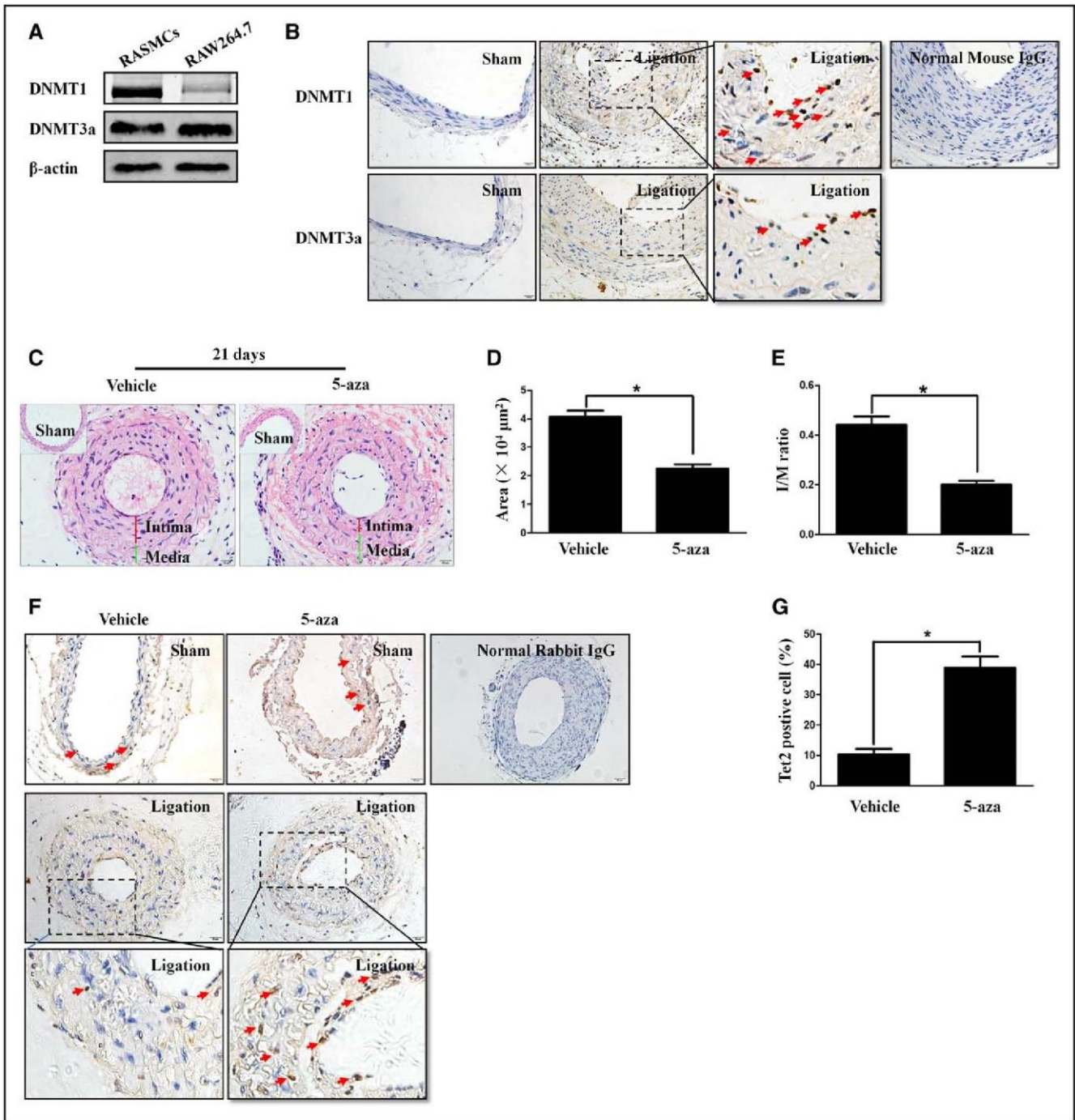


Figure 6. Inhibitory effect of 5-aza-2'-deoxycytidine (5-aza) on vascular remodeling after carotid ligation. **A**, Comparison of DNA methyltransferase 1 (DNMT1) and DNMT3a expression in rat aortic smooth muscle cells (RASMCs) and mouse macrophage RAW264.7 cells. **B**, Representative immunostaining of DNMT1 and DNMT3a in sham and ligated carotid artery. Scale bar=20 μm . Arrowheads show strong expression of DNMT1 and DNMT3a in ligated carotids. Immunohistochemical staining of normal IgG is presented as negative control experiments. **C**, Photomicrographs showing representative cross-sectional areas of ligated carotid artery from C57BL/6 mice with and without administration of 5-aza. Scale bar=20 μm . **D** and **E**, Comparison of intima area and intima/media (I/M) ratio in C57BL/6 mice with and without 5-aza treatment. Values are mean \pm SD from 4 animals in each group. * P <0.05. **F**, Representative immunohistochemistry images of cross-sectional areas of ligated carotids via anti-ten-eleven translocation (Tet2) antibody. Arrowheads show strong expression of Tet2 in carotid arteries. Immunohistochemical staining of normal IgG is presented as negative control experiments. **G**, Comparison of the percentage of Tet2-positive cells in the carotid arteries between C57BL/6 mice with and without 5-aza treatment. * P <0.05.

isoforms: DNMT1, DNMT3a, and DNMT3b. DNMT3a and DNMT3b mediate de novo DNA methylation, whereas DNMT1 acts on newly synthesized DNA to maintain methylation marks.¹⁶ Although both DNMT1 and DNMT3a localize within plaques and are upregulated after vascular

injury or PDGF treatment, 5-mC content is decreased exclusively through knockdown of DNMT1 but not affected by knockdown of DNMT3a. In accordance with in vivo observations, 5-aza treatment or DNMT1 silencing by siRNA recovers Myocardin expression, thereby inhibiting VSMC

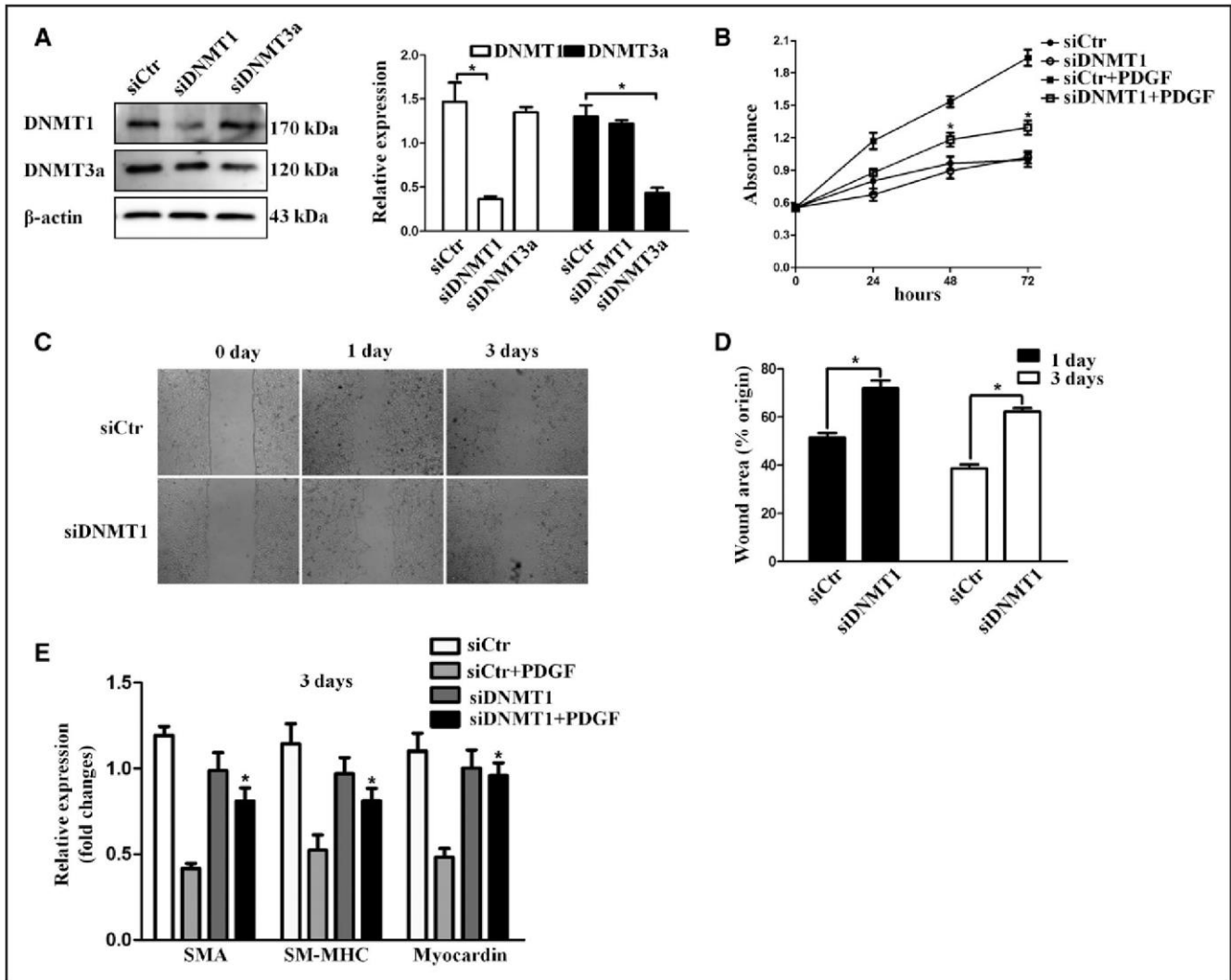


Figure 7. DNA methyltransferase 1 (DNMT1) mediates vascular smooth muscle cell (VSMC) proliferation, migration, and dedifferentiation. **A** and **B**, The efficiencies of small interfering RNA (siRNA)-mediated DNMT1 and DNMT3a silencing were confirmed by Western blot. * $P < 0.05$. **C**, Rat aortic smooth muscle cell (RASMCs) were transfected with DNMT1 siRNA followed with platelet-derived growth factor (PDGF) treatment (20 ng/mL), and cell proliferation was assayed by CellTiter 96 aqueous one solution cell proliferation assay. **C**, Representative images of wound healing assay. **D**, The extent of wound healing was calculated as the percentage of remaining cell-free area compared with the original wound area. * $P < 0.05$. **E**, The mRNA expression levels of smooth muscle action (SMA), smooth muscle-myosin heavy chain (SM-MHC), and Myocardin in RASMCs transfected with DNMT1 siRNA followed with PDGF treatment (20 ng/mL) were measured by quantitative polymerase chain reaction. * $P < 0.05$ vs siCtrl plus PDGF treatment group. Each experimental data point was performed in triplicate.

dedifferentiation, proliferation, and migration. Nevertheless, it is worth noting that DNMT3a, but not DNMT1, is shown to be associated with oxidized-low-density lipoprotein-induced inflammation and hypoxia-induced matrix damage in VSMCs in a previous study.³³ Although this finding seems to contradict our results, it should be mentioned that our study focuses only on VSMC phenotype modulation induced by PDGF. The difference with our study suggests that each DNMT is regulated by specific stimuli and plays different roles in the process of atherosclerosis. Nonetheless, because knockdown of DNMT3a mediated by siDNMT3a only partially inhibits DNMT3a expression, we could not conclusively preclude the role of DNMT3a on VSMC functions. The other limitation of our study is that we cannot totally exclude the possibility that 5-aza may alter the DNA methylation of other relevant cell types for vascular remodeling such as endothelial cells.²³ However, the in vitro experiments

in SMCs confirm that the methylation condition will affect SMC phenotype definitely.

Strong evidence and our findings consistently indicate that drifts in global DNA methylation concur with aging.^{34,35} Albeit 5-hmC comes from 5-mC and acts as an intermediate during active demethylation, 5-hmC levels fluctuate during mouse preimplantation development and vary from tissue to tissue.²⁶ In this regard, our work uncovered that 5-hmC accumulated, coinciding with a reduction in 5-mC, in normal aorta but remained unchanged in atherosclerotic aorta. This discrepancy could be attributed to Tet2 hypermethylation and inactivation in atherosclerotic aorta, which ultimately limited 5-hmC conversion. About gene-specific methylation, our results demonstrate that Tet2 hypermethylation is secondary to atherosclerosis, although most of previous studies looking across the genome suggest that disease-associated DNA methylation could arise before cancer onset.³³ It is, thus,

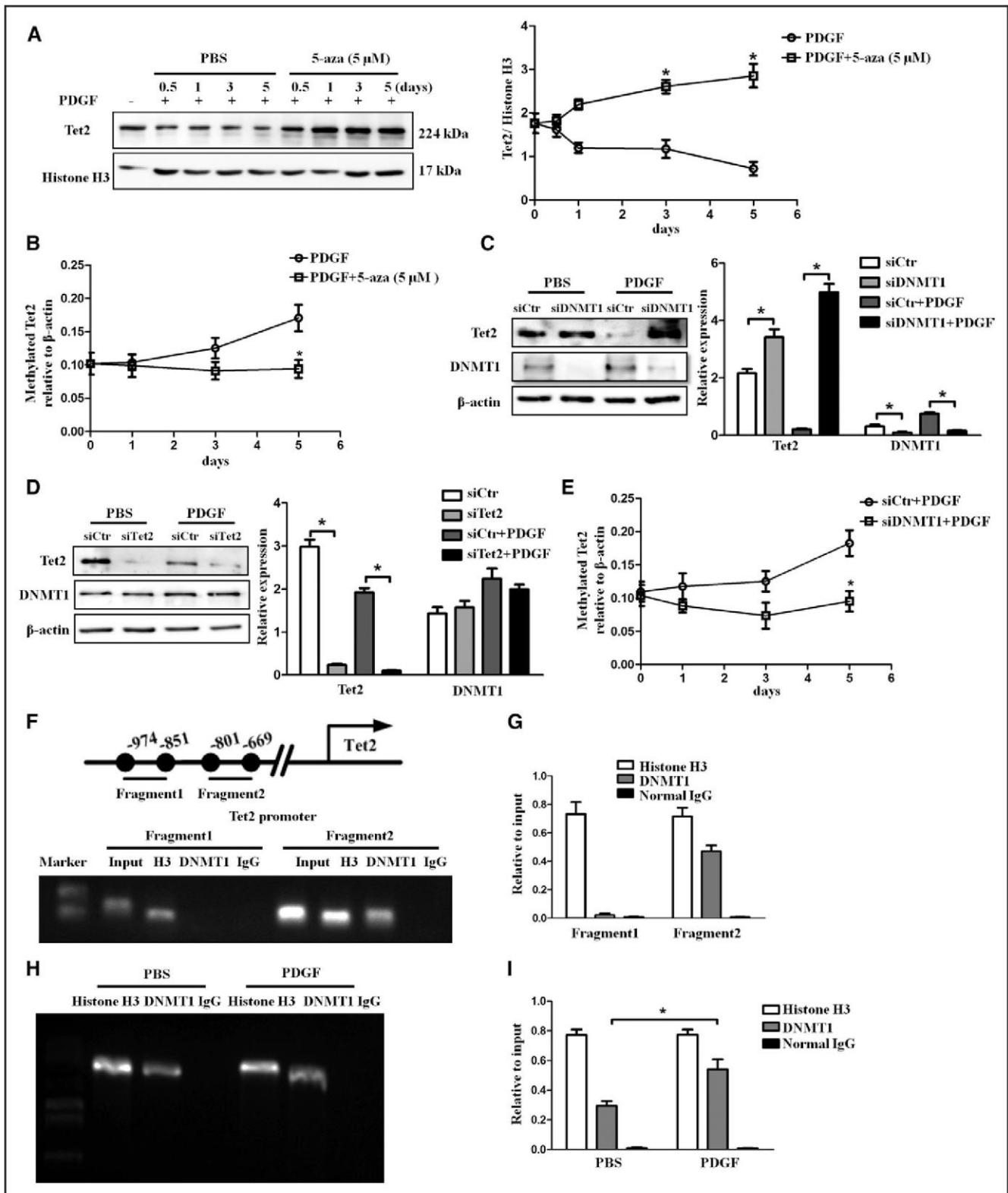


Figure 8. DNA methyltransferase (DNMT1) binds to ten-eleven translocation 2 (Tet2) promoter and is required for the maintenance of Tet2 methylation. **A**, Rat aortic smooth muscle cells (RASMCs) were cultured in serum-free medium for 24 h, then pretreated with 5-aza-2'-deoxycytidine (5-aza; 5 μ mol/L) for 24 h, and followed with platelet-derived growth factor (PDGF; 20 ng/mL) incubation for 0.5, 1, 3, and 5 d. Western blot analyses and quantitative results showed the expression of Tet2 in RASMCs at indicated time points. **B**, Quantitative methylation-specific polymerase chain reaction (PCR) showed the methylation levels of Tet2 promoter in response to 5-aza (5 μ mol/L) treatment at indicated time points. * P <0.05 vs PDGF treatment group at the same time point. **C** and **D**, RASMCs were transfected with DNMT1 or Tet2 small interfering RNA (siRNA) followed with PDGF treatment (20 ng/mL), and the protein expression of DNMT1 and Tet2 was examined by Western blot. * P <0.05. **E**, RASMCs were transfected with DNMT1 siRNA followed with PDGF treatment (20 ng/mL), and quantitative methylation-specific PCR was performed to determine the methylation levels of Tet2 promoter. * P <0.05 vs control siRNA plus PDGF-treated group at the same time point. **F** and **G**, Chromatin immunoprecipitation (ChIP) assays were performed (*Continued*)

Figure 8 Continued. to detect and quantify the binding of DNMT1 to Tet2 promoter. Histone H3 was used as a positive control, and normal IgG was used as a negative control. Each experimental data point was performed in triplicate. **H** and **I**, ChIP assays were performed to evaluate DNMT1 binding to Tet2 promoter in the presence and absence of PDGF treatment for 3 d. **P*<0.05.

conceivable that prolonged environmental exposure initiates and exacerbates atherosclerosis, as well as Tet2 methylation.

Conclusions

DNMT inhibition prevents VSMC dedifferentiation, proliferation, and migration in vitro and eventually retards vascular remodeling and atherosclerosis. The underlying mechanisms depend on a passive demethylation pathway via suppression of global 5-mC content and Tet2 hypomethylation, which in turn initiates an active demethylation pathway, characterized as enrichment of 5-hmC in the Myocardin promoter. Therefore, stringent control of the yin–yang equilibrium of DNA methylation is critical to VSMC phenotypic modulation and artery protection.

Acknowledgments

We are grateful to Dr Mark W. Feinberg from Harvard Medical School for his critical discussions and comments on the article.

Sources of Funding

This work was supported by National Natural Science Foundation of China (Grant No. 81370391) and Key Grant for Shanghai Science and Technology Foundation (14JC1401202).

Disclosures

None.

References

1. Yao L, Heuser-Baker J, Herlea-Pana O, Iida R, Wang Q, Zou MH, Barlic-Dicen J. Bone marrow endothelial progenitors augment atherosclerotic plaque regression in a mouse model of plasma lipid lowering. *Stem Cells*. 2012;30:2720–2731. doi: 10.1002/stem.1256.
2. Feig JE, Shang Y, Rotllan N, Vengrenyuk Y, Wu C, Shamir R, Torra IP, Fernandez-Hernando C, Fisher EA, Garabedian MJ. Statins promote the regression of atherosclerosis via activation of the CCR7-dependent emigration pathway in macrophages. *PLoS One*. 2011;6:e28534. doi: 10.1371/journal.pone.0028534.
3. Puri R, Nissen SE, Shao M, Ballantyne CM, Barter PJ, Chapman MJ, Erbel R, Libby P, Raichlen JS, Uno K, Kataoka Y, Nicholls SJ. Coronary atheroma volume and cardiovascular events during maximally intensive statin therapy. *Eur Heart J*. 2013;34:3182–3190. doi: 10.1093/eurheartj/eh2260.
4. Puri R, Nissen SE, Ballantyne CM, Barter PJ, Chapman MJ, Erbel R, Libby P, Raichlen JS, St John J, Wolski K, Uno K, Kataoka Y, Nicholls SJ. Factors underlying regression of coronary atheroma with potent statin therapy. *Eur Heart J*. 2013;34:1818–1825. doi: 10.1093/eurheartj/eh2084.
5. Scandinavian Simvastatin Survival Study Group. Randomised trial of cholesterol lowering in 4444 patients with coronary heart disease: The Scandinavian simvastatin survival study (4s). *Lancet*. 1994;344:1383–1389. doi: 10.1016/S0140-6736(94)90566-5.
6. Shepherd J, Cobbe SM, Ford I, Isles CG, Lorimer AR, MacFarlane PW, McKillop JH, Packard CJ. Prevention of coronary heart disease with pravastatin in men with hypercholesterolemia. West of Scotland Coronary Prevention Study Group. *N Engl J Med*. 1995;333:1301–1307. doi: 10.1056/NEJM199511163332001.
7. Sacks FM, Pfeffer MA, Moye LA, Rouleau JL, Rutherford JD, Cole TG, Brown L, Warnica JW, Arnold JM, Wun CC, Davis BR, Braunwald E. The effect of pravastatin on coronary events after myocardial infarction in patients with average cholesterol levels. Cholesterol and Recurrent Events Trial investigators. *N Engl J Med*. 1996;335:1001–1009. doi: 10.1056/NEJM199610033351401.
8. Downs JR, Clearfield M, Weis S, Whitney E, Shapiro DR, Beere PA, Langendorfer A, Stein EA, Krueger W, Gotto AM Jr. Primary prevention of acute coronary events with lovastatin in men and women with average cholesterol levels: results of AFCAPS/TexCAPS. Air Force/Texas Coronary Atherosclerosis Prevention Study. *JAMA*. 1998;279:1615–1622.
9. The Long-Term Intervention With Pravastatin in Ischaemic Disease (LIPID) Study Group. Prevention of cardiovascular events and death with pravastatin in patients with coronary heart disease and a broad range of initial cholesterol levels. *N Engl J Med*. 1998;339:1349–1357. doi: 10.1056/NEJM199811053391902.
10. Liu R, Leslie KL, Martin KA. Epigenetic regulation of smooth muscle cell plasticity. *Biochim Biophys Acta*. 2015;1849:448–453. doi: 10.1016/j.bbagr.2014.06.004.
11. Ghoshal K, Datta J, Majumder S, Bai S, Kutay H, Motiwala T, Jacob ST. 5-Aza-deoxycytidine induces selective degradation of DNA methyltransferase 1 by a proteasomal pathway that requires the KEN box, bromo-adjacent homology domain, and nuclear localization signal. *Mol Cell Biol*. 2005;25:4727–4741. doi: 10.1128/MCB.25.11.4727-4741.2005.
12. Mossman D, Kim KT, Scott RJ. Demethylation by 5-aza-2'-deoxycytidine in colorectal cancer cells targets genomic DNA whilst promoter CpG island methylation persists. *BMC Cancer*. 2010;10:366. doi: 10.1186/1471-2407-10-366.
13. Christman JK. 5-Azacytidine and 5-aza-2'-deoxycytidine as inhibitors of DNA methylation: mechanistic studies and their implications for cancer therapy. *Oncogene*. 2002;21:5483–5495. doi: 10.1038/sj.onc.1205699.
14. Issa JP, Gharibyan V, Cortes J, Jelinek J, Morris G, Verstovsek S, Talpaz M, Garcia-Manero G, Kantarjian HM. Phase II study of low-dose decitabine in patients with chronic myelogenous leukemia resistant to imatinib mesylate. *J Clin Oncol*. 2005;23:3948–3956. doi: 10.1200/JCO.2005.11.981.
15. Kohli RM, Zhang Y. TET enzymes, TDG and the dynamics of DNA demethylation. *Nature*. 2013;502:472–479. doi: 10.1038/nature12750.
16. Li E, Zhang Y. DNA methylation in mammals. *Cold Spring Harb Perspect Biol*. 2014;6:a019133. doi: 10.1101/cshperspect.a019133.
17. Ito S, Shen L, Dai Q, Wu SC, Collins LB, Swenberg JA, He C, Zhang Y. Tet proteins can convert 5-methylcytosine to 5-formylcytosine and 5-carboxylcytosine. *Science*. 2011;333:1300–1303. doi: 10.1126/science.1210597.
18. He YF, Li BZ, Li Z, et al. Tet-mediated formation of 5-carboxylcytosine and its excision by TDG in mammalian DNA. *Science*. 2011;333:1303–1307. doi: 10.1126/science.1210944.
19. Cortellino S, Xu J, Sannai M, et al. Thymine DNA glycosylase is essential for active DNA demethylation by linked deamination-base excision repair. *Cell*. 2011;146:67–79. doi: 10.1016/j.cell.2011.06.020.
20. Superko HR, Roberts R, Agatston A, Frohwein S, Reingold JS, White TJ, Sninsky JJ, Margolis B, Momary KM, Garrett BC, King SB III. Genetic testing for early detection of individuals at risk of coronary heart disease and monitoring response to therapy: challenges and promises. *Curr Atheroscler Rep*. 2011;13:396–404. doi: 10.1007/s11883-011-0198-8.
21. Gluckman PD, Hanson MA, Buklijas T, Low FM, Beedle AS. Epigenetic mechanisms that underpin metabolic and cardiovascular diseases. *Nat Rev Endocrinol*. 2009;5:401–408. doi: 10.1038/nrendo.2009.102.
22. Bressler J, Shimmin LC, Boerwinkle E, Hixson JE. Global DNA methylation and risk of subclinical atherosclerosis in young adults: the Pathobiological Determinants of Atherosclerosis in Youth (PDAY) study. *Atherosclerosis*. 2011;219:958–962. doi: 10.1016/j.atherosclerosis.2011.09.040.
23. Dunn J, Qiu H, Kim S, Jjingo D, Hoffman R, Kim CW, Jang I, Son DJ, Kim D, Pan C, Fan Y, Jordan IK, Jo H. Flow-dependent epigenetic DNA methylation regulates endothelial gene expression and atherosclerosis. *J Clin Invest*. 2014;124:3187–3199. doi: 10.1172/JCI74792.
24. Findeisen HM, Kahles FK, Bruemmer D. Epigenetic regulation of vascular smooth muscle cell function in atherosclerosis. *Curr Atheroscler Rep*. 2013;15:319.
25. Liu R, Jin Y, Tang WH, Qin L, Zhang X, Tellides G, Hwa J, Yu J, Martin KA. Ten-eleven translocation-2 (TET2) is a master regulator of smooth muscle cell plasticity. *Circulation*. 2013;128:2047–2057. doi: 10.1161/CIRCULATIONAHA.113.002887.
26. Ficz G, Branco MR, Seisenberger S, Santos F, Krueger F, Hore TA, Marques CJ, Andrews S, Reik W. Dynamic regulation of 5-hydroxymethylcytosine

- in mouse ES cells and during differentiation. *Nature*. 2011;473:398–402. doi: 10.1038/nature10008.
27. Wang YS, Chou WW, Chen KC, Cheng HY, Lin RT, Juo SH. MicroRNA-152 mediates DNMT1-regulated DNA methylation in the estrogen receptor α gene. *PLoS One*. 2012;7:e30635. doi: 10.1371/journal.pone.0030635.
 28. Andrés V. Control of vascular cell proliferation and migration by cyclin-dependent kinase signalling: new perspectives and therapeutic potential. *Cardiovasc Res*. 2004;63:11–21. doi: 10.1016/j.cardiores.2004.02.009.
 29. Feinberg AP, Vogelstein B. Hypomethylation distinguishes genes of some human cancers from their normal counterparts. *Nature*. 1983;301:89–92.
 30. Scourzic L, Mouly E, Bernard OA. TET proteins and the control of cytosine demethylation in cancer. *Genome Med*. 2015;7:9. doi: 10.1186/s13073-015-0134-6.
 31. Schübeler D. Function and information content of DNA methylation. *Nature*. 2015;517:321–326. doi: 10.1038/nature14192.
 32. Bhutani N, Burns DM, Blau HM. DNA demethylation dynamics. *Cell*. 2011;146:866–872. doi: 10.1016/j.cell.2011.08.042.
 33. Chen KC, Wang YS, Hu CY, Chang WC, Liao YC, Dai CY, Juo SH. OxLDL up-regulates microRNA-29b, leading to epigenetic modifications of MMP-2/MMP-9 genes: a novel mechanism for cardiovascular diseases. *FASEB J*. 2011;25:1718–1728. doi: 10.1096/fj.10-174904.
 34. Christensen BC, Houseman EA, Marsit CJ, Zheng S, Wrensch MR, Wiemels JL, Nelson HH, Karagas MR, Padbury JF, Bueno R, Sugarbaker DJ, Yeh RF, Wiencke JK, Kelsey KT. Aging and environmental exposures alter tissue-specific DNA methylation dependent upon CpG island context. *PLoS Genet*. 2009;5:e1000602. doi: 10.1371/journal.pgen.1000602.
 35. Hon GC, Song CX, Du T, et al. 5mC oxidation by Tet2 modulates enhancer activity and timing of transcriptome reprogramming during differentiation. *Mol Cell*. 2014;56:286–297. doi: 10.1016/j.molcel.2014.08.026.

Highlights

- DNA methylation dynamic changes would affect cells phenotypes and lead to physiological and pathological changes.
- In this study, we identify that DNA methylation influences vascular smooth muscle cell phenotype switch and vascular remodeling.
- In addition, we also indicate how the DNA methylation equilibrium is regulated from methylation enzyme, DNA methyltransferase, and demethylation, ten–eleven translocation 2.
- Mechanistic studies show that DNA methyltransferase 1 binds to ten–eleven translocation 2 promoter and is required for ten–eleven translocation 2 methylation, which in turn affects global 5- methylcytosine content, 5- hydroxymethylcytosine content, and the methylation status at Myocardin promoter as well.
- The yin–yang dynamics of DNA methylation suggests a new pathogenic mechanism of atherosclerosis, which will contribute to the development of effective therapy.
- In addition, it also provides insights into the understanding of complex interplay between environment and DNA modification.

6.5 List of genes differentially expressed in 6-month APP/PS1 mice by RNA-seq

Gene ID	Gene name	baseMean	Log2Fold	P value
ENSMUSG00000032503	Arpp21	2924.645015	-5.868639875	4.39E-09
ENSMUSG00000020601	Trib2	930.9021857	-4.694256415	2.68E-06
ENSMUSG00000036052	Dnajb5	3191.305459	-4.225546066	2.38E-05
ENSMUSG00000053279	Aldh1a1	985.8262276	-4.216140863	2.49E-05
ENSMUSG00000021765	Fst	44.23827024	-4.159144049	3.19E-05
ENSMUSG00000068762	Gstm6	171.4116411	-4.143767446	3.42E-05
ENSMUSG00000060373	Hnrnpc	4177.864451	-3.983999022	6.78E-05
ENSMUSG00000078851	Hist3h2a	332.0194559	-3.947362381	7.90E-05
ENSMUSG00000040055	Gjb6	1052.926814	-3.779729352	0.000156999
ENSMUSG00000020522	Mfap3	688.2274523	-3.746181029	0.000179547
ENSMUSG00000074968	Ano3	4953.655101	-3.715785639	0.000202573
ENSMUSG00000040653	Ppp1r14c	422.4447256	-3.715210698	0.000203034
ENSMUSG00000039770	Ypel5	2743.994254	-3.691827795	0.000222648
ENSMUSG00000042197	Zfp451	3166.765753	-3.659446262	0.000252761
ENSMUSG00000027660	Skil	2500.924297	-3.612664317	0.000303067
ENSMUSG00000043020	Wdr63	82.51718922	-3.59884295	0.000319636
ENSMUSG00000030706	Mrpl48	598.561495	-3.586733457	0.000334846
ENSMUSG00000030774	Pak1	8714.973679	-3.544020127	0.000394075
ENSMUSG00000027162	Lin7c	2694.976811	-3.525141416	0.000423257
ENSMUSG00000052726	Kcnt2	1059.173815	-3.503532134	0.000459131
ENSMUSG00000041660	Bbox1	83.03349716	-3.501800242	0.000462126
ENSMUSG00000019487	Trip10	132.7640837	-3.495256963	0.000473606
ENSMUSG00000048458	Fam212b	2787.454494	-3.491806171	0.000479766
ENSMUSG00000030704	Rab6a	14447.47988	-3.487958866	0.000486723
ENSMUSG00000006057	Atp5g1	351.6340543	-3.384463538	0.000713175
ENSMUSG00000022332	Khdrbs3	4592.868059	-3.374984972	0.000738197
ENSMUSG00000040760	Appl1	3337.868719	-3.362740956	0.000771727
ENSMUSG00000053153	Spag16	44.62016403	-3.353481364	0.000798018
ENSMUSG00000032246	Calml4	43.51669054	-3.332555806	0.000860522
ENSMUSG00000035642	Aamdc	483.1547891	-3.330019335	0.0008684
ENSMUSG00000028132	Tmem56	1701.956672	-3.324276889	0.000886481
ENSMUSG00000042182	Bend6	3288.178711	-3.309204919	0.000935613
ENSMUSG00000030317	Timp4	660.0837706	-3.295373871	0.000982908
ENSMUSG00000026072	Il1r1	333.2653974	-3.260328207	0.001112834
ENSMUSG00000034160	Ogt	10080.28109	-3.233746198	0.00122178

ENSMUSG00000020224	Llph	104.6805497	-3.224337025	0.001262647
ENSMUSG00000068428	Gmnc	95.89772882	-3.220507471	0.001279639
ENSMUSG00000027193	Api5	2054.940508	-3.213044764	0.001313358
ENSMUSG00000070544	Top1	2528.703662	-3.196677005	0.001390205
ENSMUSG00000050994	Adgb	67.69665702	-3.195371696	0.001396509
ENSMUSG00000027778	lft80	938.7878338	-3.183561159	0.001454754
ENSMUSG00000042353	Frem3	111.0817069	-3.176073442	0.001492832
ENSMUSG00000011179	Odc1	367.6248844	-3.163425624	0.001559242
ENSMUSG00000057715	A830018L16Rik	2368.251753	-3.146545562	0.001652115
ENSMUSG00000008226	Scrn3	1333.639479	-3.143664996	0.001668463
ENSMUSG00000054074	Skida1	636.9889913	-3.134590401	0.001720942
ENSMUSG00000045095	Magi1	1155.89048	-3.119181531	0.001813542
ENSMUSG00000085558	4930412C18Rik	61.64399836	-3.112420574	0.001855599
ENSMUSG00000035984	Nme5	172.2025358	-3.112022164	0.001858105
ENSMUSG00000020580	Rock2	7909.181409	-3.109062755	0.001876819
ENSMUSG00000032314	Etfa	631.5312166	-3.105891258	0.001897065
ENSMUSG00000036093	Arl5a	2305.083229	-3.07218753	0.002124962
ENSMUSG00000022247	Brix1	555.8176166	-3.057994405	0.002228237
ENSMUSG00000039114	Nrn1	7088.11175	-3.044369807	0.002331683
ENSMUSG00000028971	Cort	30.32356741	-3.031939183	0.002429882
ENSMUSG00000027654	Fam83d	28.08005748	-3.023339602	0.002500015
ENSMUSG00000047459	Dynlrb1	2173.699653	-3.022217032	0.002509306
ENSMUSG00000021520	Uqcrb	462.8993704	-3.022092887	0.002510335
ENSMUSG00000072663	Spf2	148.6403021	-3.013732867	0.002580549
ENSMUSG00000019837	Gtf3c6	308.1819107	-3.012418936	0.002591746
ENSMUSG00000027893	Ahcyl1	10745.93614	-2.998635723	0.002711913
ENSMUSG00000046447	Camk2n1	15821.42674	-2.998634375	0.002711925
ENSMUSG00000062014	Gmfb	8444.38977	-2.982288549	0.002861022
ENSMUSG00000068854	Hist2h2be	199.174588	-2.964348864	0.003033242
ENSMUSG00000096929	A330023F24Rik	1728.398425	-2.958085655	0.003095561
ENSMUSG00000030592	Ryr1	433.3648594	-2.956756847	0.003108932
ENSMUSG00000030521	Mphosph10	866.1676882	-2.947872474	0.00319969
ENSMUSG00000072473	1700024G13Rik	7.035718351	-2.945351838	0.003225876
ENSMUSG00000030469	Zfp719	673.0603406	-2.939013066	0.003292592
ENSMUSG00000043487	Acot6	258.2939326	-2.930469584	0.003384501
ENSMUSG00000021758	Ddx4	65.04387154	-2.929478741	0.00339531
ENSMUSG00000031245	Hmgn5	468.7210463	-2.921839278	0.003479711
ENSMUSG00000037640	Zfp60	1077.619378	-2.913917882	0.003569238
ENSMUSG00000037458	Azin1	4944.721262	-2.909625259	0.003618624
ENSMUSG00000060147	Serpib6a	664.0918542	-2.90647623	0.003655247

ENSMUSG00000026473	Glul	24244.03243	-2.906255438	0.003657827
ENSMUSG00000012640	Zfp715	965.5051409	-2.89821601	0.00375292
ENSMUSG00000016921	Srsf6	2834.466429	-2.89821508	0.003752931
ENSMUSG00000039395	Mreg	137.5826006	-2.891421456	0.003835034
ENSMUSG00000020390	Ube2b	4220.196228	-2.88761723	0.003881719
ENSMUSG00000020651	Slc26a4	795.5078845	-2.885570156	0.003907054
ENSMUSG00000038059	Smim3	265.5212734	-2.885040396	0.003913634
ENSMUSG00000038702	Dsel	551.8368323	-2.852002664	0.004344474
ENSMUSG00000074971	Fibin	46.42265486	-2.845343085	0.004436361
ENSMUSG00000044150	A830080D01Rik	211.0237899	-2.841461522	0.004490727
ENSMUSG00000031605	Klhl2	10194.06469	-2.839921904	0.004512458
ENSMUSG00000053907	Mat2a	3528.576144	-2.834446435	0.004590515
ENSMUSG00000047216	Cdh19	235.0257875	-2.83429597	0.004592677
ENSMUSG00000037720	Tmem33	3506.659786	-2.832859842	0.004613361
ENSMUSG00000029090	Gpr125	636.5168266	-2.823431801	0.004751253
ENSMUSG00000048070	Pirt	114.5603346	-2.81943662	0.004810803
ENSMUSG00000053931	Cnn3	1310.590924	-2.811072072	0.004937672
ENSMUSG00000097059	Fam120aos	125.8873854	-2.802176435	0.005075911
ENSMUSG00000062949	Atp11c	515.4041888	-2.799940368	0.005111205
ENSMUSG00000021798	Ldb3	260.0862748	-2.790569482	0.005261541
ENSMUSG00000019804	Snx3	2232.711876	-2.785196517	0.005349529
ENSMUSG00000020953	Coch	47.44234924	-2.780665723	0.005424756
ENSMUSG00000003814	Calr	9614.729236	-2.76995328	0.005606433
ENSMUSG00000020029	Nudt4	2262.288031	-2.76888682	0.005624817
ENSMUSG00000041180	Hectd2	933.337879	-2.768553155	0.00563058
ENSMUSG00000026028	Trak2	7050.97575	-2.767349587	0.005651412
ENSMUSG00000090272	Mndal	149.7529524	-2.760586275	0.005769772
ENSMUSG00000027375	Mal	3975.853375	-2.755551592	0.005859326
ENSMUSG00000084159	Gm12696	119.648256	-2.755179442	0.005865995
ENSMUSG00000029657	Hsph1	11805.50118	-2.750586756	0.005948864
ENSMUSG00000069184	Zfp72	100.3819047	-2.74242049	0.006098821
ENSMUSG00000020048	Hsp90b1	8186.069095	-2.741279295	0.006120046
ENSMUSG00000078427	Sarnp	163.352938	-2.732592489	0.006283803
ENSMUSG00000039771	Polr2j	365.7589441	-2.725285429	0.006424592
ENSMUSG00000036898	Zfp157	758.0109387	-2.709176694	0.006745041
ENSMUSG00000062604	Srpk2	5282.015194	-2.69409451	0.007058015
ENSMUSG00000090553	Snrpe	259.520391	-2.690520405	0.007134067
ENSMUSG00000084375	Gm11637	45.44176471	-2.687576672	0.007197258
ENSMUSG00000010080	Epn3	31.39507323	-2.686960877	0.00721054
ENSMUSG00000022048	Dpysl2	3680.201913	-2.686715195	0.007215845

ENSMUSG00000027394	Ttl	1853.062882	-2.686378801	0.007223115
ENSMUSG00000078234	Klhdc7a	466.4779519	-2.685716226	0.007237453
ENSMUSG00000050244	Heatr1	914.1183603	-2.681624917	0.007326556
ENSMUSG00000031431	Tsc22d3	1263.090865	-2.678214402	0.007401582
ENSMUSG00000025939	Ube2w	2036.203792	-2.678075537	0.007404652
ENSMUSG00000035790	Cep19	1172.422216	-2.677075405	0.007426792
ENSMUSG00000002416	Ndufb2	684.4328755	-2.669685682	0.007592228
ENSMUSG00000056296	Synpr	4022.91662	-2.668384154	0.007621706
ENSMUSG00000002015	Bcap31	1359.898977	-2.667841862	0.007634018
ENSMUSG00000072704	2700089E24Rik	3080.929373	-2.663667562	0.007729391
ENSMUSG00000025439	Clns1a	1199.668913	-2.659725697	0.007820431
ENSMUSG00000039997	Ifi203	203.3813101	-2.65719962	0.007879277
ENSMUSG00000079317	Trappc2	436.0203821	-2.656928515	0.007885616
ENSMUSG00000073293	Nudt10	502.3255113	-2.656751749	0.007889752
ENSMUSG00000028410	Dnaja1	2711.702965	-2.656483334	0.007896035
ENSMUSG00000027782	Kpna4	3466.562389	-2.653644807	0.00796276
ENSMUSG00000033967	2310014L17Rik	27.56012629	-2.649921258	0.008051053
ENSMUSG00000037685	Atp8a1	8769.100256	-2.647627948	0.008105868
ENSMUSG00000028419	Chmp5	2055.698701	-2.645259151	0.008162837
ENSMUSG00000036095	Dgkb	8374.125254	-2.644574028	0.008179381
ENSMUSG00000075486	Commd6	463.6300562	-2.640217364	0.008285287
ENSMUSG00000024097	Srsf7	2531.185816	-2.639713296	0.008297619
ENSMUSG00000007682	Dio2	1641.751167	-2.639312083	0.008307447
ENSMUSG00000024174	Pot1b	117.9092254	-2.632529862	0.008475157
ENSMUSG00000050549	5730508B09Rik	53.24581982	-2.627134848	0.00861072
ENSMUSG00000030423	Pop4	444.3658611	-2.626252965	0.008633063
ENSMUSG00000022375	Lrrc6	116.9688362	-2.624254602	0.008683884
ENSMUSG00000058254	Tspan7	21472.79907	-2.621216244	0.008761667
ENSMUSG00000029477	Morn3	14.24116922	-2.620276087	0.008785861
ENSMUSG00000052273	Dnah3	90.09355359	-2.619295314	0.008811163
ENSMUSG00000020290	Xpo1	3190.459603	-2.615744515	0.008903315
ENSMUSG00000076432	Ywhaq	1746.654494	-2.612433744	0.008990012
ENSMUSG00000047246	Hist1h2be	154.7695888	-2.611947788	0.0090028
ENSMUSG00000016386	Mpped2	912.2194009	-2.610329531	0.009045504
ENSMUSG00000003161	Sri	1196.945272	-2.608008579	0.009107067
ENSMUSG00000028333	Anp32b	792.6703591	-2.599878406	0.00932568
ENSMUSG00000015536	Mocs2	1294.296382	-2.5928575	0.00951822
ENSMUSG00000035151	Elmod2	530.0338506	-2.591670098	0.009551131
ENSMUSG00000036934	4921524J17Rik	167.6896472	-2.589412103	0.009613996
ENSMUSG00000060475	Wtap	597.7854469	-2.588666418	0.009634838

ENSMUSG00000021750	Fam107a	10169.95521	-2.583421703	0.009782567
ENSMUSG00000035852	Misp	5.875464906	-2.582514111	0.009808335
ENSMUSG00000060923	Acyp2	375.1069359	-2.580387015	0.009868964
ENSMUSG00000085793	Lin52	324.3163609	-2.579886264	0.009883286
ENSMUSG00000029130	Rnf32	371.9183414	-2.579503917	0.009894234
ENSMUSG00000019102	Aldh3a1	14.49114721	-2.578991969	0.009908909
ENSMUSG00000035179	Ppp1r32	59.17585144	-2.578378678	0.009926515
ENSMUSG00000035172	Plekhh3	137.2512424	2.575915946	0.009997495
ENSMUSG00000074406	Zfp628	131.6534212	2.582845087	0.009798931
ENSMUSG00000009739	Pou6f1	2048.506281	2.584436934	0.009753814
ENSMUSG00000042632	Pla2g6	526.5202193	2.584971734	0.009738698
ENSMUSG00000055629	B4galnt4	1560.437505	2.589984912	0.009598014
ENSMUSG00000045659	Plekha7	265.949692	2.592220896	0.009535852
ENSMUSG00000034009	Rxfp1	38.3164672	2.592453423	0.009529408
ENSMUSG00000028172	Tacr3	127.800521	2.592773774	0.009520537
ENSMUSG00000042116	Vwa1	200.9314481	2.59577112	0.009437891
ENSMUSG00000032269	Htr3a	415.9885923	2.595995617	0.009431727
ENSMUSG00000083813	Gm15502	1.134255984	2.596171328	0.009426905
ENSMUSG00000063646	Jakmip1	1181.154221	2.600020107	0.00932183
ENSMUSG00000059323	Tonsl	380.0089738	2.600707651	0.00930317
ENSMUSG00000059022	Kcp	19.35697507	2.60100748	0.009295043
ENSMUSG00000029576	Radil	147.588296	2.612450598	0.008989568
ENSMUSG00000045349	Sh2d5	1199.390181	2.61292087	0.008977208
ENSMUSG00000061306	Slc38a10	1559.04619	2.61325487	0.008968439
ENSMUSG00000021259	Cyp46a1	2070.294779	2.621057086	0.008765758
ENSMUSG00000037344	Slc12a9	506.1698952	2.628074744	0.008586965
ENSMUSG00000035969	Rusc2	2030.096458	2.629007574	0.008563445
ENSMUSG00000053465	Hs6st3	144.7123672	2.636703577	0.008371595
ENSMUSG00000079002	NA	127.2350442	2.636852138	0.00836793
ENSMUSG00000046415	B430212C06Rik	120.4121792	2.638822423	0.008319455
ENSMUSG00000036306	Lzts1	269.2914566	2.640763985	0.008271932
ENSMUSG00000068758	Il3ra	17.34205356	2.642135861	0.0082385
ENSMUSG00000041449	Serpina3h	4.811459186	2.642638887	0.008226272
ENSMUSG00000070002	Eil	411.109335	2.646343057	0.008136725
ENSMUSG00000066510	Ankdd1a	15.2316681	2.648013298	0.008096634
ENSMUSG00000074886	Grk6	1577.637188	2.653268047	0.007971654
ENSMUSG00000028789	Adc	488.6585566	2.653739706	0.007960521
ENSMUSG00000074500	Zfp558	37.30832287	2.655432063	0.007920689
ENSMUSG00000068744	Psrc1	218.3490075	2.66406053	0.007720367
ENSMUSG00000028469	Npr2	830.6332273	2.666347676	0.007668035

ENSMUSG00000028073	Pear1	46.46887935	2.66636872	0.007667555
ENSMUSG00000025876	Unc5a	2631.805731	2.66801248	0.007630142
ENSMUSG00000022489	Pde1b	2742.131385	2.669168395	0.007603932
ENSMUSG00000053552	Ebf4	141.6583182	2.672445477	0.007530061
ENSMUSG00000022568	Scrib	848.052319	2.674981949	0.007473327
ENSMUSG00000046556	Zfp319	334.231639	2.675958578	0.007451585
ENSMUSG00000001750	Tcirg1	196.7531445	2.677958461	0.00740724
ENSMUSG00000039157	Fam102a	2559.77167	2.697492172	0.006986393
ENSMUSG00000055653	Gpc3	119.3735014	2.69754017	0.006985386
ENSMUSG00000018599	Mief2	376.4491993	2.7061305	0.006807229
ENSMUSG00000038630	Zkscan16	982.2776728	2.713153706	0.006664619
ENSMUSG00000030839	Sergef	377.8810429	2.713217644	0.006663333
ENSMUSG00000052192	Gm5963	1.841810254	2.714885161	0.006629876
ENSMUSG00000071745	DXBay18	1.128138506	2.718768171	0.006552552
ENSMUSG00000075334	Rprm	264.4675037	2.719457669	0.006538906
ENSMUSG00000060279	Ap2a1	3928.804528	2.724825992	0.006433538
ENSMUSG00000074743	Thbd	170.3939565	2.738298787	0.006175794
ENSMUSG00000022665	Ccdc80	87.25289304	2.739830292	0.006147092
ENSMUSG00000027971	Ndst4	160.3503258	2.741385547	0.006118067
ENSMUSG00000048483	Zdhhc22	49.88845155	2.741890903	0.006108663
ENSMUSG00000028017	Egf	43.61375539	2.742936234	0.006089251
ENSMUSG00000076431	Sox4	63.4687448	2.747195575	0.006010728
ENSMUSG00000001918	Slc1a5	39.12480646	2.749429165	0.005969916
ENSMUSG00000020704	Asic2	1218.088203	2.754779298	0.005873174
ENSMUSG00000004707	Ly9	8.605411728	2.757727729	0.005820466
ENSMUSG000000091549	Gm6548	48.97832105	2.759634839	0.0057866
ENSMUSG00000041623	D11Wsu47e	189.0482465	2.762580734	0.005734638
ENSMUSG00000062545	Tlr12	9.621296381	2.765824347	0.005677911
ENSMUSG00000039153	Runx2	229.0980205	2.766891553	0.005659358
ENSMUSG00000026204	Ptprn	10239.05358	2.771775139	0.005575153
ENSMUSG00000043889	Gm8399	5.326831924	2.77257031	0.00556155
ENSMUSG00000030621	Me3	1660.087699	2.775256394	0.00551582
ENSMUSG00000037003	Tenc1	223.9229637	2.776736388	0.005490769
ENSMUSG00000082536	Gm13456	107.3157296	2.777721228	0.005474156
ENSMUSG00000053693	Mast1	1317.361606	2.781270098	0.005414667
ENSMUSG00000032523	Hhatl	151.0913386	2.78397899	0.005369651
ENSMUSG00000084099	Gm12929	3.470152438	2.789075532	0.005285874
ENSMUSG00000007783	Cpt1c	2682.155728	2.791345382	0.005248943
ENSMUSG00000038406	Scaf1	2575.416306	2.802609203	0.005069105
ENSMUSG00000051079	Rgs13	15.05364993	2.811551267	0.004930323

ENSMUSG00000029869	Ephb6	1831.607134	2.813147933	0.004905908
ENSMUSG00000039834	Zfp335	446.4273062	2.815678785	0.004867431
ENSMUSG00000072640	Lym9	1007.589319	2.8163598	0.004857124
ENSMUSG00000027498	Cstf1	566.4226612	2.821804648	0.004775426
ENSMUSG00000005514	Por	1314.878425	2.823834196	0.004745293
ENSMUSG00000070576	Mn1	350.2106141	2.826943022	0.004699469
ENSMUSG00000096171	Gm8055	4.614640114	2.827433355	0.004692278
ENSMUSG00000050271	D8Ert82e	862.5500634	2.832823004	0.004613893
ENSMUSG00000060166	Zdhhc8	1270.902117	2.85815191	0.004261163
ENSMUSG00000024330	Col11a2	352.7166239	2.861898159	0.004211122
ENSMUSG00000013787	Ehmt2	3440.527918	2.869135166	0.004115959
ENSMUSG00000018830	Myh11	84.93977183	2.872961474	0.004066437
ENSMUSG00000026792	Lrsam1	778.0846419	2.884970838	0.003914499
ENSMUSG00000014791	Elmo3	63.00705968	2.890671502	0.003844197
ENSMUSG00000058626	Capn11	17.45256855	2.891828717	0.003830067
ENSMUSG00000030134	Rasgef1a	7114.494104	2.903752776	0.003687192
ENSMUSG00000026842	Abl1	1287.915439	2.912959912	0.003580206
ENSMUSG00000021820	Camk2g	3579.435846	2.930912633	0.003379678
ENSMUSG00000054874	Pcnx13	1163.215816	2.939095404	0.003291717
ENSMUSG00000032172	Olfm2	417.6691775	2.939650446	0.003285827
ENSMUSG00000017760	Ctsa	1714.063045	2.953642266	0.003140478
ENSMUSG00000032120	C2cd2l	3047.570028	2.959554622	0.003080841
ENSMUSG00000051048	P4ha3	251.4181605	2.959645654	0.003079931
ENSMUSG00000000632	Sez6	3294.143112	2.963467917	0.003041938
ENSMUSG00000024952	Rps6ka4	727.6045882	2.966754043	0.003009616
ENSMUSG00000022324	Matn2	1477.076814	2.970877657	0.002969501
ENSMUSG00000020932	Gfap	8307.506336	2.971100484	0.002967347
ENSMUSG00000003657	Calb2	662.9595008	2.977801014	0.002903244
ENSMUSG00000030600	Lrfr1	381.5706094	2.99342502	0.002758653
ENSMUSG00000020701	Tmem132e	138.099532	3.003756164	0.00266669
ENSMUSG00000023009	Nckap5l	224.723444	3.012060327	0.00259481
ENSMUSG00000026930	Gpsm1	547.1663589	3.017744038	0.002546639
ENSMUSG00000002409	Dyrk1b	294.6918968	3.026521941	0.002473849
ENSMUSG00000053819	Camk2d	865.5834341	3.041087902	0.00235725
ENSMUSG00000047417	Rexo1	929.9841152	3.041251676	0.002355968
ENSMUSG00000055884	Fancm	344.4871617	3.04686062	0.002312449
ENSMUSG00000097023	Al854517	384.6000255	3.051370518	0.002277993
ENSMUSG00000060735	Rxfp3	319.4090468	3.063867875	0.002184954
ENSMUSG00000046805	Mpeg1	583.4629445	3.065368979	0.002174016
ENSMUSG00000051652	Lrrc3	150.7221466	3.06554263	0.002172754

ENSMUSG00000060594	Layn	98.76877118	3.069740665	0.002142447
ENSMUSG00000040488	Ltbp4	645.5175248	3.070936496	0.002133885
ENSMUSG00000026840	Lamc3	70.8062875	3.07167967	0.00212858
ENSMUSG00000020937	Plcd3	135.5578272	3.079189001	0.00207565
ENSMUSG00000009035	Tmem184b	1231.979801	3.080262649	0.002068181
ENSMUSG00000018819	Lsp1	49.59409308	3.096334309	0.001959293
ENSMUSG00000047502	Mroh7	119.010794	3.10252236	0.001918791
ENSMUSG00000024736	Tmem132a	952.2864523	3.109597394	0.001873425
ENSMUSG00000049728	Zfp668	236.2570138	3.140792326	0.001684915
ENSMUSG00000005357	Slc1a6	171.4263001	3.143992241	0.001666599
ENSMUSG00000033880	Lgals3bp	221.472329	3.152960752	0.001616235
ENSMUSG00000027568	Ntsr1	50.05291306	3.153109643	0.001615411
ENSMUSG00000029602	Rasal1	1685.256367	3.154077939	0.001610061
ENSMUSG00000060402	Chst8	326.0445579	3.187872833	0.001433236
ENSMUSG00000021294	Kif26a	84.08293197	3.204936684	0.001350922
ENSMUSG00000041741	Pde3a	73.12582052	3.208746155	0.001333151
ENSMUSG00000053898	Ech1	1031.233116	3.214174483	0.001308202
ENSMUSG00000066357	Wdr6	3432.907246	3.215387682	0.001302685
ENSMUSG00000020901	Pik3r5	66.96837266	3.223294664	0.001267251
ENSMUSG00000026443	Lrrn2	5059.141479	3.2323321	0.001227843
ENSMUSG00000097946	Gm8343	5.062011973	3.246071216	0.001170096
ENSMUSG00000097245	Gm5421	29.15885724	3.252860845	0.001142494
ENSMUSG00000038146	Notch3	147.0707729	3.2593757	0.001116577
ENSMUSG00000032198	Dock6	237.7813553	3.278717891	0.001042798
ENSMUSG00000033249	Hsf4	104.6504915	3.29052173	0.001000018
ENSMUSG00000066235	Pomgnt2	631.478522	3.322093421	0.000893448
ENSMUSG00000041592	Sdk2	563.3392191	3.387440674	0.00070548
ENSMUSG00000002799	Jag2	405.9567229	3.423623953	0.000617921
ENSMUSG00000039057	Myo16	654.3450293	3.42480617	0.000615238
ENSMUSG00000017721	Pigt	1080.907282	3.438103691	0.000585803
ENSMUSG00000053395	Cacng8	1564.103949	3.446051798	0.000568841
ENSMUSG00000038520	Tbc1d17	765.6911927	3.453354959	0.00055366
ENSMUSG00000028051	Hcn3	217.3449913	3.455802059	0.000548658
ENSMUSG00000017221	Psmd3	2093.286109	3.463262101	0.000533668
ENSMUSG00000018774	Cd68	130.057941	3.469985246	0.000520487
ENSMUSG00000045039	Megf8	3625.483741	3.484227216	0.00049356
ENSMUSG00000028439	Fam219a	2742.059934	3.505795296	0.000455245
ENSMUSG00000001435	Col18a1	71.5097195	3.508897159	0.000449969
ENSMUSG00000041654	Slc39a11	530.9513967	3.512669033	0.00044363
ENSMUSG00000038319	Kcnh2	435.9517188	3.540030808	0.00040008

ENSMUSG00000072875	Gpr27	48.43966069	3.592778882	0.00032717
ENSMUSG00000030123	Plxnd1	198.1674512	3.599134138	0.000319278
ENSMUSG00000030737	Slco2b1	346.1020829	3.612432569	0.000303338
ENSMUSG00000044813	Shb	100.4488684	3.612870368	0.000302826
ENSMUSG00000026854	Usp20	2873.259747	3.615589468	0.000299665
ENSMUSG00000058886	Deaf1	830.335276	3.623443084	0.000290707
ENSMUSG00000034863	Ano8	709.8091145	3.634711191	0.000278291
ENSMUSG00000079293	Clec7a	10.18073431	3.638625251	0.000274097
ENSMUSG00000053399	Adamts18	22.69072692	3.655035495	0.000257146
ENSMUSG00000000982	Ccl3	3.544989877	3.658956098	0.000253245
ENSMUSG00000032485	Scap	1378.346635	3.759391332	0.000170327
ENSMUSG00000081229	Lamr1-ps1	121.2074032	3.779282385	0.000157281
ENSMUSG00000056427	Slit3	1493.17123	3.796664989	0.000146656
ENSMUSG00000023992	Trem2	227.3834683	4.000268125	6.33E-05
ENSMUSG00000029119	Man2b2	419.3004351	4.040657761	5.33E-05
ENSMUSG00000053897	Slc39a8	66.08527131	4.049272813	5.14E-05
ENSMUSG00000040811	Eml2	2783.57873	4.054130132	5.03E-05
ENSMUSG00000037579	Kcnh3	1074.08372	4.178081129	2.94E-05
ENSMUSG00000044534	Ackr2	14.92060946	4.218075331	2.46E-05
ENSMUSG00000017417	Plxdc1	140.9632295	4.446459374	8.73E-06
ENSMUSG00000050141	BC049635	62.53808218	4.827188452	1.38E-06
ENSMUSG00000068129	Cst7	11.72707481	4.846920775	1.25E-06
ENSMUSG00000020747	2310067B10Rik	1207.75054	6.240504499	4.36E-10
ENSMUSG00000019969	Psen1	1979.980658	7.514152292	5.73E-14
ENSMUSG00000022892	App	56905.91711	14.05709688	6.97E-45
ENSMUSG00000079037	Prnp	35133.02493	16.35464497	4.03E-60

6.6 List of genes with low H3K4me3 levels in 6-month

APP/PS1 mice by ChIP-seq

Gene ID	chromosome	Gene Symbol	width	Fold	P value
16798	chr13	Lats1	1954	-5.89	7.25E-05
33862	chr4	CG9175	1781	-5.55	7.52E-05
41726	chr5	Dop1R1	2462	-5.58	0.000112
36750	chr4	Mlf	1399	-5.53	0.000129
18230	chr14	Nxn	3706	-6.03	0.000142
29528	chr2	Vamp3	1973	-5.64	0.000146
36980	chr4	-	1785	-5.63	0.00016
18633	chr14	Pex16	1633	-5.55	0.000211
21398	chr17	-	1707	-5.68	0.000256
45465	chr6	I(3)82Fb	1936	-5.59	0.000277
20855	chr16	Stc1	1550	-5.23	0.00033
23870	chr17	-	1329	-5.29	0.000331
57095	chr7	PITHD1	1542	-4.55	0.000352
32237	chr3	-	1190	-5.31	0.000361
16533	chr13	Kcnmb1	2134	-5.07	0.000532
21279	chr16	T(8;16)17H	1598	-5.47	0.000533
43061	chr5	CG10550	1663	-5.48	0.000592
18984	chr15	Por	1641	-5.3	0.000612
35816	chr4	CSN7	2153	-5.48	0.000648
44597	chr6	I(2)31Ef	1741	-4.9	0.000678
19770	chr15	-	982	-4.58	0.000695
31497	chr2	CG4078	982	-4.75	0.000842
18582	chr14	Pde6d	1190	-5.17	0.000852
4540	chr11	ND5	834	-5.18	0.000932
30700	chr2	etv4	1147	-4.85	0.000943
45730	chr6	-	889	-4.78	0.00097
39972	chr5	Ccn	1035	-4.96	0.00107
63306	chr7	-	1029	-4.48	0.00109
63723	chr7	-	966	-5.05	0.00113
31094	chr2	CG14785	1099	-5.07	0.00116
19659	chr15	Rbp1	1552	-5.34	0.00118
75111	chrX	4930512H18Rik	1742	-4.95	0.00125
31905	chr3	CG42797	797	-4.78	0.00126
66047	chr8	Mrpl54	937	-5.04	0.00128
21343	chr16	Taf6	904	-4.94	0.00128
45531	chr6	I(1)14Db	1053	-4.89	0.00129
4633	chr11	MYL2	913	-4.46	0.00131
2662	chr10	GDF10	3485	-5.23	0.00134

3823	chr11	KLRC3	1681	-4.52	0.00136
64418	chr8	TMEM168	955	-5.23	0.00138
4594	chr11	MUT	1208	-4.3	0.00143
24428	chr17	-	942	-5.19	0.00145
37043	chr4	Mapmodulin	700	-4.44	0.00155
5583	chr11	PRKCH	1271	-4.67	0.0016
20004	chr15	-	1000	-4.86	0.00171
4983	chr11	OPHN1	1297	-4.94	0.00173
20454	chr16	St3gal5	1548	-4.44	0.00175
32409	chr3	CG14410	963	-4.73	0.00176
16616	chr13	Klk1b21	1247	-5.12	0.00178
24392	chr17	Gja1	2199	-4.81	0.00178
30223	chr2	efna5b	902	-4.39	0.00185
26590	chr18	OR8B7P	1185	-4.76	0.00186
56293	chr7	Slc35g3	1270	-4.74	0.00191
59201	chr7	-	807	-3.75	0.00198
25979	chr18	DHRS7B	890	-4.17	0.00202
10311	chr12	DSCR3	1091	-4.27	0.00213
18498	chr14	-	590	-4.22	0.0022
63300	chr7	-	746	-4.79	0.00223
24077	chr17	-	984	-4.69	0.00228
16553	chr13	Kif13a	1692	-4.39	0.00234
2693	chr10	GHSR	1751	-4.87	0.00238
1472	chr1	CST4	1068	-4.81	0.00239
56296	chr7	Dmrtb1	876	-4.39	0.00239
143	chr1	PARP4	876	-5.11	0.00246
10324	chr12	KLHL41	780	-4.48	0.00247
2705	chr10	GJB1	443	-4.26	0.00254
27025	chr18	-	813	-4.54	0.00262
52154	chr7	D11Ggc2e	863	-4.13	0.00265
36049	chr4	CG2292	318	-4.28	0.00266
44741	chr6	-	971	-4.12	0.00266
45212	chr6	-	748	-4.49	0.00274
20771	chr16	Mucl1	934	-4.51	0.00288
29525	chr2	Pitpna	1071	-4.21	0.00291
66926	chr9	Trmt6	1554	-5.11	0.00298
30390	chr2	cyp19a1a	1017	-4.18	0.00309
1903	chr1	S1PR3	1475	-4.9	0.00313
32483	chr3	Gmap	1062	-4.39	0.00319
61989	chr7	D9Mit310	718	-4.66	0.00324
5715	chr11	PSMD9	3118	-4.29	0.00326
18398	chr14	-	589	-4.33	0.00327
2861	chr10	GPR37	405	-4.37	0.00329
65372	chr8	-	1799	-4.67	0.00333

32643	chr3	CG13010	2447	-5.07	0.00341
40042	chr5	MED11	1009	-4.41	0.00343
1871	chr1	E2F3	1205	-4.7	0.00344
65373	chr8	-	1543	-4.66	0.0035
5012	chr11	OTSC1	570	-4.38	0.00362
30710	chr2	igf2a	1319	-4.61	0.00365
25450	chr17	Gabrb1	2289	-4.17	0.00365
39635	chr5	CG13461	422	-3.87	0.0037
13240	chr13	Defa6	1323	-3.73	0.00371
3434	chr10	IFIT1	1780	-4.53	0.00383
32075	chr3	CG1738	1215	-4.4	0.00383
32169	chr3	Usp7	766	-4.07	0.00383
1899	chr1	-	822	-4.42	0.00388
30492	chr2	-	1528	-4.22	0.00397
121	chr1	-	658	-4.51	0.00399
45787	chr6	l(3)70Ae	1224	-4.43	0.00403
37867	chr4	Dat	1211	-3.95	0.00403
62729	chr7	D19Mit103	2998	-4.22	0.00405
29139	chr2	Dcn	767	-4.09	0.00411
30428	chr2	csnk2b	773	-4.34	0.00412
18930	chr15	-	1767	-4.47	0.00414
73987	chrX	-	761	-3.94	0.00419
66911	chr9	Nudt16l1	765	-4.56	0.0042
45365	chr6	tc	1080	-4.18	0.00423
10946	chr12	SF3A3	1151	-4.77	0.00424
37026	chr4	Sardh	534	-3.7	0.00432
17052	chr14	-	970	-4.47	0.00434
13850	chr13	Ephx2	506	-3.95	0.00436
4101	chr11	MAGEA2	529	-3.97	0.00438
23590	chr17	PDSS1	1149	-4.44	0.00439
2281	chr10	FKBP1B	761	-3.92	0.00442
38266	chr4	-	1415	-3.46	0.00454
18858	chr14	Pmp22	1012	-4.25	0.00459
45625	chr6	-	889	-4	0.00464
42691	chr5	CG45049	352	-3.67	0.00469
16012	chr13	Igfbp6	805	-3.9	0.00471
20573	chr16	-	547	-4.22	0.00477
29988	chr2	SLC2A8	972	-3.83	0.00477
62776	chr7	D16Mit143	1392	-4.05	0.00482
68080	chr9	Gpn3	813	-4	0.00484
63287	chr7	-	803	-4.12	0.00485
1163	chr1	CKS1B	849	-4	0.00485
42810	chr5	Lsd-1	1092	-4.25	0.00491
67528	chr9	Nudt7	1121	-4.31	0.00492

32680	chr3	CG4880	1105	-4.17	0.00494
20727	chr16	-	917	-3.78	0.00495
47470	chr7	-	638	-3.92	0.00499
35652	chr4	Dscam1	485	-3.82	0.00509
26792	chr18	SNORD57	990	-3.76	0.00511
31767	chr3	nAChRalpha3	764	-3.99	0.00513
59071	chr7	-	2202	-4	0.00515
16016	chr13	Ighg2b	1059	-4.1	0.00519
68413	chr9	-	1559	-4.3	0.00528
19465	chr15	Rb(10.15)23Lub	999	-4.5	0.0053
19000	chr15	-	602	-3.76	0.00532
25730	chr17	Ntf4	865	-3.96	0.00533
61980	chr7	D8Mit326	1731	-4.14	0.00536
21526	chr17	Tcra-V2.2	772	-3.95	0.00536
42025	chr5	Fas1	1835	-3.75	0.00542
190	chr1	NR0B1	660	-3.93	0.00544
32871	chr3	Atg101	537	-3.91	0.00548
3005	chr10	H1F0	853	-4.17	0.00553
65456	chr8	-	588	-4.5	0.0056
45039	chr6	Sox100B	616	-3.56	0.00562
45885	chr6	stout	2222	-3.77	0.00565
5123	chr11	-	1553	-4.07	0.00566
24004	chr17	Rai2	992	-3.88	0.00569
2110	chr1	ETFDH	1397	-3.94	0.0057
69937	chrX	-	963	-4.17	0.00574
20658	chr16	Son	1251	-4.26	0.00577
31146	chr2	CG14805	618	-3.85	0.00581
4152	chr11	MBD1	939	-3.87	0.00585
2138	chr1	EYA1	526	-3.7	0.00591
62647	chr7	D14Mit159	839	-4.41	0.00592
5127	chr11	CDK16	1071	-4.18	0.00592
19943	chr15	Rpl28	1026	-4.03	0.00595
75383	chrY	4930599N24Rik	876	-4.19	0.00597
61141	chr7	D9Mit335	872	-4.09	0.00598
52617	chr7	D16Ert550e	1109	-3.87	0.006
74550	chrX	9130007G19Rik	826	-3.71	0.00606
29333	chr2	Cd46	906	-4.12	0.00611
28442	chr19	IGHV3-23	675	-3.66	0.00612
25656	chr17	Guca2a	388	-4.02	0.00614
66186	chr8	-	998	-3.87	0.0062
40367	chr5	sa	837	-4.22	0.00631
45171	chr6	-	705	-3.41	0.00632
199	chr1	AIF1	818	-3.83	0.00633
81	chr1	ACTN4	710	-3.54	0.00633

45927	chr6	sesE	827	-4.07	0.00636
5182	chr11	PEPB	1367	-4.28	0.00649
63963	chr7	-	922	-3.74	0.00652
42408	chr5	-	562	-4.31	0.00654
68469	chr9	Sox6os	1245	-4.53	0.00661
99	chr1	-	1490	-3.91	0.00663
5667	chr11	-	665	-4.23	0.00668
62656	chr7	D15Mit100	654	-3.9	0.00669
60669	chr7	Cmklr1	2023	-4.43	0.0067
24275	chr17	-	987	-3.9	0.00687
42035	chr5	-	757	-3.54	0.00688
34730	chr4	CG16820	472	-3.85	0.00696
63782	chr7	-	1309	-3.89	0.00698
19221	chr15	Ptgfrn	1354	-4.4	0.00702
418	chr1	ART2P	1849	-4.08	0.00702
13585	chr13	-	1805	-4.57	0.00703
28307	chr19	IGHV3OR16-9	668	-4.01	0.00704
3686	chr10	-	1985	-3.72	0.00717
21550	chr17	-	2104	-3.75	0.00718
68063	chr9	-	1835	-4.64	0.00722
16587	chr13	-	1191	-4.15	0.00722
31917	chr3	Ser7	741	-3.64	0.00723
63158	chr7	-	437	-3.96	0.00732
60285	chr7	-	358	-3.65	0.00733
3545	chr10	-	1346	-3.72	0.00738
30083	chr2	nme2b.1	1207	-4.09	0.00743
30242	chr2	mest	887	-3.78	0.00743
45328	chr6	sens	1107	-4.17	0.0075
68777	chr9	Tmem53	423	-3.95	0.00754
30668	chr2	mtnr1bb	610	-3.83	0.00755
5593	chr11	PRKG2	1058	-4.19	0.00756
26814	chr18	SNORD36B	859	-3.85	0.00757
31975	chr3	Or9a	467	-3.63	0.00763
18661	chr14	-	566	-3.99	0.00765
32717	chr3	-	624	-4.05	0.00769
56987	chr7	BBX	1410	-3.79	0.00769
5531	chr11	PPP4C	554	-4.05	0.00776
4360	chr11	MRC1	666	-3.99	0.0079
39638	chr5	CG13460	563	-4.17	0.00791
63212	chr7	-	697	-3.62	0.00795
42988	chr5	CG13646	473	-3.32	0.00798
42815	chr5	-	1726	-4.06	0.00802
67769	chr9	Gpatch2	3050	-3.36	0.00809
3020	chr10	H3F3A	1136	-3.79	0.00821

21347	chr16	-	387	-3.25	0.00834
43105	chr5	LpR2	612	-4.14	0.00837
68296	chr9	-	1153	-4.02	0.00837
30065	chr2	elav1b	1035	-3.71	0.00837
31218	chr2	CG14050	580	-4.02	0.00845
27124	chr19	INPP5J	503	-3.64	0.00852
2844	chr10	GPR21	718	-3.66	0.00855
30123	chr2	wnt4a	1239	-3.82	0.00859
75091	chrX	4930520A20Rik	523	-3.58	0.00865
33527	chr4	CG15403	554	-3.57	0.0087
33657	chr4	CG15436	933	-4.09	0.00872
27128	chr19	CYTH4	627	-3.86	0.00879
3473	chr10	-	597	-3.53	0.00879
67425	chr9	Eps811	1313	-3.75	0.0088
2003	chr1	ELK2AP	1221	-3.72	0.00881
27529	chr19	D0Mnp3	1011	-4.06	0.00884
59107	chr7	Ltbp1	323	-3.85	0.00885
62707	chr7	D17Mit150	707	-3.44	0.00886
28044	chr19	D3Wsu167e	683	-3.82	0.00888
33081	chr3	Cbs	894	-3.8	0.00904
33813	chr4	-	694	-3.49	0.00905
65989	chr8	DLK2	645	-4.15	0.0091
26992	chr18	Brd7	583	-3.59	0.00912
45376	chr6	prd5	1252	-4.26	0.00915
67492	chr9	Zfand4	783	-3.74	0.00917
16034	chr13	-	983	-3.67	0.00919
45495	chr6	l(2)32Af	1139	-3.94	0.0092
67510	chr9	Tvp23b	1220	-3.61	0.00922
1559	chr1	CYP2C9	1958	-3.94	0.00933
32846	chr3	Bx	816	-3.86	0.0094
53033	chr7	-	1006	-3.84	0.0094
19417	chr15	Rasgrf1	1027	-3.77	0.00943
17056	chr14	-	1696	-4.25	0.00947
2895	chr10	GRID2	769	-3.82	0.00956
32073	chr3	GCS1	603	-3.74	0.00957
1154	chr1	CISH	839	-4.23	0.00969
65282	chr8	-	705	-4.06	0.00969
8247	chr12	-	1457	-3.96	0.00972
33828	chr4	Vm26Ac	921	-3.8	0.00976
39419	chr4	eyg	3547	-3.53	0.00988
24430	chr17	-	595	-3.98	0.00995
23427	chr17	-	483	-3.93	0.00995
16006	chr13	Igfbp1	1526	-3.49	0.00997

6.7 Curriculum Vitae

Family Name: ZHANG

First Name: Pei

Date of Birth: 20-12-1988

Nationality: Chinese

Contact Information:

CNRS/IINS UMR5297, 146 Rue Léo-Saignat

33077 Bordeaux, France

zhangp1841@gmail.com;

+33-(0)753708295

Educational Background:

2013 Sep. – 2017 Jun. PhD candidate of Neuroscience

Erasmus Mundus Joint Doctorate Scholarship/ENC-network cycle 4

Home lab: Christophe Mulle, IINS Bordeaux France;

Host lab: Andre Fischer, DZNE Goettingen Germany

2011 Sep. - 2013 Aug. Master of Neuroscience

Erasmus Mundus Joint Master's Scholarship/Neurasmus

Charité Universitätsmedizin, Berlin Germany + University of Bordeaux, France

2005 Sep. - 2011 Jul. Bachelor of Clinical Medicine

Medical School, Tongji University, Shanghai, China

2010 Jul. - 2010 Sep. Clinical Internship

Department of Anesthesia and Department of Neuropsychiatry

UMass Memorial Hospital, Massachusetts, USA

2007 Oct. - 2008 Sep. NISP exchange program

courses in biomedicine and Japanese language, research internship

Neuroanatomy Department of medical school, Nagasaki University, Japan

Research Experiences:

1) PhD project (Supervisor: Prof. Dr. Christophe Mulle, IINS, Bordeaux, France; Prof. Dr. Andre Fischer, DZNE, Goettingen, Germany)

Plasticity of local CA3 circuits in mouse models of Alzheimer's disease: involvement of epigenetic mechanisms.

2) Computational Neuroscience Workshop project (OCNC2016, Okinawa University, Japan)

Predicting the major interneuron subtype in feedforward inhibition in a hippocampal DG-CA3 circuit model

3) Master thesis project (Supervisor: Prof. Dr. Stephan Oliet, Dr. Aude Panatier, INSERM, Bordeaux, France)

Electrophysiological study on astrocytes in rat hippocampal CA1 area: how astrocytes regulate synaptic transmission in tripartite synapses?

4) Master lab rotation 2 (Supervisor: Prof. Dr. Andrew Plested, Leibniz Institute for Molecular Pharmacology, Berlin, Germany)

Random mutagenesis in GluA2 ligand binding domain and kinetic analysis of mutant iGluRs using outside-out patch-clamp and ultrarapid perfusion technique.

5) Master lab rotation 1 (Supervisor: Prof. Dr. Ulf Strauss, Charite University of Medicine, Berlin, Germany)

Lysophosphatidic Acid (Fuhrer et al.) Increases mEPSC Frequency in Neuronal Cultures and Reduces Ih in both HEK293 Cells and Acute Mice Hippocampal Slices.

6) Lab Assistance in molecular biology research (Supervisor: Prof. Dr. Mori Nozomu, University of Nagasaki, Japan)

Laboratory skills:

electrophysiology (whole-cell patch-clamp in acute slices and neuronal cultures, outside-out patch-clamp)

behavioral tests (contextual fear conditioning, Morris water maze, Y-maze, open-field object recognition)

genetic & epigenetic methods (qPCR, mutagenesis, CHIP-seq, transcriptome-seq)

cell culture (HEK cells, hippocampal primary neurons, cortical astrocytes)

confocal imaging of mossy-fiber terminals (3D reconstruction and deconvolution using Imaris software)

optogenetics (stereotaxic injection and ex-vivo recording)

Western blot, and immunohistochemistry.

Publications:

1) Silva SV, Haberl M, **Zhang P**, Bethge P, Lemos C, Goncalves N, Gorlewicz A, Malezieux M, Goncalves FQ, Grosjean N, Blanchet C, Frick A, Nägerl V, Cunha R, Mulle C. Early synaptic deficits in the APP/PS1 mouse model of Alzheimer's disease involve neuronal adenosine A2A receptors. *Nature Communication*, #NCOMMS-15-09884B

2) Zhuang J, Luan P, Li H, Wang K, **Zhang P**, Xu Y, Peng W. The Yin-Yang Dynamics of DNA Methylation Is the Key Regulator for Smooth Muscle Cell Phenotype Switch and Vascular Remodeling. *Arterioscler Thromb Vasc Biol.* 2017 Jan;37(1):84-97.

3) **ZHANG P**; IKEJIMA T; MORI N. Regulatory effects of Shc-related phosphotyrosine adaptor proteins on aging [J]. *Acta Pharmaceutica Sinica*, 43 (8): 793-800, 2008

4) Accepted at Nature Neuroscience as co-second author: Altered surface mGluR5 dynamics provoke synaptic NMDAR dysfunction and cognitive defects in Fmr1 knockout mice. NCOMMS-16-09515D.

5) Submitted as co-first author: Input-specific synaptic alterations in CA3 pyramidal cells at an early stage in a mouse model of Alzheimer's disease.

Awards and Honors:

2016: Travel grant for FENS 2016 by French Neuroscience Society

2013-2016: Erasmus Mundus Scholarship for Joint Doctorate program

2011-2013: Erasmus Mundus Scholarship for European Master's program

2009: the National Scholarship

first-class scholarship for excellent study of Tongji University

honor of outstanding student of medical school of Tongji University

2008: JASSO (Japanese Student Service Organization) scholarship

2007: first-class scholarship for excellent study of Tongji University

third prize of Academic Festival of medical school of Tongji University

2006: the National Scholarship

first-class scholarship for excellent study of Tongji University

third prize of National English Contest for College Students (NECCS)

honor of outstanding student of Tongji University

Computational and language skills:

R: Basic knowledge in R programming and its application in RNA-seq data analysis

Visual Basic: National Certificate in Computing, Level 2

Octave: Coursera online education completed: Machine learning (11-week course, by Dr. Andrew Ng, Stanford University). Also basic knowledge in **Python**, and **MATLAB**.

Chinese: mother tongue

English: Certificate of Shanghai English Interpretation Accreditation (Advanced Level)

GRE (2010.6) ----- 670 (Verbal, 95%) + 800 (Quantitative, 94%) + 3.5 (Analytical Writing)

TOFEL (2010.7) ----- 113 (IBT: Reading 30 + Listening 28 + Speaking 26 + Writing 29)

Japanese: Language Proficiency Test Level 1 (the most advanced level)

German language level: B2 (Goethe Certificate B2)

French language level: B2 (DELFB2 Certificate)